The Experimental Design of Radio-over-Fibre System for 4G Long Term Evolution

Thavamaran Kanesan

A thesis submitted in partial fulfilment of the requirements of the University of Northumbria at Newcastle for the degree of Doctor of Philosophy

Research undertaken in the School of Computing, Engineering and Information Sciences

February 2013

Abstract

The 3rd Generation Partnership Project (3GPP) Long Term Evolution (LTE) is the potential key to meet the exponentially increasing demand of the mobile end users. The entire LTE network architecture and signal processing is carried out at the enhanced NodeB (eNB) level, hence the increased complexity and cost. Therefore, it is not efficient to deploy eNB for the purpose of extending the network coverage. As a solution, deployment of relay node (RN), with radio-over-fibre (RoF) acting as the interface between eNB and RN is proposed. Due to the high path loss and multipath fading, wireless interface would not be the ideal channel between eNB and RN. A detailed investigation is carried out by comparing the Rayleigh multipath fading channel with the optical fibre channel, where the latter achieved a ~31 dB of signal-to-noise ratio (SNR) gain. The distributed feedback laser (DFB) is selected as the direct modulated laser (DML) source, where the modulation method introduces a positive frequency chirp (PFC). The existing mathematical expression does not precisely explain on how the rate equations contribute to PFC. Therefore, an expression for PFC is proposed and derived from the carrier and photon densities of the rate equations. Focusing on theoretical development of DML based RoF system, a varying fast Fourier transform (FFT) scheme is introduced into LTE-Advanced (LTE-A) technology as an alternative design to the carrier aggregation. A range of FFT sizes are investigated with different levels of optical launch power (OLP), the optimum OLP has been defined to be within the range of ~-6 to 0 dBm, which is known as the intermixing region. It is found that FFT size-128 provides improved average system efficiency of ~54% and ~65% in comparison to FFT size-64 and FFT size-128, respectively, within the intermixing region. While fixing FFT size to 128, the investigation

is diverted to the optimisation of optical modulators. The author revealed that the performance of dual electrode-Mach Zehnder modulator (DE-MZM) is superior to both DML scheme and single electrode (SE)-MZM, where DE-MZM achieved a transmission span of 88 km and 71 km for 16-quadrature amplitude modulation (QAM) and 64-QAM, respectively. At the initial experimental link design and optimisation stage, an optimum modulation region (OMR) is proposed at the optical modulation index (OMI) of 0.38, which resulted in an average error vector magnitude (EVM) of ~1.01% for a 10 km span. The EVM of ~1.01% is further improved by introducing the optimum OLP region at –2 dBm, where the observed average EVM trimmed to ~0.96%. There is no deviation found in the intermixing region by transmitting the LTE signal through a varying transmission span of 10 to 60 km, additionally, it was also revealed that the LTE RoF nonlinear threshold falls above the OLP of 6 dBm. The proposed system was further developed to accommodate 2×2 multiple-input and multiple-output (MIMO) transmission by utilising analogue frequency division multiplexing (FDM) technique. The studies procured that the resulting output quality of signal at 2 GHz and 2.6 GHz is almost identical with a twofold gain in the peak data rate and no occurrence of intermodulation (IMD). In order to emulate the complete LTE RoF solution, an experimental design of full duplex frequency division duplex (FDD) system with dense wavelength division multiplexing (DWDM) architecture is proposed. It is found that channel spacing of 50 MHz between the downlink (DL) and uplink (UL) introduces severe IMD distortion, where an adjacent channel leakage ratio (ACLR) penalty of 14.10 dB is observed. Finally, a novel nonlinear compensation technique utilising a direct modulation based frequency dithering (DMFD) scheme is proposed. The LTE RoF system average SNR gain observed at OLP of 10 dBm for the 50 km transmission span is ~5.97 dB. External modulation based frequency dithering (EMFD) exhibits ~3 dB of average SNR gain over DMFD method.

Acknowledgements

The journey of my PhD studies was the most challenging and interesting with a steep learning curve that I have been through so far. I would like to sincerely express my deepest gratitude to all the people who guided me through my PhD journey and effectively aided me in reaching to this end point.

First and foremost, I would like to thank my principal advisor, Dr. Wai Pang Ng, who gave me the opportunity to carry out research within the optical communications research group. I am very fortunate to have such great advisor with excellent experience, who not only guided me through the technical phase, but also strongly advised on being a good researcher and overall on how to be a person with excellent personality. I was amazed with his expertise of breaking down problems, which thought me the skill of looking at any problems with different perspective. Prof. Zabih Ghassemlooy, another great teacher who I am greatly indebted to. In addition to his excellent ideas and research feedback, he thought me the management skills and inspired me by doing so much in a very little time. I wish to express my sincere gratitude to Dr. Krishna Busawon for helping me in the toughest phase of my PhD that resulted in the finding of a new equation. I would also like to thank Prof. Lu Chao from The Hong Kong Polytechnic University for his constructive comments during the dissemination of the results that I produced throughout my PhD study.

Northumbria University Studentship had played a big role in my PhD, thus I would like to express my gratitude to the Faculty of Engineering and Environment, Northumbria University. My colleagues had contributed both directly and indirectly to my research, Arash Bahrami who thought me the basics of MATLAB, Ahmed Abd El Aziz Shalaby who worked with me to solve the laser rate equations, Sujan Rajbhandari who was always

there when I seek for help, Richard Jay Brown who volunteered to prove read my thesis, and the rest of my colleagues from E411 and E409 of Ellison building that made my life exceptionally interesting.

Finally, I owe everything that I have achieved to my family. My parents who have invested most of their savings into my education and still lives far apart to support my expenses here, my brother who inspired me and showed the importance of education, my sister in law that always encouraged me, and finally I thank my lovely girlfriend for her strong support and endless encouragement throughout my journey here.

As a conclusion to my journey, I dedicate this thesis and all the hard work to my family.

Declaration

I declare that the work contained in this thesis has not been submitted for any other award and that it is all my own work. I also confirm that this work fully acknowledges opinions, ideas and contributions from the work of others.

Name: Thavamaran Kanesan

Signature:

Date:

Table of Contents

Glossary of Acronyms

1G	1st generation
2G	2nd generation
3G	3rd generation
3GPP	3rd Generation Partnership Project
4G	4th generation
ACLR	Adjacent channel leakage ratio
AF	Amplifying and forwarding
AGW	Access gateway
AMPS	Advanced mobile phone system
APD	Avalanche photodiode
ARB	Analogue radio bandwidth
ASE	Amplitude spontaneous emission
BER	Bit error rate
BFS	Broad frequency spacing
BS	Base station
BSC	Base station controller
BTB	Back-to-back
BTS	Base transceiver station
BWDM	Broad wavelength division multiplexing
CAPEX	Capital expenditure
CD	Chromatic dispersion

CO-OFDM	Coherent optical-orthogonal frequency division multiplexing
CP	Cyclic prefix
CS	Central station
CWDM	Coarse wavelength division multiplexing
CWG	Continuous wave generator
DAC	Digital-to-analogue converter
DC	Direct current
DD	Direct detection
DE-MZM	Dual electrode-Mach Zehnder modulator
DF	Demodulation and forward
DFB	Distributed feedback laser
DFT	Discrete Fourier transform
DL	Downlink
DM	Direct modulation
DMFD	Direct modulation based frequency dithering
DML	Direct modulated laser
DSM	Dynamic single mode
DWDM	Dense wavelength division multiplexing
EDFA	Erbium doped fibre amplifier
EMFD	External modulation based frequency dithering
eNB	Enhanced NodeB
EVM	Error vector magnitude
FDD	Frequency division duplex

FDM	Frequency division multiplexing
FFT	Fast Fourier transform
FWHM	Full-width half-maximum
FWM	Four wave mixing
GPRS	General packet radio service
GSM	Global System for Mobile Communications
hNodeB	Home NodeB
HPA	High power amplifier
ICI	Inter-carrier interference
IF	Intermediate frequency
IFFT	Inverse fast Fourier transform
IFS	Intermediate frequency spacing
i.i.d	Independent and identically distributed
IMD	Intermodulation
IIP3	Third-order input intercept point
IM	Intensity modulation
InGaAsP	Indium Gallium Arsenide Phosphide
ISI	Inter-symbol interference
ITU	International telecommunication union
LED	Light emitting diode
LI	Light current
LNA	Low noise amplifier
LO	Local oscillator

LTE	Long Term Evolution
LTE-A	Long Term Evolution-Advanced
MCF	Mode confinement factor
MCM	Multi-carrier modulation
MIMO	Multiple-input and multiple-output
MMF	Multimode fibre
MZM	Mach Zehnder modulator
NF	Noise figure
NFS	Narrow frequency spacing
NLOS	Non-line-of-sight
OBE	Out-of-band emission
OBPF	Optical bandpass filter
OFDM	Orthogonal frequency division multiplexing
OIP3	Third-order output intercept point
OLP	Optical launch power
OMI	Optical modulation index
OMR	Optimum modulation region
OOFDM	Optical orthogonal frequency division multiplexing
OPEX	Operating expenditure
OSA	Optical spectrum analyser
OSNR	Optical signal-to-noise ratio
PAPR	Peak-to-average ratio
PD	Photodetector

PFC	Positive frequency chirp
PM	Phase modulation
POLMUX	Polarization multiplexing
QAM	Quadrature amplitude modulation
QoS	Quality-of-service
QPSK	Quadrature phase shift keying
RF	Radio frequency
RIN	Relative intensity noise
RN	Relay node
RNC	Radio network controller
RoF	Radio-over-fibre
RSOA	Reflective semiconductor optical amplifier
SA	Signal analyser
SBS	Stimulated Brillouin scattering
SC-FDM	Single carrier-frequency division multiplexing
SCM	Single carrier modulation
SE-MZM	Single electrode-Mach Zehnder modulator
SFDR	Spurious free dynamic range
SMF	Single mode fibre
SMSR	Side mode suppression ratio
SNR	Signal-to-noise ratio
SPM	Self phase modulation
SRS	Stimulated Raman scattering

UE	User equipment
UL	Uplink
UMTS	Universal mobile telecommunication system
VCSEL	Vertical cavity surface emitting laser
VOA	Variable optical attenuator
VSG	Vector signal generator
WCDMA	Wideband code division multiplexing
WDM	Wavelength division multiplexing
WLAN	Wireless local area network
XPM	Cross phase modulation

Glossary of Symbols

A	Magnitude of the applied current
A_{12}	Absorption coefficient
A_{21}	Spontaneous emission coefficient
a	Optical fibre core radius
a_n	Coefficient of polynomial fitting on the curve
B	Bimolecular carrier recombination coefficient
B_{21}	Stimulated emission coefficient
B_d	Data rate of the propagating signal
B_T	Total bandwidth of OFDM signal
B_w	Bandwidth of signal
C	Auger carrier recombination coefficient
c	Speed of light
D	Chromatic dispersion parameter
$\check{D}(z,t)$	Linear operator
d	Thickness
dN/dt	Rate of change of carrier density
$dN_{1,abs}/dt$	Absorption rate
$dN_{2,spon}/dt$	Spontaneous emission rate
$dN_{2,stim}/dt$	Stimulated emission rate
dS/dt	Rate of change of photon density
$dx(t)/dt$	Represents rate of change of carrier density, photon density, and optical phase for numerical solving

dZ/dt	Rate of change of instantaneous process
E_1	Energy at ground state
E_2	Energy at excited state
$E\{.\}$	Expectation operator
$E_i(t)$	Input optical field of MZM
$E_o(t)$	Output optical field of MZM
e	Electronic charge
$erfc(x)$	Complementary error function
f	Operating frequency of the propagating signal
f_d	Dithering frequency
f_L	Dithering boundary limit
f_m	Signal frequency
f_{RF}	Carrier frequency of the OFDM signal
f_{UL}	Uplink carrier frequency
G	Linear optical gain coefficient
g_B	SBS gain
h	Planck's constant
h_s	Propagation steps taken to reach the actual complete SMF length
hv	Photon energy
I_1	Average photocurrents corresponding to one symbol level
I_2	Average photocurrents corresponding to zero symbol level
I_d	Input signal
$I_{d1}(t)$	First tone for SFDR measurement

$I_{d2}(t)$	Second tone for SFDR measurement
$I_{two\text{-}tone}(t)$	Two-tone input for SFDR measurement
k	Adiabatic chirp coefficient
k_B	Boltzmann's constant
L	Transmission length
$L(I_d(t))$	Output optical power in terms of light
LW	Linewidth enhancement factor
l	Length
l_t	Localized topology
M	FFT length for signal spreading
$M_{b/s}$	Bits/symbol that varies with modulation schemes
m	Subcarrier index
N	Carrier density
N_1	Ground state
N_2	Excited state
N_{cp}	CP length
N_e	Excess carrier density
N_s	Total subcarriers
N_t	Transparency carrier density
$\check{N}(z,t)$	Nonlinear operator
n	Time domain index
n_1	Refractive index of core
n_2	Refractive index of cladding

n_{cp}	CP subcarrier index
n_{nl}	Nonlinear refractive index
n_{np}	Number of photons in the laser resonator
n_{o}	Linear refractive index
n_{p}	Phase refractive index
n_{r}	Optical fibre refractive index
$OSNR_{1nm}$	OSNR measurement at 1 nm scale
P	Optical power
P_{avg}	Optical average power
P_{pp}	Optical peak-to-peak power
$P^{SBS}{}_{th}$	SBS threshold
$P(v)$	Spectral density of electromagnetic energy
$P(z,t)$	Optical power with a respective propagated distance
Q	Quality factor
R_{max}	Maximum magnitude of the ideal transmitted symbol
$R_{RFDL}(t)$	Received downlink signal
$R_{RFUL}(t)$	Received uplink signal
S	Photon density
$S_{CPUL}(t)$	Uplink signal with CP appended
$S_{cp}(n)$	OFDM signal with CP
$S_{cp}(t)$	Continuous OFDM signal with CP
$S_{d}(t)$	Dithering signal
$S(n)$	OFDM signal

$S_{RF}(t)$	Up-converted RF OFDM signal
$S_{RFUL}(t)$	Uplink signal up-converted to RF signal
$S_r(n)$	Received OFDM signal
$S_t(n)$	Transmitted OFDM signal
$S_{UL}(n)$	Localized mapped SC-FDM signal
T	Absolute temperature
T_{coh}	Coherence time of the laser after dithering
T_o	Time step
t	Continuously varying time of the input signal
t_B	Temporal boundary condition
t_{lim}	Symbol period
t_o	Beginning of a symbol period
u	Frequency domain spreading/subcarrier index
V	Normalized frequency
V_{bias}	MZM biasing voltage
$V(t)$	Input electrical signal to MZM
V_π	Half-wave voltage
v_g	Group velocity
w	Width
w_h	Horizontal widths
w_v	Vertical widths
X	Coupling efficiency
$X(m)$	Composite subcarriers of zeros and modulated symbols

$x(t)$	Represents carrier density, photon density, and optical phase for numerical solving
$X_{UL}(l_t)$	Frequency domain symbols mapped with localized topology
$X_{UL}(m)$	Composite subcarriers of zeros and modulated symbols for uplink
$X_{UL}(u)$	Frequency domain symbols
Z	Instantaneous process
z	Distance propagated
α	SMF attenuation
$\alpha_{sig\text{-}se}$	Polarization factor
β_2	Second order dispersion coefficient
Γ	Mode confinement factor
Δ	Normalized index difference
Δf	Subcarrier frequency
$\Delta S_d(t)$	Equivalent of Wiener process
Δv_B	SBS linewidth
Δv_L	Laser linewidth
$\Delta v(t)$	Instantaneous frequency deviation
$\Delta\phi(t)$	Van-der-Pol model of laser noise
ε	Nonlinear gain coefficient
ζ	Fraction of spontaneous emission
λ	Propagating wavelength
σ_0	Standard deviation of the zero symbol level
σ_1	Standard deviation of the one symbol level
τ_c	Carrier decay rate

τ_{coh}	Coherence time of the laser
τ_{cohd}	Coherence time of the dithering signal
τ_p	Photon decay rate
ω_{RF}	Carrier frequency converted from Hz to rad
Φ	Optical phase
ϕ_{NL}	Nonlinear phase impairment
ω	Optical frequency
ω_1	Frequency of the first tone for SFDR measurement
ω_2	Frequency of the second tone for SFDR measurement
ω_o	Central frequency
ω_{RFUL}	Uplink carrier frequency converted from Hz to rad/s

List of Figures

CHAPTER 1 INTRODUCTION

CHAPTER 2 AN OVERVIEW OF RADIO-OVER-FIBRE

CHAPTER 8 NONLINEAR COMPENSATION OF LTE ROF LINK

List of Tables

CHAPTER 1 INTRODUCTION

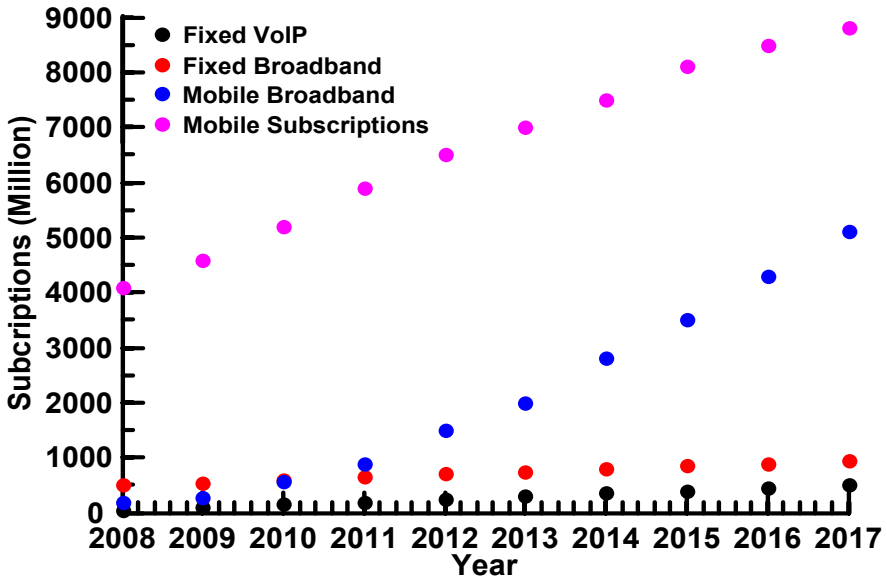

Figure 1.1: The growth of fixed and mobile services [4]

A tremendous growth in information and communication technologies were observed as the end of the millennium approached. Lately, mobile communications matured rapidly from simple voice and text message services to more complex data-driven applications, namely live video streaming, multimedia message and cloud services [1]. Due to the luxurious data-driven applications in mobile communications as an addition to the existing voice application, from 2005 onwards, fixed telephony (wired) services experienced a slow growth pattern [2]. There are also two other fundamental reasons to the rapid evolution of the mobile communication technology, which are as follow [3]:

- Popularization of IEEE 802 wireless technologies
- Market globalization with improved vendors and operators coming from this new framework.

1.1 Growth and Evolution in the Field of Communications

Figure 1.1 illustrates the subscription growths measurement and prediction carried out by Ericsson [4], for both fixed and mobile services from 2008 to 2017. As depicted in

Figure 1.1, fixed line services experienced very minor growth, which has almost reached saturation throughout the year span. In contrast, the mobile broadband as a sub-segment of mobile subscriptions are expected to reach almost 2 billion subscriptions, with complete mobile subscriptions predicted at 7 billion. The reason behind the increase in mobile services subscription compared to fixed services is that mobile operators offer large bundles for free voice calling, and also in some cases, free data services [5].

The actively growing end user subscriptions with bandwidth hungry, high specification, real-time, and delay-sensitive applications have driven mobile communications and as well as the pure wireless communication technologies to continuously progress [3]. From the statistics shown by AT&T, from 2006 to 2009, the mobile data traffic has increased by 5000%. T-Mobile USA reported that the mobile data traffic increased by 45% between the second and third quarter of 2009. The rapid growth in mobile traffic is directly related to the user friendliness in accessing wireless internet via

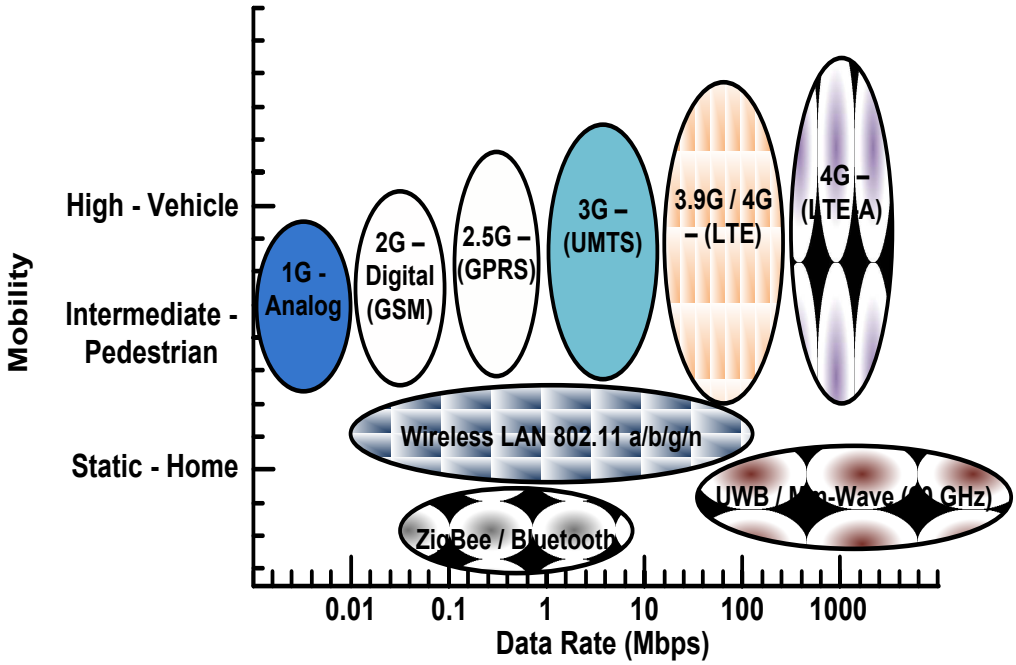

Figure 1.2: The past, present and future of mobile communications.

smartphones and tablet computers [5]. In order to support the rapid increase in mobile traffic, mobile operators have introduced many different network topologies as shown in Figure 1.2. The 1st generation (1G) technology was the pioneer of mobile communications introduced by 3GPP and advanced mobile phone system (AMPS), which operated in the analogue domain, and the successor of 1G was followed by 2nd generation (2G) Global System for Mobile Communications (GSM) operated in the digital domain [6]. Both 1G and 2G were designed for voice transmission, thus an add-on technology was incorporated into GSM, known as general packet radio service (GPRS) to provide the data transmission or mobile broadband for long range communication [7]. All the aforementioned technologies were deployed for intermediate to high mobility scenarios. In parallel, there were also active pure wireless communication technologies, namely wireless local area network (WLAN) - 802.11 a/ b/ g/ n, Zigbee, Bluetooth, ultra-wideband, and the millimetre wave technology designed for short range communications with reduced mobility [8-11].

The 3rd generation (3G) mobile communication technology known as the Universal Mobile Telecommunication System (UMTS) provided an integrated voice and data services [12]. But, as data requirement became increasingly critical, 3GPP established a standard known as LTE and build up frameworks as an evolution to the existing 3GPP radio technologies. The LTE frameworks precisely focus on a development path for GSM and UMTS. The frameworks were divided into two phases where the initial framework involved in the completion of first LTE standardisation and the following framework was focused on the LTE development path towards actual 4th generation (4G) specification known LTE-A. TeliaSonera launched the first commercial LTE service in Stockholm, Sweden, and Oslo, Norway [5]. The detailed specification of both mobile and wireless

communications are presented in Table 1.1, which clearly shows the technology evolution coordinating to the increasing data rate [13].

1.1.1 The Infrastructure of LTE and LTE-A

The principal emphasis of this thesis is on the physical layer of the LTE technology, denoted as the 4G network, shown in Figure 1.2. The first framework of LTE - release 8 was commissioned in December 2008, followed with LTE-A - release 10 established in March 2011 with additional features. There are also controversies that LTE-A technology is the true 4G evolution from 3G, and the LTE technology being the 3.9G network venturing into the 4G domain. Due to the high number of mobile technologies, the labels are merely defined to classify every framework; the crucial matter here is the system evolution, capabilities and meeting the end-user demand. In other words, LTE and LTE-A are the same technology with the common infrastructure, and the latter being the advancement of LTE as a criteria of the International Telecommunication Union (ITU) [13].

The radio access features of LTE and LTE-A technologies are listed in Table 1.2, where the given parameters highlight the explicit difference between the technologies. Since LTE and LTE-A shares the same infrastructure, thus the technologies are designed with some common features, namely the single carrier modulations (SCMs), multi-carrier modulations (MCMs) and receiver equalizer. However, LTE operates with symmetrical transmission, where at any given time, the DL and UL transmits the same bandwidth with uniform transmission parameters. For an example, if DL operates at 20 MHz bandwidth, the occupied subcarriers and FFT size will be 1200 and 2048, respectively, with a fixed cyclic prefix (CP) size and UL will maintain the same configurations. In the case of LTE-A, carrier aggregation comes into play and the available bandwidth ranges from 40 to 100

Table 1.1: Overview of wireless technologies [7-11, 13]

Technology	Tendered Spectrum	Peak Data Rate	Signal Range	Typical Usage
GSM	900 / 1800 MHz	9.6 kbps	35 km	Voice
GPRS	900 / 1800 MHz	160 kbps	35 km	Data
UMTS	873 / 1900 MHz	2 Mbps	2 km	Voice, Data and Multimedia
802.11 a	5 GHz	54 Mbps	100 / 30 m	WLAN
802.11 b	2.4 GHz	11 Mbps	110 / 35 m	WLAN
802.11 g	2.4 GHz	54 Mbps	110 / 35 m	WLAN
802.11 n	2.4 / 5 GHz	150 Mbps	250 / 70 m	WLAN
ZigBee	2.4 GHz	250 kbps	10 m	WPAN
Bluetooth	2.4 GHz	2.1 Mbps	10 m	WPAN
LTE	1.8 / 2.6 GHz	100 Mbps	1 km	High Speed Data
LTE-A	1.8 / 2.6 GHz	1 Gbps	1 km	High Speed Data
UWB	3.1 - 10.6 GHz	> 100 Mbps	10 m	WPAN
Mm-Wave	57 - 64 GHz	> 1 Gbps	10 m	WPAN

MHz are shared asymmetrically with non-uniform transmitter parameters. In other word, the DL bandwidth could be 20 MHz and the UL bandwidth could be 100 MHz with enabling parallel transmission of multiple LTE signals [14].

In the LTE network architecture, the design is altered with a cost efficient 2 node architecture, namely the access gateway (AGW) and eNB which operates as the core network and radio access network, respectively. Compared to the legacy GSM base transceiver station (BTS) and UMTS NodeB or otherwise known as home NodeB (hNodeB) specifically designed for indoor wireless applications with similar operating characteristics as NodeB [15], LTE eNB is by far more complicated than any of its counterpart. The reason behind this is that eNB have a huge built in density of all relevant signal processing equipments and major network architectures [16, 17].

Table 1.2: Overview of LTE and LTE-A [80]

Parameters	LTE	LTE-A
Single carrier modulations	QPSK, 16-QAM and 64-QAM	QPSK, 16-QAM and 64-QAM
Multi-carrier modulations	Downlink: OFDM, Uplink: SC-FDM	Downlink: OFDM, Uplink: SC-FDM
Occupied subcarriers	72, 180, 300, 600, 900, and 1200	Carrier aggregation
FFT size	128, 256, 512, 1024, 1536, and 2048	Carrier aggregation
Cyclic prefix length	Normal: 1/14, Extended: 1/4	Carrier aggregation
Radio bandwidth	1.4, 3, 5, 10, and 20 MHz	Carrier aggregation into 20 to 100 MHz
Duplexing	FDD and TDD, Symmetrical	FDD and TDD, Symmetrical and asymmetrical
MIMO	Up to 4x4	Up to 8x8
Capacity	800 active users per cell in 20 MHz bandwidth	Up to 3 times higher than LTE
Receiver equalizer	Zero forcing	Zero forcing

1.2 Problem Statement

In the radio access network of LTE, eNB functions as the base station similar to GSM BTS and UMTS NodeB, but the contrast in eNB reflects via the 2 node architecture leading to an operating characteristic of not depending in a central controller. In the case of GSM BTS or UMTS NodeB, there is an independent central controller consists of the radio network controller (RNC) and a base station controller (BSC). Conversely, the eNB architecture is designed with all the built-in function of a central controller with the radio access network as well, which makes it a smart, costly and complex BS of LTE [17].

In addition, the vastly allocated spectrum for LTE in urban locations throughout the world are either 2.6 GHz or 1.8 GHz, with the legacy 3G core band of 2 GHz might be re-farmed for LTE applications in the near future [13, 18, 19]. The drawbacks of such a configuration would be [18-20]:

- In the operating spectrum of urban locations, the LTE signal would face a high path loss from air transmission compared to the technologies operating at lower frequencies [19]. For an example, the typical free space isotropic path loss at 1 km transmission distance and an operating frequency of 2.6 GHz is ~100.75 dB. In addition, the extended Okumura Hata model demonstrates a 1 km path loss of ~107 dB at 2.6 GHz band [21].

- Urban locations have the nature of non-line-of-sight (NLOS) operating condition, which will result in multipath propagation and considering the aforementioned path loss, the defect would be highly severe to LTE signals in terms of the coverage area [19].

- The cell size of eNB in urban locations is much smaller than any of its former technology where the typical cell radius is 1 km [18, 22, 23]. The user equipments (UE) at the cell edge will experience critical problems due to the deterioration in SNR owing to the high path loss and multipath propagation. A trivial solution for this problem is to employ a high density of eNB to achieve the satisfactory capacity [20], in other word, deploy eNB at every 1 km radius [18, 22, 23].

- The scenario of increased eNB deployment will lead to access growth of the capital expenditure (CAPEX) and operating expenditure (OPEX), hence higher cost per delivered bit [24].

- Injecting more power from eNB and UE to overcome the path loss will add to the complexity and burdens the high-power amplifiers (HPA) at eNB. It also greatly effects the battery lifetime of the respective UEs due to the power consumption caused by HPAs [19].

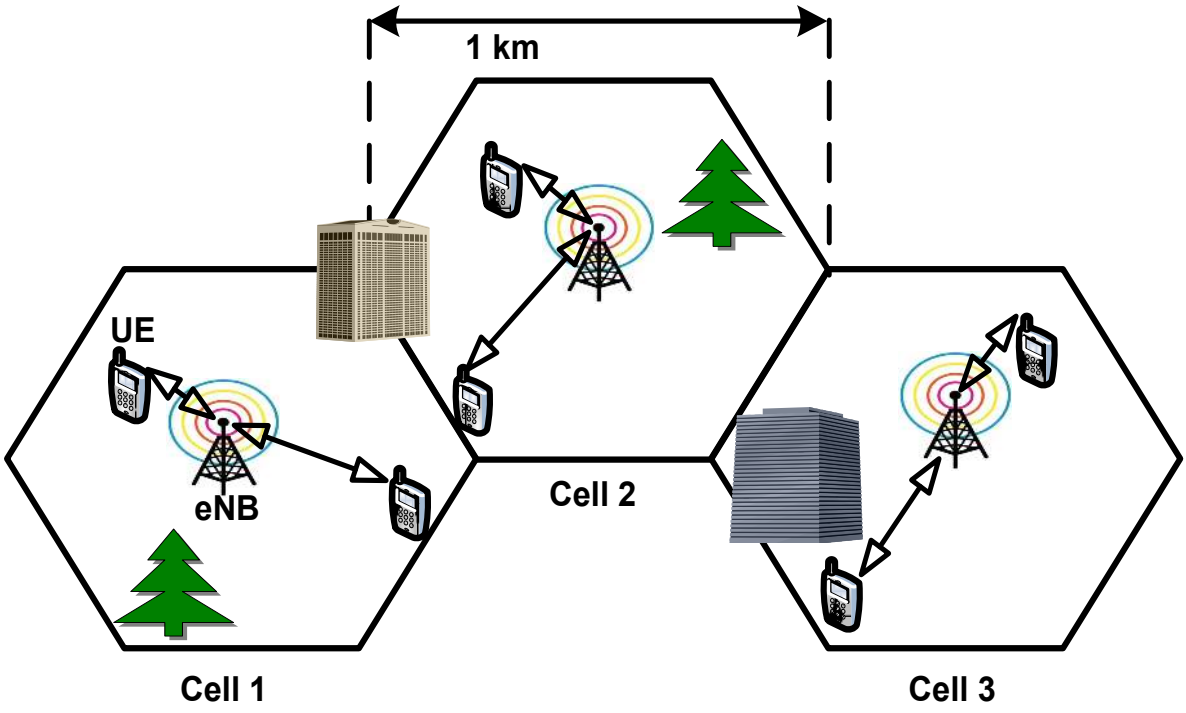

Figure 1.3: Conceptual full duplex LTE radio access network structure in urban area.

Hence, the LTE structure is not realistic in terms of the capacity, coverage, quality-of-service (QoS) and the deployment cost using the existing infrastructure, i.e. increasing eNB. Despite the fact that LTE radio access network employs complex technologies, including varying SCMs, orthogonal frequency division multiplexing (OFDM), and varying radio bandwidths as shown in Table 1.2, these complex technologies will not aid in improving the cell edge throughput. The urban LTE spectrum and NLOS connectivity induces severe loss and multipath propagation, respectively, which can be mitigated by transmitting lower order SCMs for reduced data rate, but such mitigation defeats the purpose of LTE technology. The criticalness of the path loss can be observed in [18, 22, 23] where the cell size of eNB is limited to 1 km. Furthermore real-time data from [25] exhibits that UE potentially receives a data rate of less than 20 Mbps at the cell edge from eNB, with NLOS path in an urban environment due to multipath propagation. Figure 1.3 illustrates the conceptual existing field deployment of LTE network in an urban area, where eNB is deployed at every consecutive cell with a 1 km radius to provide adequate

coverage and such scenario directly increases the CAPEX and OPEX due to the high complex structure of eNB. Cells are labelled as cell 1, cell 2, and cell 3, and the eNB is wirelessly connected to the UE within the respective cell. In order to avoid the increasing cost and to further improve the cell edge performance for LTE, a network extension solution with seamless integration is required for urban areas. Radio relaying with deploying RN at the cell edge and connected to eNB appears to be one of the most promising solutions.

There are various types of relay schemes exist for physical layer realizations, including [26]:

- The amplifying and forwarding (AF) type RN is widely known as a repeater, where a receiving signal is simply amplified and forwarded to UE. This AF scheme is very low in complexity, which reflects a lower cost and importantly only adds a small delay to the incident latency. The shortcoming of AF scheme is that it amplifies the noises that co-exist with the receiving signal.

- Selective decode and forward type RN decodes and examines the received signal using cyclic redundancy check, where signals with high QoS will be forwarded to UE. This scheme is effective for avoiding the low QoS signal with a requirement of long processing delay and strongly increases the latency.

- Demodulation and forward (DF) type RN demodulates the received signal, performs a hard decision, re-modulate and transmits the new signal to UE. DF method enhances the QoS of the new signal, but adds delay to the existing latency.

The previously reported research on LTE cell extension only deployed DF type RN as the preferable relaying technique with wireless interface between eNB and RN [23, 25, 27,

28]. As wireless interface is limited by the path loss and multipath propagation, AF type RN is not the desired method. Nagata *et al* [27] demonstrated throughput gains of 6.1% and 10.3% at the cell edge, by employing AF and DF type RN with wireless interface, respectively, which shows the shortcoming of AF type RN. Peng *et al* [23] presented a throughput gain of 8.73 Mbps at cell edge of 1 km radius with DF type RN. The cell radius of LTE was extended to 3.9 km utilising DF type RN by Wirth *et al* [25], where at the cell edge a throughput of up to 70 Mbps was achieved. As mentioned earlier, DF type relay adds additional delay to the existing latency of LTE technology, as well as increased complexity and fails to seamlessly integrate RN into the LTE networking structure. The main objective of adding RN to the LTE network is to increase the QoS at the cell edge and at the same time to reduce the deployment of eNB, thereby reducing the CAPEX and OPEX. Thus, it is essential to maintain a low complexity RN, favourably AF type RN, however wireless interface cannot handle AF type RN efficiently, which effectively defeats the purpose of RN deployment.

The problem with wireless interface can be countered by implementing RoF system as the interface between eNB and RN, the typical loss of a single mode optical fibre is 0.2 dB/ km with no characteristics of multipath propagation makes RoF an excellent candidate. Reduction of the bit error rate from 10^{-2} to 10^{-3} in optical fibre only takes 1 or 2 dB of SNR [29]. The low impairment properties nominates RoF as an appealing alternative for the wireless interface, and the SNR improvement characteristic makes it more suitable for AF type RN's. In RoF system, the incoming radio frequency (RF) signal modulates the intensity or phase of the laser diode, which is then launched into an optical fibre in order to facilitate wireless access. Cell extension of eNB based on RoF was proposed in [30] with a multi-cooperative scheme and achieved an extension up to 2.1 km. In addition, commercial LTE-RoF integration has been realised for the indoor distributed antenna system by

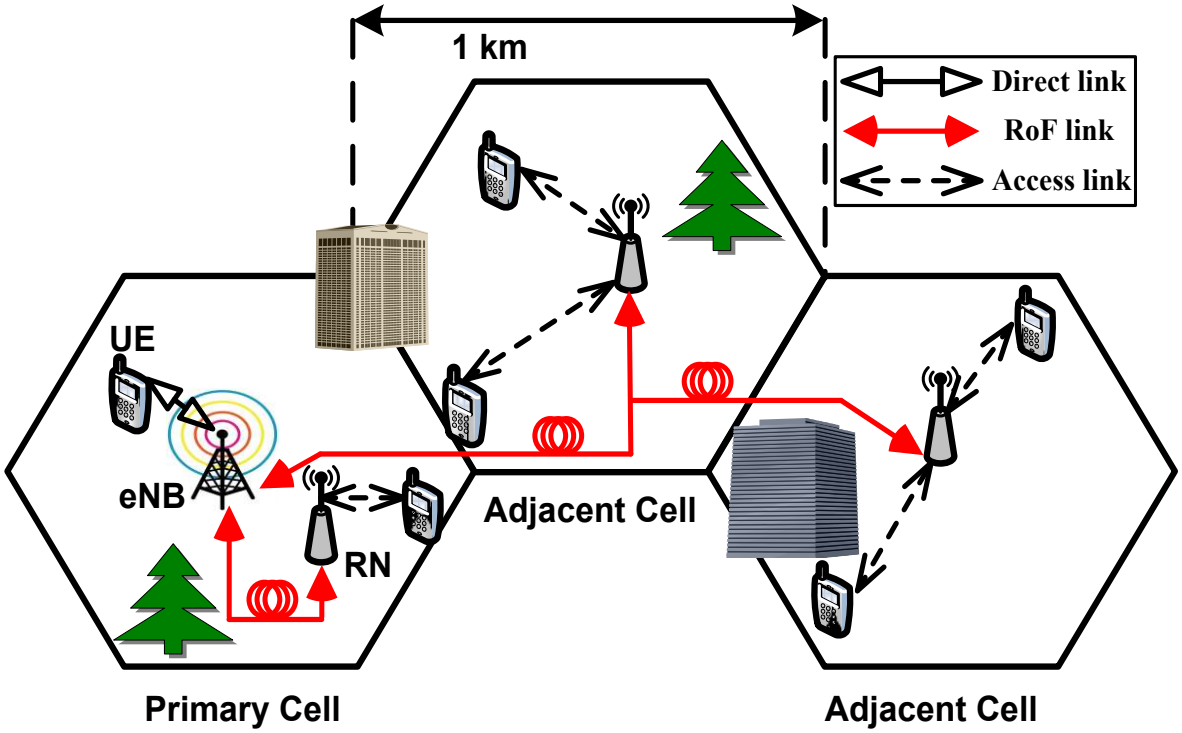

Figure 1.4: Proposed conceptual full duplex LTE radio access network structure in urban area with relay nodes

Zinwave to overcome the RF signal penetration losses for in-building applications [31]. Chapter 2 is dedicated for further clarification of RoF. In Figure 1.4, the proposed method of this thesis is shown. The cell labelled as primary cell is the location for eNB connected to nearby UE via direct link (wireless), the eNB is connected to RN via RoF link which aids UE at the cell edge via access link (wireless). Due to the capability of RoF, RN is deployed at the adjacent cell to support distant UEs from the eNB. As a result, only a single eNB is required for this scenario in the primary cell and effectively reduces CAPEX and OPEX. In the RoF link for adjacent cells, the optical signals will split to deliver signal to adjacent cell, the split can be performed passively with a varying ratio of 10:90 to 50:50. It is important to specify that the proposed cell extension method will affect the capacity of the single eNB due to the sharing scenario among the users at every adjacent cell. However, since capacity is an issue dealt above the physical layer, and this thesis is completely focused in the physical layer, the analysis of the capacity impact and associated

improvements are beyond the scope of this thesis. All RN in the proposed method operates at the same frequency; i.e. the proposed network topology adopts in-band relaying.

Implementation of RoF as the interface would give the idea of increased the cost and complexity from the new deployment of optical fibre and optical related equipments. However, the fact would be that the whole concept could be deployed with the existing legacy backhaul infrastructure, which was utilised by former technologies in the dense urban locations [32].

Direct modulation (DM) is adopted as the dominant optical modulation method in this thesis, due to its low complexity, cost effective and commercial friendly nature. But, DM introduces a destructive impairment, known as the PFC. The intrinsic characteristic of PFC is similar to the chromatic dispersion (CD), thus the modulated signal experiences severe QoS degradation. Since LTE network operates with OFDM modulation with time domain noise-like feature, the existing PFC expression describes both adiabatic and transient chirps, but OFDM is only transient chirp dependent [33].

As shown in Table 1.2, the LTE system is designed with varying occupied subcarriers and FFT sizes relative to the radio bandwidths. However, LTE-A system does not operate in a fixed condition as it adopts both symmetrical and asymmetrical carrier aggregation techniques, and that means LTE-A will be transmitting a composite of multi-type bandwidth signals within the limit of 40 to 100 MHz with the corresponding FFT sizes. Since carrier aggregation is substantially complex compared to the LTE transmitter, as an example, at 100 MHz bandwidth, generation of 5 simultaneous OFDM signals are required for 5×20 MHz bandwidth signals to fulfil the entire bandwidth. In order to minimize the complexity, an alternative method is proposed by adopting the LTE varying FFT sizes method into LTE-A. Investigations on the FFT size optimisation was initiated by Jansen *et*

al [34] and Adhikari *et al* [35] for coherent optical-OFDM (CO-OFDM) systems while taking all the optical propagation perspective, which resulted in the optimum OLP of -8 dBm and -4 dBm, respectively across all FFT sizes. The optical receiver utilised in this thesis is based on the direct detection (DD) scheme and therefore the results given in [35] and [34] cannot be taken as a guideline. However, Pham *et al* [36] optimised FFT sizes for DD based optical OFDM (OOFDM) system, unlikely the investigation contains limited analysis in the optical propagation domain, hence this work did not cover the optimum OLP point. Since DM induces PFC that correlate with CD and jointly distorts the propagating signal, investigation on PFC effect is required in the perspective of performance evaluation for an end-to-end LTE RoF system.

The motive of introducing OFDM into the LTE network is due to the inherent ability of providing better resilience to multipath propagation owing to the characteristic of long symbol duration, which is also a key advantage in the RoF system by providing improved tolerance to the inter-symbol interference (ISI) induced by PFC and CD [37]. On the contrary, the prominent problem of OFDM is its high peak-to-average ratio (PAPR), which will have a direct impact on the optical modulation and the relative OMI.

The importance of LTE technology is to yield high data rate transmission for end users, therefore 3GPP introduced the MIMO topology to enhance the data rate [38]. Transmitting MIMO signals over RoF system is not trivial because the group of signals in MIMO is configured at the same carrier frequency, hence the RoF system will not be able to provide the required diversity for MIMO signals. Jansen *et al* [39] introduced externally modulated optical polarization multiplexing (POLMUX) system with coherent detection to solve the diversity problem for MIMO modulation in optical systems. However, the POLMUX system significantly increases the cost of implementation and system complexity with

respect to the number of MIMO antennas. As an alternative for MIMO configuration, analogue electrical FDM seems convenient. Kobayashi *et al* [40] experimentally transmitted FDM-OFDM method up to 80 km of single mode fibre (SMF) with external modulation and coherent detection, which is also a highly regarded costly and complex system architecture. On the other hand, Liu *et al* [41] experimentally demonstrated FDM based directly modulated RoF system by utilising 550 m multimode fibre (MMF), which is limited to indoor applications.

All the aforementioned problems are part of the design and development process of LTE-RoF system with incorporating only the DL system of LTE. Letian *et al* [42] proposed the coverage extension of eNB with AF type RN and wireless interface for a full duplex LTE system, which achieved an extension of 2 km with a 13.05 Mbps throughput. The achieved throughput and coverage extension reported in [42] demonstrates that the wireless interface offers insignificant impact on the eNB coverage, as the actual LTE technology aimed to deliver a throughput of 100 Mbps.

In order to transmit the LTE signals over the RoF system with a high OLP, the optical fibre nonlinear characteristic will be a major obstacle, which in this case is 6 dBm. Considering the LTE signal power required in RN for UE delivery, it is important for the LTE-RoF system to operate in the nonlinear propagation region to enhance the power budget. At a high level of OLP, a frequency dithering method was introduced in baseband optical applications by Yariv *et al* [43] and Willems *et al* [44] to mitigate nonlinearity induced distortion. However, the methodology of frequency dithering in the RoF system is substantially different compared to baseband optical systems.

1.3 Aims and Objective

Enhancing the eNB coverage can be achieved with the implementation of RN in the networking structure of LTE. The aim of this research is to seamlessly integrate eNB and AF type RN by adopting RoF as the interface into the LTE networking structure. As a rule of thumb, RoF is aimed to be designed in a simple and least sophisticated technology for easy adaptability into LTE networking structure; or in other word as a commercial friendly RoF interface.

The objective of this research includes:

1. Proposing an analytical closed form expression for PFC via the derivation of the laser rate equation, which actually induces the phase distortion.

2. Numerical modelling of the RoF system with incorporating all LTE and LTE-A requirements as a platform for eNB cell extension.

3. Build an LTE RoF test-bed for experimental verification of the numerical modelling; propose an alternative method for the diversity problem in MIMO transmission over RoF and a full duplex LTE RoF system design with DWDM method.

4. Propose a compensation method for nonlinear propagation in LTE RoF system to provide an enhanced power budget in RN.

1.4 Original Contributions

In order to address all the shortcomings in the Problem Statement of Section 1.2, this thesis introduces a number of original contributions to the knowledge that are summarised as follows:

- Investigation on the impact of wireless interface against RoF is analysed and discussed for eNB cell extension scenario with AF type RN in Chapter 2.

- In a directly modulated RoF system, PFC is a major impairment that requires addressing. Chapter 3 presents a new closed form expression for OFDM modulation based chirping is derived from the laser rate equation to describe the nature of distortion introduced while performing numerical integration in a computer simulation.

- Varying FFT scheme is proposed for LTE-A system as an alternative to carrier aggregation. The varying FFT sizes are optimised for directly modulated RoF system relative to all optical propagation characteristics in Chapter 4 to identify the theoretical optimum OLP range.

- As a continuation in Chapter 4, an end-to-end LTE-A RoF system performance evaluation is carried out to investigate the impact of PFC in a transmission system. The investigation is carried out by introducing DM and two types of external modulators, namely SE-MZM and DE-MZM. It is well known that external modulators do not induce PFC during the modulating operation. Although the fact that external modulators are higher in cost and complexity [45], it is still important to exploit the advantage of external modulators for LTE-A RoF system.

- As a solution to mitigate the high PAPR problem associated with OFDM signal while performing DM, a new modulation region is proposed in Chapter 5 by utilising the LTE RoF experimental link. In addition, the investigation is further carried out in the same LTE RoF experimental link with transmission spans ranging

from 10 km to 60 km. The wide transmission spans are important to identify the impact on the optimum OLP and the nonlinear limit of LTE-RoF system.

- As a solution to the MIMO configuration for RoF transmission, the OFDM over analogue FDM (FDM-OFDM) scheme is proposed in Chapter 6 for LTE in the context of 2×2 MIMO. The objective of the proposed method is to practically implement a simple directly modulated link with DD for FDM-OFDM and achieving transmission span of 60 km.

- In order to provide a complete LTE RoF solution, the design of a full duplex FDD LTE RoF system will be introduced in Chapter 7 with DWDM architecture.

- The DMFD method is proposed for nonlinear propagation compensation. A new frequency range is discovered to reinstate this method for RoF system and is presented in Chapter 8. Since external modulator is PFC free, and frequency dithering method operates solely based on frequency chirping, the proposed method is further investigated with externally modulated LTE-RoF system.

The overall contribution of this thesis is graphically illustrated with a research road map as depicted in Figure 1.5.

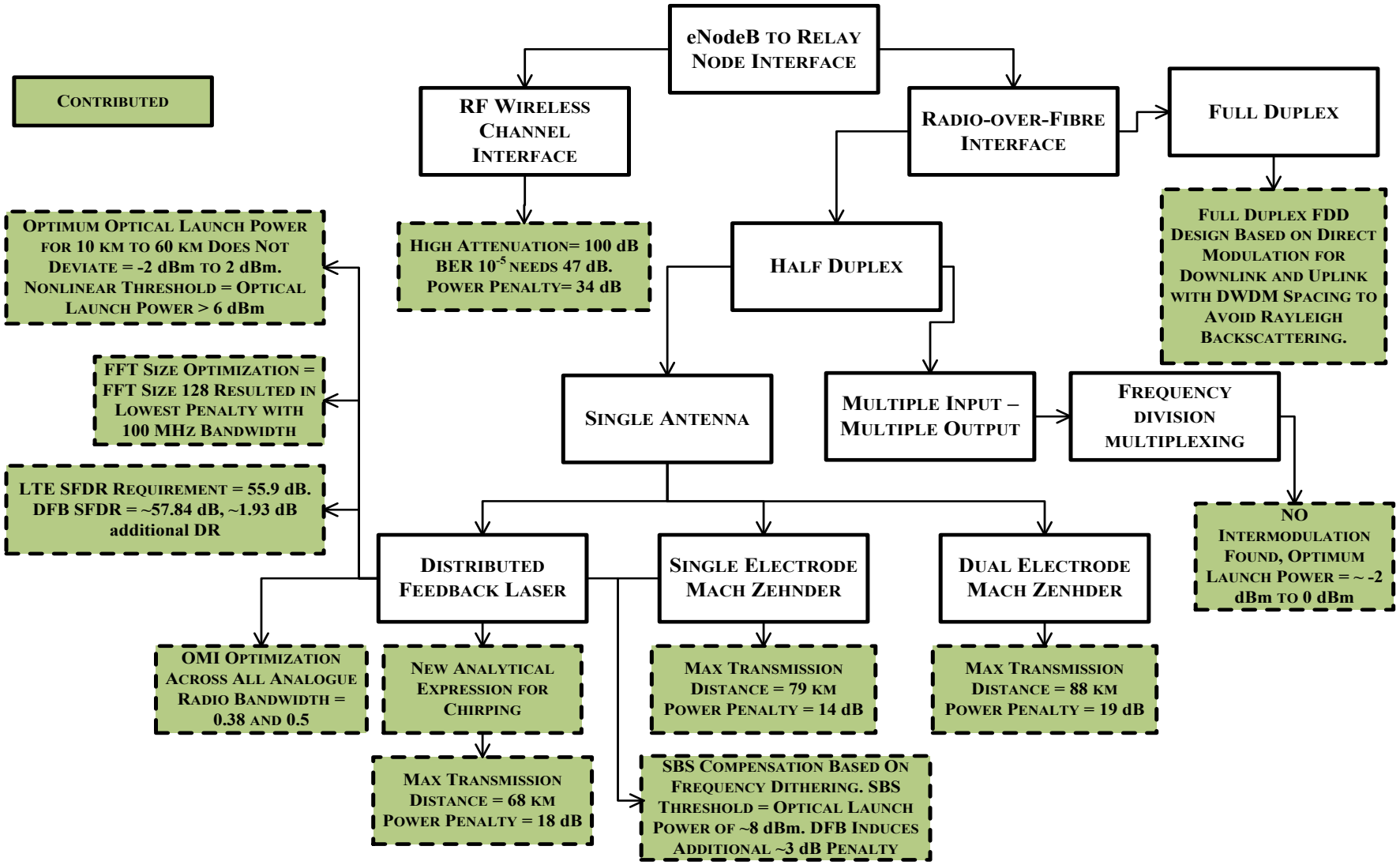

Figure 1.5: Research road map

1.5 Research Outcome

The below list represents the conferences and journals that are published and under review, based on the results obtained from the aforementioned contributions.

1.5.1 Conference Papers

[C1] A. Bahrami. T. Kanesan, W. P. Ng, Z. Ghassemlooy, A. Abd El Aziz, S. Rajabhandari "Performance Evaluation of Radio-over-Fibre (RoF) System Using Mach-Zehnder Modulator (MZM) and On-Off Keying (OOK) Modulation Schemes," in *The 11th Annual Postgraduate Symposium on the Convergence of Telecommunications, Networking & Broadcasting Conference* (*PGNET 2010*), Liverpool, UK, pp. 1-4, 21-22 June 2010.

[C2] A. Bahrami. T. Kanesan, W. P. Ng, Z. Ghassemlooy, C.Qiao, "Performance Evaluation of Radio-over-Fibre Systems Using Mach-Zehnder Modulator," in *London Communication Symposium (LCS)* London, University College London, pp. 1-4, 10 Sept 2010.

[C3] T. Kanesan, W. P. Ng, Z. Ghassemlooy, J. Perez, "Radio relaying for long term evolution employing radio-over-fibre," *Networks and Optical Communications (NOC), IEEE 16th European Conference on* , Newcastle upon Tyne, UK, pp.212-215, 20-22 July 2011

[C4] T. Kanesan, W. P. Ng, Z. Ghassemlooy, C. Lu, "FFT size optimization for LTE RoF in nonlinear fibre propagation," *Communication Systems, Networks & Digital Signal Processing (CSNDSP), IEEE 8th International Symposium on*, Poznan, Poland, pp.1-5, 18-20 July 2012

[C5] T. Kanesan, W. P. Ng, Z. Ghassemlooy, and C. Lu, "Theoretical and Experimental Design of an Alternative System to 2x2 MIMO for LTE over 60 km Directly Modulated RoF Link," in *Global Telecommunications Conference (GLOBECOM 2012)*, *IEEE*, Anaheim, USA, pp.1-5, 03-07 Dec 2012.

[C6] T. Kanesan, W. P. Ng, Z. Ghassemlooy, and C. Lu, "Impact of Optical Modulators in LTE RoF System with Nonlinear Compensator for Enhanced Power Budget," in *Optical Fiber Communication (OFC), collocated National Fiber Optic Engineers Conference (NFOEC), Conference on (OFC/NFOEC)*, Anaheim, USA, 19-21 March 2013.

[C7] T. Kanesan, W. P. Ng, Z. Ghassemlooy, and C. Lu, "Experimental Demonstration of the Compensation of Nonlinear Propagation in LTE RoF system with Directly Modulated Laser," in *Communications (ICC), IEEE International Conference on,* Budaphest, Hungary, 09-13 June 2013. (Accepted for Publication)

1.5.2 Journal Papers

[J1] T. Kanesan, W. P. Ng, Z. Ghassemlooy, and J. Perez, "Optimization of Optical Modulator for LTE RoF in Nonlinear Fiber Propagation," *Photonics Technology Letters, IEEE*, vol. 24, pp. 617-619, 2012.

[J2] W. P. Ng, T. Kanesan, Z. Ghassemlooy, and C. Lu, "Theoretical and Experimental Optimum System Design for LTE-RoF Over Varying Transmission Span and Identification of System Nonlinear Limit," *Photonics Journal, IEEE,* vol. 4, pp. 1560-1571, 2012.

[J3] T. Kanesan, W. P. Ng, Z. Ghassemlooy, and C. Lu, "Experimental Verification of Optimized LTE Signal over a Directly Modulated RoF System for eNB Cell Radius Improvement," *Photonics Technology Letters, IEEE*, vol. 24, pp. 2210-2213, 2012.

[J4] T. Kanesan, W. P. Ng, Z. Ghassemlooy, and C. Lu, "Experimental Full Duplex Simultaneous Transmission of LTE over DWDM Directly Modulated RoF System," *Optical Communications and Networking, IEEE/OSA Journal of,* vol. -, pp. -, 2013. (Under Review)

[J5] T. Kanesan, W. P. Ng, Z. Ghassemlooy, and C. Lu, "Optical Modulators Diversity for Optimized Nonlinear Compensator in a LTE RoF System," *Lightwave Technology, IEEE/OSA Journal of,* vol. -, pp. -, 2013. (Under Review)

1.6 Thesis Organization

This thesis is mainly focused on the research work dedicated to the LTE and RoF seamless integration. The literature reviews, original contributions, conclusions and future works are divided into 9 chapters.

Chapter 1 provides the introduction of mobile communication growth and the relative technologies with the main emphasis on LTE and LTE-A, including the problem statement, aims and objectives with explanation on the original contributions of this research and the resulting publications. Chapter 2 gives an in-depth introduction on RoF and optical devices required to construct a RoF system, and as well as the advantage of RoF compared to wireless channel will be shown.

Chapter 3 focuses on lasers with major concentration given to the DFB, rate equation analysis and mathematical derivation to explain the PFC characteristic. Chapter 4 is dedicated for the theoretical development of LTE-A with varying FFT sizes as an alternative to carrier aggregation, integration of the proposed LTE-A and RoF system with introducing the optimum OLP region and the results obtained from this integration. In

addition, a diversity scheme is introduced in terms of the optical modulators for the proposed LTE-A system along with performance optimisation.

Chapter 5 introduces the experimental link designed for LTE-RoF system, with the development stage focused on the OMI, optimum OLP and its characteristic towards varying transmission span. Chapter 6 consists of the advance LTE-RoF system design, where an alternative solution is proposed to solve the diversity problem experienced by MIMO for RoF transmission. In addition, a full duplex system FDD based LTE-RoF system is designed and developed with all the relative results presented within Chapter 7.

Chapter 8 is dedicated to the nonlinear compensation by proposing DMFD method for LTE-RoF system to improve the respective QoS while the system operates at a high level of OLP. Since DMFD operates based on PFC, the adherence of external modulation schemes is investigated. Finally, Chapter 9 concludes this thesis by summarising all the research findings with the future works that could bring the LTE-RoF system to the next level.

CHAPTER 2 AN OVERVIEW OF RADIO-OVER-FIBRE

In the early 1980s, the United States introduced the integration of wireless and optical fibre to accommodate military requirements, such as radar systems where optical fibre were utilised as an interface between the central station (CS) and the wireless antenna. The conventional transporting interfaces for RF signals were copper cables and waveguides, which induce high losses. The advantages of optical fibre, namely lower loss and a large bandwidth made it an efficient alternative interface. The application of radar is what transpired into the widely known the RoF system, where Cooper [46] initially adopted RoF into cordless and mobile communications.

This chapter is dedicated to the RoF system and its building blocks. The RoF system plays an important role in wireless communications due to the tremendous growth of end-users that has lead to higher bandwidth and higher data transfer requirements. Furthermore, RoF system is an alternative solution when the wireless communication systems operate on a small cell size, where the utilised carrier frequencies are not adequate to be transported over co-axial cables or when the radio coverage experiences dead-zones [47]. Both of these requirements can be fulfilled by utilising the optical fibre that offers a bandwidth in excess of 50-THz [48]. In addition, RoF system is also known for extending the radio coverage of a CS for wireless applications [49]. This scenario could be achieved by extending the transmission link between CS and the base station (BS) to bring the access network closer to every mobile user by deploying optical fibre as the medium. Some of the real time applications for RoF systems were carried out in the 2000 Olympic Games in Sydney, Osaka Station in Japan and Bluewater Shopping Centre in the United Kingdom [47].

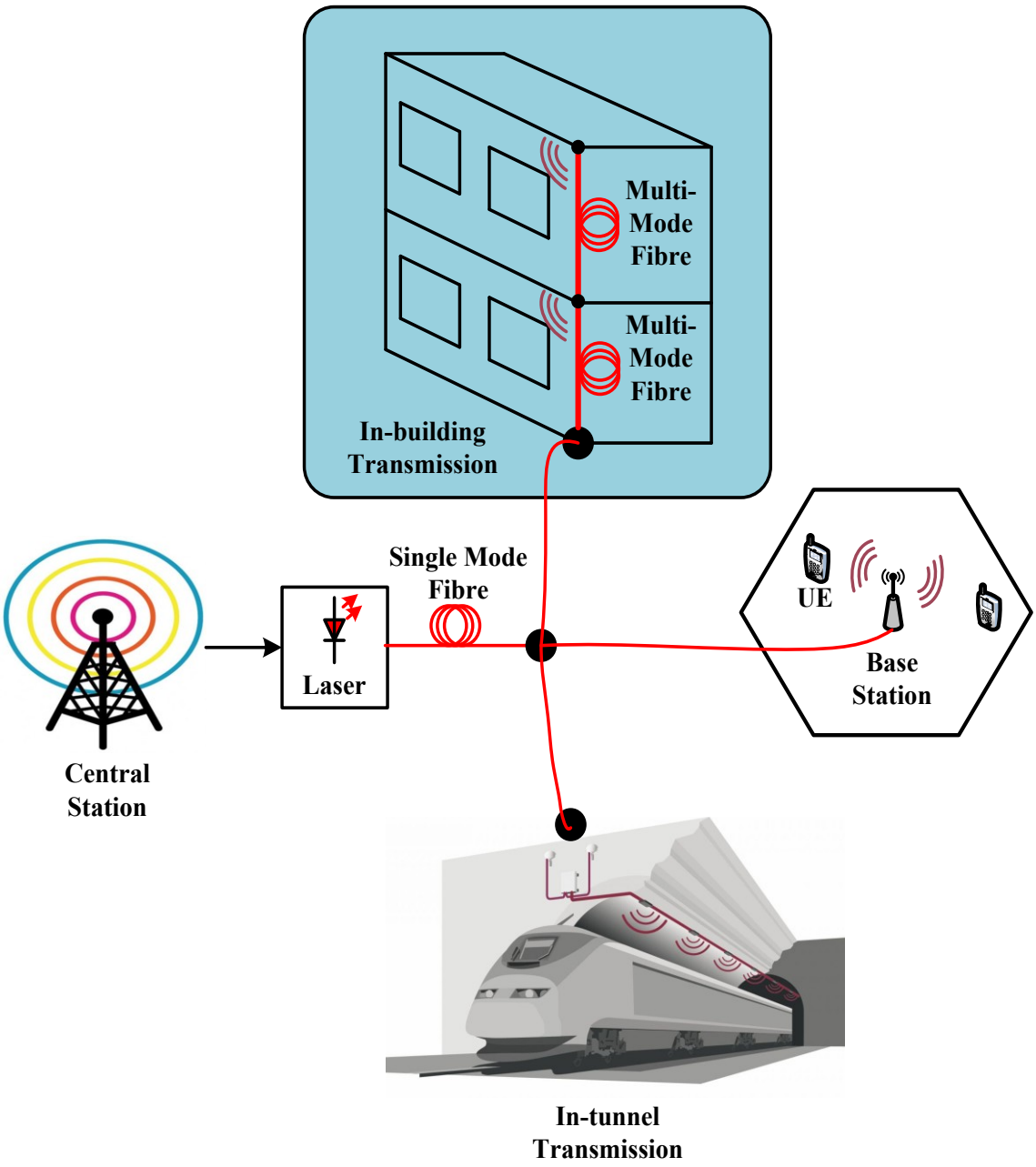

Figure 2.1: The usage of RoF system in challenging RF signal penetration areas and distributed antenna systems.

2.1 Overview of Radio-over-fibre

A simple explanation for RoF system is that it connects a CS to many BSs by carrying the DL signal from CS to BSs for transmission to mobile users via wireless connectivity while at the same time RoF system also carries the UL signal from mobile users back to CS via BSs.

The importance of the RoF system topology is that it could directly transmit RF signals over the fibre without any further processing at the BS. All the complicated RF modem and signal processing functions remain at the CS [49]. Therefore it directly introduces reduction in the system wide installation and maintenance costs, reduces and simplifies BS complexity, and allows a transparent and distributed system. Since the BS complexity is significantly reduced, a single high capacity CS could be utilised to handle multiple BSs to cover the dead zones or as a solution to the cell edge problem experienced by any CS. Figure 2.1 illustrates the CS connected to a RoF system, where the signal is distributed to dead zones via passive splitting, namely in-building and in-tunnel transmission, and as well as for BS cell extension purpose.

On the other hand, there are also coexisting optical fibre communication architecture, namely the intermediate frequency (IF)-over-fibre system and the baseband-over-fibre system. Generally, IF-over-fibre system architecture are utilised when the optoelectronic devices in the CS is insufficient to support signals with high carrier frequency. However IF-over-fibre system architecture increases the complexity of BS. Since the original RF signals will be down-converted to an IF frequency in CS, when the signal reaches BS, an up-conversion will be required for wireless transmission. Thus, the element of distributed system that exists in the RoF system architecture is not viable with utilising IF-over-fibre system due to the increased complexity in BS [50].

The baseband-over-fibre system is another well-known architecture that could be utilised as an alternative to RoF. The optoelectronic devices for the baseband transmission have matured over times and therefore offering reduced CS complexity. However, the BS complexity significantly increases as most mobile communication operates at high frequencies, thereby requiring costly components for up-conversion and down-conversion

for end-user transmission and CS delivery, respectively [50]. Since the complexity accumulates in BS, the distributed system applicable with the RoF system is not suitable for baseband-over-fibre system. Therefore, RoF system would be the most suitable solution for dead-zones and radio coverage extension.

2.1.1 Typical System of Radio-over-fibre

Figure 2.2 illustrates a simple full duplex RoF system deployed between the transceiver of a CS and BS. The CS receives the DL electrical data from a core network, up-converted to the frequency required for wireless transmission, and subsequently modulating a laser adopting intensity modulation (IM). This operation is known as the electrical-to-optical

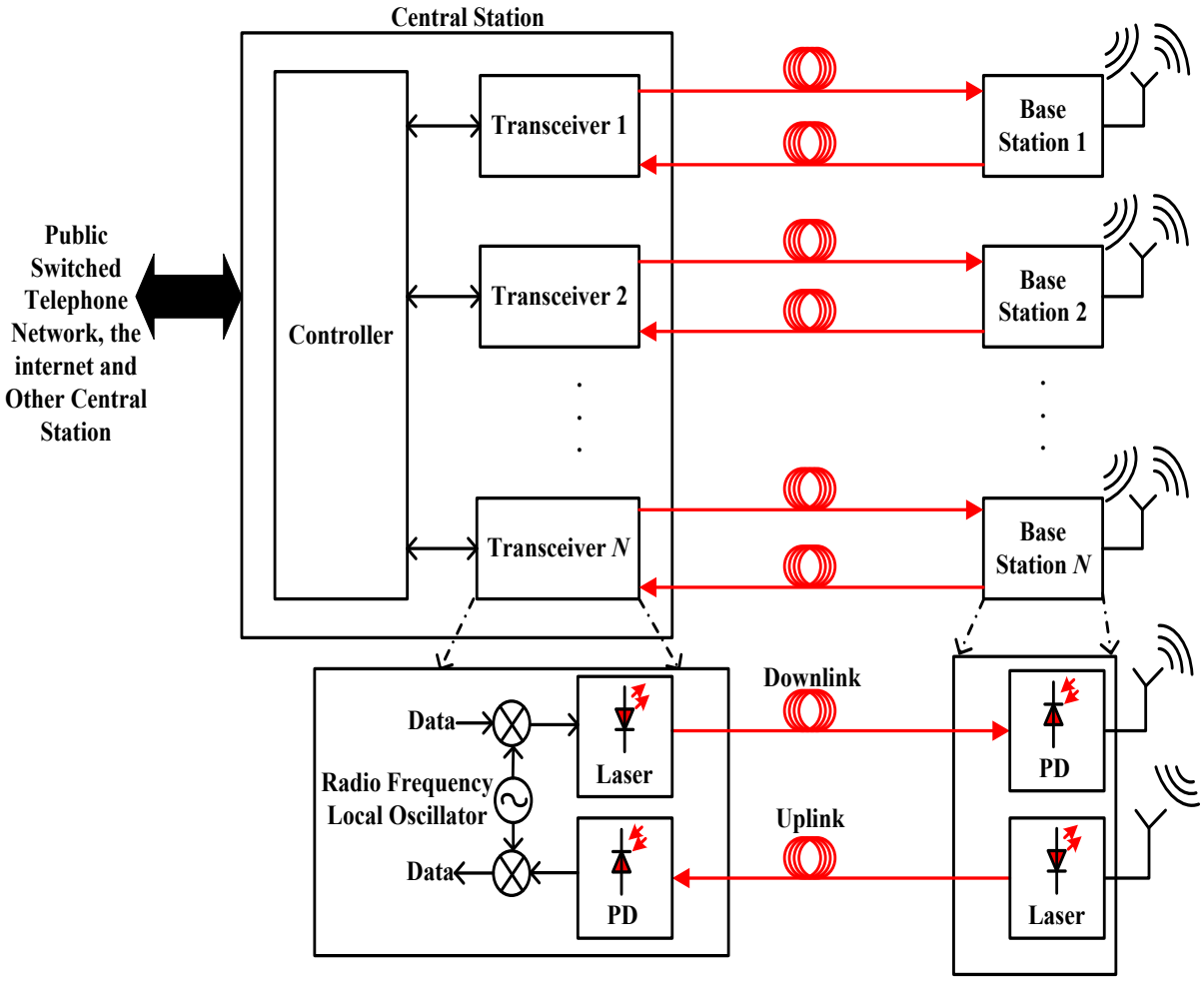

Figure 2.2: Overview of radio-over-fibre

conversion. The modulated optical signal is then coupled into a SMF for BS transmission. At the BS, the receiver is a simple photodetector (PD) performing optical-to-electrical conversion, subsequently transmitting the converted signal to mobile users via an antenna. The UL transmission is exactly the reverse process of DL. It is clear from Figure 2.2 that CS is designed with all the required features leaving BS with only an optical receiver and a laser for DL and UL connectivity, respectively.

2.1.2 Radio-over-fibre Indoor and Outdoor Applications

Throughout this thesis, the RoF system is only considered as an analogue signal distribution link. Some of the known commercial investigations utilising analogue RoF systems are in the area of mobile communications, namely the GSM and the UMTS. Single mode fibre based RoF system for the outdoor application was introduced by Andrew corporation [51]. In terms of in-building applications, the RoF system with MMF was introduced by Zinwave corporation [52], LGCWireless corporation [53], and ADC corporation [54]. Research on integrating mobile communication and the RoF system was mostly focused on the criteria of performance limit. Prior research work on the RoF system performance limit with mobile communication was carried out in [55] and [56], which investigated the interference of GSM with the wideband code division multiplexing access (WCDMA) system and WCDMA with WLAN, respectively.

The traditional channel for an outdoor RoF system is SMF owing to the low attenuation and a high bandwidth. Typical RF signals are designed as a narrow-band, therefore SMF can provide a near ideal channel with almost no loss or distortion. The SMF only induces impairments at very high frequency and a long span transmission, namely the millimetre wave transmission and transoceanic links, respectively. The notable impairments are the exponentially increasing attenuation and the CD, which contributes

the most distortion at a low OLP level. On the other hand, MMF does not get much attention at this transmission condition due to its modal dispersion and a high attenuation that has a stronger effect on the propagating signal. The MMF has limited usable bandwidth, which is much lower compared to the SMF. This bandwidth limiting factor only allows a transmission distance less than 250 m for any the 3G cellular system signal distribution in MMF [57].

2.2 Optical Modulation Methods and Transmitters

As explained in the previous section, the RoF system is known for extending the radio coverage range. In this research, the focus is to modulate the LTE and LTE-A up-converted analogue signal onto RoF and deliver it to a RN. Normally an analogue electrical signal will be converted into an optical signal by directly modulating (i.e. IM) the laser diode, or by means of external modulation. The latter method could be either IM or phase modulation (PM) and is most suitable for much higher data rates. All optical modulation methods reported here is converted back into the electrical domain at the receiver by means of the DD method.

The laser diode is the most important element of the RoF system, as it could operate both as an optical transmitter or an optical carrier provider for external modulators. The prominent operating wavelengths of the laser diode lie at 1300 nm and 1550 nm, relative to the reduced dispersion and attenuation [58], respectively.

2.2.1 Direct Modulated Laser

Most commercially available RoF systems are designed with the DML with IM-DD [59]. This concept of electrical-to-optical conversion is done by applying a respective analogue signal with a sufficient bias current directly onto a laser via a bias-tee. The bias-

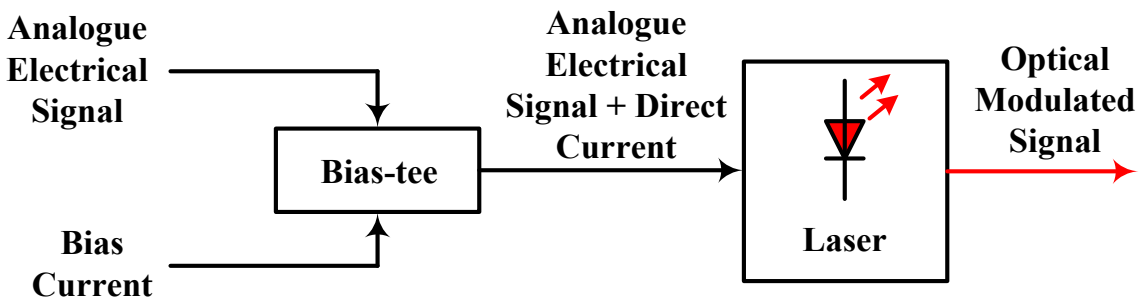

Figure 2.3: Procedure of directly modulating a laser with electrical signal

tee is an important device needed to shift the bipolar analogue electrical signal to form the unipolar signal to drive the laser. This operation could be easily done with any commercially available bias-tee as shown in Figure 2.3. The fundamental of DM is illustrated in Figure 2.4 via the light current (LI) curve of a laser. The optical power increases weakly near the threshold region due to the spontaneous emission dominated process at low bias current. However, the optical power increases rapidly after the threshold region where the recombination process is quicker from the rapidly evolving stimulated emission and allows the laser to operate coherently. The rapid increase of optical power gradually stops due to the development of heat within the laser junction that results in the carrier leakage and internal losses, which effectively saturates the laser [60].

In terms of modulation, the analogue electrical signal is summed with a sufficient bias current to ascertain the signal modulation being performed in the linear region as shown in Figure 2.4, where modulation of the electrical signal is basically switching the intensity of the laser to generate an optical modulated signal. It is important that the bias current is high enough so that the analogue electrical signal does not fall close to the vicinity of the threshold region to avoid nonlinear impairments, namely turn-off delay and lower peak clipping. On the other hand, the bias current should not be extensively high to evade the analogue electrical signal falling close to the saturation / back-off region, as shown in

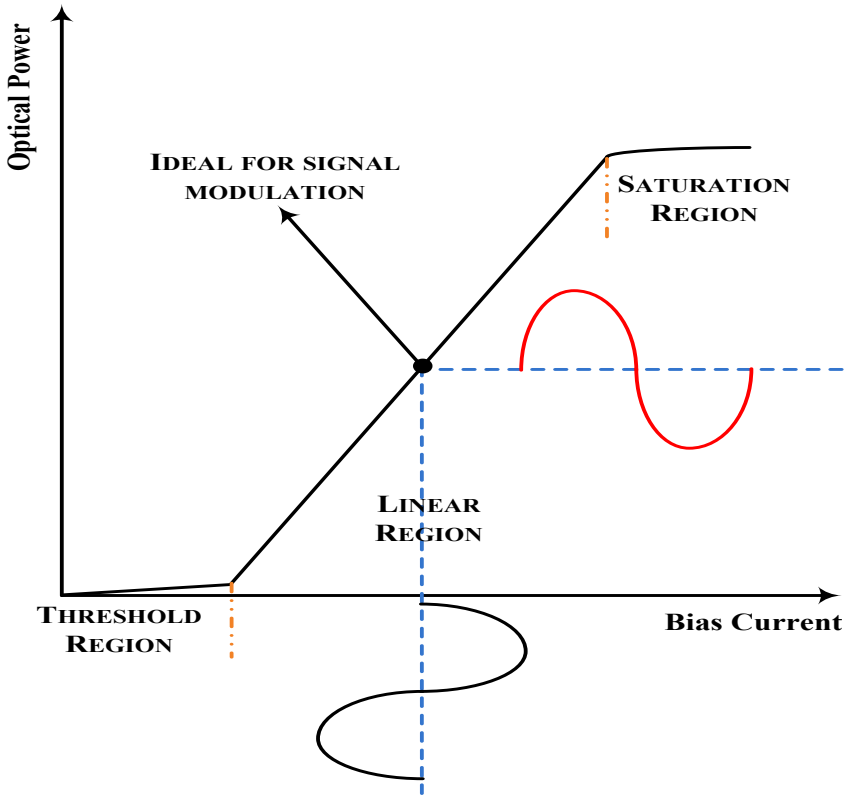

Figure 2.4: The fundamentals of laser light current curve

Figure 2.4. Modulating the signal close to the saturation region will induce a higher peak clipping.

As with every electronic or optoelectronic devices, there are always shortcomings from various perspectives. In terms of a laser, there are a few limitations that need addressing for systems that operate solely based on DML:

Modulation bandwidth: The major shortcoming of a laser is its available bandwidth to operate as a DML, where it is an important parameter in RoF system due to the high operating carrier frequency of RF signals. The frequency response of a laser improves relative to the bias current, and as a result increasing the carrier density and the laser modulation bandwidth. However excessive bias current will force the laser to operate in the saturation region and the stops the bandwidth growth due to gain compression. Laser

with high modulation bandwidth was reported in [61] by implementing the multiple quantum well method at the 1550 nm window. Bach *et al* [62] reported bandwidth enhancement of up to 37 GHz with the distributed Bragg reflector laser. There are also external methods on enhancing laser modulation bandwidth, primarily the injection locking method, where Chrostowski *et al* [63] and Lau *et al* [64] demonstrated extended laser modulation bandwidth with injection locking of up to 50 GHz and 44 GHz, respectively.

Noise emission: Spontaneous emission is the major element that induces noise in a laser and most active at the near threshold region, because above threshold, stimulated emission is dominant. The phase and wavelength of spontaneous emission are completely random, which as adds to the phase noise and acts as a function of linewidth. The random nature of phase noise induces random fluctuation to the output power, commonly known as relative intensity noise (RIN) and is measured via the SNR. The RIN measurement with SNR can be obtained by the expression of SNR = $m^2/2$ RIN [65, 66], where m is the modulation index. As specified earlier, above threshold region, stimulated emission becomes dominant thus phase noise, linewidth and RIN reduces as the optical power increases.

Frequency chirp: The natural phase noise, linewidth and RIN of a laser without any DM eventually reduces as the optical power increases. However, when DM occurs at high optical power, albeit it is the stimulated emission dominant area, a residual optical PM occurs which broadens the linewidth and shifts the emitting wavelength [67]. The DM induced optical PM is widely known as frequency chirping, which fundamentally arises from carrier density change within the cavity corresponding to the continuously varying input bias current. Frequency chirping is a critical problem in RoF system, as it magnifies the effect of CD due to the similar signal-distorting characteristic. Since the LTE-RoF integration proposed in this thesis is aimed at designing a commercial friendly system,

DML is the best choice due to its simplicity and cost effectiveness. The DFB is picked as the DML of the LTE-RoF system due to its inherent characteristic of narrow linewidth, thereby reducing the frequency chirp [68]. Additional details on the characteristics of various semiconductor lasers, including DFB laser are discussed in Chapter 3 where a new expression for frequency chirp will be presented. There are several techniques in reducing frequency chirp of a laser. The most well known method on almost completely eliminating the residual optical PM is by utilising external modulation.

2.2.2 External Modulation

In RoF system, external modulation with the MZM is a well-known technique for high frequency signals or long spans transmission. The complexity and cost of this method is higher than DML because it requires two different optical components, including a continuous wave laser and a MZM. However, a RoF system with MZM could offer improved immunity to noise and distortion compared to a conventional DML. The main advantage of MZM is the minimum frequency chirp based modulation, albeit it still has refractive index variation relative to the modulating signal, but the effect on the optical modulated signal is negligible. Therefore, MZM are widely used at microwave range frequencies or high bit rate systems. There are two types of MZM, the first type is SE-MZM and the second type is DE-MZM.

In SE-MZM, only IM can be performed, where as with DE-MZM both IM and PM can be performed [69, 70]. Figure 2.5 illustrates the modulation overview of SE-MZM and DE-MZM, both modulators are supplied with a continuous wave laser source. The analogue electrical signal after bias-tee is directly applied to SE-MZM for IM. In the case of DE-MZM, the analogue electrical signal will be split and applied to the first electrode of DE-MZM with no intentional phase change, and with 90° phase shift to another electrode.

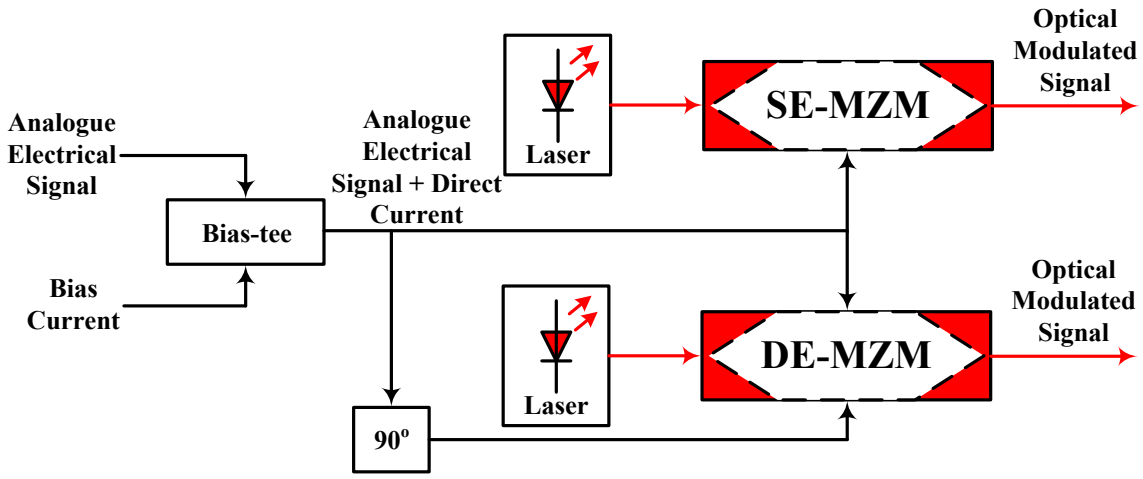

Figure 2.5: Procedure of external modulation of electrical signal with SE-MZM and DE-MZM

Figure 2.6 shows the transfer function illustration of MZM which operates as a sinusoidal function [45].

Similar to DML, MZM exhibits nonlinear characteristic for signal modulation performed at maximum or minimum biasing point. Therefore, it is advisable to always

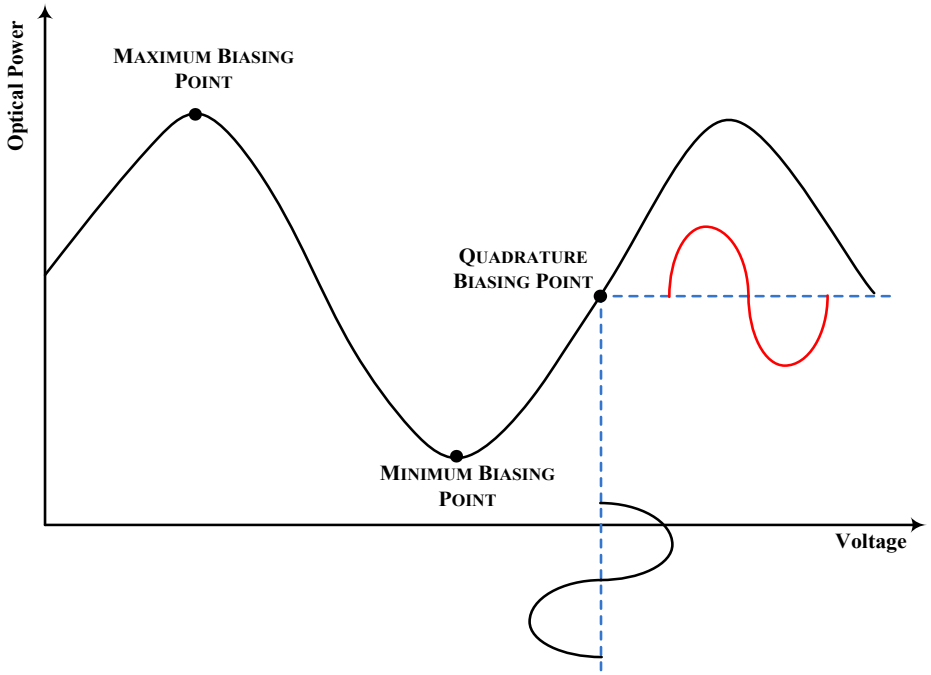

Figure 2.6: The operating characteristic of MZM modulator.

operate MZM at quadrature biasing point for linear modulation, unless otherwise required. The electrical signals with different phases will be modulated onto DE-MZM and the optical modulated signals will have different refractive index with respect to each other. At the output of DE-MZM, the signals are rejoined with either constructive or destructive interference resulting in an optical PM signal. After the photodetection, the PM occurred between the two paths appears as an IM [71].

2.2.3 Optical Fibre

Optical fibre serves as the medium of RoF system and the wide interest in this medium is due to the ultimate advantage of both high bandwidth and low loss, which allows the propagation of high speed or high frequency signals over a long transmission span. Classifications of optical fibres are divided into two categories, MMF and SMF, where the former allows multimode propagation and the latter is suitable for single mode propagation. Since MMF constitutes multimode propagation, the modes arrive at the receiver at different time instants giving rise to phenomenon known as multimode dispersion or intermodal dispersion [72]. The multimode dispersion of MMF severely distorts the signal and imposes limitation on signal bandwidth, therefore the usage of MMF is suitable for indoor application [57]. Since this thesis completely concentrates on eNB cell extension for outdoor application that requires long span transmission, the discussion of optical fibre will be concentrated towards SMF.

The multimode dispersion does not exist in SMF due to single mode propagation. An optical fibre's ability to handle the number of modes can be calculated from the V number, otherwise known as the normalized frequency [72]:

$$V = \frac{2\pi a}{\lambda}\sqrt{n_1^2 - n_2^2} \tag{2.1}$$

where a is the optical fibre core radius, λ is the propagating wavelength, and, n_1 and n_2 are the refractive indices of core and cladding of an optical fibre, respectively. The V number needs to be maintained ≤ 2.405 for mitigating multimode dispersion, or in other word to maintain a single mode propagating fibre. The V number can be maintained within the aforementioned limit by reducing the core radius with following the law of normalized index difference [72]:

$$\Delta = \frac{n_1 - n_2}{n_1} \tag{2.2}$$

where Δ should between 0.2% and 0.3%.

However, SMF do introduce impairments in many different forms and could be divided into linear and nonlinear distortions. The well-known linear impairments are attenuation and CD, these parameters vary according to the transmission window. 1300 nm and 1550 nm are the widely utilised transmission windows in optical fibre communications, where the attenuation and CD at the former wavelength are ~1 dB/km and zero dispersion, and the latter wavelength are ~0.25 dB/km and 17 ps/(nm km), respectively. Recently, the interest has shifted more to the 1550 nm window, not only due to the low loss characteristic, but also owing to the availability of erbium doped fibre amplifier (EDFA) at this wavelength [73].

Since the proposed work of this thesis completely operates in the 1550 nm window owing to low attenuation for a long transmission span, CD is the major linear impairment to arise from the variation of propagating velocities of different spectral components within the same mode. There are two elements involved in CD, namely material dispersion and waveguide dispersion. The dispersion induced by the material is subject to the variation of the optical fibre refractive index, which is a function of wavelength. In other

word, material dispersion causes different wavelength to travel at different velocity due to the change in refractive index, which is different to the intermodal dispersion as the modes in MMF travel through different paths and experience varying delay. On the other hand, the physical design of an optical fibre leads to waveguide dispersion, where normalized index difference is typically small resulting in almost equal core and cladding refractive indices, thus the propagation is not confined absolutely within the optical fibre core leading to a weakly guided signal [72].

Apart from linear impairments, nonlinear distortions severely degrade signal quality at high OLP. The nonlinearities in optical fibre can be divided into two categories; i) propagation induced variation in the refractive index resulting in nonlinear PM, known as self phase modulation (SPM) and cross phase modulation (XPM), and generation of new frequencies via nonlinear optical mixing known as four wave mixing (FWM). All aforementioned phenomena are the Kerr effects of optical fibre, which corresponds to the refractive index change proportional to the square of the electric field rather than varying linearly with it; ii.) nonlinearities subject to vibration dynamics that results in scattering process, namely stimulated Raman scattering (SRS) and stimulated Brillouin scattering (SBS) [74].

The LTE systems operate based on OFDM as explained in Chapter 1, where the modulation scheme is designed with narrowly spaced subcarriers packed together. Furthermore, the LTE-RoF system design presented in this thesis utilises both SMF and 1550 nm as the emission wavelength and the proposed work solely operates based on single wavelength transmission. Albeit OFDM has many subcarriers, the nature of its transmission is equivalent to a packet based orthogonally packed subcarriers altogether up-converted to 2.6 GHz in LTE system, which is equivalent to a single mode in optical

spectral. Therefore, the system is only subject to SPM distortion and not XPM distortion [75-77]. On the other hand, the nature of highly dispersive transmission of the proposed work disables the effectiveness of FWM, because at high dispersion rate the optically transmitted signal would have uncorrelated phase [76, 78]. In terms of the scattering phenomena, SRS ineffectiveness in the proposed system is twofold, the first element is that SRS is only active in a wavelength division multiplexed (WDM) system and the second element is that the distortion is only applicable to transmission frequencies of less than 500 MHz [76]. Thus, the only nonlinear distortions that affect the LTE-RoF system are SPM and SBS.

2.2.4 Optical Receiver

In a RoF system, the optical receiver portion consists of a PD with a bandwidth large enough to convert the optical RF signal back into an electrical signal. The common types of PD used in RoF system are either PIN PD or avalanche PD (APD). The PIN PD is constructed with a p-type and n-type layer and an intrinsic layer (i-layer) placed in between. When PIN PD is reversed biased, the output current generated is proportional to the intensity of the incident optical signal at the input of the PD. The output current is generated relative to incident optical signal with a ratio known as responsivity, where PIN PD's typical responsivity is around 0.5 - 0.7 A/W [79]. The optical receiver responsivity can be greatly improved with APD, because of an additional p-type layer inserted between i-layer and n-type layer. Under the reverse bias condition, the additional p-type layer exhibits a high electric field with the generation of secondary electron-hole pairs via the impact of the ionization process. The additional electron-hole pairs effectively increase the responsivity of an APD by several orders of magnitude higher than PIN PD.

The disadvantage of APD is the high generation of noise level and the temperature dependent gain. Furthermore, PIN PD is cheaper, has a reduced sensitivity towards temperature and requires lower bias level. Therefore, PIN PD will be adopted as the ideal receiver for the proposed LTE-RoF system [79].

2.3 Implication of Radio-over-fibre over Wireless Channel

So far in Chapter 2, a detailed overview of RoF and its properties were discussed. The major objective of the RoF channel is to operate as the interface of eNB and RN with an aim of replacing the wireless interface. Thus, it is important to analyse and discover the improvement that RoF can provide to the LTE technology compared to the wireless channel for the scenario of cell extension. The author has modelled two different systems as the interface between eNB and RN. The first system is inclusive of LTE signal from eNB and demodulation at RN with a wireless channel as the interface. Rayleigh fading channel is used as the wireless channel due to its inherent ability of simulating NLOS connectivity. The second system utilises similar transmitter and receiver configurations, but the interface is designed using a RoF system instead of a wireless channel for performance measure.

The system model considered for this investigation is illustrated in Figure 2.7, which was mathematically modelled in MATLAB^{TM}. The incoming serial binary data sequence is mapped into a serial complex data using the 16-QAM modulation format and converted into parallel formation to represent the 180 subcarriers. The 180 parallel subcarriers are converted to 256 parallel subcarriers by performing zero padding to meet the requirement of both LTE and FFT algorithm [80]. The composite subcarriers of zeros and modulated symbols can be expressed as $\boldsymbol{X}(m)$ where $\{\boldsymbol{X}(m) : m = 0, 1, \ldots, N_s\text{-}1\}$, where m is the subcarrier index and $N_s = 256$ are the

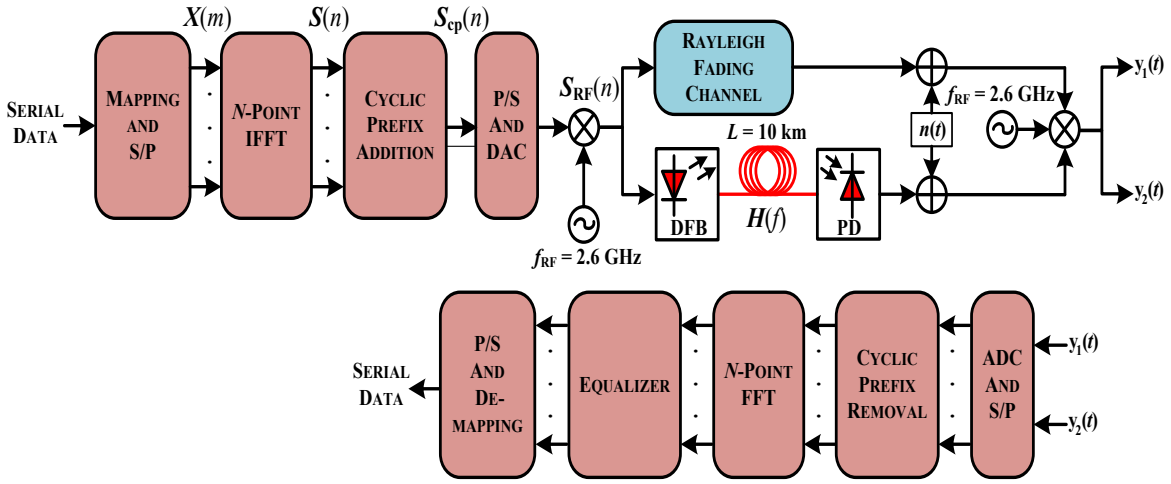

Figure 2.7: LTE system designed with wireless and RoF interface. Abbreviation: S/P: serial-to-parallel conversion, IFFT: inverse fast Fourier transform, P/S: parallel-to-serial converter, DAC: digital-to-analogue converter, DFB: distributed feedback laser, PD: photodetector, ADC: analogue-to-digital converter, and FFT: fast Fourier transform

subcarriers. An N_s-point inverse FFT (IFFT) is then applied to the 256 parallel subcarriers $\boldsymbol{X}(m)$ to generate OFDM signal $\boldsymbol{S}(n)$:

$$\mathrm{S}(n) = \frac{1}{\sqrt{N_\mathrm{s}}} \sum_{m=0}^{N_\mathrm{s}-1} \mathrm{X}(m) e^{j2\pi mn / N_\mathrm{s}} \tag{2.3}$$

where $\{n=0, 1, \ldots\ldots, N_s - 1\}$ is the time domain index. After adding the CP at the rate of ¼, equation (2.3) can be expressed as:

$$\boldsymbol{S}_{\mathrm{cp}}(n) = e^{-j2\pi mn_{\mathrm{cp}} / N_\mathrm{s}} \cdot \sum_{m=0}^{N_\mathrm{s}-1} \boldsymbol{X}(m) e^{j2\pi mn / N_\mathrm{s}} \tag{2.4}$$

where n_{cp} is the index referring to the CP subcarriers. The addition of CP is important to avoid ISI. Finally the CP appended signal $\boldsymbol{S}_{cp}(n)$ is passed through a parallel-to-serial converter and a digital-to-analogue (DAC) converter. The continuous signal $\boldsymbol{S}_{cp}(t)$ at the output of the DAC module is up-converted by a local oscillator (LO) at a carrier frequency f_{RF} of 2.6 GHz, specified for LTE urban environment operation can be described as [81]:

$$\boldsymbol{S}_{\mathrm{RF}}(t) = \mathrm{Re}\{\boldsymbol{S}_{\mathrm{cp}}(t)\} * \cos(\omega_{\mathrm{RF}} t) + \mathrm{Im}\{\boldsymbol{S}_{\mathrm{cp}}(t)\} * \sin(\omega_{\mathrm{RF}} t) \tag{2.5}$$

$$\omega_{\mathrm{RF}} = 2\pi f_{\mathrm{RF}}, \tag{2.6}$$

The modulated signal is transmitted via the Rayleigh fading wireless channel as well as being directly applied to the DFB module to produce an OOFDM signal with an IM. After the optical modulation, the signal is coupled into a SMF link and subsequently passed through a PD for optical-to-electrical conversion. Both channels are modelled to simulate a transmission span of 10 km. At the electrical receiver, additive white Gaussian noise is added before down-conversion to the signals that propagated through both paths. Identical LO are used at the transmitter and receiver to ensure perfect synchronisation. The remaining part of the receiver is exactly the inverse of the transmission process except for the equalization module. The equalizer implemented in the receiver is a single-tap least square filter which operates in the frequency domain utilised for the compensation of the phase distortion induced by wireless and the optical propagation.

2.3.1 Rayleigh Fading Channel

Wireless propagation is very complex in nature, especially in urban environment with widely populated high rise buildings that mostly implicate NLOS propagation paths. The scenario of NLOS paths will introduce heavy distortions to the propagating signal, namely reflection, diffraction and scattering. The three distortion phenomena happen at random locations, which are known as multipath propagation. In the NLOS environment, the instantaneous received signal will experience rapid power fluctuation subject to the summation of signals arriving from different paths with random phases, where the summed components act as a noisy signal. Hence, the Rayleigh fading channel can be represented as statistical

model assuming that the magnitude of propagating signal passed through a medium will vary randomly. Furthermore, Rayleigh fading is suitable to simulate wireless transmission of 1 to 20 km, thereby meets the requirement of the investigation [82-84].

The most utilised spectrum for LTE is at 2.6 GHz, which induces phenomenal loss in wireless propagation. In addition to Rayleigh fading, isotropic path loss between two antennas for 10 km span is considered in the simulation [82-84].

2.3.2 Optical Layer

The optical layer in this investigation consists of DFB laser for IM, SMF as the channel and PD operates as the receiver. The description of DFB laser will be presented in detail as part of Chapter 3. However, the interest in utilising DFB laser as the optical modulator is due to its inherent advantages of low cost, reduced power consumption, compactness, and high output power. The corresponding advantages are very important for commercial deployment [33].

The transmission medium is composed of SMF where the transfer function is given as [85]:

$$H(f) = 10^{\frac{-\alpha L}{10}} \exp\left(- j\left[\pi D \frac{\lambda^2}{c} L B_{\mathrm{d}}{}^2 \left(\frac{f}{B_{\mathrm{d}}} \right)^2 \right] \right) \tag{2.7}$$

where α is the SMF attenuation (0.25 dB/km); L is the transmission length; D is the CD parameter 17 ps/(nm km); λ is the operating wavelength (1550 nm), B_{d} is the data rate and f is the operating frequency. For simplicity, only the linear impairments of optical fibre are considered in this investigation, which is

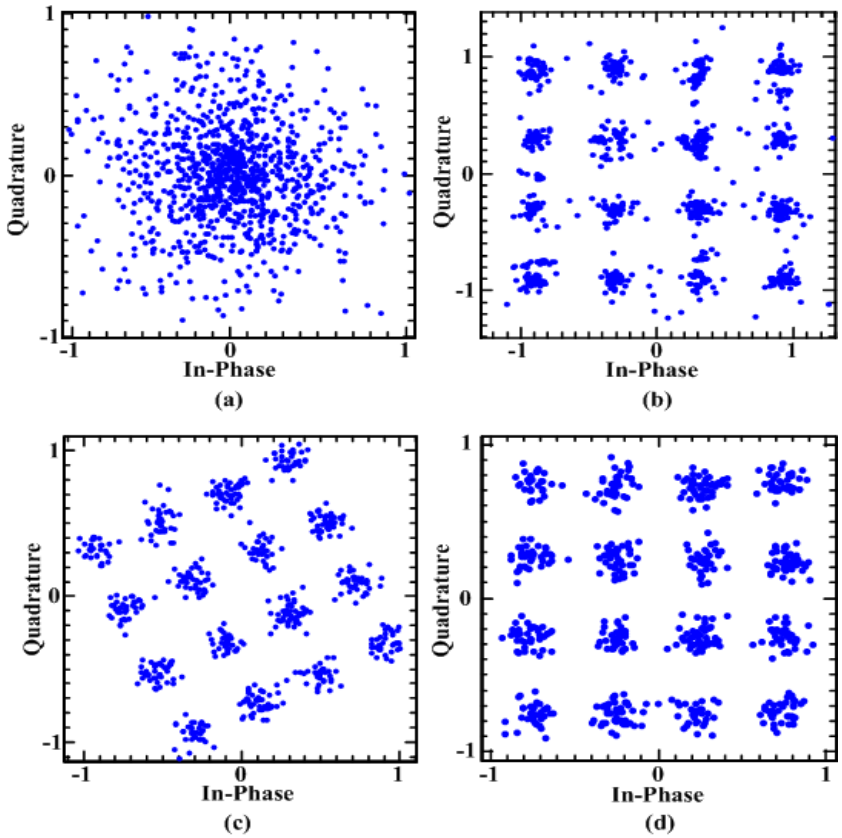

Figure 2.8: Constellation of received symbols at 10 km of transmission distance. (a) and (b) are received symbols of Rayleigh fading channel, (c) and (d) are received symbols of optical fibre channel. (a) and (c) are un-equalised constellation, (b) and (d) are equalized constellation

achievable in real-time transmission by lowering OLP. The optical receiver adopted in this investigation is based on DD with square-law detection.

Following this investigation, the author has published the resulting output in [86]. Figure 2.8 shows the constellation of received symbols after transmitting for 10 km through Rayleigh fading channel and SMF. Figure 2.8(a) is the constellation of the received symbols at a SNR of 16 dB prior to equalization. The constellation points are spread all over the phase angles due to high multipath fading. The constellation for equalized case using the frequency response of Rayleigh fading is illustrated in Figure 2.8(b). In terms of RoF, Figure 2.8(c) depicts the received symbols of the un-equalized optical fibre channel showing only a phase shift due to

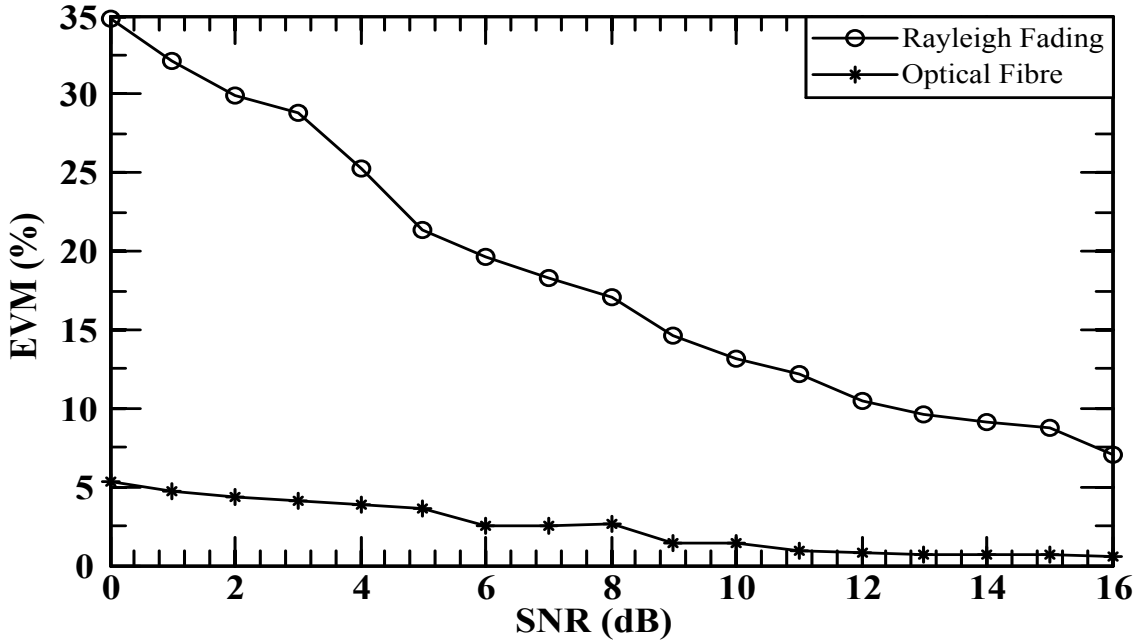

Figure 2.9: Error vector magnitude against the SNR for optical fibre and Rayleigh fading channels

the chirping effect of DFB laser and the fibre CD. Finally, the equalized constellation is shown in Figure 2.8(d).

In order to further quantify the constellation points, EVM is utilised to measure the precision and spreading of the constellation points. The EVM metric can analytically expressed as [87]:

$$EVM = \frac{\sqrt{\frac{1}{N_s}\sum_{n=1}^{N_s}\left|S_r(n) - S_t(n)\right|^2}}{R_{max}} \tag{2.8}$$

where $S_r(n)$ and $S_t(n)$ are the received and transmitted OFDM signals, and R_{max} is the maximum magnitude of the ideal transmitted symbol utilised for normalization. The EVM for both channels (Rayleigh and fibre) is shown in Figure 2.9 for a 10 km link span. At an SNR of 16 dB, which is the required value to achieve the optimum performance for RoF decided based on the bit error rate (BER) measurement, EVM for Rayleigh fading and optical fibre channels are 7.01% and 0.601%, respectively.

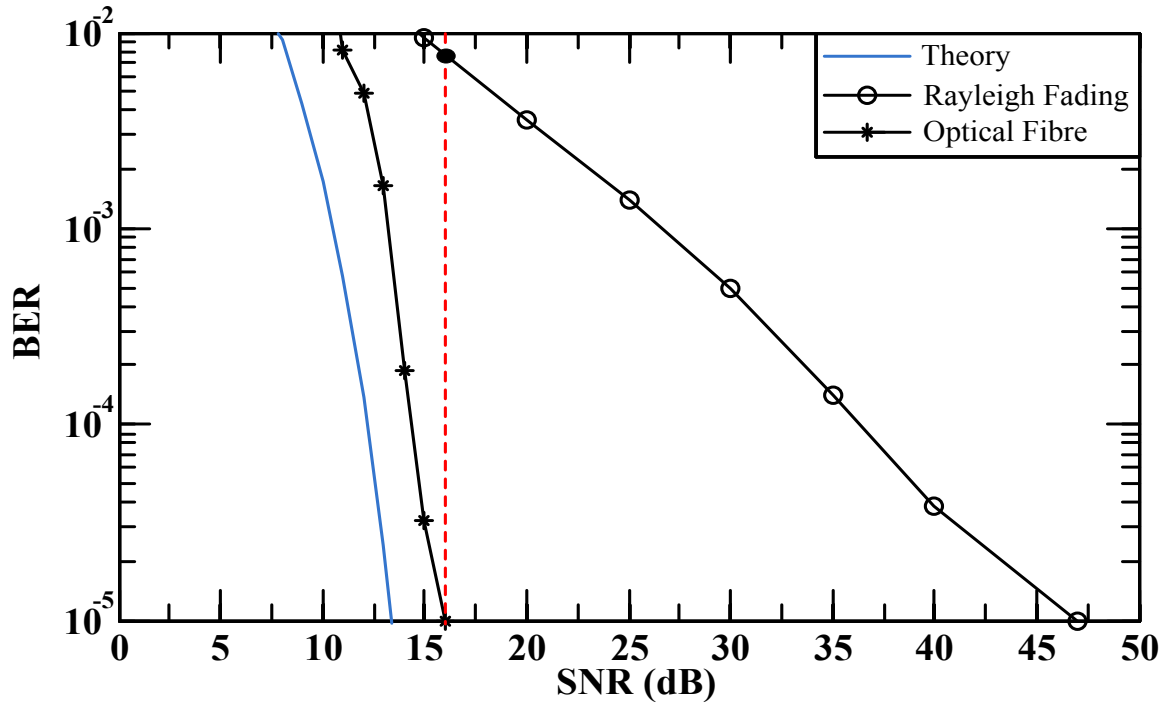

Figure 2.10: Simulated BER against the SNR for Rayleigh fading and optical fibre channels as well as the theoretical BER

In Figure 2.10, the BER performance against the SNR for both Rayleigh fading and optical fibre channels, as well as the predicted response of 16-QAM over a link span of 10 km are presented, where the BER measurement can be expressed as [72]:

$$BER = \frac{1}{2} erfc\left(\frac{Q}{\sqrt{2}}\right), \; Q = \frac{I_1 - I_0}{\sigma_1 + \sigma_0} \tag{2.9}$$

where $erfc(x)$ is the complementary error function, Q is the quality factor, I_1 and I_0 are the average photocurrents corresponding to one- and zero-symbol levels, and σ_1 and σ_0 are corresponding standard deviations. A BER of 10^{-5} is the required value for an un-coded wireless communication system [88]. At a BER of 10^{-5} the additional gains required for optical fibre and Rayleigh fading channels compared to the predicted case are ~3 dB and ~34 dB, respectively. In the perspective of SNR, Rayleigh fading channel at 16 dB only achieved BER of slightly better than

10^{-2} showing the superiority of RoF system efficiency. Finally, using RoF system the improvement is 31 dB compared to the wireless channel to achieve BER of 10^{-5} at 10 km transmission span.

2.4 Summary

This chapter was dedicated to the overview of RoF system and its in-build optoelectronic devices. Optical modulation methods are an important element of RoF system whereby detailed explanation was given with fair comparison between DM and external modulation. In terms of RoF channel, SMF was thoroughly investigated in comparison with wireless channel. Here, RoF improved the link viability with 31 dB of SNR gain, which is a remarkable gain in commercial application. Since the RoF system proposed in this thesis is mostly comprise of DML, an in-depth theoretical breakdown and a new frequency chirp expression will be presented in the following chapter.

CHAPTER 3 DISTRIBUTED FEEDBACK LASER AND FREQUENCY CHIRPING

Recent researches have shown much progress and interest in DML based analogue optical links, best known as IM scheme for RoF applications [57]. The possibility of low cost design has driven all interest to DML, which is also the main motivation of this project. Semiconductor lasers are proven as an appropriate transmission source by adopting DML concept into optical communication.

In order to meet the long haul transmission requirement of RoF system in this research, a laser source with low noise, low distortion, and high output power with a relatively low bias current are required [33]. The dynamic single mode (DSM) is an important criterion for a laser that operates as a modulator in long haul transmission, which means the laser should have a large side mode suppression ratio (SMSR) (>30 dB) [89]. A DFB is a suitable candidate with all the required characteristics for a RoF system that aims at long haul transmission. A DFB generates high output power at 1550 nm wavelength (operating wavelength of this project) that is efficient enough for regenerator spacing of 80-100 km [90].

3.1 Theoretical Overview of Lasers

The term laser is derived from the process of Light Amplification by Stimulated Emission of Radiation. As the process construes, a laser solely operates based on stimulated emission for high coherent radiation. The role of laser in RoF system is mostly to act as either an optical modulator or optical source for external modulation. The process of light generation in a laser is relative to the recombination of electron and holes in p-n junction with material such as Indium Gallium Arsenide Phosphide (InGaAsP) or other III-V compound semiconductors sandwiched between the junctions [72, 79].

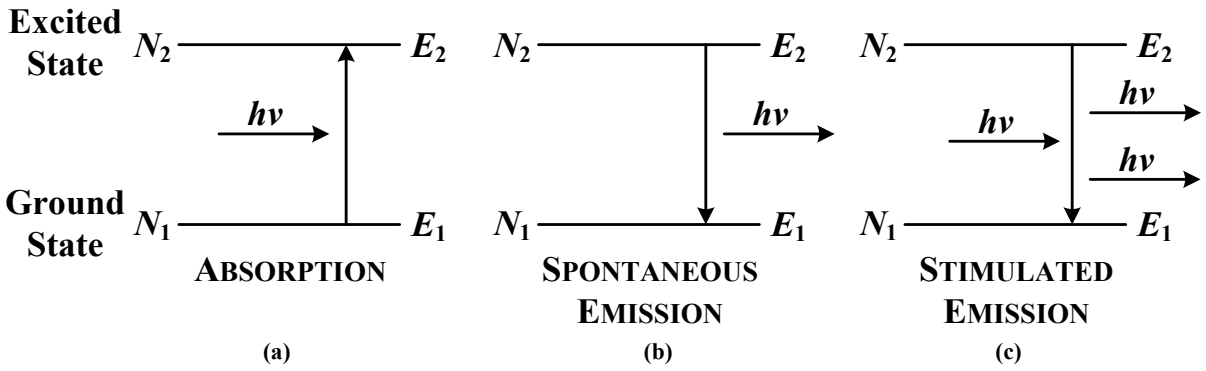

Figure 3.1: The three process of recombination, (a) Absorption, (b) Spontaneous emission and (c) Stimulated emission

The nature of recombination process separates the light-emitting diode (LED) from a conventional laser. In LED, the recombination process results in spontaneous emission with broad spectral characteristic, thus the radiation field is large and operates as an incoherent source. On the other hand, the recombination process in laser is almost completely based on stimulated emission and allows a coherent operation with narrow field radiation [72]. The recombination process occurring from the bias current injection in a semiconductor material can be classified into three processes, namely absorption, spontaneous emission and stimulated emission. Figure 3.1 graphically illustrates the three processes. In the ground state N_1 the number of electrons with energy E_1 is substantially higher than the number of electrons in the excited state N_2 with energy E_2. At the uniform temperature state, the ratio between ground state and excited state can be described following the Boltzmann's statistics [91]:

$$\frac{N_2}{N_1} = \exp\left(-\frac{h\nu}{k_B T}\right) = \exp\left(-\frac{E_2 - E_1}{k_B T}\right) \tag{3.1}$$

where h is Planck's constant, ν is the optical frequency, and $h\nu$ represents a photon energy generated through the difference between the energy levels E_2 - E_1, k_B is the Boltzmann's constant and T is the absolute temperature. The absorption rate $dN_{1,abs}/dt = A_{12}P(\nu)N_1$ is

shown in Figure 3.1(a), where A_{12} is the absorption coefficient, $P(v)$ is the spectral density of electromagnetic energy. Basically, absorption occurs to excite electrons, whereby initiating both the spontaneous emission rate $dN_{2,spon}/dt = A_{21}N_2$, where A_{21} is the spontaneous emission coefficient and stimulated emission rate $dN_{2,stim}/dt = B_{21}P(v)N_2$, where B_{21} is the stimulated emission coefficient [72]. Figure 3.1(b) shows that the electrons in the excited state spontaneously decay and fall back to ground state, effectively generating a photon from the energy obtained via the transition. In terms of stimulated emission, Figure 3.1(c) illustrates that photons are emitted from the energy differences E_2 - E_1 between excited state and ground state.

When the excited state is higher than the ground state, stimulated emission rate will exceed the absorption rate, where this phenomenon is known as population inversion and the gain of the laser will be above unity. Laser operates based on population inversion achieved via an external energy source pumping and raising the population from ground to the excited state. The stimulated emission is governed by three components, namely, the pump source, active region, and feedback mirrors. Conventionally, the pump is electrical, active region is solid, gaseous, or liquid in nature. These are the basic principles of Fabry-Perot laser, which evolved into DFB and vertical cavity surface emitting lasers (VCSEL).

3.2 Types of Lasers

There are many ways in reflecting light through the active region into the cavities, with different materials serves as the gain mediums and light confining regions. The three well known semiconductor lasers that served widely in optical communication sector are: 1) Fabry-Perot lasers, 2) VCSELs and 3) DFB [89].

Fabry-Perot lasers, illustrated in Figure 3.2(a) are used in optical communication since 1960's and the structure is the simplest of all semiconductor lasers with radiation through the edge of the laser. The internal structure of Fabry-Perot lasers is built by epitaxially

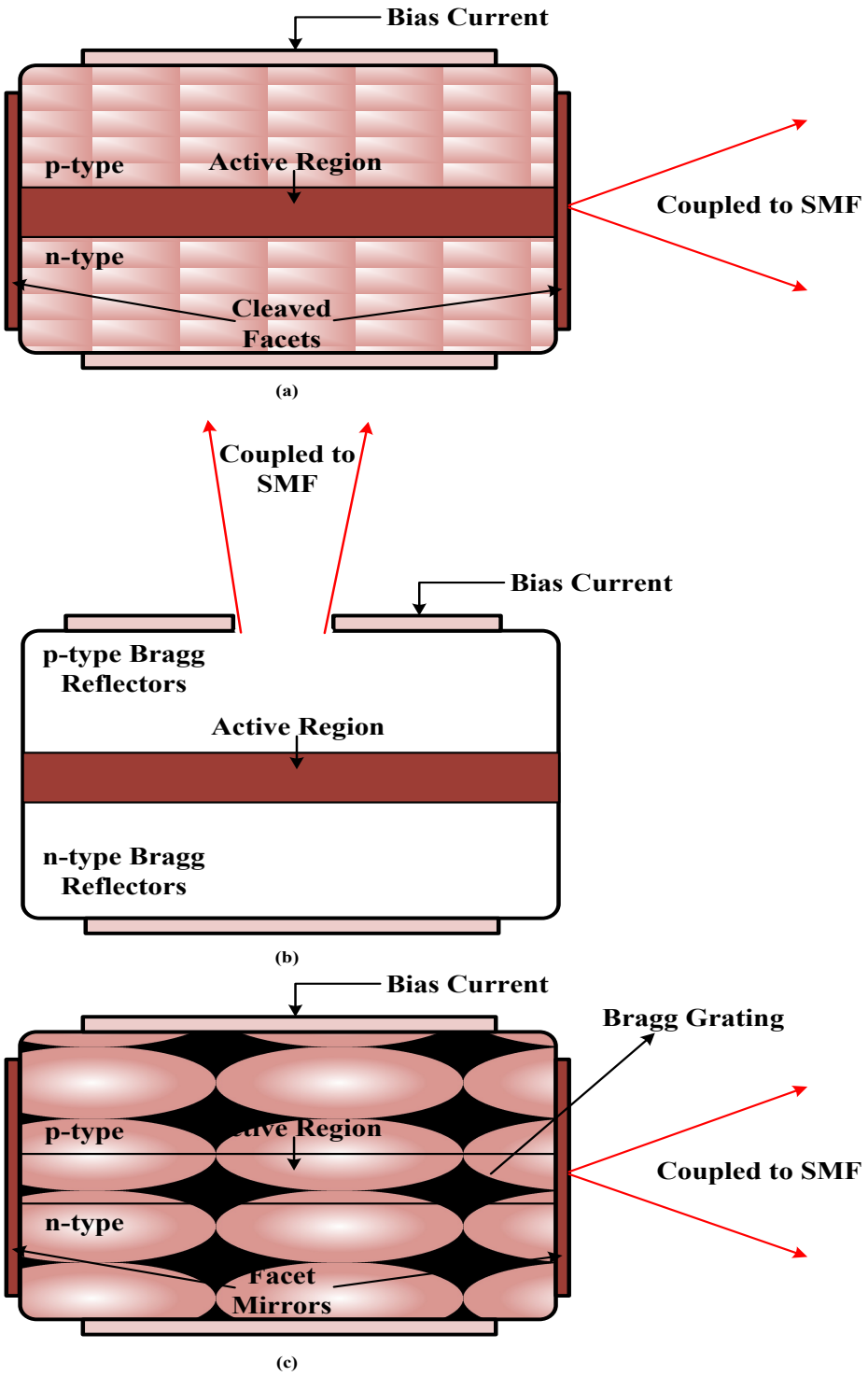

Figure 3.2: Internal structures of (a) Fabry-Perot laser, (b) VCSEL, and (c) DFB laser.

growing the cladding and active layers for active region, while the cavity or mirrors are formed by cleaving the semiconductor. The mirrors at the both end of the optical cavity, within the active region, are used for reflections to produce constructive interference and form the longitudinal mode at the required wavelength. The resonating length of Fabry-Perot cavity is normally in the order of several hundred micrometres, much larger than the corresponding lasing wavelength, thus many longitudinal modes will exist in the optical spectrum. Since many modes exist from the forward and backward reflecting waves over a long cavity, the SMSRs are very low and will be subject to heavy frequency chirp. Therefore, Fabry-Perot lasers do not satisfy the requirements of DSM transmission [89].

There is another important type of semiconductor laser that emits light vertical with respect to the active plane layer, known as VCSELs as shown in Figure 3.2(b). Fabry-Perot laser structure is modified into VCSEL, where its lasing axis is now placed vertical to the cavity instead of in-plane. The highly complex VCSELs structure consists of a distributed Bragg-reflector section, a multiple quantum wells in the active layer and finally with another distributed Bragg-reflector section. Although VCSELs demonstrate the ability of emitting DSM output due to the short cavity structure, the VCSEL-to-fibre coupling is very sensitive that might result in misalignment and subsequently emitting multimode optical spectrum [73, 92].

The only semiconductor laser that is proven to be highly efficient with DSM characteristic is the DFB, which was first proposed by Kogelnik *et al* [93]. The first step of DFB fabrications is epitaxially growing the p-i-n structure, similar to a Fabry-Perot laser. A periodic Bragg grating is formed in the DFB cavity by applying holographic exposure or by electron beam lithography [68]. Figure 3.2(c) provides the overview of a typical DFB structure. Since Fabry-Perot laser exhibit multimode characteristic due to high resonating

length, DFB is designed with a Bragg grating within the laser cavity to effectively select one longitudinal mode and suppress the rest [73]. Owing to this enhanced capability of the DFB with demonstrating high output power, it became the ultimate choice as the DML of this project.

3.3 Rate Equation Approach for Distributed Feedback Laser

In DFB, input bias current, coupled with a RF signal if required, will enter the laser as the pump source. It is important to determine the carrier density growth relative to the input bias current for analysing any modulation-induced impairment. The laser dynamics can be modelled and analysed by utilising the rate equations of a laser. A few coupled nonlinear differential equations can be adopted as the DFB rate equations to describe the interactions between input signal I_d, rate of change of carrier density *dN*/*dt* and the relative carrier density *N*, and rate of change of photon density *dS/dt* and the relative photon density *S*. The initial form of rate equation could be described as [94]:

$$\frac{dN}{dt} = \text{Input signal rate} - \text{Carrier decay rate} - \text{Net stimulated emission rate}$$

$$\frac{dS}{dt} = \text{Net stimulated emission rate} + \text{Spontaneous emission rate} - \text{Photon decay rate}$$

The detailed form of the rate equations that were adopted into this thesis is given by [95]:

$$\frac{dN}{dt} = \frac{I_d}{edwl} - \frac{N}{\tau_c} - BN^2 - CN^3 - G\frac{(N - N_t)}{1 + \varepsilon S}S \tag{3.2}$$

$$\frac{dS}{dt} = \frac{G(N - N_t)}{1 + \varepsilon S}S + \zeta BN^2 - \frac{S}{\tau_p} \tag{3.3}$$

$$P = x w_v w_h h w_o \frac{Sc}{2n_g} \tag{3.4}$$

$$\frac{d\Phi}{dt} = \frac{1}{2}\Gamma LWGv_g(N - N_t) \tag{3.5}$$

$$\omega = \omega_o\left(1 - \frac{\Gamma G v_g (N - N_t)}{n_p}\right) \tag{3.6}$$

where P, Φ, and ω are the optical power, optical phase, and optical frequency, respectively; the volume of the DFB is described as the thickness d, width w, and length l; e is the electronic charge; τ_c is the carrier decay rate; B is the bimolecular carrier recombination coefficient; C is the Auger carrier recombination coefficient; G is the linear optical gain coefficient; N_t is the transparency carrier density; ε is the nonlinear gain coefficient; Γ is the mode confinement factor (MCF); ζ represents the fraction of spontaneous emission; τ_p is photon decay rate; x is the coupling efficiency from the laser chip to the SMF; w_v and w_h are the vertical and horizontal widths of the guided mode power distributions; h is the Planck's constant; c is the speed of light in vacuum; LW is the linewidth enhancement factor; v_g is the group velocity; ω_o is the central optical frequency; n_p is the phase refractive index. Refer to Table 3.1 for all parameter values.

Equations (3.2) and (3.3) are numerically modelled to modulate the RF signal onto an optical carrier that can be observed via equation (3.4). In addition, equations (3.5) and (3.6) can be modelled to observe the optical phase and optical frequency at the output facet. Numerical calculation of the rate equations of (3.2), (3.3) and (3.5) in MATLAB^{TM} can be performed using equation (3.7), where $x(t)$

Table 3.1: Parameters Used in Simulation [33, 94].

Parameter	Parameter Symbols	Parameter values
N	Carrier density	-
S	Photon density	-
P	Optical power	-
Φ	Optical phase	-
ω	Optical frequency	-
ω_o	Central frequency	193.5 THz
I_d	Input current	-
d	Thickness	0.033 μm
w	Width	2 μm
l	Length	300 μm
e	Electronic charge	$1.6\text{x}10^{-19}$ C
τ_c	Carrier decay rate	10 ns
B	Bimolecular carrier recombination coefficient	$1\text{x}10^{-16}$ m^3/s
C	Auger carrier recombination coefficient	$6.5\text{x}10^{-41}$ m^6/s
G	Linear optical gain coefficient	$1.1\text{x}10^{-12}$ m^3/s
N_t	Transparency carrier density	$1.5\text{x}10^{24}$ m^{-3}
ε	Nonlinear gain coefficient	$7.4\text{x}10^{-23}$ m^{-3}
Γ	Mode confinement factor	0.8
ζ	Fraction of spontaneous emission	$1\text{x}10^{-5}$
τ_p	Photon decay rate	3.6 ps
χ	Coupling efficiency	37%
w_v	Vertical widths	0.47 μm
w_h	Horizontal widths	1.80 μm
h	Planck's constant	$6.63\text{x}10^{-34}$ m^2kg/s
c	Speed of light	$3\text{x}10^8$ m/s
LW	Linewidth enhancement factor	3
v_g	Group velocity	$8.1\text{x}10^7$ m/s
n_p	Phase refractive index	3.7
N_e	Excess carrier density	$1.1\text{x}10^{25}$ m^{-3}

represents carrier density, photon density, and optical phase in conjunction to the temporal boundary condition t_B.

$$x(t + t_B) = x(t) + \frac{dx}{dt} \times t_B \tag{3.7}$$

3.3.1 Rate Equation Based Chirp Analysis

DM of laser results in IM with respect to the input signal, where saliently it also induces laser phase fluctuations. Such phenomenon occurs because DM leads to changes in the laser active region, thus affecting the refractive index and consequently the phase of the generated optical signal [96]. This phenomenon is known as PFC. The dynamic chirp

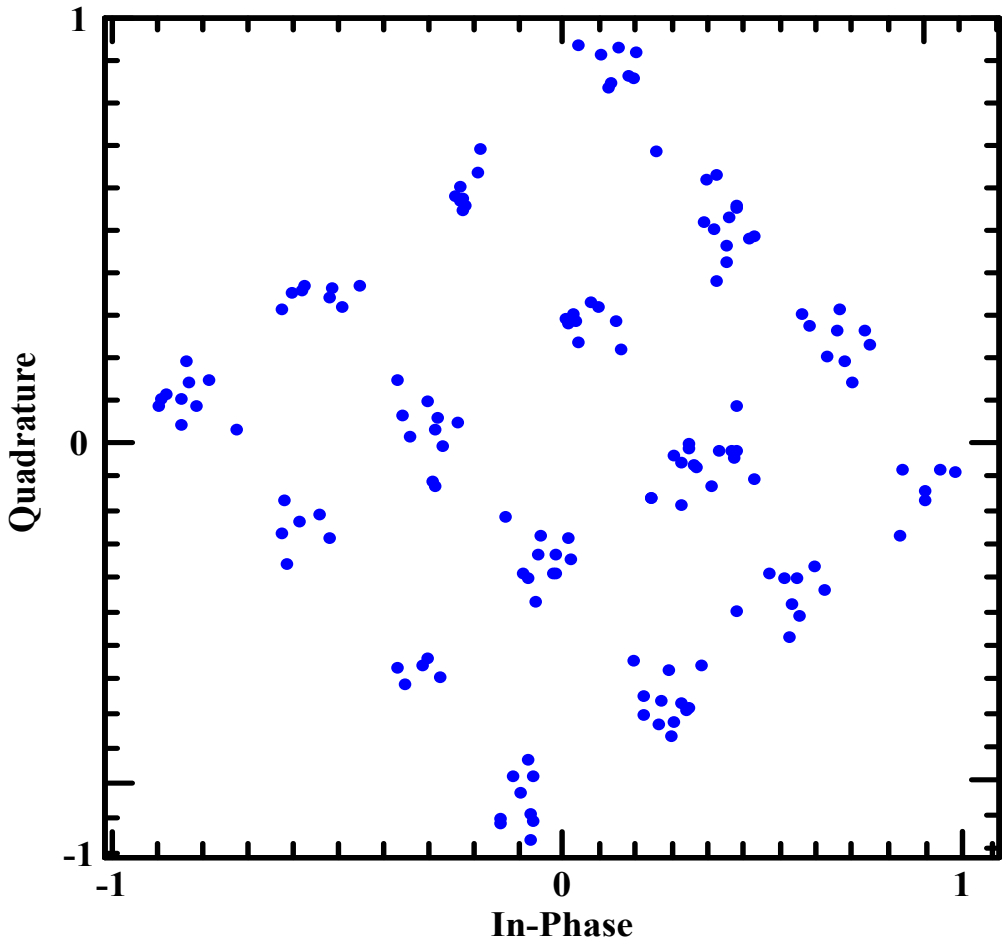

Figure 3.3: Constellation of 16-QAM with frequency chirp effect

characteristic of a DFB is in the form of blue rising edge and red trailing edge, which means rising edge propagates quicker than the trailing edge resulting in a spread out signal. In other word the rising edge of the time domain pulse will experience a upward shift and the falling edge will experience a downward shift. Such shifts in the rising and falling edge of a pulse due to PFC will couple with the pulse spreading effect of CD of optical fibre, and induces severe distortion to the propagating signal and massive reduction in transmission distance via SMF [33].

Figure 3.3 illustrates the 16-QAM constellation with an average phase shift of ~8º. This phase shift and the spread of constellation points indicate the noise factor introduced by the chirping effect alone without any CD effects. Therefore, modulating the RF signal onto the

DFB via the given rate equations of (3.2) and (3.3) are contributing to the PFC effect that results in a phase distortion and noise. Earlier work in this particular area only derived a closed form expression for PFC via equations (3.5) and (3.6), given as [33] [97-99]:

$$\Delta v(t) = \frac{LW}{4\pi}\left(\frac{d}{dt}\left[\ln P(t) + kP(t)\right]\right) \tag{3.8}$$

where Δv is the instantaneous frequency deviation, k is the adiabatic chirp coefficient. The integral of the instantaneous frequency deviation is relative to the integral of equation (3.5) [97]:

$$\Phi(t) = 2\pi\int_0^t \Delta v(t)dt \tag{3.9}$$

and the solution to equation (3.9) is:

$$\Phi(t) = \frac{LW(\ln P(t) + kP(t))}{2} \tag{3.10}$$

The end result to describe the PFC is defined by the equation (3.10). From theoretical point of view, equation (3.10) is adequate to describe the impact of PFC on the modulated optical signal. But, the actual PFC affect that arises in a numerical simulation initiates from integrating equations (3.2) and (3.3). Therefore, the author proposes to investigate on the relationship between equations (3.2) and (3.3), which happens to be the core for PFC affect, observed in Figure 3.3. Since equation (3.2) is complex for further analytical investigation, the author adapted the unmodified rate equations of DFB which was employed by Bjerkan *et al* [100]:

$$\frac{dN}{dt} = \frac{I_d}{edwl} - \frac{N}{\tau_c} - G\frac{(N - N_t)}{1 + \varepsilon S}S \tag{3.11}$$

$$\frac{dS}{dt} = \frac{\Gamma G(N - N_t)}{1 + \varepsilon S} S - \frac{S}{\tau_p} + \frac{\Gamma \zeta N}{\tau_c} \tag{3.12}$$

The differences between equations (3.2) and (3.3) compared to equations (3.11) and (3.12), respectively, is the reduction of decay rate in equation (3.11), and the modified spontaneous emission factor in equation (3.12). The result of these changes only contributes to increased output power from integrating equation (3.11) and (3.12) due to not considering the non-radiative recombination.

3.3.2 Carrier and Photon Density Relationship

Investigation of PFC requires detailed derivation of equations (3.11) and (3.12). The derivation is carried out based on the relativity of stimulated emission between equations (3.11) and (3.12) arising from coupled wave theory. The author has published the resulting output of the derivation in [101]. Starting from defining equation (3.11) as the equivalent of stimulated emission and substitute it into equation (3.12) results in:

$$\frac{dS}{dt} = \Gamma\left(-\frac{dN}{dt} + \frac{I_d}{edwl} - \frac{N}{\tau_c} \right) - \frac{S}{\tau_p} + \frac{\Gamma \zeta N}{\tau_c} \tag{3.13}$$

Now, equation (3.13) establishes the presence of the carrier density into the generation of the equivalent photon density. A simple rearrangement of equation (3.13) will introduce mathematically that the rate of change of carrier density is relative to the MCF and the rate of change of photon density:

$$\Gamma\left(\frac{dN}{dt} \right) + \frac{dS}{dt} = \Gamma \frac{I_d}{edwl} - \Gamma \frac{N}{\tau_c} + \frac{\Gamma \zeta N}{\tau_c} - \frac{S}{\tau_p} \tag{3.14}$$

Equation (3.15) is defined to concisely express the relationship unveiled in equation (3.14):

$$\frac{dZ}{dt} = \Gamma\left(\frac{dN}{dt}\right) + \frac{dS}{dt} \tag{3.15}$$

From the principal of laser emission, equation (3.15) represents the process of electron hole recombination with respect to the MCF. Theoretically, MCF is the ratio of the carrier volume/photon volume that is inversely proportional to the density factor based equations (3.11) and (3.12). Therefore, in the case of density, the MCF ratio changes to the aspect of photon density/carrier density. The detailed operation of Equation (3.15) basically demonstrates the rate of change of instantaneous process *dZ*/*dt* of total current injected, that result in carrier density relative to the MCF, then through the recombination process results in the photon density.

The respective solution of equation (3.15) is:

$$Z = \Gamma N + S \tag{3.16}$$

where *Z* is the instantaneous process that results from the direct integral of equation (3.15).

By substituting equation (3.15) into equation (3.14), the following expression is obtained:

$$\frac{dZ}{dt} = \Gamma\frac{I_d}{edwl} - \Gamma\frac{N}{\tau_c} + \frac{\Gamma\zeta N}{\tau_c} - \frac{S}{\tau_p} \tag{3.17}$$

A few assumption need to be made to equation (3.17) to achieve equation (3.16). In order to perform that, equation (3.17) will be reformed with the aid of equation (3.16):

$$\frac{dZ}{dt} = \Gamma\frac{I_d}{edwl} - \frac{-1+\zeta}{\tau_c}Z + \left(-\frac{1}{\tau_p} + \frac{1-\zeta}{\tau_c}\right)S \tag{3.18}$$

The final term of equation (3.18) can be effectively eliminated with some assumptions. The carrier decay rate is the inverse of bimolecular carrier recombination and excess carrier density, N_e, as shown [94]:

$$\tau_c = \frac{1}{BN_e} \tag{3.19}$$

The photon decay rate incorporating bimolecular carrier recombination can be expressed as [94]:

$$\tau_p = \frac{8.85 \times 10^{-26}}{B} \tag{3.20}$$

Substituting equations (3.19) and (3.20) into equation (3.18), with further derivation would lead to the elimination of the final term. Since optical modulation only occurs high above the threshold region, the fraction of spontaneous emission is neglected [94]. Thus, the resulting expression from the derivation will be:

$$\frac{dZ}{dt} = \Gamma \frac{I_d}{edwl} - \frac{1}{\tau_c} Z \tag{3.21}$$

Equation (3.21) is the new closed-form expression for the rate of change of electron hole recombination that generates a photon within the active region. The rate of change of carrier density and photon density is confined within equation (3.21). Hence, equation (3.21) carries the properties of both the rate of change of carrier density and photon density. The solution of equation (3.21) can be obtained by applying the integrating factor method, which yields:

$$Z(t) = e^{-\frac{1}{\tau_c}(t_{\lim} - t_0)} Z(t_0) + \int_{t_0}^{t_{\lim}} e^{-\frac{1}{\tau_c}(t_{\lim} - t)} \frac{\Gamma}{edwl} I_d(t) dt \tag{3.22}$$

where t_o is the beginning of a symbol period, $t_{\lim}$ is the symbol period and t is the continuously varying time of the input signal. The 1st term of equation (3.22) represents the initial condition and the 2nd term shows the actual integral of the input signal that is bounded within the MCF. Transient chirping or general frequency chirping is related to the changes in carrier density, which in turn reflects the changes in the refractive index. In equation (3.8), the expression only describes chirping with respect to the optical power, but

the input current also induces chirping. The instantaneous process $Z(t)$ explicitly shows that input current actually alters the carrier density, taking carrier decay rate into consideration. The LTE technology operates based on MCM, namely OFDM. Generally, OFDM has a noise-like envelope due to the Gaussian distribution arising from central limit theorem. Mathematically, an integral function of a sinusoidal signal is a cosinusoidal signal as a result of phase variation. Therefore, integral of an input current in equation (3.22) is composed of the noise-like time varying OFDM signal with Gaussian distribution. This phenomenon will directly affects the refractive index of DFB and deduce the characteristics of transient chirp.

3.4 Summary

This chapter explained the core reasons for using DFB as the optical transmitter of this project. The DFB outperforms Fabry-Perot lasers and VCSELs in various technical aspects, including the most important requirement of DSM. In a DFB, PFC is an important impairment for long haul transmission because of its ability to coordinate with CD and jointly distort the optical signal. The existing mathematical expression does not precisely explain on how rate equations contribute to PFC that effectively distorts the modulated optical signal. This chapter explained the author's contribution on a new analytical expression to explain how the rate equations are actually the factor that produced PFC effect in a computer simulation. Withstanding on the focus of laser transmitter, next chapter will unfold the optimisations of LTE transmitter relative to laser transmitter. In addition, new optical transmitters will be introduced to further investigate on the actual impact of PFC to the LTE-RoF link.

CHAPTER 4 THEORETICAL DESIGN AND OPTIMISATION OF LTE-A ROF LINK

The advantage of RoF compared to wireless channel was shown in Chapter 2 for the application of LTE, where RoF demonstrated high power efficiency. As a detailed design step for LTE-RoF system, Chapter 3 was dedicated to the introduction of DFB and the frequency chirping characteristic that occurs from the DML technique.

Continuing the focus on theoretical development, this chapter is dedicated to the LTE-A and RoF integration. The major differences between LTE and LTE-A are the introduction of carrier aggregation, and the maximum bandwidth of 100 MHz to support higher data rate, as shown in Table 1.2. In other word, LTE-A will be transmitting a composite of multi-type bandwidth signals within the limit of 40 to 100 MHz [14]. The carrier aggregation method is substantially complex compared to the conventional LTE transmitter. For an example, at 100 MHz bandwidth, 5×20 MHz simultaneous OFDM signals are required to fulfil the entire bandwidth [102, 103]. Furthermore, to achieve aggregation, 4 additional LOs at different frequencies are required to shift the baseband OFDM signals to passband domain. In order to minimize the complexity, this chapter proposes to adopt the varying FFT sizes scheme of LTE into LTE-A. The proposed method will effectively slice the 100 MHz bandwidth into narrow subcarriers, which potentially leads to the requirement of only a single OFDM signal generation at 100 MHz bandwidth and single LO for passband up-conversion.

Both LTE and LTE-A utilises OFDM as the MCM technique. Weinstein *et al* [104] first proposed the usage of FFT instead of discrete Fourier transform (DFT) in OFDM, which revolutionized the modern communication world. The number crunching ability with the FFT algorithm is much more efficient, where a FFT size-1024 operation only takes a few seconds in conventional home computers [105]. The original DFT algorithm performs complex multiplications of approximately equivalent to N_s^2, while FFT algorithm

performs similar operation in the form of $(N_s)*\log_2 N_s$, where N_s is the DFT/FFT size. The complex calculation carried out via $(N_s)*\log_2 N_s$ (FFT) imposes significant reduction in calculations compared to N_s^2 (DFT), particularly for large N_s. Thus, FFT algorithm is an efficient algorithm for OFDM modulation in LTE, with FFT sizes ranging from 128 to 2048. However, in the case of LTE-A with carrier aggregation, the 100 MHz bandwidth is composed of 5×20 MHz signals with each 20 MHz bandwidth consists of FFT size-2048, see Table 1.2. Thus, the maximum bandwidth of 100 MHz will be composed of FFT-size 10240, which shows the inefficiency of carrier aggregation process. Although FFT performs quick calculation, the proposed method of this chapter with single processor would provide a much efficient operation in commercial LTE-A deployment.

4.1 LTE-A and RoF Link with Varying FFT sizes

The LTE-A transmitter is configured with SCMs of quadrature phase shift keying (QPSK), 16, and 64-QAM. These SCMs are then modulated onto OFDM with scaled FFT sizes of 128, 256, 512 and 1024, as shown in equation (2.3) [106]. For a 100 MHz bandwidth, small FFT size generates large subcarrier frequency resulting in short symbol length, making it susceptible to ISI, and contrariwise for large FFT size. However, the shortcoming of large FFT size is that the subcarrier frequency will be significantly narrow and closely spaced, thus it will be more sensitive towards inter-carrier interference (ICI) [107].

The linear impairments (linear propagation region), namely PFC and CD introduced by DML and SMF, respectively, will lead to ISI for small FFT size. Conversely, the nonlinear impairment (nonlinear propagation region) of SMF actuates nonlinear phase noise and introduces ICI for large FFT size. Therefore, it is important to optimise the FFT sizes relative to the impairments induced by the RoF system.

Jansen *et al* [34] and Adhikari *et al* [35] optimised the FFT size in CO-OFDM system, while taking the linear and nonlinear optical fibre propagation into consideration. In [34], the FFT size-1024 (the highest FFT size investigated) exhibits higher distortion compared to smaller FFT size in the nonlinear propagation region due to ICI. Likewise in [35], FFT size-4096 (highest FFT size investigated) experiences higher distortion compared to smaller FFT size in nonlinear region, which is a factor of ICI as well. In terms of ISI occurrence from linear impairments, [35] demonstrated that FFT size-512 (the smallest size investigated) is more susceptible to distortion compared to FFT-size 4096. The findings reported in [34, 35] are limited to coherent detection scheme and since this research concentrates on DD scheme, it is important to investigate the impact of FFT sizes in the DD scheme. Pham *et al* [36] optimised the FFT size for DD-OOFDM system for the linear impairments (PFC and CD). Hence, the analysis presented in [36] is not sufficient enough to address the contribution of nonlinear phase noise to the varying FFT sizes.

In this chapter, the DD-OOFDM signal for LTE-A RoF system is proposed with FFT sizes of 64, 128, 256, 512 and 1024 over SMF. The optical propagation is evaluated in terms of A) linear, B) intermixing, and C) nonlinear regions. The intermixing region is part of the contribution proposed in this chapter. The detailed explanations of linear impairments were given in Chapters 2 and 3, namely CD and PFC, respectively. In addition, overviews of the nonlinear impairments were given in Chapter 2. Hence a dedicated section will be allocated to explain the phenomenon of the intermixing region which arises from the transition of linear to nonlinear propagation state and nonlinear to linear propagation state, with increasing and decreasing OLP, respectively. The author has published the outcome of the proposed method in [108].

4.2 The Intermixing Region

The interaction between the PFC and CD can be minimized with accurate control of OLP by utilising optical attenuator or amplifier, where the OLP is a switch-like mechanism that determines the nonlinearity level and controls the propagation state. The nonlinear characteristic of optical fibre with respect to the OLP, can be described through the dependence of the optical fibre refractive index n_r on the optical signal power $P(t)$ [109]:

$$n_{\mathrm{r}} = n_{\mathrm{o}} + n_{\mathrm{nl}}\left|P(t)\right|^2 \tag{4.1}$$

where n_{o} is the linear refractive index, n_{nl} is the nonlinear index coefficient. The refractive index dependence on the optical signal envelope gives rise to nonlinear impairment, namely SPM. The combination of SPM with CD and the PFC can reduce the dispersion induced power penalty at an appropriate OLP, known as the intermixing region.

The SMF model that governs the properties of linear and nonlinear impairments, associated with the propagation can be expressed by the generalized nonlinear Schrödinger equation [109]:

$$\begin{aligned} &\frac{\partial P(z,t)}{\partial z} - \check{D}(z,t) = -\check{N}(z,t), \\ &\check{D}(z,t) = -\frac{j}{2}\beta_2 \frac{\partial^2 P(z,t)}{\partial {T_o}^2} + \frac{\alpha}{2}P(z,t), \\ &\check{N}(z,t) = j\frac{2\pi}{\lambda} n_2 \left|P(z,t)\right|^2 P(z,t), \end{aligned} \tag{4.2}$$

where $P(z,t)$ is the OLP comprises of the distance propagated z, $\check{D}(z,t)$ is the linear operator, $\check{N}(z,t)$ nonlinear operator for SPM, $\beta_2 = (-\lambda^2/2\pi c)*D$ is the second order dispersion coefficient with λ is the optical wavelength, c is the speed of light, and D is the optical fibre dispersion parameter, $T_o = t - z/v_{\mathrm{g}}$ is the time in a step that

propagates at the group velocity v_g, α is the SMF attenuation coefficient. Equation (4.2) can be numerically modelled using the symmetrical split-step method, as follows [110]:

$$P(z+h_s,t)=\left[\exp\left(\frac{h}{2}\overset{\vee}{D}(z,t)\right)\times\exp\left(\int_{z}^{z+h}\overset{\vee}{N}(z,t)dz\right)\times\exp\left(\frac{h}{2}\overset{\vee}{D}(z,t)\right)\right]P(z,t) \quad (4.3)$$

where h_s is the step taken to reach the actual propagated distance.

The nonlinear phase distortion induce by SPM is shown in equation (4.4), the nonlinear phase impairment occur as a function distance propagated and the OLP.

$$\phi_{NL}(z,t)=-\frac{1-\exp(-\alpha z)}{\alpha}\frac{2\pi}{\lambda}n_{nl}\left|P(z,t)\right|^2 \quad (4.4)$$

It is important to be aware that operating at the 1550 nm transmission window in the SMF, the impairment associated with CD results in signal spreading, which is why it correlates with PFC, because both impairments saliently induces phase to amplitude distortion. However, as shown in equation (4.4), the SPM induced nonlinear phase distortion is based on negative chirping. In other word, PFC and CD evolve as blue shifted rising edge and red shifted trailing edge, leading to signal spreading. Contrariwise for SPM, where it exhibits red shifted rising edge and blue shifted trailing edge resulting in signal compression [111, 112]. When the mixing of PFC and CD with SPM occur, the system penalty will effectively reduce, which is known as the intermixing region. In other word, the intermixing region provides a range of optimum OLP by an interchangeable compensation between PFC and CD with the SPM, without any additional components.

In terms of DD systems, Ramos *et al* [109] initially proposed the intermixing region based compensation. The finding reported in [109] is limited to the frequency-length product analysis for a simple binary transmission system. Park *et al* [113] utilised the

intermixing region, with highly dispersed pulses to compensate optical fibre nonlinearity and effectively achieved optimum OLP at around ~6 dBm. In [114], Ali *et al* demonstrated the nonlinearity impact on DD-OOFDM system, which arises from 5 dBm onwards. However, the analysis in [114] did not address the intermixing region, as the OLP analysis was carried out from 3 dBm to higher OLP. Interestingly, in [115], the DD-OOFDM system experienced nonlinearity from the OLP of -4 dBm onwards. It is unusual for DD-OOFDM system to experience nonlinear distortion at such low OLP, due to the high rate of CD in DD scheme compared to coherent detection [107, 116]. However, the occurrence of nonlinearity is also dependent on the OFDM equalizer's ability to compensate nonlinear phase rotation, which logically will change for every equalization method.

In this chapter, as part of the proposed LTE-A with varying FFT size scheme and its optimisation, the intermixing region is introduced for efficient LTE-A RoF integration. The optical compensating scheme based on intermixing region is very attractive because there is no additional optical equalizer required. Hence, designing the LTE-A RoF system with intermixing region demonstrates cost effectiveness, since there is no additional optical equalizing device required as part of the system design.

4.3 Transmission Link for LTE-A RoF

The DD-OOFDM system shown in Figure 4.1 is the overview block diagram for LTE-A RoF system. At the transmitter in eNB, 62, 126, 254, 510, and 1022 parallel data streams are generated, and mapped into a parallel complex data using QPSK, 16, and 64-QAM modulation formats within SCM module for all the respective number of data.

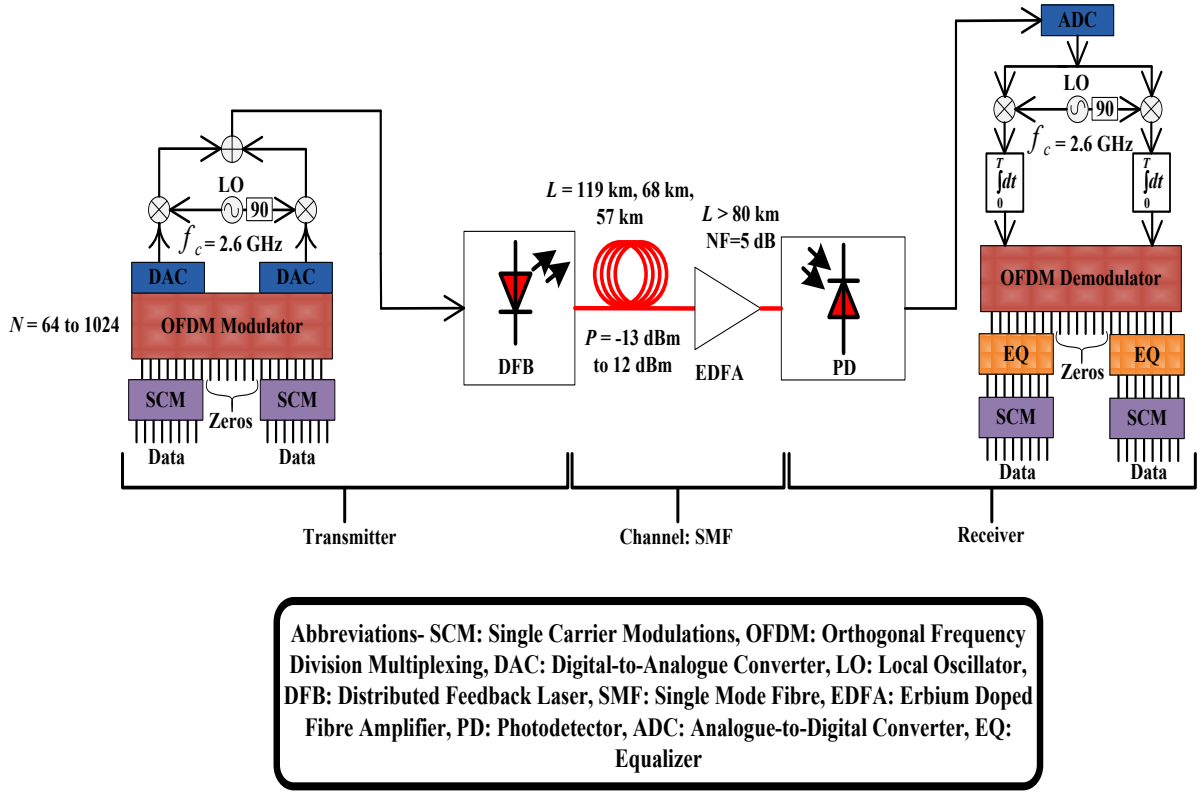

Figure 4.1: Overall block diagram of LTE-A RoF

The OFDM modulator module is important as the FFT size scaling is carried out in this module during the operation, as shown in equation (2.3). Within this module, the 62, 126, 254, 510, and 1022 modulated symbols are added with 2 zeros for direct current (DC) subcarriers. Then IFFT is applied to the parallel complex data in order to generate the OFDM symbols, and subsequently added with ¼ CP rate within the OFDM modulator module. The symbols are converted into a continuous signal using two DAC modules for the real and imaginary parts of the signal. The data rate for QPSK, 16-QAM and 64-QAM OFDM with all subcarrier configurations are shown in Table 4.1. The original LTE-A carrier aggregation at 100 MHz provides a minimum and maximum data rate of 160 Mb/s and 500 Mb/s, for QPSK and 64-QAM, respectively. The data rate of per 20 MHz bandwidth signal can be calculated by adapting the following expression, $B = N_s \times \Delta f \times \log_2 M_{b/s}$, where B is the data rate of per 20 MHz bandwidth, Δf is the subcarrier

Table 4.1: Combinations of data rate for proposed varying FFT scheme in LTE-A

Single carrier modulations	Data subcarriers / FFT size *N*	Data rate
QPSK	62 / 64	157.8 Mb/s
	126 / 128	158.3 Mb/s
	254 / 256	159.1 Mb/s
	510 / 512	160.3 Mb/s
	1022 / 1024	161.1 Mb/s
16-QAM	62 / 64	318 Mb/s
	126 / 128	318.8 Mb/s
	254 / 256	319.3 Mb/s
	510 / 512	320.1 Mb/s
	1022 / 1024	321 Mb/s
64-QAM	62 / 64	481 Mb/s
	126 / 128	482.3 Mb/s
	254 / 256	484 Mb/s
	510 / 512	487 Mb/s
	1022 / 1024	491 Mb/s

frequency, and $M_{b/s}$ is the bits/symbol that changes with modulation schemes. For the case of 100 MHz bandwidth, the total data rate is simply the multiplication of 5 and B that represents 5×20 MHz bandwidth signals. Therefore, the subcarrier allocation and FFT sizes are chosen to meet the minimum requirement. Undoubtedly, FFT size of 2048 and above will effectively increase the data rate, however, such design step is neglected. The rationale for avoiding higher FFT size will be explained with the aid of results in the upcoming section.

After the DAC, the continuous signal is up-converted to a carrier frequency of 2.6 GHz by a LO according to the allocated spectrum for LTE and LTE-A in an urban location [81]. The combined real and imaginary electrical signals are then applied to the DFB laser directly to generate OOFDM signals. As explained earlier, the DM of DFB induces the PFC. The OOFDM signals are then coupled into the SMF with link spans of ~119 km, ~68 km, and ~57 km, corresponding to the maximum achievable distances of QPSK, 16-QAM and 64-QAM, respectively. An EDFA is utilised for link span L of above 80 km with 15 dB gain and 5 dB noise figure (NF) [117].

At the receiver side, the optical signals are converted into electrical signals via a single PD adopting DD. Identical LOs are used to ensure perfect synchronization between transmitter and receiver modules. The remaining part of the receiver is the reverse process of the transmitter except for the equalization module. The frequency domain equalizer is a single-tap least square filter used for phase distortion compensation induced by PFC, CD and SPM. The system evaluation is carried out based on the OLP characteristics and the system BER.

4.3.1 System Model

As depicted in figure 4.1, the raw data is first passed through the SCM module that consists of QPSK, 16-QAM, and 64-QAM schemes. The SCM modulated symbols are fed into the OFDM module to carry out the serial-to-parallel conversion. The parallel symbols are converted into OFDM signal by applying IFFT operation, and CP addition as shown in equation (2.3) and (2.4), respectively. After DAC, the RF up-conversion models are adopted into this chapter from equations (2.5) and (2.6). From equation (2.3), the data subcarriers will be varied between 62, 126, 254, 510 and 1022 according to the higher data rate requirement. The corresponding subcarrier frequency spacing for the aforementioned data subcarriers will be in the range of ~1.28 MHz, ~633 kHz, ~314 kHz, ~157 kHz and ~78 kHz, which can be calculated from $\Delta f = B_T/(N_S+N_{cp})$, where B_T is total bandwidth of 100 MHz and N_{cp} is the CP length. The reducing subcarrier frequencies indicate the transition of smaller to larger OFDM symbol length, or broader to narrower subcarrier spacing.

The DFB and SMF models are adopted from equations (3.2-3.6) of Chapter 3 and equation (4.3) herein, respectively.

4.3.2 Results on Optimal LTE-A RoF Performance

The conventional wireless communications aim to achieve a BER of 10^{-5}, thus the results presented throughout this chapter will be assessed based on this metric [88, 118].

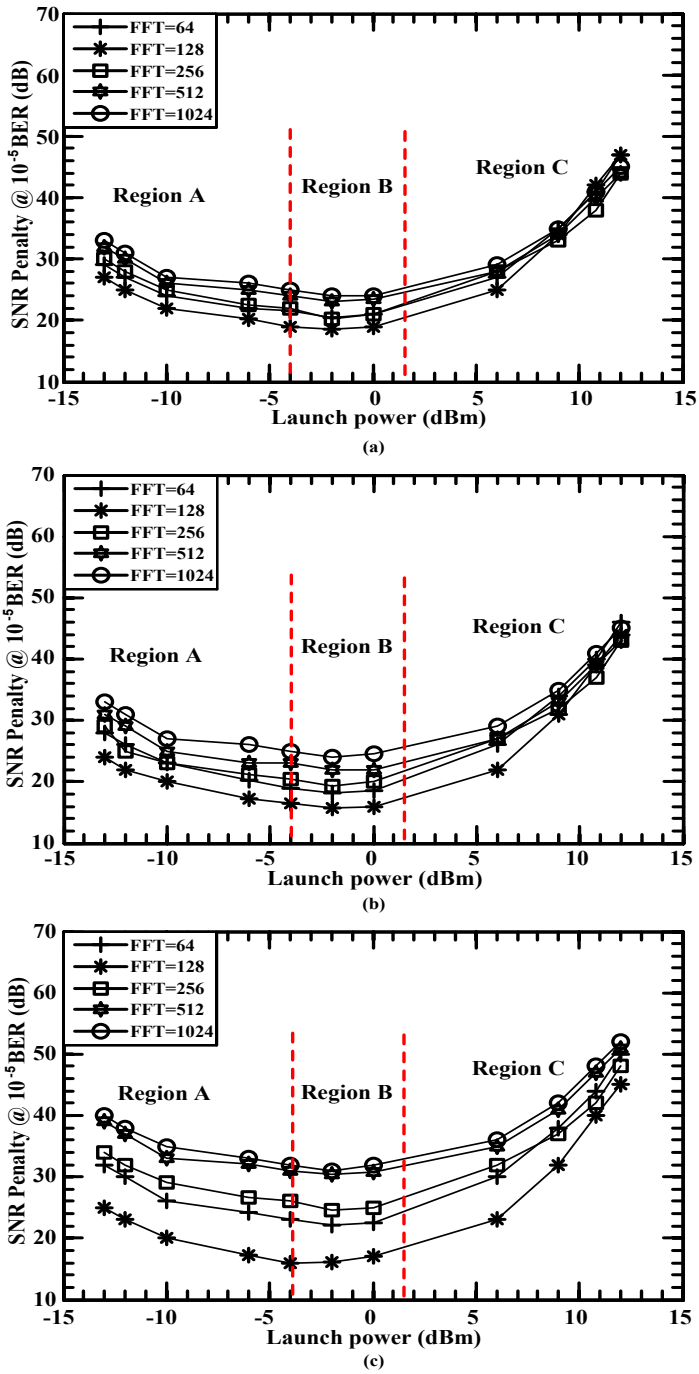

Figure 4.2: OLP against SNR penalty analysis of DD-OOFDM, with (a) QPSK-119 km, (b) 16-QAM-68 km, and (c) 64-QAM-57 km

Figure 4.2(a), (b), and (c) depict the OLP against the SNR penalty of QPSK, 16-QAM and 64-QAM DD-OOFDM, respectively. The SNR penalty is measured on the comparison basis of the incident link to the back-to-back (BTB) link. The maximum link spans achieved herein are ~119 km, ~68 km, and ~57 km for QPSK, 16-QAM, and 64-QAM, respectively. The system OLP is varied in the range of -13 dBm to 12 dBm to precisely identify the intermixing region. In Figure 4.2(a), (b), and (c), there are three distinctive regions: A) linear - PFC and CD induced power penalty, B) intermixing - optimised OLP via the compensation of SPM with PFC and CD, and C) nonlinear - SPM induced power penalty.

In region A of QPSK, 16-QAM and 64-QAM systems, for the range of OLP less than -4 dBm, the SNR penalty increases with decreasing OLP for all FFT sizes. In principal, as OLP decreases, the SNR decreases, thus illustrating the linear relationship with respect to the impairments occurred in the region A. For QPSK system (Figure 4.2(a)), the SNR penalty variations between all FFT sizes are relatively small. However, the pattern in region A changes as the modulation schemes changes, where SNR penalties between the FFT sizes increased for 16-QAM (Figure 4.2(b)), and further deteriorated for 64-QAM (Figure 4.2(c)). The reason for such deterioration is due to the increase in data rate arising from higher level modulation scheme with closely placed symbols and reduced Euclidean distance that requires higher SNR. But, FFT size-64 exhibits unusual SNR penalty compared to FFT size-128, albeit FFT size-64 composed of lower data rate. Such phenomenon occurs for FFT size-64 due to the large frequency spacing producing shorter OFDM symbol, hence resulting in ISI. The optimum FFT size for QPSK, 16-QAM and 64-QAM is FFT size-128 with subcarrier frequency proportionally compromising between ISI and data rate. The SNR penalties for FFT size-128 at OLP of -13 dBm are ~27 dB, ~25 dB, and ~25 dB, for QPSK, 16-QAM, and 64-QAM, respectively.

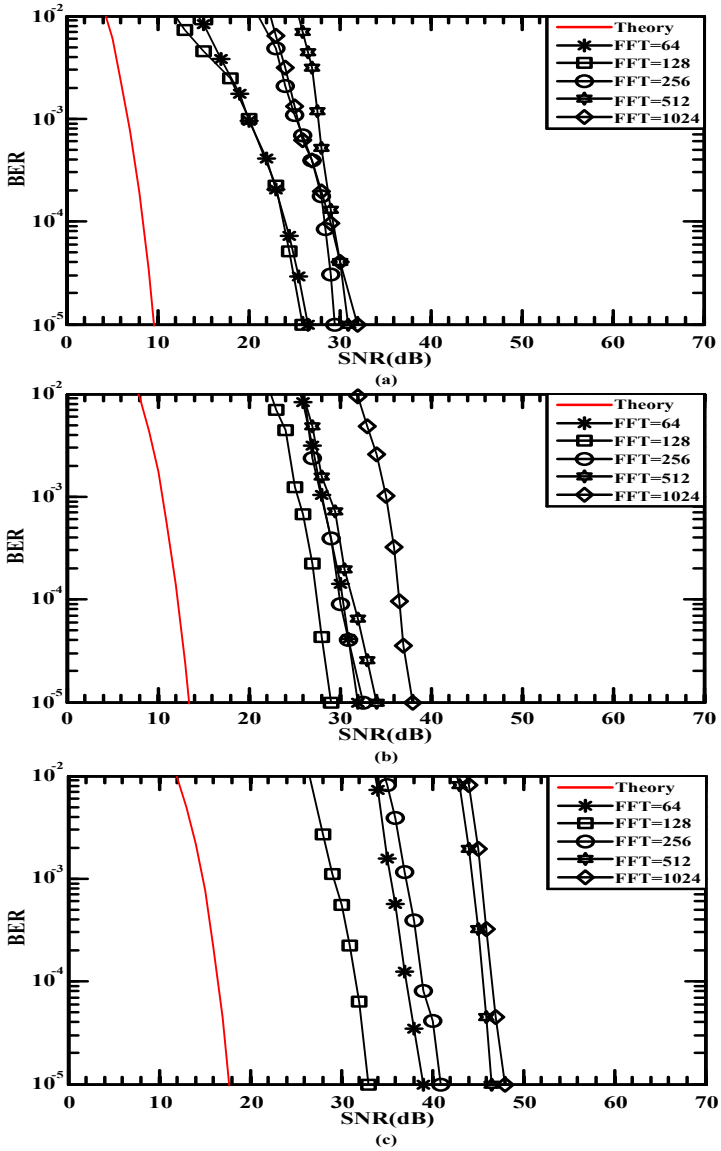

Figure 4.3: BER analysis of DD-OOFDM, with (a) QPSK-119 km, (b) 16-QAM-68 km, and (c) 64-QAM-57 km

For nonlinear region, the discussion now shifts to region C of Figure 4.2(a), (b), and (c) for QPSK, 16-QAM, 64-QAM, respectively. Despite the increase in OLP, the SNR penalty still increases, which proves the anomalous response of region C, primarily due to the nonlinear phase distortion. In Figure 4.2(a) for QPSK, the distortions are almost similar for every FFT sizes. However, as the modulation level increases, the SNR penalty deviation between the FFT sizes increases, resulting in large FFT sizes experiencing higher distortion rate. Fundamentally, such phenomenon occurs due to the vulnerability of narrow

and closely spaced subcarriers in large FFT sizes that deteriorate subject to heavy ICI. The optimum FFT size in the nonlinear region is FFT size-128. At the OLP of 12 dBm, the QPSK, 16-QAM and 64-QAM SNR penalties for FFT size-128 resulted in ~43 dB, ~43.5 dB, and ~45 dB, respectively.

In region B also known as the intermixing region, the optimum OLP ranges from ~-4 dBm to ~2 dBm, where this region clearly indicates that FFT size-128 demonstrates the best gain. For the case of QPSK system (Figure 4.2(a)), the SNR penalty differences between FFT size-128 and FFT size-64 are relatively small. All the systems would not be able to achieve BER of 10^{-5} for transmission of above the distance demonstrated herein. The SNR penalty observed for FFT size-128 at -2 dBm, for QPSK, 16-QAM, 64-QAM are ~18.5 dB, ~16.8 dB, and ~16.1 dB, respectively. The rest of the analysis will be carried out at -2 dBm OLP, which falls in the range of ~-4 dBm to ~2 dBm within the intermixing region.

In order to clearly observe the evolution of distortion in the intermixing region, BER measurement is carried out. At the BER of 10^{-5}, from Figure 4.3(a), (b), and (c) of QPSK, 16-QAM, and 64-QAM, respectively, the farthest transmission is ~119 km with lowest average SNR of ~27 dB, achieved by QPSK system with FFT size-128 and 64. The accomplishment was made possible from the usage of intermixing region with no additional device and rigorous optimisation of FFT size. Corresponding to the same QPSK system, FFT-size of 256, 512 and 1024 requires higher SNR of ~29 dB, ~32 dB and ~33 dB, respectively, to achieve the transmission distance of ~119 km. In Figure 4.3(b) and (c), it is observed that the FFT size-64 requires higher SNR as the data rate increases. This is due to higher subcarrier frequency of 1.28 MHz for FFT size-64, where the walk-off rate is relatively low because the distortion affects a bigger division from the total channel

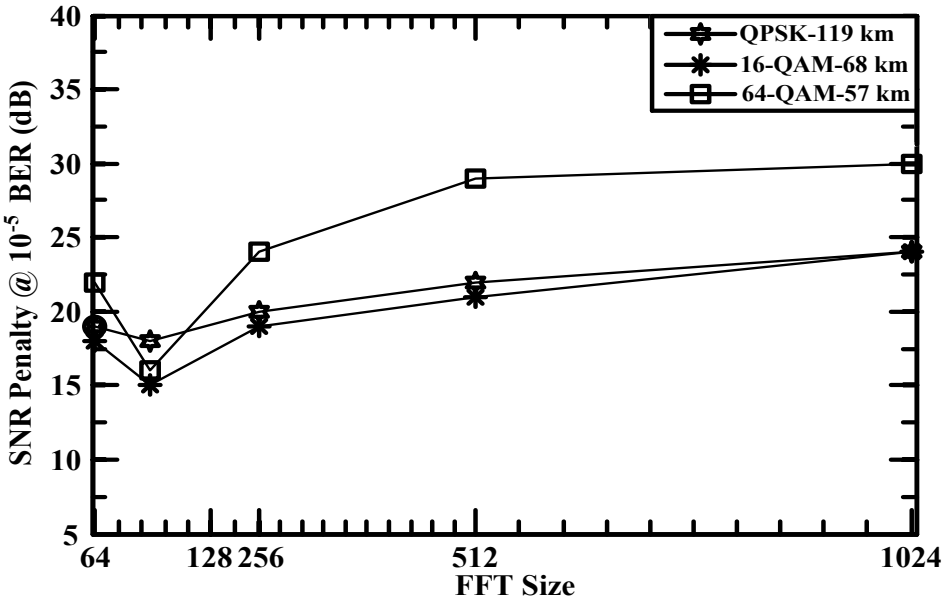

Figure 4.4: FFT size against power penalty with optimum FFT size corresponding to lowest power penalty

bandwidth of 100 MHz. As the data rate increases, the allocated data within a large subcarrier increases which leads to higher requirement of SNR for a specific BER.

Figure 4.4 presents the summarized output of the FFT size analysis for DD-OOFDM with QPSK, 16-QAM, and 64-QAM transmitted at the optimised OLP of -2 dBm. From Figure 4.4, as explained earlier, the QPSK DD-OOFDM system achieves almost identical power penalty at FFT size-64 and 128 demonstrating similar walk off rate. Above this data rate, FFT size-64 has higher effect due to the higher frequency spacing, effectively reducing the walk off rate, which is due to the increase in the data rate within a subcarrier. The FFT size-128 achieves the lowest power penalty across all modulation schemes. For the FFT size of more than 128, subcarrier spacing are narrower with respect to the increment in subcarrier numbers, which will be easily affected by phase distortion that leads to ICI. Therefore, the system design proposed in this chapter is limited to FFT size-1024. The electrical transmitter for the proposed application has been thoroughly examined

and optimised. Since, electrical-to-optical conversion is a crucial part of LTE-A RoF system design, next section will present the optimisation of optical modulator.

4.4 Optimisation of Optical Modulators

The optimisation of FFT size from the previous section demonstrated that FFT size-128 is the most optimum with 100 MHz bandwidth transmission for all propagation conditions. Since PFC is a major obstacle in achieving high data rate in long span transmission, as clearly explained in Chapter 3 with a new closed form expression (equation 3.22). This section will introduce diversity in terms of optical modulators, where in addition to DML external modulators will be part of the system design. Despite the costly nature of external modulators, it is important to consider the usage of these modulators due to the ability of mitigating PFC. Resilience towards PFC is possible with external modulators, because the modulation switching will be performed externally, and not by the laser itself. The optimisation in optical modulators will be complemented with the analysis of optical propagation, where the impact of intermixing region will be investigated with different optical modulators. The resulting output of the investigation from this section was published in [101] by the author.

The physical layer connectivity from eNB according to the proposed varying FFT size based LTE-A system is modelled using 16-QAM and 64-QAM as the SCMs. The SCMs are then modulated onto OFDM with only FFT size-128, due its optimum performance. The data subcarriers, data rate and bandwidth remain the same as the previous section.

The investigation is focused more on the optical link, with different RoF configurations to observe the variation in transmission distance with respect to optical modulators. The RoF system designed for each case under study is based on: (i) DFB based on IM, (ii) SE-

MZM based IM, and (iii) DE-MZM based PM. Conventional optical fibre systems utilise optical phase modulator to perform PM. However it is shown in [119] that DE-MZM, as a single integrated device exhibits similar performance to conventional optical phase modulator that composed of several different devices. Therefore, DE-MZM is adopted into this investigation for cost efficiency. Since the LTE-A is composed of OFDM, the optical modulated signal will be termed again as DD-OOFDM. Previous work on the optimisation of the optical modulator for OOFDM was only reported for the Quadrature MZM and DE-MZM [120]. The findings reported in [120] was limited to only linear propagation, with no emphasis on the nonlinear propagation and intermixing region.

The analysis of this section will be carried out on characterizing PFC dependent and non-dependent modulator, its interaction with CD and SPM, and the inevitable impact on transmission distance. It is important to analyse the maximum achievable transmission distance to study the distance of RN that can be placed in the adjacent cells, as discussed in Chapter 1. Further studies on different RoF configuration provides more ideas on the placement distances with respect to the primary cell.

The optical receiver is based on DD. All the proposed configurations are transmitted over SMF, with considering only CD and SPM to maintain consistency with the previous section. The evaluation of individual configurations is performed based on the individual optical modulator OLP condition, and the resulting BER.

4.4.1 Transmission Link

The DD-OOFDM shown in Figure 4.5 is the overview block diagram of LTE-A RoF system configured with different optical modulators. At the transmitter side, 126 parallel data streams are generated and mapped into a parallel complex data using 16 and 64-QAM

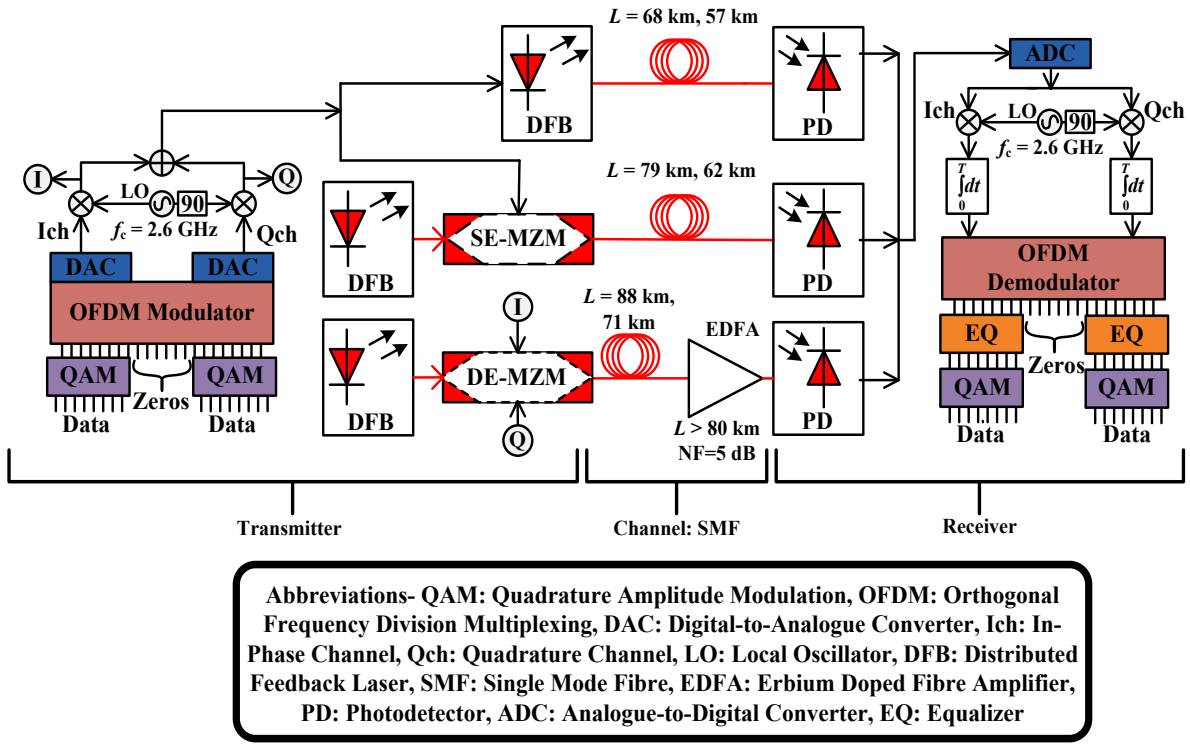

Figure 4.5: Overall block diagram of LTE-A RoF for optimization of optical modulators

mapping formats. Within the OFDM modulator module, there are three important processes of which are i) the addition of 2 zeros for DC subcarriers to achieve the formation of 128 parallel subcarriers to meet the IFFT and FFT algorithms requirements [121], ii) the 128 parallel complex data are then fed into an IFFT modulator to generate the OFDM symbols, and iii) the OFDM symbols are then appended with CP at the rate of ¼ of the total 128 parallel subcarriers. After parallel-to-serial conversion, the discrete OFDM symbols are converted into a continuous signal using two DACs modules for the real and imaginary parts of the signal. The continuous signal is then up-converted to a carrier frequency of 2.6 GHz by a LO.

The combined real and imaginary electrical signals are applied to three optical modulation schemes, (i) DFB for IM, (ii) SE-MZM, with DFB as the source, for IM and (iii) DE-MZM, with DFB as the source, for optical PM.

At the receiver side, the optical signals are converted into electrical signals via optical receivers and are subsequently demodulated. Since the proposed system operates based on DD, the complete advantage of the optical PM could not be utilized, as coherent detection is required to detect the phase of the optical signal. Identical LOs are used to ensure perfect synchronization between transmitter and receiver modules. The remaining part of the receiver is exactly the reverse process of the transmitter except for the equalization module. The single tap least square algorithm based frequency domain equalizer, is used for compensation of phase distortion in the received constellation for all schemes used.

The OFDM, DFB and SMF models in this section are identical to that expressed in equations (2.3-2.6) of Chapter 2, equation (3.2-3.6) of Chapter 3 and equation (4.3), respectively. On the other hand, for the first time, SE-MZM and DE-MZM models will be introduced in this chapter.

4.4.2 SE-MZM and DE-MZM models

The description on external modulation inclusive of SE-MZM and DE-MZM was given in Section 2.2.2 of Chapter 2. It is appropriate to present the model of the respective external modulators herein, because it is specifically applied in this chapter. Equations (4.5) and (4.6) illustrate the SE-MZM and DE-MZM, respectively [110, 122]:

$$E_{\mathrm{o}}(t) = E_{\mathrm{i}} \cos\left[\frac{\pi}{2}\frac{(V(t)+V_{\mathrm{bias}})}{V_{\pi}}\right] e^{-j\left[\frac{\pi}{2}\frac{(V(t)+V_{\mathrm{bias}})}{V_{\pi}}\right]} \tag{4.5}$$

$$E_{\mathrm{o}}(t) = \frac{E_{\mathrm{i}}}{2}\left[e^{j\pi\frac{(V(t)+V_{\mathrm{bias}})}{V_{\pi}}} + e^{j\pi\frac{-(V(t)+V_{\mathrm{bias}})}{V_{\pi}}}\right] \tag{4.6}$$

where $E_o(t)$ and E_i are the output and input optical fields of the MZM, respectively and $V(t)$ is the input electrical signal, V_{bias} is the MZM biasing voltage, V_π is the half-wave voltage.

In the system shown in Figure 4.5, the SE-MZM and DE-MZM are biased at the quadrature biasing point, where V_{bias} = 1.75 V and V_π = 0.5 V. The MZM biasing voltage is fixed to 1.75 V to be sufficient enough to push the input electrical signal to the quadrature biasing point, see Figure 2.5. However, it is important to maintain a small half-wave voltage, so that the input electrical signal does not drift to maximum or minimum biasing point. Under this condition, both modulators will operate within the linear region.

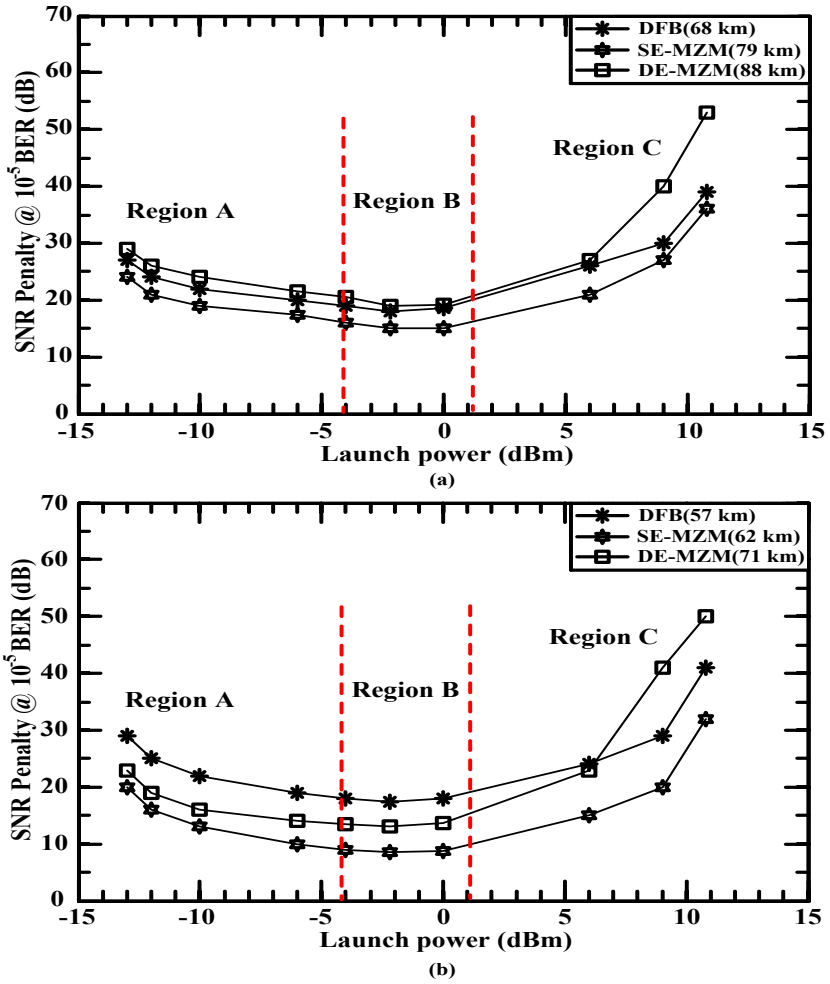

Figure 4.6: OLP against SNR penalty analysis of (a) 16-QAM DD-OOFDM and (b) 64-QAM DD-OOFDM

4.4.3 Results on Optimised Optical Modulators

Figure 4.6(a) and (b) depict the SNR penalty against OLP for 16-QAM and 64-QAM DD-OOFDM signals, respectively, at the facet of optical modulators for a BER of 10^{-5}. The maximum link spans achieved for 16-QAM scheme are, DFB: ~68 km, SE-MZM: ~79 km, and DE-MZM: ~88 km, while 64-QAM scheme resulted in, DFB: ~57 km, SE-MZM: ~62 km and DE-MZM: ~71 km. In both figures there are three distinctive regions: A) CD or CD and PFC induced power penalty (linear), B) the optimum OLP due to the intermixing effect of SPM with CD and the PFC (DFB), and C) the SPM induced power penalty (non-linear).

Region A of Figure 4.6 becomes active and effectively deteriorates the signal for OLP of less than ~-4 dBm, which agrees well with results observed in Figure 4.2. In region A of Figure 4.6(a) and (b), as OLP decreases, the SNR decreases uniformly for both 16-QAM and 64-QAM, respectively. This phenomenon illustrates the linear relationship with respect to the impairments occurred in the region A. For 16-QAM system, the DE-MZM experiences higher SNR penalty due to the accumulated CD for longer span transmission, as it is well known that CD accumulates with propagated distance [123]. In the same modulation scheme, although DFB only propagated up to 68 km, the SNR penalty is very close to DE-MZM due to the nature of PFC induced by DML. In terms of the external modulators, the SNR penalty differences between DE-MZM and SE-MZM arise from the lower propagated span of SE-MZM that result in lower CD rate. In the 64-QAM system of Figure 4.6(b), DFB exhibits higher SNR penalty emerging from the data rate dependent PFC. The reason for SNR penalty differences between SE-MZM and DE-MZM for 64-QAM system is likewise to the 16-QAM system. At the OLP of -13 dBm, the SNR penalties observed in 16-QAM system are DFB: ~27 dB, SE-MZM: ~24 dB, and DE-

MZM: ~29 dB. In 64-QAM system with the same OLP, the SNR penalties for DFB, SE-MZM and DE-MZM are ~29 dB, ~20 dB, and ~23 dB, respectively. The SNR penalty of DFB increases with the data rate. However, since external modulators are PFC free, the distortion in region A is distance dependent, thus resulting in lower SNR penalty for 64-QAM system compared to 16-QAM system. But, the electrical equalizer employed in the proposed system, could only compensate all the RoF configurations up to the distances mentioned.

In the nonlinear region, the discussion is concentrated towards region C of Figure 4.6(a) and (b) for 16-QAM and 64-QAM, respectively. Albeit the increase in OLP, the SNR penalty effectively increases, thus showing the anomalous response occurring in region C, primarily due to the nonlinear phase distortion. In Figure 4.6(a), the DE-MZM exhibits higher SNR penalty, due to the amplitude-to-phase coupling arises from the SPM affect, which effectively distorts the optical PM. Both DFB and SE-MZM resulted in lower SNR penalty compared to DE-MZM due to the nature of IM, which demonstrated lower sensitivity towards nonlinearity compared to optical PM. Likewise, 64-QAM system of Figure 4.6(b) demonstrated similar pattern for all optical modulators. For OLP of 12 dBm, the 16-QAM SNR penalties for DFB, SE-MZM and DE-MZM are ~39 dB, ~36 dB, and ~53 dB, respectively. At the same OLP, the SNR penalties for 64-QAM are DFB: ~41 dB, SE-MZM: ~32 dB, and DE-MZM: ~50 dB. It is strongly advisable to avoid DE-MZM signal from nonlinear propagation.

The intermixing region (region B) illustrated in Figure 4.6(a) and (b) for 16-QAM and 64-QAM, respectively, resulted in optimum OLP within the range of ~-6 dBm to ~0 dBm. It is important to specify that the optimum OLP region for SE-MZM and DE-MZM would deviate towards lower range of OLP for lower transmitted distance. The region B offers the lowest penalties, where at -2 dBm, the SNR penalties for 16-QAM based DFB, SE-MZM

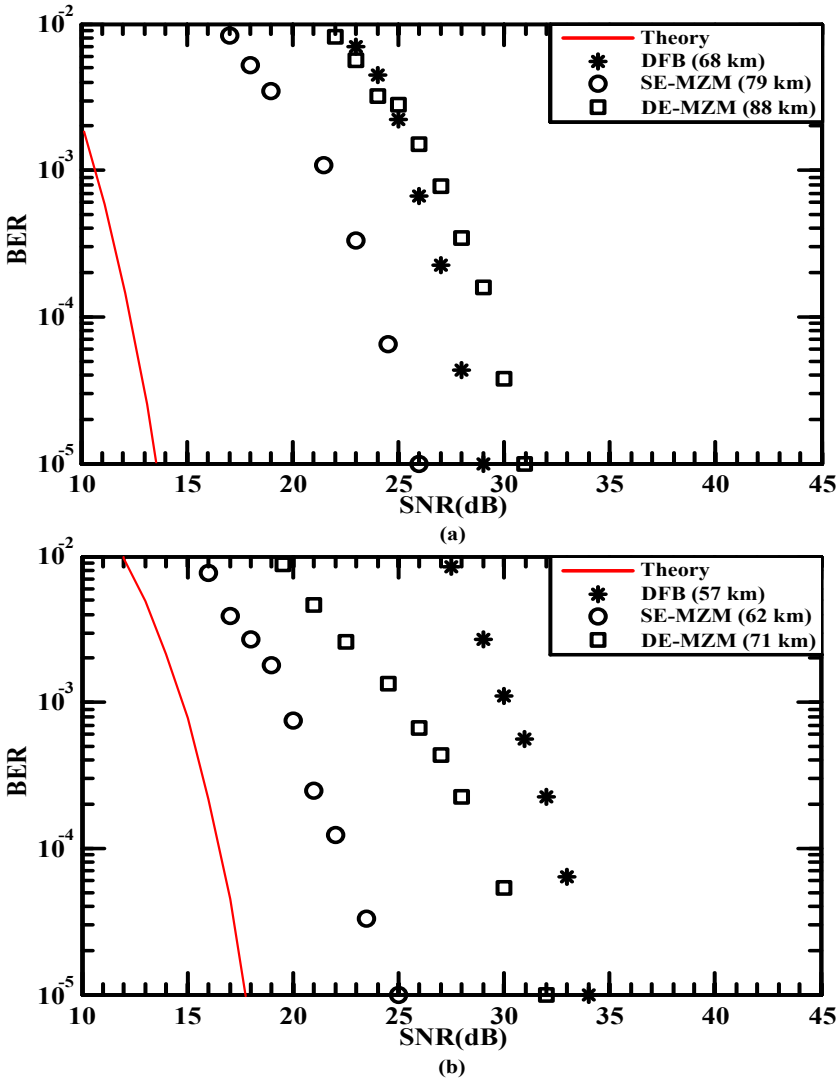

Figure 4.7: Simulated BER against SNR for (a) 16-QAM DD-OOFDM and (b) 64-QAM DD-OOFDM across all type of optical modulators

and DE-MZM are ~18 dB, ~15 dB, and ~19 dB, respectively. In terms of 64-QAM at –2dBm OLP, the SNR penalties for DFB: ~17.5 dB, SE-MZM: ~8.5 dB, and DE-MZM: ~13 dB. Overall, SE-MZM offers lowest SNR penalty, but with lower transmission span compared to DE-MZM. In the case of DE-MZM, since the optical PM has the modulation embedded into the phase, thus demonstrating higher resilient towards the intensity noise induced by CD [124]. The shortcomings of both external modulators are the implementation complexity and associated cost, which are vital for a commercial design

and deployment. Hence, DML based on DFB will be the ultimate choice due to its simplicity, but with the drawback of shorter transmission span.

Figure 4.7(a) illustrates the BER values for 16-QAM DD-OOFDM scheme, where the highest achievable transmission distance between all the RoF configurations is ~88 km with the DE-MZM modulator at the SNR of ~32 dB. Observation shows that the lowest achievable transmission distance of ~68 km with the DFB adopting IM scheme requires SNR of ~29 dB, while SE-MZM with the same IM scheme able to achieve ~79 km with SNR of ~26 dB. As explained earlier, the DFB scheme achieved shorter transmission distance compared to both external modulators (SE-MZM and DE-MZM), is due to the PFC affect that magnifies CD. It is important to observe the system capability of RoF for the proposed LTE-A system with FFT size-128, and its optimisation with respect to optical modulators, simply to learn how far the eNB could connect to a RN outside of its cell limit.

Likewise, the same signal degrading pattern applies to Figure 4.7(b) for 64-QAM DD-OOFDM scheme with a reduced link span to achieve the required BER. This is due to the smaller Euclidean distances between the constellations points for 64-QAM compared to 16-QAM, which effectively explains the bandwidth distance product. These results strongly emphasize the indirect proportional relationship between the spectral efficiency and the transmission link span.

4.5 Summary

In this chapter, the optimisation of OLP condition with respect to the varying FFT-sizes was carried out. The optimum OLP or the intermixing region, which mostly falls in the range of ~-6 dBm to ~0 dBm for QPSK, 16-QAM, and 64-QAM were discovered. This particular region was achieved by the interchangeable compensation between PFC and CD,

with SPM. For the FFT size-64, the analysis unfold that the walk-off rate gradually decreases with the increase of data rate, especially for 16-QAM and 64-QAM schemes. For FFT size of more than 256, the power penalty increases significantly for QPSK, 16-QAM, and 64-QAM due to the vulnerability towards ICI. The finding for FFT size optimisation reveals that FFT size-128 provides the minimum power penalty across all investigated modulation schemes. The average system efficiency that FFT size-128 provides are 54% and 65% with respect to the FFT size-64 and FFT size-256, respectively. The symbol length and subcarrier frequency spacing of FFT size-128 could provide enough tolerance and higher walk off to ISI and ICI, respectively.

After determining the optimum FFT size for electrical transmitter, the investigation was further carried out on the performance evaluation and optimisation of optical modulators, using DML and external modulators. The optimum OLP is consistent and conforms to the range that was unfolded in the previous investigation herein. The investigation shows that the performance of external modulation schemes in terms of transmission distance is superior to DML scheme. Between SE-MZM and DE-MZM, the latter proved to be a preferred option for externally modulating the signal since it offers improved immunity to the fibre CD, hence achieved longer transmission span. However, DE-MZM is vulnerable towards nonlinearity due to the modulation taking place in the phase of the optical source. It is clearly shown that the cell extension with a simple DFB modulated RoF configuration could extend the coverage of eNB beyond its area, and even further with external modulation. Overall, this chapter provided in-depth design of the proposed varying FFT-sizes based LTE-A and its integration with RoF. In the next chapter, the theoretical and experimental design of DML based LTE-RoF system will be presented.

CHAPTER 5 EXPERIMENTAL DEMONSTRATION OF LTE ROF INTEGRATION

The previous chapters are solely dedicated to the numerical modelling of eNB cell extension for LTE-A. The LTE-A architecture was redesigned with varying FFT size, and the coverage of eNB was extended with RoF system. For the first time in this thesis, this chapter will cover the experimental design of LTE RoF integration. The predecessor of the LTE-A is the LTE, but both technologies comprise of almost the same characteristics. The differences between LTE and LTE-A are shown in Table 1.2 of Chapter 1. Although, LTE-A is progressive in terms of data rate, but the drawback with carrier aggregation is significant due to the complexity.

Nagate *et al* [30] implemented RoF link into the networking structure of LTE and extended the eNB cell to a limited distance of 2.1 km. The shortcomings of the design reported in [30] are, i) since the predicted LTE subscriptions will be about 456 million by end of 2015 [125], the reported performance analysis is rather limited for network operators to accelerate the LTE-RoF integration, ii) the work is confined to signals with 10 MHz analogue radio bandwidth (ARB), however the actual eNB operates with a varying bandwidth in the real-time case , see Table 1.2. Since the analysis in [30] is limited with a fixed 10 MHz bandwidth, the eNB cell extension with RN via RoF interface requires detailed system metrics for easy adaptability and seamless integration in the ongoing deployment stage.

Therefore, the experimental LTE RoF integration herein will unfold some of the important metrics with detailed analysis, namely OMR for varying ARBs, deviation of intermixing region relative to ARBs and transmission spans, and identification of the LTE RoF system nonlinear limit. Since this chapter introduces the experimental link of LTE RoF, characterization of the RoF link will be presented and discussed beforehand. The RoF

link designed for LTE is based on DML, thereby the characterization will emphasize on the DFB acting as the DML and the complete RoF link.

Henceforth, the experimental demonstration of the LTE signal transmission to an AF RN, via a 10 km RoF interface will be carried out. The LTE signal is configured with QPSK, 16 and 64 QAM data. These mapped data are then modulated onto OFDM. The OFDM signals are transmitted at RF of 2.6 GHz with varying ARBs of 3 MHz, 5 MHz, 10 MHz, 15 MHz and 20 MHz [81, 126]. The RoF interface is composed of a DML and DD based optical receiver, thus the LTE signal will be termed as DD-OOFDM. The prominent problem of OFDM is the characteristics of high PAPR, where it has a direct impact on the OMI. As a part of practical system design, the OMR will be presented as an important performance metric.

The intermixing region was theoretically introduced with numerical simulation, which demonstrated a range of optimum OLP for LTE-A in Chapter 4. As part of the LTE RoF system optimisation herein, an investigation on the impact of intermixing region with varying ARBs will be performed. In addition, the transmission span will be varied between 10 km and 60 km to study on the deviation of intermixing region, and the identification of the nonlinear limit.

5.1 Device Characterization

The system proposed in this chapter consists of a DFB as the DML. The detailed background of DML and its important characteristics were given in Section 2.2.1 of Chapter 2 and throughout Chapter 3. The characterizations of the DML in this chapter will be the LI curve, RIN, linewidth, and the modulation bandwidth. In addition, as a complete

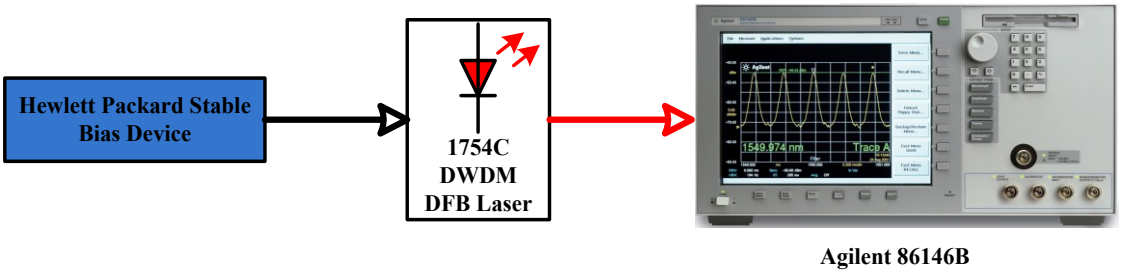

Figure 5.1: LI curve and RIN measurement setup

nonlinear response of the BTB link, the spurious free dynamic range (SFDR) measurement will be performed.

5.1.1 LI Curve

The LI curve of a laser is the major element that needs characterization, as it will present the threshold, best modulation region and saturation region of the device under test. The DFB used for the experimental work throughout this thesis is the 1754C DWDM laser from Emcore Corporation. The measurement setup for LI curve is illustrated in Figure 5.1, where the DFB laser is switched on by a Hewlett Packard stable bias device. The LI measurement is varied between 20 mA to 140 mA, as the threshold is at ~18 mA. The output power of the DFB laser is measured with Agilent 86146B optical spectrum analyser (OSA). Figure 5.2 depicts the LI curve, where it can be observed that the saturation starts at above ~100 mA. The centre wavelength at 60 mA is 1551.11 nm with ± ~1.26 nm for decreasing and increasing bias current.

5.1.2 RIN Measurement

Phase noise is the dominant noise factor in a laser, the nature of phase noise introduces random fluctuation to the output power, widely known as the RIN. Thus, the measurement of RIN is necessary to understand the noise level of the DFB laser. The optical SNR (OSNR) measurement is carried out as illustrated in Figure 5.1, where the measured OSNR

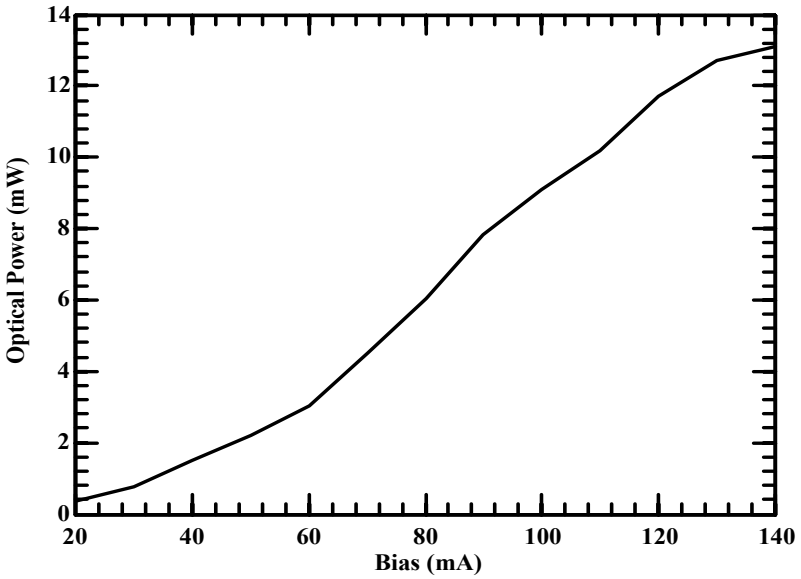

Figure 5.2: The LI curve of 1754C DWDM DFB laser

as a function of bias current, is used for RIN computation. The equivalent model used for the RIN computation is as follows [127]:

$$RIN(\text{dB/Hz}) = 10 * \log(\alpha_{\text{sig–se}}) + 20 * \log(\lambda) - OSNR_{1\text{nm}} - 174.8 \qquad (5.1)$$

where $\alpha_{\text{sig-se}}$ is the polarization factor, λ is the centre wavelength, $OSNR_{1\text{nm}}$ is the OSNR measurement at 1 nm scale. The model shown in equation (5.1) is specifically defined for Agilent 86146B instrument for RIN measurement. The calculation performed using equation (5.1) also agrees well with RIN measurement based on electrical spectrum analyser and oscilloscope [127]. The measured RIN relative to the bias current is shown in Figure 5.2, which decreases with the increase in bias current. The decreasing pattern in RIN occurs because as the bias current increases, stimulated emission becomes the dominant output, thus spontaneous emission dependent phase noise depletes.

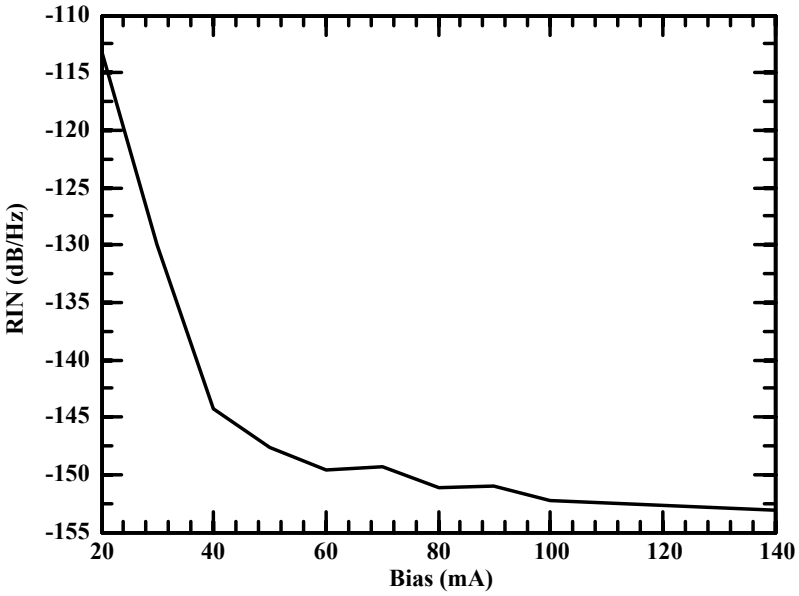

Figure 5.3: The RIN characterization relative to bias current for 1754C DWDM DFB laser

5.1.2 Linewidth Measurement

As explained earlier, the phase noise distorts the laser output. The additional laser characteristic that will be affected from the phase noise is the laser linewidth. Since the primary optical transmitter of this research work is DML, linewidth characterisation is important as it will deviate relative to modulation. The DFB laser utilised in the experimental setup emits narrow linewidth, hence the direct measurement of linewidth is peculiar with the conventional method.

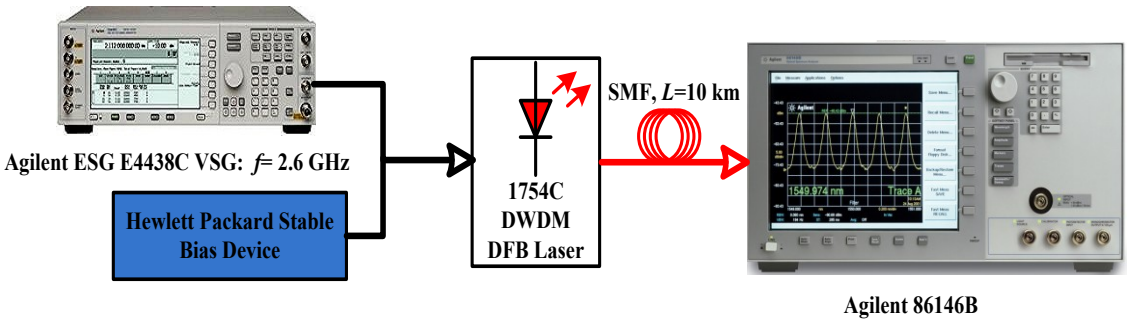

Figure 5.4: Measurement setup for linewidth characterization

Table 5.1: Linewidth measurement

Bias (mA)	30	40	50	60	70	80	90	100	120	140
Linewidth (MHz)	511.15	18.74	11.7	11.4	10.4	6.51	5.12	3.81	3.1	2.89

The technique used in this section for linewidth characterization is shown in Figure 5.4. The RIN is recalculated with additional modulated signal at frequency f of 2.6 GHz and transmission over 10 km span L of SMF. The measured and calculated RIN via the OSA is used for the linewidth estimation, with the following expression given by Emcore [128]:

$$\Delta v = \frac{\Delta RIN(f)}{\{4\pi(D\lambda^2 L/c)^2 f^2\}} \tag{5.2}$$

where D is the optical fibre dispersion parameter, and c is the speed of light. Since both RIN and linewidth are functions of phase noise, linewidth can be computed from the RIN. As shown in Table 5.1, linewidth decreases as the bias current increases, where the linewidth is 11.4 MHz at 60 mA. As to validate the linewidth estimation using equation (5.2), an alternative measurement was carried out with high resolution OSA, BOSA 200 by Aragon Photonics. The resulting linewidth with a high resolution OSA was 11.14 MHz at 60 mA bias current, thus proving the accuracy of the measurement shown in Table 5.1.

5.1.3 Bandwidth Measurement

The modulation bandwidth is an important parameter of the proposed design, due to the high operating frequency of LTE at 2.6 GHz. Therefore, it is important to identify the modulation response of the DFB. The usage of frequency domain characterization is an efficient and precise method to identify the bandwidth of a device and the cut-off frequency. In order to achieve this, a setup was constructed as shown in Figure 5.5 for S_{21}

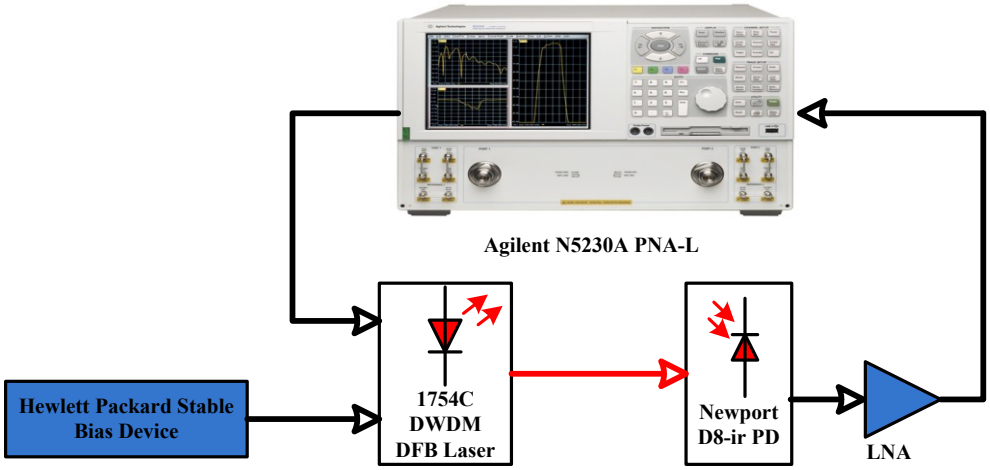

Figure 5.5: Measurement setup for modulation bandwidth characterization

measurement. As usual, the DFB is biased to linear region, and coupled with the modulation signal from the network analyser, Agilent N5230A PNA-L. The DFB is directly connected to Newport D8-ir PD for optical signal detection. The characteristics of the PD are 0.42 responsivity and -17 dBm sensitivity. The detected signal is coupled into a low noise amplifier (LNA), with 18 dB gain and 2.5 dB NF. The amplified signal is subsequently received by the network analyser for S_{21} measurement.

The resulting output of the S_{21} measurement is shown in Figure 5.6. The region of interest for the proposed application experiences ~5 dB penalty, which can be easily compensated by the LNA. Above 3.5 GHz, the DFB response rapidly decreases. However, it is possible to modulate above 3.5 GHz with the trade-off of higher amplification.

5.1.4 Dynamic Range Measurement

In order to maintain a low cost system, the proposed RoF link for LTE is designed with IM by directly modulating a DFB laser and detection through a PD. The DM exhibits nonlinear characteristics due to the gain compression, which results from several factors, namely gain saturation, spatial hole burning and leakage current [129]. The nonlinearity of

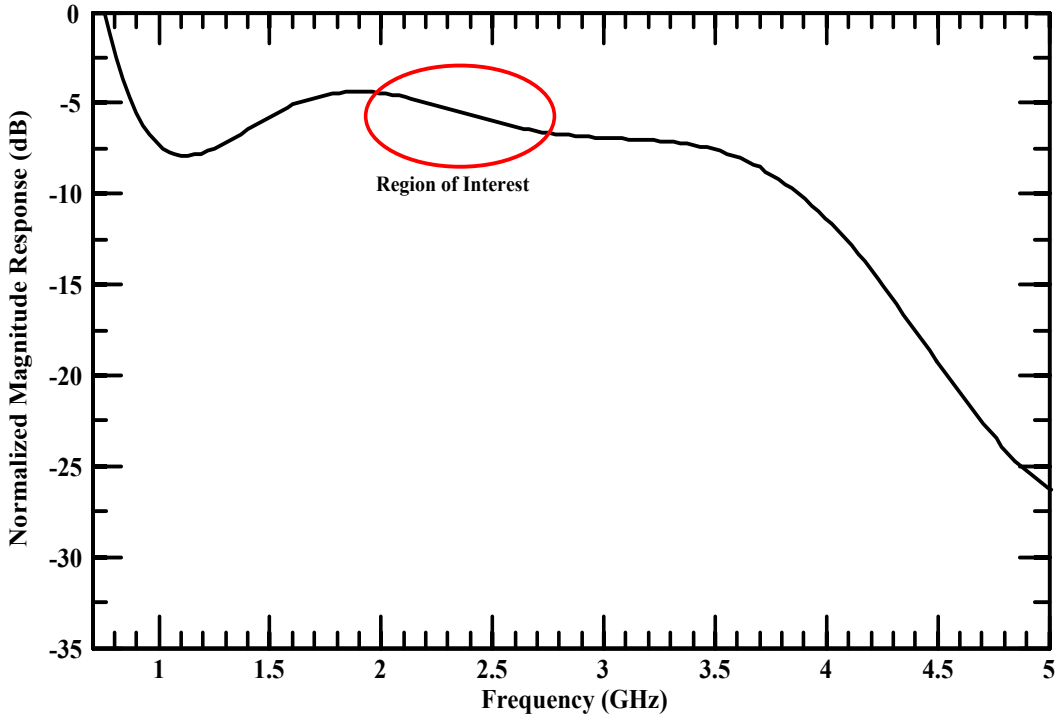

Figure 5.6: The modulation response of DFB laser

the DFB will result in spurious signals, which are also known as harmonics and IMDs. Harmonics is independent of the input signal, which means harmonics will occur even with the single tone input. In contrast, IMDs only occurs for input signals with more than one tone. Furthermore, harmonics are spurious signals that occur at a distance from the fundamental frequency, and so do the even order IMDs. A two-tone IMD analysis is sufficient to characterize the spurious signals, for both harmonics and IMDs [130]. The output of the DFB with respect to the LI curve can be described with Taylor series:

$$L(I_{\mathrm{d}}(t)) = a_1 I_{\mathrm{d}}(t) + a_2 {I_{\mathrm{d}}}^2(t) + a_3 {I_{\mathrm{d}}}^3(t) + \ldots, \tag{5.3}$$

where $L(I_{\mathrm{d}}(t))$ is the output optical power operates as a function of input current $I_{\mathrm{d}}(t)$; a_n represents the coefficient of polynomial fitting on the curve, shown in Figure 5.2, with respect to the order n; $I_{\mathrm{d}}(t)$, ${I_{\mathrm{d}}}^2(t)$, and ${I_{\mathrm{d}}}^3(t)$, are the fundamental, second order spurious and third-order spurious signals, respectively. The two-tone input can be expressed as:

$$I_{\text{two-tone}}(t) = I_{\text{d1}}(t) + I_{\text{d2}}(t) = A(\cos(\omega_1 t) + \cos(\omega_2 t)), \tag{5.4}$$

where $I_{\text{two-tone}}(t)$ is the composite signal of the first tone $I_{\text{d1}}(t)$ modulated at a frequency ω_1 and the second tone $I_{\text{d2}}(t)$ modulated at a frequency ω_2, and A is the magnitude of the applied current. The first tone $I_{\text{d1}}(t)$ and second tone $I_{\text{d2}}(t)$ are transmitted at frequencies ω_1 of 2.59 GHz and ω_2 of 2.61 GHz. The spacing between ω_1 and ω_2 is 20 MHz, which represents the bandwidth of the LTE signal.

The second order spurious signals can be expressed as:

$$\begin{aligned} a_2 I_{\text{d}}(t)^2 &= a_2 (A\cos(\omega_1 t) + A\cos(\omega_2 t))^2 \\ &= a_2 \left\{ \frac{A^2}{2}(1+\cos(2\omega_1 t)) + \frac{A^2}{2}(1+\cos(2\omega_2 t)) + A^2(\cos(\omega_1 - \omega_2)t + \cos(\omega_1 + \omega_2)t) \right\} \end{aligned} \tag{5.5}$$

where the first and second terms of the solution in equation (5.5) comprises of second order harmonics at the frequency multiples of ω_1 and ω_2. The third and forth terms shows the second order IMD products. The second order harmonics and IMDs are outside the band and therefore they will be omitted for rest of the analysis. However, the odd order IMDs tends to be close to the transmitting signal. Therefore, only the third-order IMD is considered in this analysis, as that is the only component that falls closely to the fundamental signal. The analytical expression focusing on the third-order IMD can be shown as:

$$
\begin{aligned}
a_3 {I_d}^3 &= a_3 (A\cos(\omega_1 t) + A\cos(\omega_2 t))^3 \\
&= a_3 \left\{ A^3(\cos^3(\omega_1 t)) + A^3(\cos^3(\omega_2 t)) + 3A^3(\cos^2(\omega_1 t)\cos(\omega_2 t)) + 3A^3(\cos^2(\omega_2 t)\cos(\omega_1 t))t \right\} \\
&= a_3 \left\{ \begin{array}{l} \dfrac{9A^3}{4}\cos(\omega_1 t) + \dfrac{9A^3}{4}\cos(\omega_2 t) + \dfrac{A^3}{4}\cos(3\omega_1 t) + \dfrac{A^3}{4}\cos(3\omega_2 t) \\ + \dfrac{3A^3}{4}\cos(2\omega_1 t - \omega_2 t) + \dfrac{3A^3}{4}\cos(2\omega_1 t + \omega_2 t)) + \dfrac{3A^3}{4}\cos(2\omega_2 t - \omega_1 t) \\ + \dfrac{3A^3}{4}\cos(2\omega_2 t + \omega_1 t)) \end{array} \right\}
\end{aligned}
\tag{5.6}
$$

In equation (5.6), the solution shows the first and second terms as the in-band spectral re-growth phenomena. The third and the forth terms are the third-order harmonics and these terms are clearly outside the frequency band and could easily be filtered. The sixth and eighth terms of equation (5.6) tend to be outside the frequency band as well. Finally, the critical terms that are closer to the fundamental frequency are the fifth and the seventh terms of equation (5.6), where frequencies are 2.57 GHz and 2.63 GHz, respectively. From equation (5.6), it is clear that the in-band spectral re-growth evolves with the fifth and the seventh terms, indicating the criticalness of third order nonlinearity. However, if the nonlinear terms are small, the in-band spectral re-growth is negligible [73].

In order to characterize the SFDR with respect to the third-order IMDs, the two-tone IMD signal analysis is carried out theoretically and experimentally. Figure 5.7 shows the experimental setup for the two-tone signal transmission for IMD analysis. Two continuous wave generators (CWGs), Agilent E8247C, CWG1 and CWG2 were utilised to generate signals at frequencies ω_1 of 2.59 GHz and ω_2 of 2.61 GHz, respectively. The generated signals are composed of sinusoidal signals, these signals are then summed to form a two-tone signal. The two-tone signal is then directly applied to the DFB laser to perform IM. The optical two-tone signal is then transmitted over a short patch cord and detected via PD.

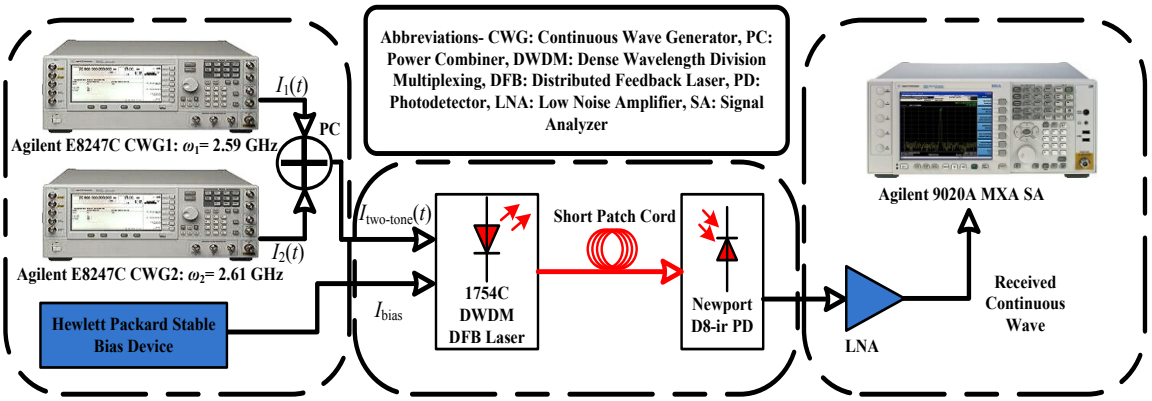

Figure 5.7: Experimental setup of two-tone signal for IMD analysis

The signal is subsequently amplified to mitigate the conversion loss induced by PD, and SFDR measurement is carried out using a signal analyser (SA), Agilent 9020A MXA.

Figure 5.8 depicts theoretical and experimental results of the two-tone IMD analysis. The input powers of signals $I_{d1}(t)$ and $I_{d2}(t)$ are investigated in the range of 2 to 11 dBm via CWG1 and CWG2, respectively, after taking the 5 dB loss of the power combiner into consideration. When the input power is below 2 dBm, it is difficult to observe the third-order IMD as it is very close to the noise floor of -77.93 dB. Meanwhile, since the limit of CWG is 16 dBm (which effectively means input power of 11 dBm due to the power combiner's loss), the linear prediction technique is used to estimate the output power for the given input power below 2 dBm and above 11 dBm. All factors have similar consideration between theory and experiment to maintain the consistency. Additionally it is important to state that all the output metrics presented in Figure 5.8 are integrated over a 20 MHz bandwidth.

The third-order input/output intercept point (IIP3/OIP3) provides an important metric. At this intercept point, the distortion due to the nonlinearity is severe as the third-order IMD has an equivalent output power to the fundamental signal. The IIP3 of the DFB is 29 dBm, which result in an OIP3 of 8.89 dBm, and almost the same outcomes can be

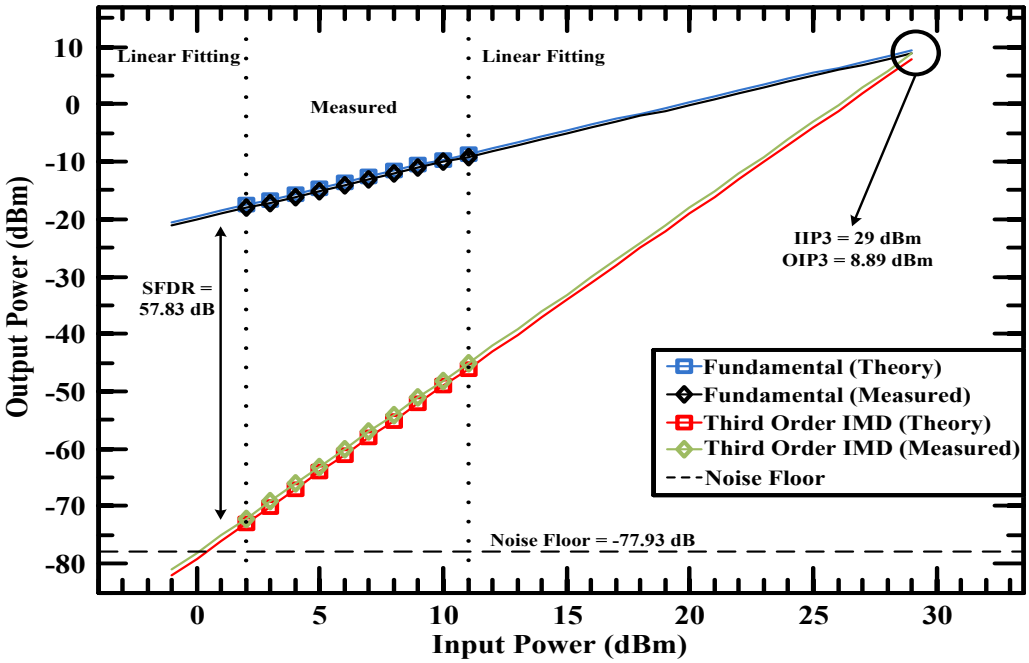

Figure 5.8: First and third order output powers with respect to input power

observed with the theoretical simulation. However, such a high power is not an envisaged input power for the proposed system of this thesis. From the estimation, the third-order IMD rises above the noise floor at the input power of 1 dBm.

From Figure 5.8, the theoretical and measured average SFDR of the complete link is ~57.83 dB and the LTE requirement for SFDR metric is 55.9 dB [131]. The RoF link designed for LTE could provide an additional SFDR of ~1.93 dB. Additionally, it is desirable to maintain the input power close to 1 dBm for a minimum third-order IMD because the actual LTE signal is composed of OFDM modulation which has a high PAPR. A lower dynamic range for OFDM signal modulation is not advisable, as it is very sensitive towards phase noise. Although, 1 dBm input power to the laser could avoid third order IMDs, the bias level in DFB could drive the laser either to threshold or saturation region. In order to avoid such situation, the next section will optimise the OMI. .

5.2 OMI analysis

In DML based systems, OMI optimisation is an important criterion that allows high OLP from the laser, while effectively avoiding nonlinear distortions. Moreover, LTE signal is composed of OFDM modulation with high PAPR. The construction of OFDM signal from the multiple independent and identically distributed (i.i.d) subcarriers lead to significant increase in PAPR. Due the combination of uncorrelated subcarriers, OFDM signal results in noise like waveform with Gaussian approximation, owing to the central limit theorem. In addition to the noise like waveform, the low probability of very high peak occurrence is due to the random phase matching between the subcarriers that leads to constructive interference. Thus, OFDM is very sensitive towards threshold or roll-off region, and strongly constrained to linear modulation [132]. Pre-clipping is deliberately not performed on the OFDM signal to verify the impact of OMI optimisation in DML based LTE RoF system.

Modulating the OFDM signal near the lasing threshold level (high OMI) or the saturation region (low OMI) of DML, will result in nonlinear optical modulation induced distortions. The distortions near the threshold and saturation regions are the lower peak clipping with the turn-on delay and gain compression factor, respectively. Gain compression introduces several nonlinear affects, namely finite number of carries, spatial hole burning, and leakage currents [68]. Apart from optical modulation induced distortions, low OMI also introduces high OLP, which results in nonlinear propagation and has critical effect on the system performance. The criticalness of nonlinear propagation was theoretically shown in Chapter 4. As an initiation of optimisation, OMR is introduced to reduce the optical modulation induced nonlinear distortion for all ARBs. In addition at lower values of OMI, which results in higher OLP, the gain compression based distorted

signal propagating down a 10 km SMF will experience nonlinear propagation induced phase noise. The impairments from optical modulator nonlinearity and nonlinear propagation have been investigated individually in [133] and [75], respectively. However, this section investigates the individual and the combined effects of gain compression and nonlinear propagation on the OFDM signal, in a unified approach for better system characterization.

5.2.1 Experimental Setup for OMI Analysis

Figure 5.9 shows the practical setup of OMI analysis for LTE RoF system. At the transmitter, LTE signals generated are QPSK, 16-QAM and 64-QAM with OFDM. The LTE signal has varying ARBs of 3, 5, 10, 15 and 20 MHz. The parameters associated with all ARBs of LTE are given in Table 1.2. Additional information on the LTE ARBs data rate and PAPR product are shown in Table 5.2 for all modulation schemes. The PAPR values clearly indicate an increment pattern relative to the increasing bandwidth, due to the increase in the number of subcarriers. Signals are then generated in the passband frequency of 2.6 GHz via the vector signal generator (VSG).

The output of VSG is applied to the DFB for IM. To ensure that the DFB is not biased close to the lasing threshold (< 40 mA) and the saturation region (> 100 mA), biasing is carried out between 40 mA and 100 mA. The DD-OOFDM signal is transmitted through

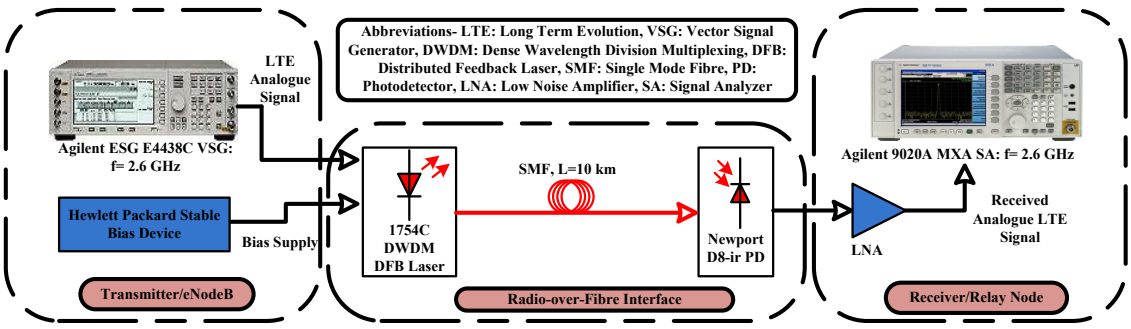

Figure 5.9: Practical setup for OMI analysis

Table 5.2: LTE ARB bit rate product

Modulations	3 MHz: data rate-PAPR	5 MHz: data rate-PAPR	10 MHz: data rate-PAPR	15 MHz: data rate-PAPR	20 MHz: data rate-PAPR
QPSK	5 Mb/s-6.92 dB	8 Mb/s-9.07 dB	16 Mb/s-9.54 dB	25 Mb/s-10.73 dB	33 Mb/s-11.16 dB
16-QAM	10 Mb/s-6.95 dB	16 Mb/s-9.15 dB	33 Mb/s-9.59 dB	50 Mb/s-10.75 dB	67 Mb/s-11.3 dB
64-QAM	15 Mb/s-7.02 dB	25 Mb/s-9.25 dB	50 Mb/s-10.38 dB	75 Mb/s-10.93 dB	100 Mb/s-11.67 dB

10 km of SMF for OMI analysis. At the receiver, a PD followed by a LNA is used to recover the signal for all three links. It is important to specify that throughout the thesis, LNA is configured as a AC coupled input and DC coupled output. The SA is then used to analyse and characterize the signal quality. All relevant system parameters are shown in Table 5.3.

5.2.2 Results on OMI analysis

The EVM measurement is used throughout the experimental analysis as an important metric. The 3GPP had defined 8% EVM as the minimum LTE requirement [134]. The author has published the outcome of the analyses herein in [135].

The OMI is an important performance metric describing the modulation efficiency of a respective electrical signal onto the optical carrier, where it can be expressed as:

$$OMI = \frac{P_{\text{pp}} / 2}{P_{\text{avg}}} \tag{5.7}$$

where P_{pp} is the optical peak-to-peak power and P_{avg} is the optical average power. The optical average power is the optical carrier, while the optical peak-to-peak power

Table 5.3: System Parameters

Parameters	Values
SCM modulations	QPSK, 16-QAM, 64-QAM
Baseband multiplexing	OFDM
Carrier frequencies	2.6 GHz
RF power	2 dBm
DFB bias	40 mA to 100 mA
OMI	1 to 0.18
Optical power	-8 dBm to 10 dBm
SMF length	10 km
EDFA gain, noise figure	2 dB to 6 dB, 3.5 dB
PD responsivity	0.42
LNA- gain, NF	18 dB to 24 dB, 2.5 dB

represents the signal modulated onto the optical carrier. In this work, OMI values of 1, 0.5, 0.38, 0.25 and 0.18, which correlates to the bias current values of 40, 50, 60, 80 and 100 mA, and OLPs (P_{pp}) of 3.8, 4.3, 4.8, 7 and 10.5 dBm, respectively, are investigated. The maximum and minimum level of OMI can be arbitrary, as long as the optimum OMI falls within the range.

The received LTE spectrum centered at the 2.6 GHz band is shown in Figure 5.10(i) for QPSK, with a range of OMI. The QPSK spectrum for ARB of 3MHz shows the out-of-band emission (OBE) for OMI of 1, 0.25 and 0.18. The OMI characteristics can be categorized into three distinctive regions: A) the over-modulation region (OMI = 0.25 and 0.18), B) OMR (OMI = 0.38 and 0.5), and C) the under-modulation region (OMI = 1), as shown in Figure 5.10(ii) and (iii). Region A is close to the upper saturation region while region C is close to the lasing threshold. Regions A and C are described as the over-modulation and under-modulation regions corresponding to higher and lower values of

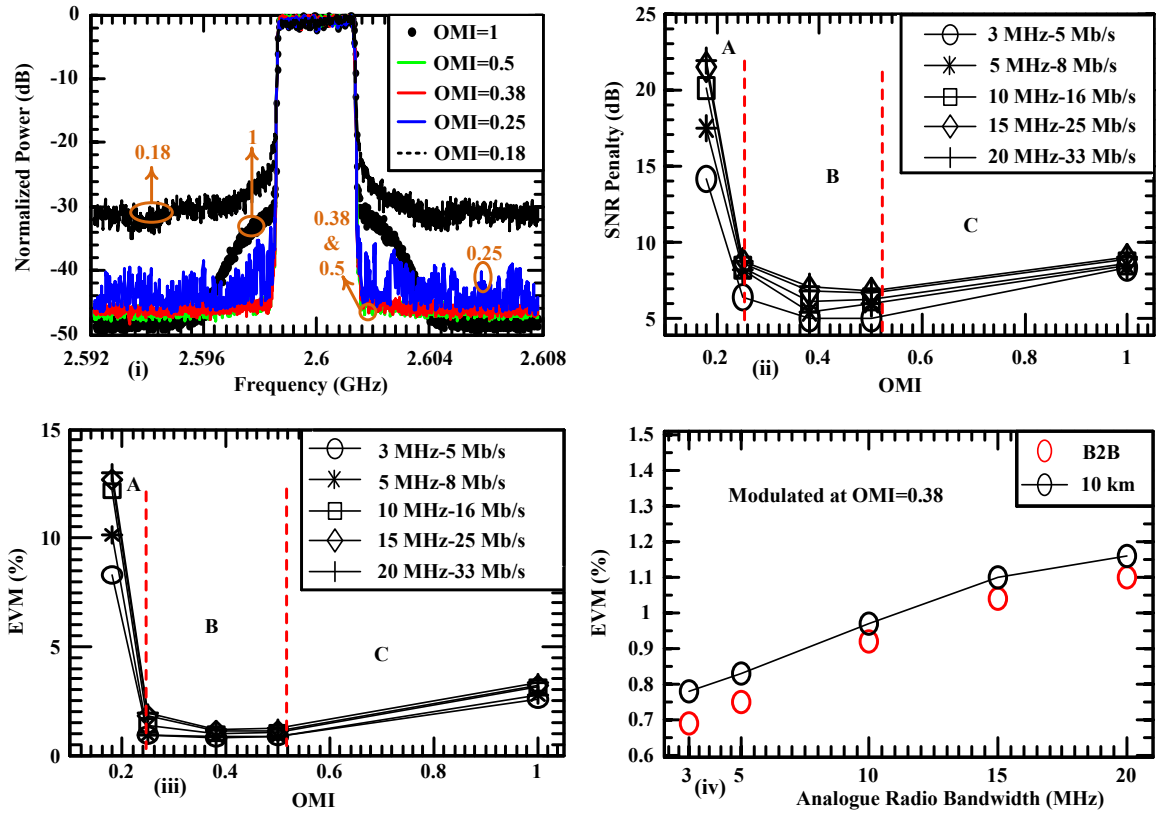

Figure 5.10: OMI analysis of QPSK with (i) spectral analysis, (ii) overall power penalty, (iii) overall EVM measurement, and (iv) EVM measurement for ARBs at OMR (OMI=0.38)

input bias current, respectively. The OBE for OMI of 1 or the region C in Figure 5.10(ii) and (iii), results in lower peak clipping of the OFDM signal. Additionally modulating in the region C will result in the minimum drive current to drop below the lasing threshold, which will induce nonlinear distortion from the turn-on delay [129]. Likewise, the observation for 16-QAM and 64-QAM in figures 5.11 and 5.12, respectively, resulted in similar spectral and region C distortion. In figures 5.10(ii), 5.11(ii) and 5.12(ii), the average SNR penalties across all ARBs for QPSK, 16-QAM, and 64-QAM at OMI of 1, are ~8.69 dB, ~8.89 dB, and ~9.02 dB, respectively. The SNR penalties increases with modulation level due to the increasing PAPR, see Table 5.2. At the same OMI, the resulting average EVM in figures 5.10(iii), 5.11(iii), and 5.12(iii), for QPSK, 16-QAM,

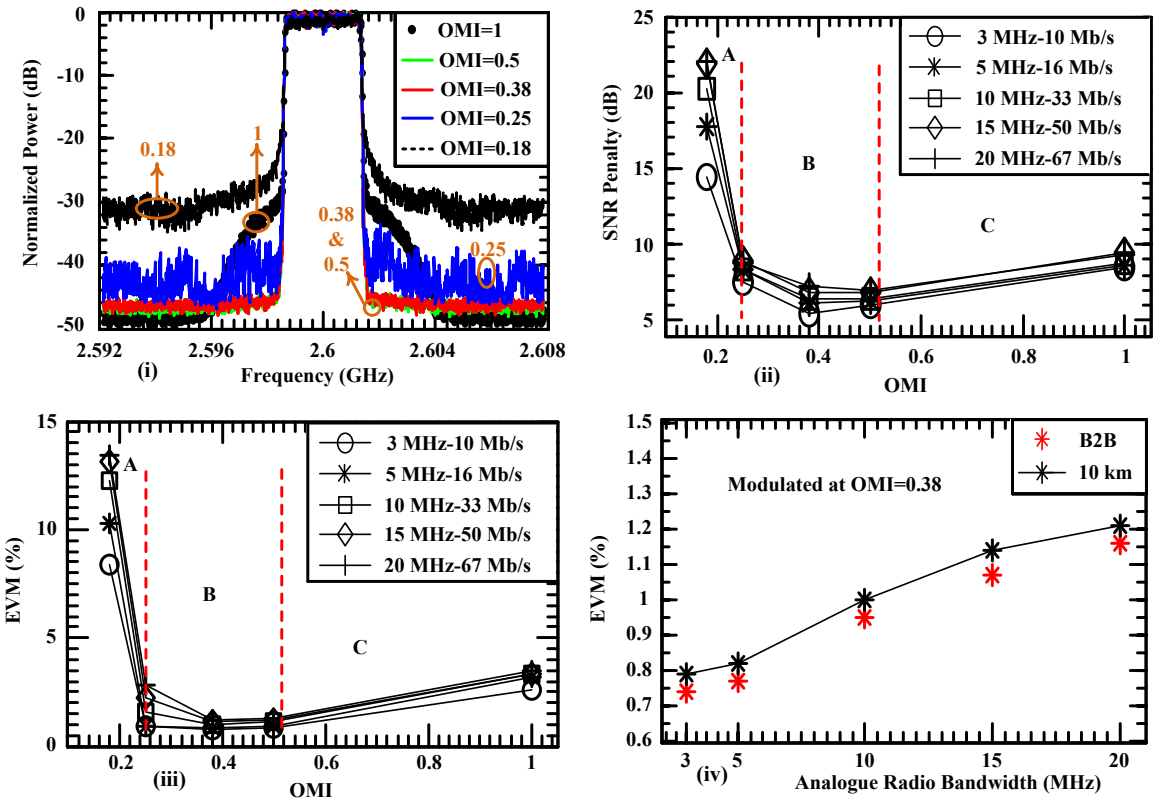

Figure 5.11: OMI analysis of 16-QAM with (i) spectral analysis, (ii) overall power penalty, (iii) overall EVM measurement, and (iv) EVM measurement for ARBs at OMR (OMI=0.38)

and 64-QAM are ~3.004%, ~3.18%, and ~3.34%, respectively. The EVMs are below the targeted 8%.

When modulating at OMI of 0.25, as shown in of figures 5.10(i), 5.11(i), and 5.12(i), the occurrence of OBE is relative to the nonlinear propagation. This is because to achieve lower OMI, the input bias current will be relatively high (80 mA), which proportionally increases the OLP. At an OMI of 0.25, the nonlinear propagation effect is constrained to the SPM and the SBS, which are critical in DD-OOFDM. Since Chapter 4 is concentrated in the intermixing region, only SPM was considered, as SBS only occurs at high OLP. In the experimental system designed herein, SBS becomes active at OLP of above ~6 dBm, further discussion on SBS will be carried out in Chapter 8.

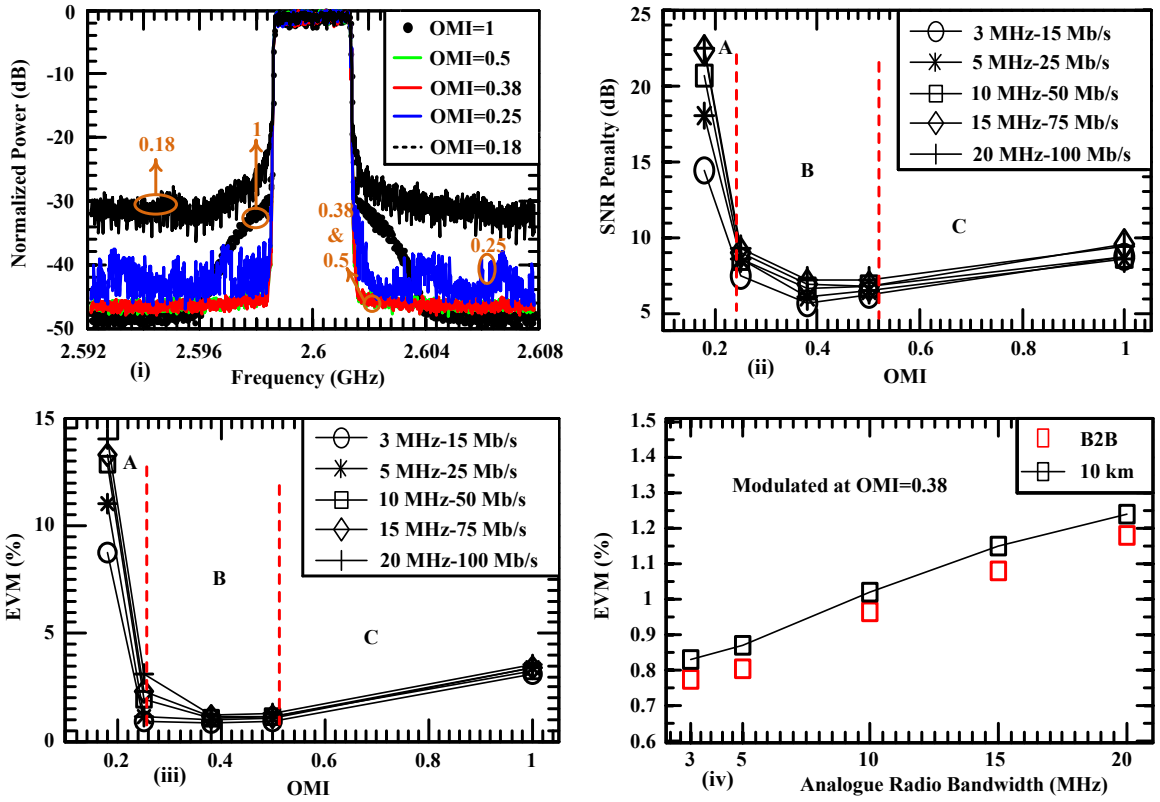

Figure 5.12: OMI analysis of 64-QAM with (i) spectral analysis, (ii) overall power penalty, (iii) overall EVM measurement, and (iv) EVM measurement for ARBs at OMR (OMI=0.38)

Nonlinear propagation is a serious issue, because nonlinear phase noise and backscattering arising from the propagation would deliberately reduce the walk-off rate, which ultimately results in severe ICI. However, it is important to specify, that OMI of 0.25 would not induce any distortion if the output of DFB is passed through an optical attenuator. This is because, the OMI of 0.25 is modulated linearly and clearly observable from Figure 5.2 that 80 mA bias is away from the saturation region.

Finally, effects of gain compression and nonlinear propagation can be observed for the OMI of 0.18 in figures 5.10(i), 5.11(i), and 5.12(i). The distortion induced by the OMI of 0.18 is shown in the region A of figures 5.10(ii), 5.11(ii), and 5.12(ii). The average SNR penalties at OMI of 0.18, for all ARBs are ~19.04 dB, ~19.28 dB and ~19.58 dB, for QPSK, 16-QAM and 64-QAM, respectively. It is clear that in this region, the combination

of gain compression and nonlinear propagation effects are degrading the OFDM signal severely. The average EVM values, across the ARBs shown in figures 5.10(iii), 5.11(iii), and 5.12(iii), for the same OMI, are ~11.26%, ~11.48% and ~11.96%, respectively. The resulting EVM values in region A for QPSK, 16-QAM, and 64-QAM are higher than the boundary defined by 3GPP. In conclusion regions A and C are not ideal for DD-OOFDM.

In figures 5.10(i), 5.11(i), and 5.12(i), for an OMI of 0.5 and 0.38, a flat noise floor can be observed, which corresponds to the nonlinear distortion free. The effect of the flat noise floor can be observed in region B of figures 5.10(ii) and (iii), 5.11(ii) and (iii), and 5.12(ii) and (iii). The OMI of 0.5 and 0.38 could be interchangeably utilised as the OMR. As shown in figures 5.10(ii), 5.11(ii), and 5.12(ii) for OMI of 0.38, the average SNR penalties for QPSK, 16-QAM and 64-QAM, are ~6.12 dB, ~6.34 dB and ~6.46 dB, respectively. The average EVM values for the same modulation schemes, shown in 5.9(iii), 5.10(iii), and 5.11(iii) are ~0.98%, ~1.01% and ~1.06%, respectively. As mentioned earlier, OMI of 0.25 will perform similarly to OMRs with an optical attenuator. However, attenuation and amplification for OMI of 0.18 and 1, respectively, will not result in OMR due to nonlinear modulation, thus strictly need to be avoided.

Figures 5.10(iv), 5.11(iv), and 5.12(iv) depict the QPSK, 16-QAM, and 64-QAM EVM versus ARBs, for the BTB and a 10 km link at an OMI of 0.38. The 10 km link profile follows the BTB pattern with a negligible penalty. From the outcome of this analysis, 60 mA bias current will be used throughout this thesis for DML. The error level reflected from the gain compression with nonlinear propagation induced distortions (region A) compared to the clipping with turn-on delay induced distortions (region C), shows that the nonlinear propagation dependent distortion is severe. In order to further emphasize on the

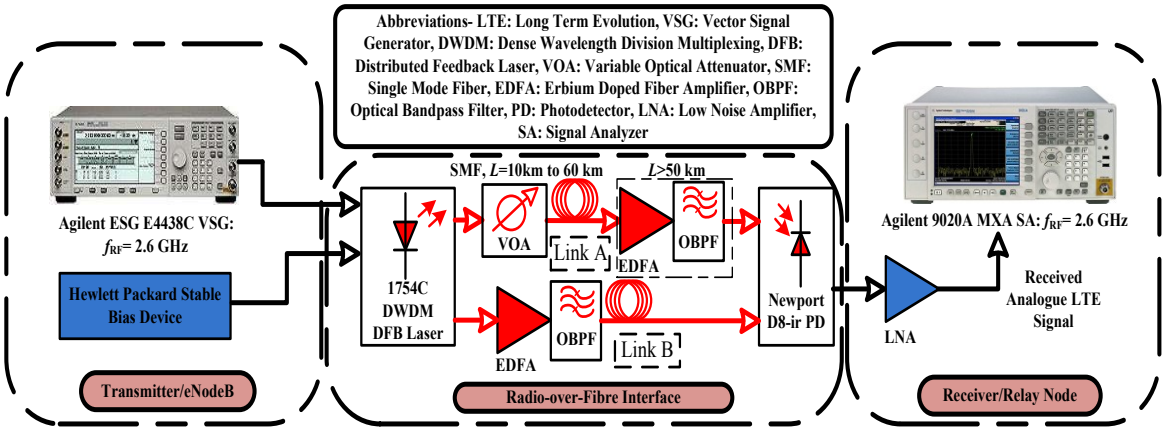

Figure 5.13: Experimental setup for LTE RoF system for 10 km and beyond

propagation characteristic, the next section is dedicated to the analysis of nonlinear propagation and OLP optimisation.

5.3 Impact of OLP with varying ARBs

The experimental setup for OLP analysis is illustrated in Figure 5.13. The transmitter and receiver are similar to OMI analysis, shown in Figure 5.9. However, the RoF interface is designed with some additional devices to analyse OLP. The modulated signal at the output of DFB in Figure 5.13 will be coupled into link A for lower OLP analysis, where it is composed of a variable optical attenuator (VOA). On the other hand, link B consists of EDFA and the optical bandpass filter (OBPF) for higher OLP analysis. In this section, only SMF of 10 km will be analysed, therefore the EDFA and OBPF modules utilised in link A can be ignored.

The most feasible approach of compensating optical fibre based nonlinear propagation is to launch the signal in the intermixing region. The theoretical detail of the intermixing region was given in Section 4.2 of Chapter 4. The intermixing region based propagation can further optimise the proposed system and provide a lower EVM with respect to the BTB system. The result herein was published in [135]. Figure 5.14(a, b, and c)(i) depict

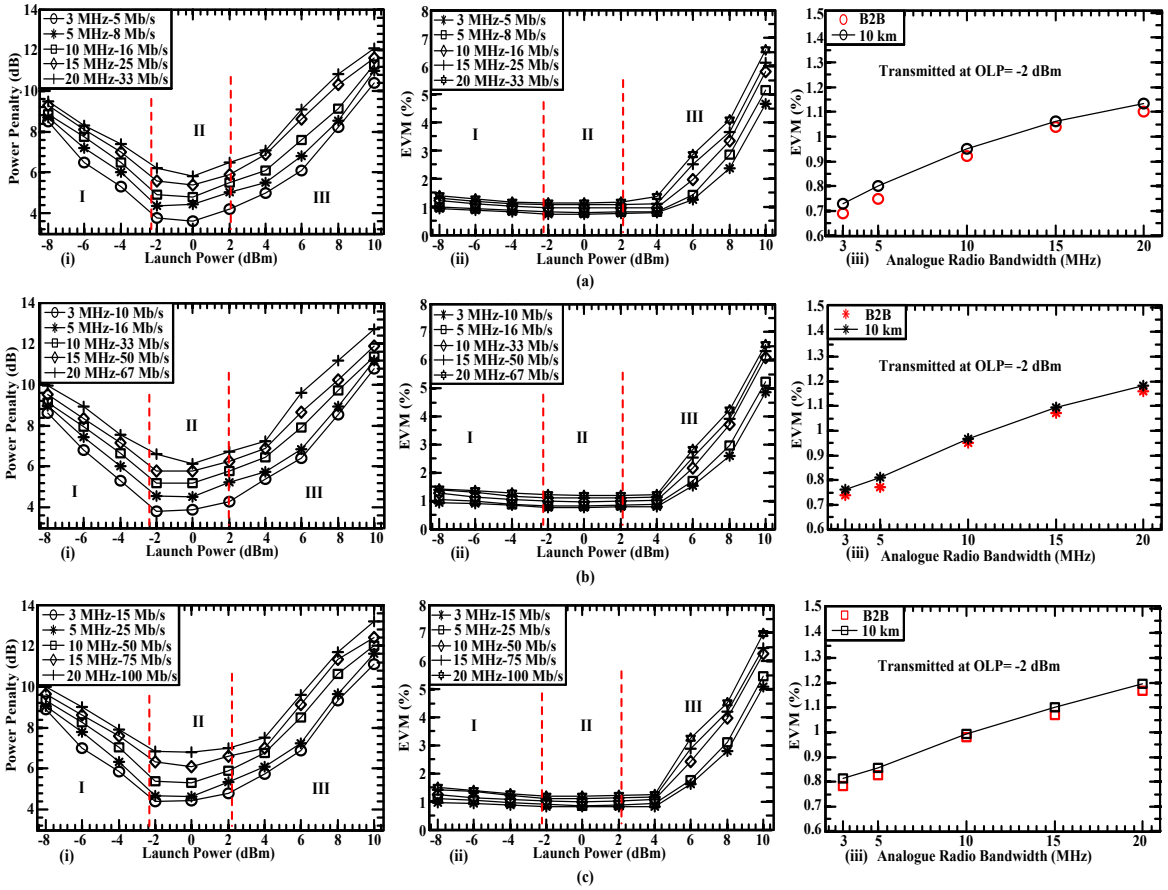

Figure 5.14: OLP analysis of (a) QPSK, (b) 16-QAM, and (c) 64-QAM, with (i) power penalty, (ii)EVM, and (iii) EVM at optimum OLP (-2 dBm)

the SNR penalty of 10 km transmission against OLP for QPSK, 16-QAM, 64-QAM, respectively for all ARBs. It is important to note that the launched optical signal is modulated at the OMI of 0.38. The OLP is varied in the range of -8 dBm to 10 dBm to investigate optical power transmission regions. There are three distinctive regions defined in Figure 5.14(a, b, and c), of which are I) linear region-PFC and CD induced distortion, II) intermixing region-optimum SNR penalty from the interaction between CD and PFC with nonlinearity, and III) nonlinear region-nonlinearity induced distortion. These regions were theoretically analysed in Chapter 4.

For the range of OLP less than -3 dBm (region I), in Figure 5.14(a, b and c)(i), the SNR penalty increases significantly with decreasing OLP. In principal, as OLP decreases, the

SNR decreases, thus proving the linear relationship associated with the impairments within the region I. In Figure 5.14(a, b and c)(i), at -8 dBm of OLP, the average QPSK, 16-QAM and 64-QAM SNR penalties for all ARB are ~8.97 dB, ~9.24 dB and ~9.38 dB, respectively. The average EVM values for QPSK, 16-QAM and 64-QAM observed in Figure 5.14(a, b and c)(ii) are ~1.17%, ~1.21%, and ~1.24%, respectively. Such high SNR penalty at -8 dBm OLP has low impact on the system performance. This is because it is a linear impairment where there is no occurrence of in-band IMD. It is also important to state that the in-band IMD will actuate the spectral re-growth within the finite bandwidth of the DD-OOFDM signal [136].

In the region III of Figure 5.14(a, b and c)(i), the QPSK, 16-QAM and 64-QAM SNR penalty increases with the OLP, which indicate a drop in SNR, although the OLP is higher. This is mainly due to the nonlinear phase distortion at higher values of OLP. At the OLP of 10 dBm the average SNR penalties are ~11.28 dB, ~11.59 dB and ~12.06 dB for QPSK, 16-QAM and 64-QAM, respectively. The resultant average EVM for QPSK, 16-QAM and 64-QAM, shown in Figure 5.14(a, b and c)(ii), are ~5.67%, ~5.81% and ~6.04%, respectively. For regions I and III, the values are well below the required of 8% EVM. The associated EVM gains in these regions could be used for improving the link budget. The EVM shown in region III of Figure 5.14(a, b and c)(ii) and region A of figures 5.10-5.12(iii), proves that nonlinear propagation induced distortion significantly introduces additional impairment to the existing gain compression affect. The DD-OOFDM signal is very susceptible to nonlinear propagation due to the nonlinear phase noise, which will obliterate the orthogonality of the DD-OOFDM subcarriers.

The intermixing region (region II) provides the optimum SNR penalty and EVM, ranging from -2 dBm to 2 dBm. In Figure 5.14(a, b and c)(i), the QPSK, 16-QAM and 64-

QAM average power penalties are ~4.8 dB, ~5.07 dB and ~5.45 dB, respectively at OLP of -2 dBm. The resulting average EVMs (Figure 5.14(a, b and c)(ii)) at these SNR penalties are ~0.93%, ~0.96% and ~0.99%. Reinstating the average EVMs achieved in the OMR region for QPSK, 16-QAM and 64-QAM, shown in Figure 5.10(iv), 5.11(iv), and 5.12(iv), are ~0.98%, ~1.01% and ~1.06%, respectively. The improvement of -2 dBm OLP outlines the benefit of the proposed optimisation scheme. The resultant EVM measured in the region II is much lower than the 8% EVM margin set by 3GPP and therefore this region provides the optimum OLP.

The overall optimisation is shown Figure 5.14(a, b and c)(iii), for QPSK, 16-QAM and 64-QAM EVM against the ARBs, respectively. The EVM deviation for QPSK, 16-QAM and 64-QAM compared to BTB are ~0.033%, ~0.028% and ~0.034%, respectively. The proposed system design with OMR and optimum OMI could compensate the clipping, gain compression and nonlinear propagation, and finally the nonlinear propagation induced distortions.

In order to complete the analysis on the intermixing region, it is important to investigate whether varying the transmission spans would cause deviation to the location of the minimum SNR penalty. Hence, next section would be completely analysing the LTE RoF in the perspective of varying transmission spans.

5.4 Deviation of Intermixing Region with Transmission Spans

The experimental system remains as shown in Figure 5.13. The LTE signal is fixed to 20 MHz bandwidth in this investigation, where QPSK, 16-QAM and 64-QAM is fixed to the data rate of 33, 67 and 100 Mb/s, respectively. The only changes is the transmission distance varying between 10 km and 60 km, with additional EDFA and OBPF utilised in link A due to the low responsivity of PD, which makes the receiver more sensitive towards

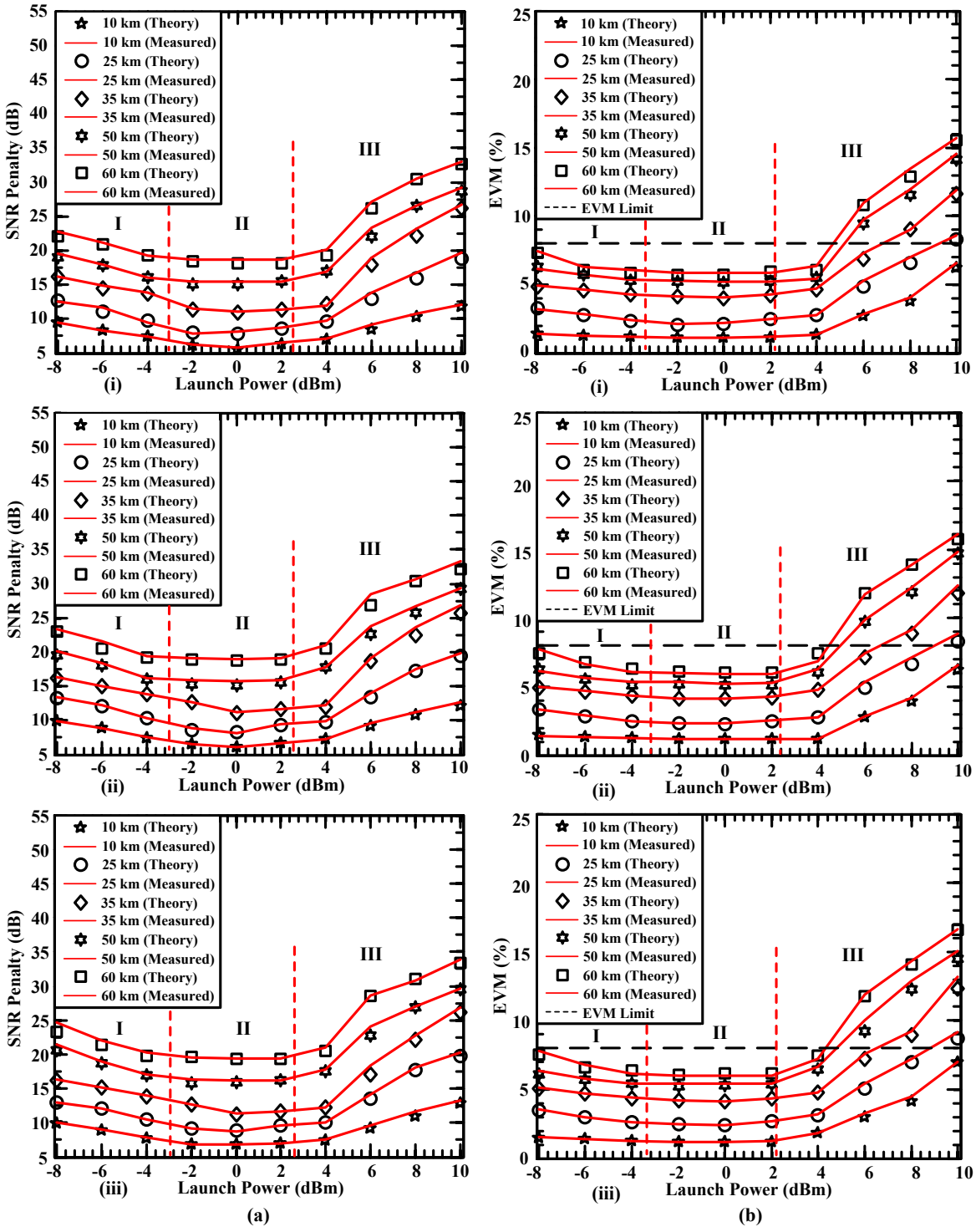

Figure 5.15: OLP against (a) power penalty and (b) EVM analysis, for (i) QPSK, (ii) 16-QAM, and (iii) 64-QAM with transmission spans of 10 km to 60 km

attenuation. The maximum transmission span is fixed to 60 km due to the limited availability of SMF. The finding within this section was published in [137] by the author.

The region I, II, and II carries the same description as explained in Section 5.3. Figure 5.14(a)(i, ii, and iii) depicts the SNR penalty of QPSK, 16-QAM and 64-QAM systems, compared to the BTB system, respectively, for transmission spans of 10 km, 25 km, 35 km, 50 km and 60 km. For consistency to Section 5.3, the OLP is varied in the range of -8 dBm to 10 dBm. The discussion on results is focused to the shortest transmission span of 10 km and farthest transmission span of 60 km, as all curves exhibits similar pattern. At the lowest OLP of –8 dBm for 10 km transmission span (region I), QPSK, 16-QAM, and 64-QAM systems experience SNR penalties of ~9.48 dB, ~9.97 dB and ~9.98 dB, respectively while at 60 km, the SNR penalties are ~22.8 dB, ~23.4 dB and ~24.6 dB, respectively. It is clear from 5.14(a)(i, ii, and iii) that the SNR penalties of the theoretical system match the experimentally measured values with negligible deviations, thus validating the system design.

In the region III of Figure 5.15(a)(i, ii, and iiii), at the OLP of 10 dBm for 10 km transmission span, QPSK, 16-QAM and 64-QAM systems SNR penalties are ~12.1 dB, ~12.7 dB and ~13.2 dB, respectively while at 60 km, the SNR penalties are ~33 dB, ~33.33 dB and ~33.9 dB, respectively. The penalties in the region III is higher than the region I is due to the nonlinear distortion that actuates OBE, and increases the noise floor level. In other word, the actual power of the optical signal is transferred and modulated to the back-reflected stokes signal. The reflected signal will arrive at the PD as a random time varying Gaussian noise with a broad spectral characteristic centered on the received signal and directly increases the noise floor [43, 138]. The power transfer of the optical signal and the rise in the noise floor are the major factors of the high SNR penalty. The nonlinear propagation will also induce additional in-band distortion, which will be analysed and discussed with the aid of EVM measurement later in this section.

The optimum SNR penalty is achieved in the region II (intermixing region), from -2 dBm to 2 dBm as shown in Figure 5.15. It can be observed from Figure 5.15 that for all modulation schemes, as the transmission link increases, the intermixing region remains within this range. The intermixing range is consistent with the investigation performed in Section 5.3. Linear distortions are known to accumulate with the distances [123], but the investigation fundamentally shows that both linear and nonlinear impairments increases proportionally with the transmission span. In the region II, average SNR penalties for QPSK, 16-QAM and 64-QAM systems at the transmission span of 10 km are ~6.17 dB, ~6.48 dB and ~6.88 dB, respectively while at 60 km, the resultant SNR penalties are ~18.64 dB, ~19.08 dB and ~19.47 dB, respectively. Considering the 60 km transmission span, the improvement observed in the intermixing region (region II) for the QPSK system with respect to the region I (OLP = -4 dBm) and the region III (OLP = 4 dBm) are ~0.66 dB and ~1.46 dB, respectively. Likewise, for the 16-QAM system, comparing with the region I (OLP = -4 dBm) and region III (OLP = 4 dBm), the improvements are ~0.42 dB and ~1.88 dB, respectively. The improvement associated with the 64-QAM system with respect to region I (OLP = -4 dBm) and the region III (OLP = 4 dBm) are ~0.83 dB and ~1.53 dBm, respectively.

The impact of distortion induced within the finite bandwidth of the signal can be characterized by the EVM. As a rule of thumb again, the proposed system is designed to achieve EVM lower than the required 8% specified by the 3GPP for LTE [134]. Figure 5.15(b)(i, ii, and iii) depict the EVM of QPSK, 16-QAM and 64-QAM systems, respectively. Graphs are categorized into three distinctive regions similar to the SNR penalty analysis. The observed EVMs for QPSK, 16-QAM and 64-QAM systems at the OLP of -8 dBm (region I) for 10 km transmission span are ~1.402%, ~1.43% and ~1.51%, respectively while at 60 km, the EVMs are ~7.42%, ~7.73% and ~7.82%, respectively. It is

shown in 5.14(b)(i, ii, and iii) that the linearly distorted DD-OOFDM signals in this region I are below the specified EVM. In the region III, at the OLP of 10 dBm, QPSK, 16-QAM and 64-QAM systems have achieved EVMs of ~6.57%, ~6.55% and ~6.97%, respectively for 10 km transmission span, while at 60 km, the resultant EVMs are ~15.732%, ~16.1% and ~16.6%, respectively. It is clearly shown in Figure 5.15(b) that only the 10 km transmission span has achieved less than 8% EVM at 10 dBm OLP (region III). This is due to the nonlinear propagation that induces in-band distortion, which will lead to the severe ICI for longer spans.

The intermixing region (region II) provides the optimum EVM. In Figure 5.15(b)(i, ii, and iii), for QPSK, 16-QAM and 64-QAM systems at 10 km transmission span have achieved average EVMs of ~1.144%, ~1.2% and ~1.21%, respectively while at 60 km, average EVMs are ~5.86%, ~5.96% and ~6.01%, respectively. The aforementioned EVMs for 60 km are the best achievable case for LTE signal transmission over RoF without any optical equalization devices. In terms of the deviation in the optimum region, the optimum OLP range are consistent throughout the 10 km to 60 km transmission range, which proves that the linear and nonlinear distortion increases proportionally with transmission distance.

5.4.1 Nonlinear Threshold of LTE RoF

It is important to understand the evolving nature of linear and nonlinear distortions with respect to the transmission distance. Figure 5.16(a), (b), and (c) illustrate the QPSK,

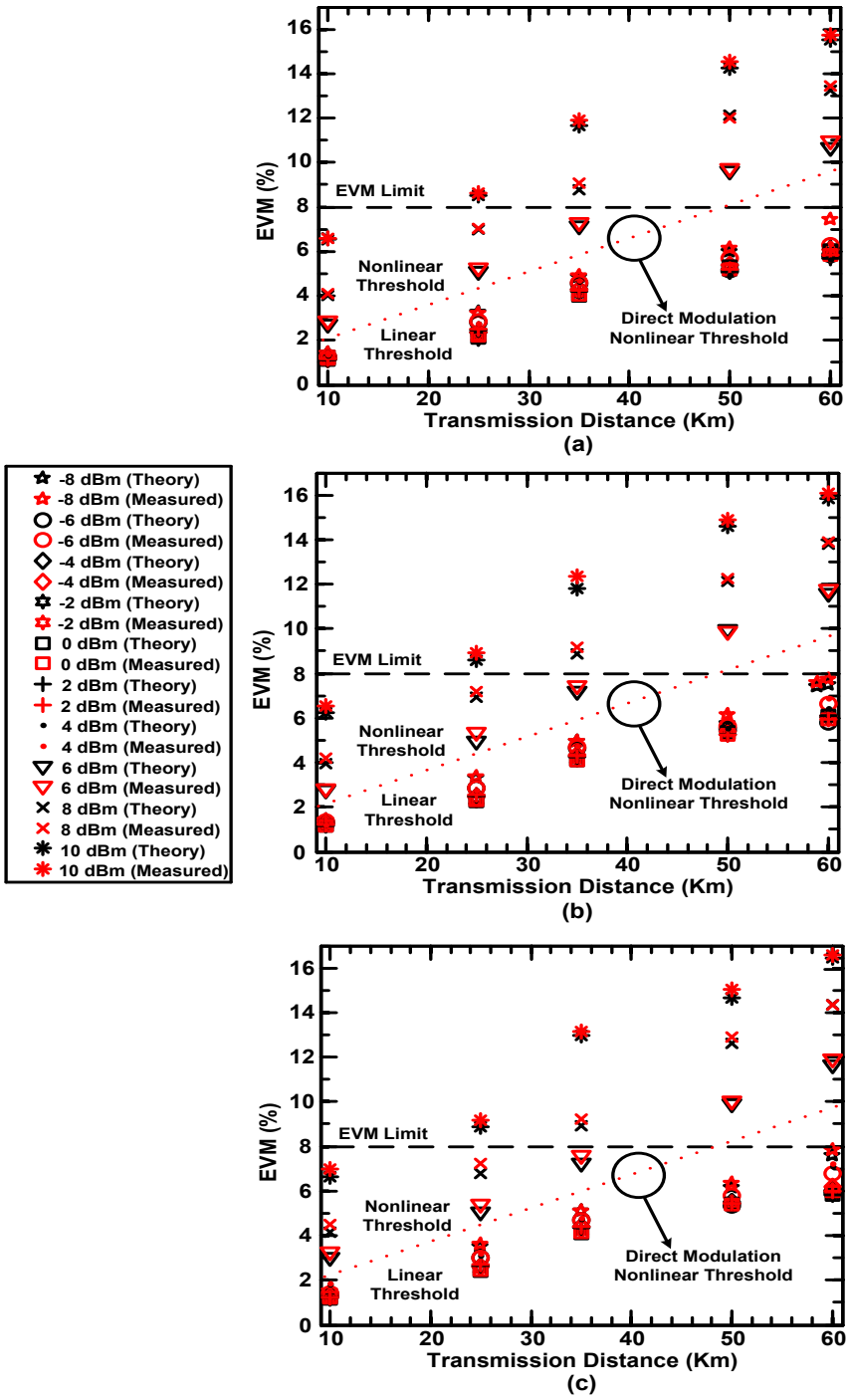

Figure 5.16: Transmission distance against EVM analysis of (a) QPSK, (b) 16-QAM, and (c) 64-QAM

16-QAM, and 64-QAM propagation characteristics for a range of OLP with respect to EVM. It is clear that QPSK, 16-QAM and 64-QAM systems experience a pronounced nonlinear distortion for OLP of more 6 dBm. As a result, OLP at 6 dBm is the "DM nonlinear threshold" where for OLP above this threshold, the signal will experience a severe EVM degradation. Graphs also indicate that irrespective of the propagation state, the distortion linearly increases with transmission distance.

5.5 Summary

In this chapter, the LTE RoF experimental system design was presented. As a first step of the link design, the characterization of the RoF system was carried out with the continuation to the optimisation of the OMI for the DML. In the OMR region, the QPSK, 16-QAM and 64-QAM achieved average EVM across all ARBs of ~0.97%, ~1.01%, and ~1.06%, respectively. In this operating scenario, the system achieved significantly lower than the 3GPP EVM margin of 8%.

As a further improvement to the system, the intermixing region was deliberately introduced which is a function of OLP. In this region, the QPSK, 16-QAM and 64-QAM average EVM further trimmed to ~0.93%, ~0.96% and ~0.99%, respectively. The results also revealed that, for low OMI, nonlinear propagation significantly adds to the existing gain compression affect, thus strictly needs to be avoided. In terms of higher transmission distance, investigation on transmission up to 60 km unfolded that intermixing region does not deviate.

Finally, the chapter presents the DM nonlinear threshold for LTE-RoF system. The investigation shows that both linear and nonlinear distortion increases linearly, and that the system experiences severe nonlinear distortion for OLP of more than 6 dBm. Since this

chapter presented the detailed basic experimental design of LTE RoF, next chapter will unfold some of the advance LTE RoF system design.

CHAPTER 6 ADVANCE LTE-ROF LINK WITH MIMO

The initiation of LTE and RoF system integration was demonstrated in the previous chapter. It was shown that the OMR and intermixing region significantly improved the LTE RoF performance. The design and findings of the previous chapters are confined to the single antenna based LTE system. But as shown in Table 1.2 of Chapter 1, LTE system can span up to 4×4 MIMO transmission. Adding MIMO transmission to the existing LTE system is important, as it effectively improves the incident throughput at the receiver end. The operating characteristic of MIMO can be defined as adding multiple antenna elements, both at the transmitter in the eNB and receiver in the UE. The idea of such design is to combine the multi-antenna transmitted signals at the receiver end, and improve the end-user experience with higher data rate. The important techniques require to achieve MIMO transmission are spatial multiplexing and diversity, due to the multiple passband LTE signals configured at the same frequency. By achieving the required conditions, the MIMO signals arriving at the receiver will be composed of varying channel coefficients. The equalizer in the OFDM scheme can easily rectify the MIMO signals, from the given wireless propagation diversity [139].

6.1 MIMO Transmission over Optical Fibre

It is clear that this thesis emphasizes on the implementation of RN, with RoF interface for eNB cell extension within the primary cell, and as well as to the adjacent cells. Therefore it is important that the RoF system has the competency to accommodate the LTE MIMO technology. However, transmitting MIMO signals over RoF is not trivial, because the group of signals in MIMO is configured at the same carrier frequency. The initial problem arises when this group of signals are combined and modulated onto the same corresponding optical carrier. In addition, after the photodetection, it is impossible to recover individual electrical signal with filtering because the photodetection causes a

mixing effect in the electrical domain. In summary, the potential failures occurs in providing the necessary diversity to the MIMO signals from different antenna are due to combining the signals prior to optical modulation, and the mixing effect upon photodetection [41].

The straightforward solution to this problem is to utilise individual lasers, optical fibers, and PDs for each MIMO antenna by introducing WDM, with an individual wavelength carrier for each MIMO signals [41]. Jansen *et al* [39] has also introduced externally modulated POLMUX system, with coherent detection to solve the associated problem with MIMO modulation in optical system. All the aforementioned solutions will significantly increase the cost of implementation with respect to the number of MIMO antennas and as well as the system complexity. Recently, there is considerable interest growing in the area of MIMO transmission over multi-core optical fibre. Although this method demonstrates the advantage of spectral efficiency, but the multi-core optical fibre technology for MIMO transmission is immature with very high complexity [140, 141]. Furthermore, this thesis proposes the idea of LTE and RoF integration on the basis of utilising the legacy backhaul infrastructure, which are mostly based on SMF [32]. Hence, simply installing a new group of multi-core optical fibres for MIMO transmission will not certainly be a commercial friendly idea.

As an alternative solution to this problem, this chapter proposes, both theoretically and experimentally, the design of FDM-OFDM technique for LTE in the context of 2×2 MIMO. Kobayashi *et al* [40] experimentally transmitted FDM-OFDM up to 80 km SMF with external modulation and coherent detection, which also increases the cost and complexity of the optical system. On the other hand, Liu *et al* [41] experimentally demonstrated FDM based directly modulated RoF system for indoor application by

utilising 550 m MMF.

The LTE spectrum is prominently defined at 2.6 GHz, with most researches also being carried out at 2 GHz as a potential spectrum in near future [18, 81, 142]. Therefore, the FDM-OFDM technique will be achieved by utilising 2 GHz and 2.6 GHz bands. The dual band transmission from RN to UEs is practically possible by employing single multiband antenna technology [143]. The RoF system for the proposed application is designed based on DML method, with the intention of lowering the cost of LTE-RoF integration. In Chapter 5, it was shown that 60 km transmission achieves better QoS then the LTE requirement. Hence, the FDM-OFDM signal will be transmitted over 60 km SMF to investigate if this method introduces any additional distortion, which might result in QoS worst than the LTE EVM limit. The receiver utilised for the system is based on DD.

In terms of system design, the investigation of the physical layer connectivity is according to the LTE standard, namely QPSK at 33 Mb/s, 16-QAM at 67 Mb/s, and 64-QAM at 100 Mb/s, which are the SCMs with OFDM. After performing FDM-OFDM at 2 GHz and 2.6 GHz bands, the data rate doubles for all modulation schemes. In the optical layer, a DFB is used as the DML adopting IM scheme to generate DD-FDM. The author has published the findings of DD-FDM system in [144].

6.2 Transmission Link for DD-FDM System

The experimental system shown in Figure 6.1 is modelled in MATLAB^{TM}. There are multiple theoretical models adopted to construct the DD-FDM system. Initially, the OFDM and its equivalent RF passband up-conversion models are utilised to generate the FDM-OFDM signal, as shown in equations (2.3-2.6) of Chapter 2. Subsequently, the DML scheme is emulated using the rate equations (3.2-3.4) of Chapter 3 for the generation of DD-FDM signal. Thereafter, the DD-FDM signal is transmitted down a 60 km of SMF,

where the propagation characteristics are simulated using the symmetrical split-step algorithm shown in equation (4.3) of Chapter 4. Since it was clear from Chapters 4 and 5 that nonlinear propagation severely distorts the traversing signal, thus it is completely neglected in this system design by proper control of the OLP. The optical receiver is modelled as DD with a square-law detector. The electrical receiver is the reverse process of the transmitter, except for the frequency domain equalizer module used for distortion compensation.

6.2.1 Experimental Link

The overall experimental setup for LTE RoF system is shown in Figure 6.1. All system parameters are presented in Table 6.1. All the experimental devices and components are similar to Chapter 5, thus the characterizations performed in Chapter 5 are applicable here. The LTE signals generated for this experiment are QPSK, 16-QAM, and 64-QAM with OFDM, respectively. The number of occupied subcarriers are 1200, FFT size of 2048, and CP size rate of ¼, which resulted in an ARB of 20 MHz, as shown in Table 1.2 of Chapter 1. At the complementary cumulative distribution function of 0.001%, the PAPRs are

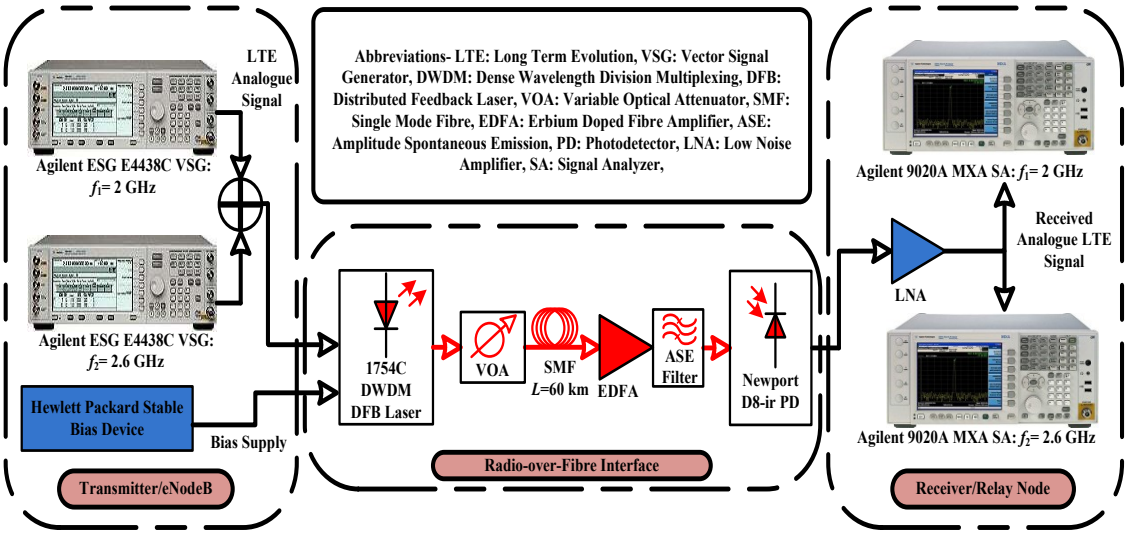

Figure 6.1: Overall experimental setup of optical FDM

Table 6.1: DD-FDM system parameters

Parameters	Values
SCM modulations	QPSK, 16-QAM, 64-QAM
Baseband multiplexing	OFDM
PAPR	QPSK=11.16 dB, 16-QAM=11.3 dB, and 64-QAM=11.67 dB
Passband multiplexing	FDM
Data rate	QPSK=66 Mb/s, 16-QAM=134 Mb/s, and 64-QAM=200 Mb/s
Signal bandwidth	OFDM=20 MHz, FDM-OFDM=40 MHz
Carrier frequencies	2 GHz and 2.6 GHz
RF power	2 dBm
DFB bias	60 mA
Linewidth	11.4 MHz
RIN	-149.6 dB/Hz
Wavelength	1551.11 nm
Optical launch power	-8 dBm – 0 dBm
SMF length	60 km
EDFA- gain, NF	6 dB, 3.5 dB
PD responsivity	0.42
LNA- gain, NF	20 dB to 24 dB, 2.5 dB

~11.16 dB, ~11.3 dB and ~11.67 dB for QPSK, 16-QAM and 64-QAM, respectively. The VSGs, Agilent ESG E4438C, will then generate the real-time LTE signal based on the respective modulation scheme, and subsequently up-converted to the first frequency band of f_1 = 2 GHz and second frequency band of f_2 = 2.6 GHz. The signals at the frequency bands of 2 GHz and 2.6 GHz are summed to form the FDM-OFDM signal. Figure 6.2 shows the frequency spectrum of the FDM-OFDM for both theoretical and experimental results. The experimental results are consistent to the theoretical prediction.

In the RoF interface shown in Figure 6.1, the FDM-OFDM LTE signal is directly applied to the DFB, 1754C DWDM laser to perform IM. The DFB laser is biased at 60 mA to carry out the IM in the OMR. After the modulation, the optical FDM-OFDM LTE signal (DD-FDM) is then coupled into a VOA to maintain the OLP, within the intermixing and

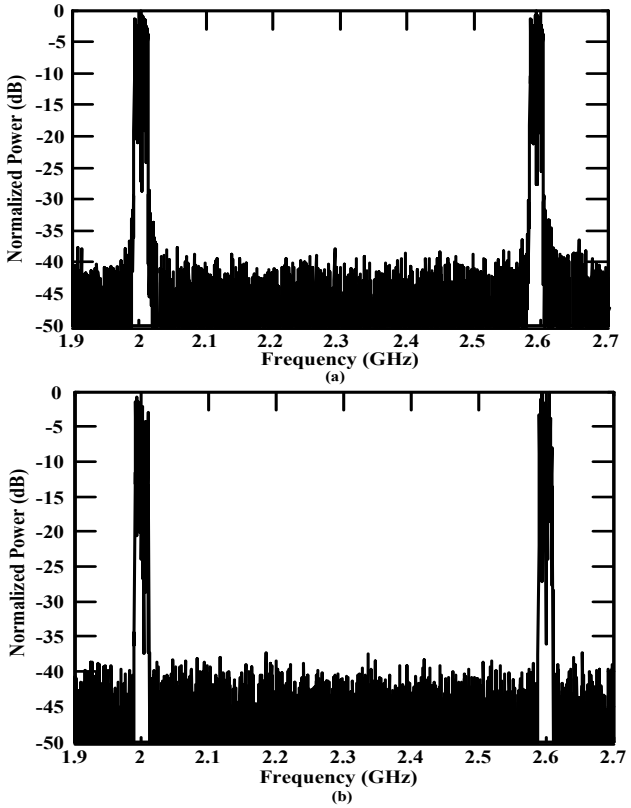

Figure 6.2: Frequency spectrum of the FDM-OFDM signal of (a) theoretical and (b) experimental

linear region of 0 dBm to -8 dBm. The OLP range for intermixing and linear regions conforms to that presented in Chapters 4 and 5. After the VOA, signal traverses through 60 km of SMF and post-amplified via EDFA with a gain of 6 dB and NF of 3.5 dB. The amplified signal is subsequently filtered with amplitude spontaneous emission (ASE) filter before DD. The DD used is performed with a PD, Newport D8-ir, at the responsivity of 0.42.

At the RN, a LNA is used for the compensation of PD's low responsitivity. The amplified signal is split and then analysed by individual SAs, Agilent 9020A MXA, to ascertain the signal quality. The next section will discuss the performance of the system, which is measured using the SNR and EVM metrics.

6.2.2 Results on DD-FDM System

Figure 6.3(a), (b), and (c) depict the OLP against SNR penalty for QPSK, 16-QAM and 64-QAM DD-FDM, respectively. Both theoretical and experimental measurements are captured after 60 km of transmission span. The theoretical and experimental result of all three modulation schemes shows minimum SNR penalty between -2 dBm and 0 dBm OLP. The average SNR penalty between 2 GHz and 2.6 GHz is ~1.3 dB. The penalty

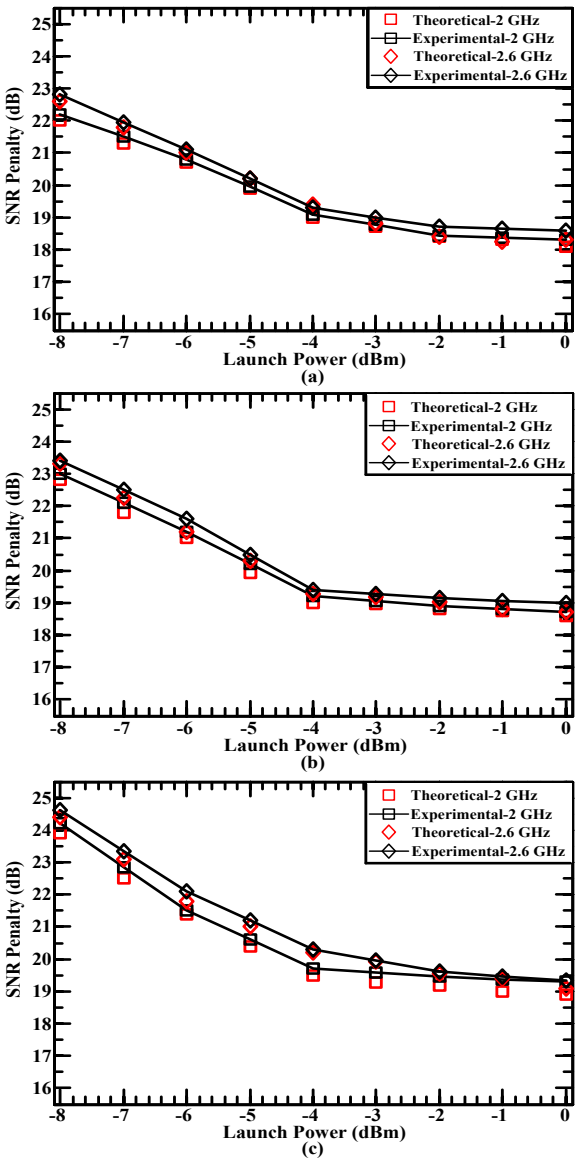

Figure 6.3: OLP against SNR penalty analysis of (a) QPSK DD-FDM, (b) 16-QAM DD-FDM and (c) 64-QAM DD-FDM

between both frequencies arise due to the higher magnitude response of the DFB laser at 2 GHz, see Figure 5.6 of Chapter 5. This factor was manually added to the theoretical system to be consistent with the experimental results. As it can be seen from Figure 6.3(a), (b), and (c), the theoretical and experimental SNR penalties for both 2 GHz and 2.6 GHz resulted in close proximity. Thus, the discussion of the results will be focused on the experimental system.

At OLP of 0 dBm for 2 GHz signal, QPSK, 16-QAM, and 64-QAM resulted in SNR penalties of ~18.3 dB, ~18.7 dB, and ~19.3 dB, respectively. For 2.6 GHz signal with the same OLP, the SNR penalties of QPSK, 16-QAM, and 64-QAM are ~18.6 dB, ~18.98 dB, and ~19.35 dB, respectively. Launching the signals at lower OLP significantly worsens the system's QoS. At -8 dBm OLP, the QPSK, 16-QAM, and 64-QAM, of 2 GHz signal resulted in SNR penalties of ~22 dB, ~23 dB, and ~24.2 dB, respectively. In the case of 2.6 GHz signal at the same OLP, the SNR penalties are ~23 dB, ~23.5 dB, and ~24.6 dB, for QPSK, 16-QAM, and 64-QAM, respectively. Both 2 GHz and 2.6 GHz signals exhibit similar degradation pattern, however, 2 GHz achieves better SNR gain due to the higher modulation response. The observed degradation pattern relative to the decreasing OLP is due to the drop in overall SNR.

Apart from SNR penalty analysis, EVM measurement is essential to define the exact system quality, as the 3GPP has set the EVM limit for LTE to be less than 8% [134]. Figure 6.4(a), (b), and (c) represent the EVM analysis of QPSK, 16-QAM, and 64-QAM DD-FDM system, respectively. The results in Figure 6.4(a), (b), and (c) provide the EVM of the theoretical and experimental systems, for 2 GHz and 2.6 GHz signals. It is clear that the theoretical and experimental systems exhibit

lowest EVM at OLP of 0 dBm, across all the investigated modulation schemes. The summary of the EVM data is shown in Table 6.2 for 0 dBm OLP.

As shown in Figure 6.4 and Table 6.2, the theoretical and experimental results have negligible deviations, thus proving the accuracy of the theory. Hereafter, the discussion will be focused on the experimental results. For 2 GHz signal, at 0 dBm OLP, the EVM of the QPSK, 16-QAM, and 64-QAM systems are ~5.82%, ~5.85%, and ~5.94%, respectively. At the same OLP, the 2.6 GHz signal resulted in EVM of ~5.86%,

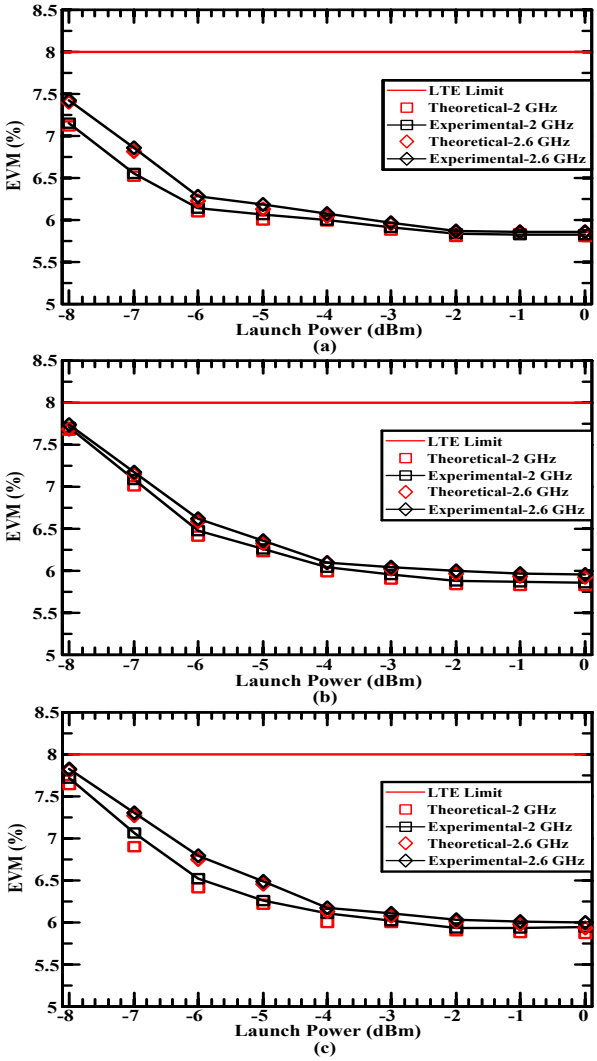

Figure 6.4: OLP against EVManalysis of (a) QPSK DD-FDM, (b) 16-QAM DD-FDM and (c) 64-QAM DD-FDM

Table 6.2: Theoretical and experimental EVM data of 0 dBm OLP

	2 GHz		2.6 GHz	
Modulation Scheme	**Theory**	**Experimen**	**Theory**	**Experimen**
QPSK	5.8%	5.82%	5.85%	5.86%
16-QAM	5.82%	5.85%	5.92%	5.95%
64-QAM	5.86%	5.94%	5.93%	5.99%

~5.95%, and ~5.99% for QPSK, 16-QAM, and 64-QAM, respectively. It is observable that 2.6 GHz signal endures slightly worsened EVM, which is consistent to the SNR penalty metric analysed earlier. In Figure 6.3, the EVM deteriorates as the OLP decreases. At the OLP of -8 dBm, the QPSK, 16-QAM, and 64-QAM systems resulted in EVMs of ~7.15%, ~7.65%, and ~7.71%, respectively, for 2 GHz signal. Launching the 2.6 GHz signal at the same OLP resulted in EVMs of ~7.42%, ~7.73%, and ~7.82%, for QPSK, 16-QAM, and 64-QAM, respectively.

The qualitative measurement of the proposed system can be performed with respect to the 3GPP-LTE EVM limit of 8%. In the best case operating point at the OLP of 0 dBm, the 2 GHz and 2.6 GHz bands achieved low EVM (see Table 6.2) compared to the 8% EVM limit. For the worst case operating point at the OLP of -8 dBm is still within the limit of 3GPP-LTE requirement. Although the nonlinear region is not considered for DD-FDM system, but from figure 5.14, it is clear that the system will experience severe distortion that will result in EVM higher than the 3GPP-LTE limit. Hence, it is a preferred option to omit the system from operating in the nonlinear region.

Since transmitting signals at two different frequencies simultaneously incurs the nature of two-tone transmission, hence there are chances of IMD distortion. The

single antenna based 60 km transmission system in Chapter 5 (Section 5.4) resulted in SNR penalties of ~18.64 dB, ~19.08 dB and ~19.47 dB, for QPSK, 16-QAM, and 64-QAM, respectively, within the intermixing region. Herein, as discussed earlier, the SNR penalties for 2.6 GHz signal is ~18.6 dB, ~18.98 dB, and ~19.35 dB, for QPSK, 16-QAM, and 64-QAM, respectively. The comparison of SNR penalties at the same frequency, transmission region and transmission span, but different antenna system, shows similar response. Therefore, the proposed system indicates to be free of IMD at the proposed analogue FDM condition. In addition, the comparative analysis also shows the transparency of the designed RoF system, for both single and multi-antenna transmissions.

The proposed design as an alternative to MIMO transmission transpired a high QoS at 0 dBm OLP, which is part of the intermixing region. Thus, the proposed system could advance to MIMO 4×4 by introducing additional bands. It is straightforward to accomplish this, as the required architecture had been introduced and discussed in detail.

6.3 Summary

In this chapter, an alternative method for 2×2 MIMO systems in LTE over 60 km RoF was proposed. The implementation of the alternative method was realized by introducing DD-FDM, both theoretically and experimentally. Taking into account the advantage of LTE spectrum allocation and the proposed solution, a two-fold gain in the peak data rate has been achieved in the 2x2 MIMO configuration. The studies revealed that the resulting output quality of the signal is almost identical for both the 2 GHz and 2.6 GHz bands. At 200 Mb/s (64-QAM), the experimental system could achieve EVMs of ~5.935% and ~5.99%, for 2GHz and 2.6 GHz system, respectively. In the proposed system, the EVM performance is within the 8% stipulated 3GPP LTE requirement. A thorough analysis was carried out for half-duplex multi-antenna solution in this chapter, both theoretical and

experimental designs were carried out and subsequently proving the viability of the proposed system. Therefore, the next chapter will introduce the full duplex LTE RoF system to emulate the complete design cycle of eNB to RN and RN to eNB connectivity.

CHAPTER 7 LTE ROF FULL DUPLEX SYSTEM BASED ON DWDM ARCHITECTURE

The findings reported in the former chapters were concentrated to half duplex LTE RoF integration, for DL transmission. For the first time, this chapter will introduce the full duplex LTE RoF integration for eNB cell extension, with AF type RN. The author has submitted the new findings of this section to the following publication [145]. In full duplex LTE system connected to AF type RN via wireless interface, an eNB coverage extension of 2 km with a throughput of 13.05 Mb/s was observed in [146]. The achieved throughput and the coverage extension reported in [146] demonstrates that the wireless interface offers insignificant impact on the eNB coverage, as the actual LTE technology aims to deliver a peak throughput of 100 Mb/s. It is shown that for full duplex system, the impact of wireless interface based eNB coverage extension had resulted in very low throughput. Hence, the usage of wireless interface should be neglected for the purpose of coverage extension.

This section proposes an experimentally designed architecture for the seamless integration of full duplex LTE with RoF system. The FDD topology will be adopted as the LTE full duplex scheme, with the RoF interface for eNB coverage extension. As mentioned earlier, the extension will be achieved via AF type RN, with a span of 10 km from the eNB.

7.1 DWDM Based LTE RoF Architecture

The conventional optical fibre based full duplex system delivers DL and UL signals over separate dedicated optical fibres without the wavelength re-use scheme [147, 148]. In contrary, some previous research reports on individual optical fibre allocated for DL and UL with the wavelength re-use scheme [149-152]. The wavelength re-use scheme is basically a full duplex system designed with a single wavelength for DL and UL usage. Full duplex system with dedicated DL and UL optical fibres is the direct solution to avoid

Rayleigh backscattering and optical interference as these are the major performance limiting factors [20, 21]. However, infrastructures with separate dedicated optical fibres would significantly increase the CAPEX and OPEX. Furthermore, a single optical fibre is competent enough to handle both DL and UL due to its vast unused bandwidth.

Rayleigh backscattering is one of the mechanism that induces optical fibre propagation loss from the material density fluctuations. A random fluctuation of the optical fibre refractive index arises from these density fluctuations. In the optical fibre medium with fluctuating refractive index, the incident beam will experience a scattering phenomenon, known as Rayleigh scattering. Signal propagating in optical fibre at a respective wavelength will experience Rayleigh scattering as a loss mechanism, from the resulting back-reflecting power, at any OLP. However, the back-reflecting power from Rayleigh backscattering will not distort the unidirectional signal. But, in full duplex transmission, the backscattered power of single wavelength based DL and UL signals will effectively distort the UL and DL signals, respectively [153]. In other word, the Rayleigh backscattered power produced by a propagating signal, will effectively interfere with the same wavelength based counter-propagating signal. The mixing of Rayleigh backscattered power to the counter-propagating signal produces noise from the intensity fluctuations converged due to phase fluctuations [154].

There are research works reported on transmitting DL and UL signals simultaneously over the same optical fibre employing the wavelength reuse scheme [155, 156]. As specified earlier, Rayleigh backscattering and optical interference degrade the QoS of systems operating with same wavelength for bidirectional transmission [155, 156]. It is also shown in [155], that Rayleigh backscattering actuates increased noise level surrounding the vicinity of the received signal. Furthermore, it is important to note that all the aforementioned optical fibre based full duplex systems are designed based on the

external modulation scheme. The vastly utilised DML method throughout this thesis exhibits PFC. Conversely, the external modulated system enables a free PFC transmission. The topic on chirping was thoroughly analysed in Chapters 3 and 4. The PFC and the CD jointly distorts the system, which in turn degrade the performance of DML compared to the externally modulated system [45]. But, as shown in Chapters 4 and 5, maintaining the OLP within the optimum region, the distortions effect will be minimized. In addition, it is imperative to adopt a DML scheme, because externally modulated systems are complex and costly. Thus DML acts as an additional positive factor on lowering CAPEX and OPEX.

In order to mitigate Rayleigh backscattering and optical interference, the proposed system is designed with two dedicated wavelengths, each for DL and UL. The wavelength spacing is in the range of DWDM to maintain the optical spectral efficiency. There are three wavelength based multiplexing techniques in optical fibre communication systems. The very first technique introduced was broad wavelength division multiplexing (BWDM), which utilised wavelengths at 1310 nm and 1550 nm. The shortcoming of BWDM is that EDFA cannot be implemented at the 1310 nm wavelength. Furthermore, the sparse usage of optical spectrum is unnecessary. The next multiplexing method introduced was Coarse wavelength division multiplexing (CWDM), which operates at multiple wavelengths across 1271 nm to 1661 nm with 20 nm spacing. Long span transmission that requires EDFA, only operates in the C-band (1530 nm to 1565 nm), hence very limited wavelengths at 20 nm CWDM spacing available in the C band. Finally, DWDM is picked as the impeccable multiplexing technique due to its narrowly spaced wavelength channels of 0.8 nm, which allows a multiplexing of over 40 wavelengths, all within the C-band range. Thus, multiple eNB can be connected to multiple RNs in a full duplex transmission, by utilising DWDM technique. However, in this chapter, only a single eNB and RN are

experimentally emulated as a proof of concept.

In addition, the advantage of having dedicated optical carriers for DL and UL signals will enable the instantaneous connections between eNB and UE, via RN. It is important to introduce the instantaneous feature, to provide the opportunity for either eNB or UE to initiate the connection in real communication scenario. Therefore, the wavelength re-use scheme as proposed by [149-152, 155, 156] will not be realistic in real-time application for mobile communication.

The proposed system specification is designed according to the LTE requirement as stated in [157]. The baseband system is designed with the QPSK, 16-QAM, and 64-QAM as the SCM schemes. Subsequently, the SCM schemes are modulated onto the OFDM and single carrier-frequency division multiplexing (SC-FDM) for DL and UL transmission, respectively, as the MCM schemes. The full duplex system operates with the FDD mode.

Table 7.1: System parameters for full duplex system

Parameters	**Values**	
SCM modulations	QPSK, 16-QAM, and 64-QAM	
Signal bandwidth (MHz)	20	
RF power (dBm)	-10 to 2	
DFB bias (mA)	60	
SMF (km)	10	
PD responsivity	0.42	
LNA-gain, NF (dB)	18, 2.5	
	DL	**UL**
MCM modulations	OFDM	SC-FDM
PAPR (dB)	11.16, 11.3, and 11.67	7.59, 7.71, and 7.86
Data rate (Mb/s)	33, 66, 100	30, 61, 92
Carrier frequencies (GHz)	2.62-2.69	2.5-2.57
Optical power (dBm)	1.06	1.19
RIN (dB/Hz)	-149.6	-151.219
Optical Wavelength (nm)	1551.11	1550.31

The DL signal operates at carrier frequencies f_{DL} ranging from 2.62 to 2.69 GHz, while the UL signal is up-converted to carrier frequencies f_{UL} from 2.5 to 2.57 GHz according to the LTE-FDD specification [158].

In the optical layer, DL and UL signals directly intensity modulate the respective DFBs. A DD scheme is employed for both DL and UL. The relevant system parameters are presented in Table 7.1. The system evaluation for DL and UL are performed following the DD. The evaluation is carried out both in the passband and baseband with the adjacent channel leakage ratio (ACLR) and the EVM, respectively.

7.1.1 Fundamentals of the Experimental System

The full duplex LTE RoF experimental system setup is shown in Figure 7.1. The fundamental theories that govern the transmitter, channel, and receiver have mostly been described in the previous half duplex chapters. The DL signal is generated via the VSG_{DL}, Agilent ESG E4438C. The modulated signal in the baseband is composed of QPSK, 16-QAM, and 64-QAM SCMs. The theoretical expressions of the DL signal, which is composed of OFDM and the equivalent passband up-conversion, were shown in equations (2.3-2.6) of Chapter 2. In OFDM modulation, the number of occupied subcarriers are 1200, FFT size of 2048, and CP size rate of ¼, which resulted in an ARB of 20 MHz, as shown in Table 1.2 of Chapter 1. The passband up-converted carrier frequencies range from 2.62 to 2.69 GHz.

In the proposed system, the UL signal is based on SC-FDM modulation according to the LTE standard. The UL signal is realized via VSG_{UL} and the instrument model is consistent to the VSG_{DL}. In the LTE technology, SC-FDM is adopted as the MCM instead of OFDM for UL transmission. This is due to the prominent PAPR problem associated with the OFDM scheme. Since the usage of SC-FDM is initiated in this section due to the

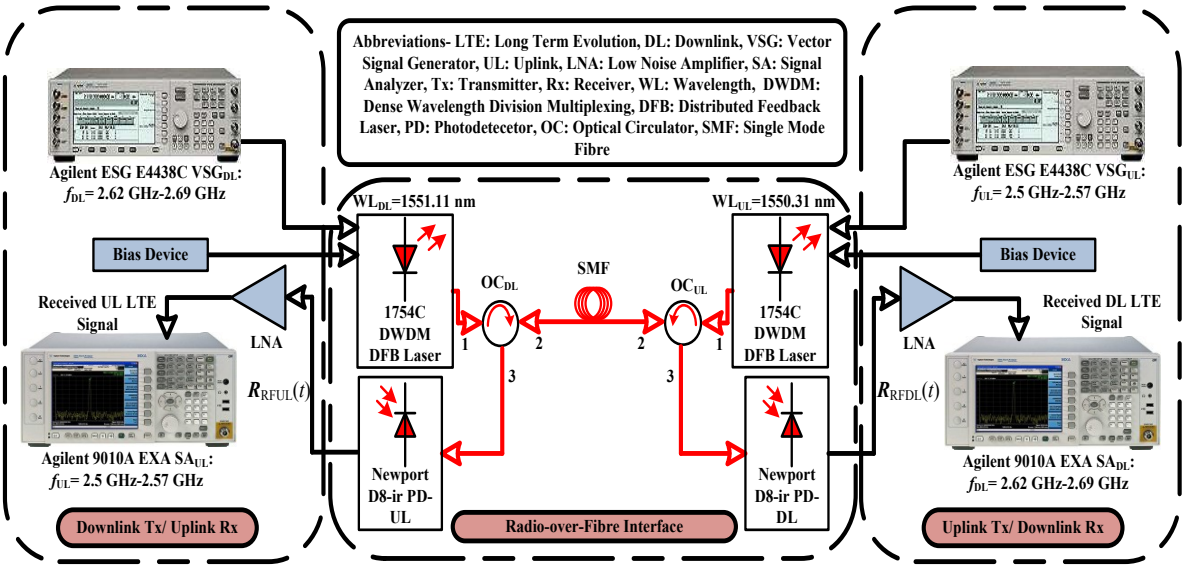

Figure 7.1: Full duplex LTE RoF experimental setup

full duplex demonstration, the theoretical formulation that describes the generation of SC-FDM signal will be shown. The SCM modulated symbols with QPSK, 16-QAM and 64-QAM can be expressed as $\boldsymbol{X}_{\mathrm{UL}}(m)$ where $\{\boldsymbol{X}_{\mathrm{UL}}(m) : m=0, 1, \ldots, M\text{-}1\}$ and m is the spreading/subcarrier index. The SCM symbols $\boldsymbol{X}_{\mathrm{UL}}(m)$ are transformed to the frequency domain by applying a M-point FFT, where $M = 1024$ [157]:

$$\boldsymbol{X}_{\mathrm{UL}}(u) = \sum_{m=0}^{M-1} \boldsymbol{X}_{\mathrm{UL}}(m) e^{-j2\pi mu/M}, \tag{7.1}$$

where $\{\boldsymbol{X}_{\mathrm{UL}}(u) : u = 0, 1, \ldots, M\text{-}1\}$ is the frequency domain of the SCMs, u is the frequency domain spreading/subcarrier index. The M-point FFT is applied to spread the signal energy to the entire spectrum to reduce the PAPR. The pre-FFT operation places the symbols across the whole frequency range, thus creating a correlation between subcarriers. As explained in Chapter 5, the high PAPR associated with OFDM is due to the construction of subcarriers with uncorrelated data. The contrast of the spreading can be observed from Table 7.1 in terms of PAPR values of SC-FDM and OFDM. The frequency domain SCMs $\boldsymbol{X}_{\mathrm{UL}}(u)$ are mapped with the localized topology $\boldsymbol{X}_{\mathrm{UL}}(l_t)$, where l_t is the

mapping index. The localized topology for symbol mapping $\{\boldsymbol{X}_{\mathrm{UL}}(l_{\mathrm{t}}) : l_{\mathrm{t}} = 0, 1, \ldots, N_{\mathrm{s}}\text{-}1\}$ can be described as:

$$\boldsymbol{X}_{\mathrm{UL}}(l_{\mathrm{t}}) = \begin{cases} \boldsymbol{X}_{\mathrm{UL}}(k), 0 \le k \le M-1 \\ 0, M \le k \le N_{\mathrm{s}}-1 \end{cases} \tag{7.2}$$

The localized mapped symbols $\boldsymbol{X}_{\mathrm{UL}}(l_{\mathrm{t}})$ are then converted to the time domain samples with N-point IFFT, denoting that $N_{\mathrm{s}} > M$, and $N = 2048$:

$$\boldsymbol{S}_{\mathrm{UL}}(n) = \frac{1}{N_{\mathrm{s}}} \sum_{l=0}^{N_{\mathrm{s}}-1} \boldsymbol{X}_{\mathrm{UL}}(l_{\mathrm{t}}) e^{j2\pi n l_{\mathrm{t}} / N_{\mathrm{s}}}, \tag{7.3}$$

where $\{\boldsymbol{S}_{\mathrm{UL}}(n) : n = 0, 1, \ldots, N_{\mathrm{s}}\text{-}1\}$ is the localized mapped SC-FDM signal in the time domain. As mentioned earlier, PAPR of the UL signal is lower than the DL signal. The PAPR is analytically expressed as $\mathrm{PAPR}\{\boldsymbol{S}_{\mathrm{DL/UL}}(n)\} = \max\{\boldsymbol{S}_{\mathrm{DL/UL}}(n)^2\}/\mathrm{E}\{\boldsymbol{S}_{\mathrm{DL/UL}}(n)^2\}$, where the subscript DL/UL denotes DL or UL signal, while E{.} refers to the expectation operator. The SC-FDM signal is then appended by CP at the rate of ¼, $\boldsymbol{S}_{\mathrm{CPUL}}(t)$.

The baseband to passband up-conversion process is similar to that expressed in equation (2.5) and (2.6) of Chapter 2. The SC-FDM signal up-conversion after DAC is shown in (7.4) and (7.5), where $\boldsymbol{S}_{\mathrm{RFUL}}(t)$ is the passband SC-FDM signal modulated at the carrier frequencies of 2.5 to 2.57 GHz.

$$\mathrm{S}_{\mathrm{RFUL}}(t) = \mathrm{Re}\{\mathrm{S}_{\mathrm{CPUL}}(t)\} * \cos(\omega_{\mathrm{RFUL}} t) + \mathrm{Im}\{\mathrm{S}_{\mathrm{CPUL}}(t)\} * \sin(\omega_{\mathrm{RFUL}} t) \tag{7.4}$$

$$\omega_{\mathrm{RFUL}} = 2\pi f_{\mathrm{UL}}, \tag{7.5}$$

In the case of optical transmitter, the DML method is employed. Owing to the bipolar nature of electrical signal, a 60 mA of bias current is coupled with the DL and UL signals to perform modulation within the OMR. The optical modulation of DL and UL signals are carried out by the 1754C DWDM DFB lasers, at the operating wavelengths of 1551.11 nm

and 1550.31 nm, respectively. The fundamentals of DML adopting IM can be defined through the laser rate equations (3.2-3.4) of Chapter 3.

The optical circulator for DL (OC_{DL}) and UL (OC_{UL}) induces an optical loss of ~3.8 dB and~5.9 dB, respectively. The DL and UL OLPs at the output port 2 of OC_{DL} and OC_{UL} are ~1.06 dBm and ~1.19 dBm, respectively, see Figure 7.1. The losses associated with the OC_{DL} and OC_{UL} are due to the signal leakage from port 2 to port 3. Consequently, the leakage will manifest itself as a crosstalk and will be analysed via ACLR measurement.

The DL and UL signals, at the output of port 2 of OC_{DL} and OC_{UL}, respectively, are concurrently launched into a single 10 km SMF. The analytical model that governs the propagation properties of SMF can be expressed by the generalized nonlinear Schrodinger equation, see equation (4.2) of Chapter 4. The OLP is maintained within the intermixing region to avoid any nonlinear interference.

After propagating through 10 km of SMF, the DL and UL signals are detected at the port 3 of OC_{UL} and OC_{DL}, respectively. The signal detection at port 3 of OC_{UL} and OC_{DL} are performed via a Newport D8-ir PD with the DD scheme. Following the photodetection, the received passband DL signal $\boldsymbol{R}_{RFDL}(t)$, and UL signal $\boldsymbol{R}_{RFUL}(t)$ are amplified via a LNA, and subsequently demodulated using the Agilent 9010A EXA SA. The demodulation is the reverse of the transmission process, except for the additional least square estimation with frequency domain equalizers for distortion compensation.

7.1.2 Results on DWDM Based Full Duplex System

The full duplex LTE-FDD system operates at DL carrier frequencies of 2.62 to 2.69 GHz and UL carrier frequencies of 2.5 to 2.57 GHz. The leakage of DL and UL signals

in OC_{DL} and OC_{UL} will effectively interfere with the receiving UL and DL signals, respectively, in port 3. In principal, no interference will occur between the leakage of DL signal and the receiving UL signal in OC_{DL}, which is the same case for leakage of UL signal and the receiving DL signal in OC_{UL}. However, photodetection will instigate IMD products between leakages and the received signal for both DL and UL signals. The IMD products arise from the subcarrier-subcarrier mixing where ACLR metric is applied to measure this phenomenon.

The ACLR measurement is exploited to measure the IMD of the received signals, at DL and UL receivers. The analytical expressions of ACLR are shown as:

$$ACLR1 = \frac{\int_{f_{DL/UL}-3B_W/2}^{f_{DL/UL}-B_W/2} \boldsymbol{R}_{RFDL/RFUL}(f)df + \int_{f_{DL/UL}+B_W/2}^{f_{DL/UL}+3B_W/2} \boldsymbol{R}_{RFDL/RFUL}(f)df}{\int_{f_{DL/UL}-B_W/2}^{f_{DL/UL}+B_W/2} \boldsymbol{R}_{RFDL/RFUL}(f)df} \tag{7.6}$$

$$ACLR2 = \frac{\int_{f_{DL/UL}-5B_W/2}^{f_{DL/UL}-3B_W/2} \boldsymbol{R}_{RFDL/RFUL}(f)df + \int_{f_{DL/UL}+3B_W/2}^{f_{DL/UL}+5B_W/2} \boldsymbol{R}_{RFDL/RFUL}(f)df}{\int_{f_{DL/UL}-B_W/2}^{f_{DL/UL}+B_W/2} \boldsymbol{R}_{RFDL/RFUL}(f)df}, \tag{7.7}$$

where ACLR1 and ACLR2 are the first and second adjacent band measurements, respectively. Equation (7.6) for ACLR1 measures the adjacent band of 30 MHz spacing from the centre frequencies of DL and UL. Whereas ACLR2 covers the adjacent band for 50 MHz band away from the DL and UL centre frequencies. This is because, in the chosen FDD duplex band, the minimum spacing between DL carrier frequency and UL carrier frequency is 50 MHz. The parameter B_w is the 20 MHz signal bandwidth, and $\boldsymbol{R}_{RFDL/RFUL}(f)$ is the Fourier transformed received analogue signal of both DL and UL. The integrated bandwidth of adjacent cell measurement is 20 MHz.

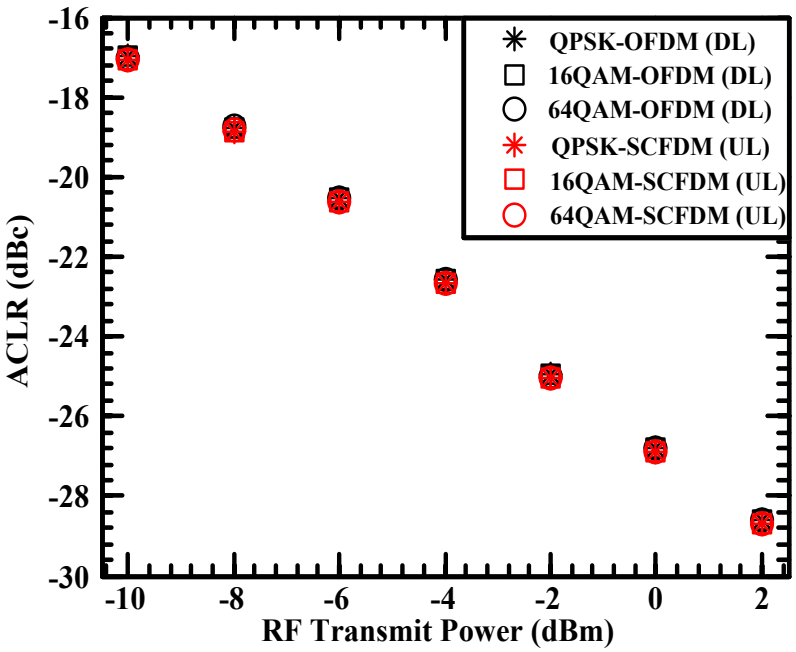

Figure 7.2: The ACLR measurement for half duplex system of DL and UL after 10 km transmission

Figure 7.2 shows the half duplex ACLR measurements of the DL and UL systems, where the results are recorded while the counter-propagating signal is switched off. The DL system is composed of QPSK, 16-QAM and 64-QAM with OFDM, while the UL system is modulated with the same SCMs, but SC-FDM as the MCM. Result in Figure 7.2 is measured using SA after 10 km transmission span with a varying RF transmit power. At 2 dBm RF transmit power, the average ACLR value across all SCMs of DL signal is ~-28.60 dBc, while the average ACLR observed for UL SCMs is ~-28.65 dBc. Figure 7.2 also indicates that SCMs of both DL and UL have resulted in similar ACLR, hence, rest of the ACLR analysis will be only carried out for the highest data rate SCM, which is 64-QAM in this case.

As mentioned earlier, in the FDD scheme, the frequency range of DL and UL signals are 2.62 to 2.69 GHz and 2.5 to 2.57 GHz, respectively. As an initial system design step, it is vital to investigate the interference between the given frequency spacing. Figure 7.3(a)

shows the measurement recorded after the photodetection for DL and UL signals at 2 dBm transmit power. In this investigation, DL signal is swept through 2.62 to 2.69 GHz for a given interfering UL signal. The frequency spacing between DL and UL signals vary between 190 MHz to 50 MHz. The broad frequency spacing (BFS) of 190 MHz could be

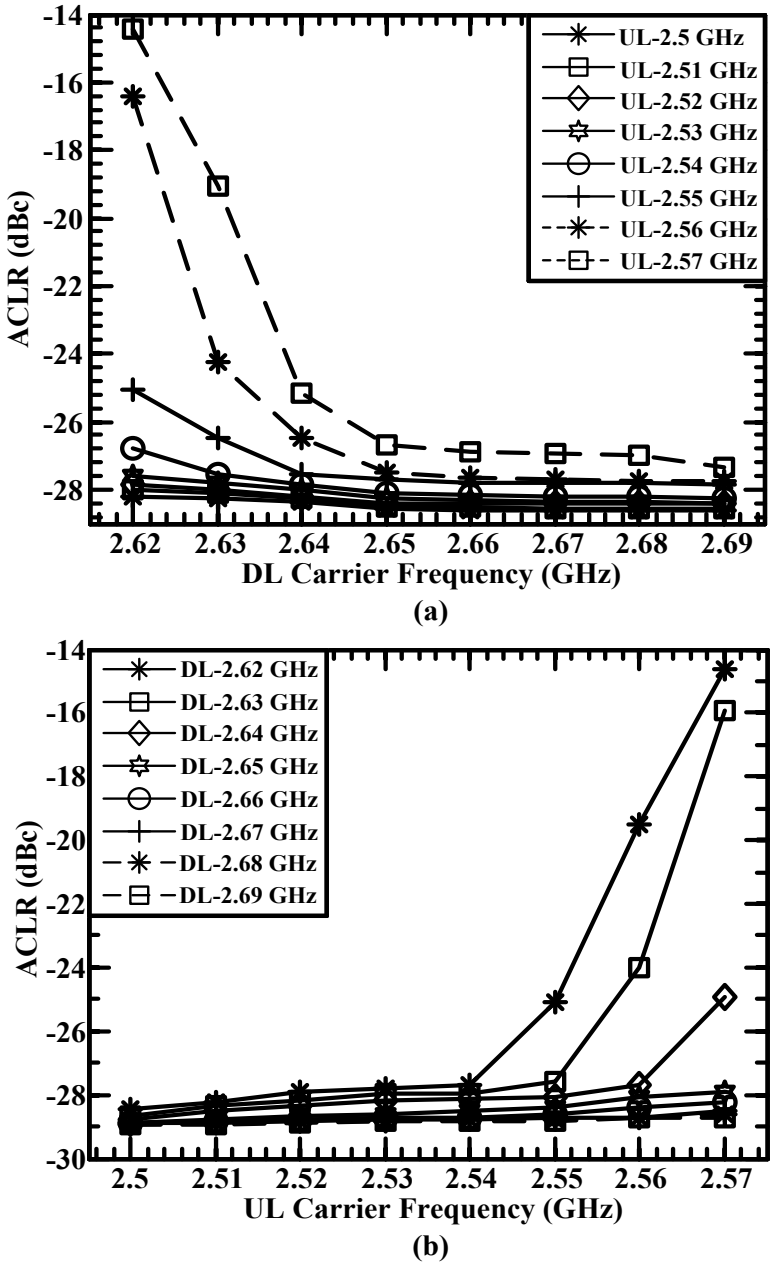

Figure 7.3: The ACLR measurement of full duplex system with (a) DL transmission and interfering UL signal and (b) UL transmission and interfering DL signal, for 64-QAM SCM

Table 7.2: DL and UL frequency spacing

DL carrier frequency	UL carrier frequency	Frequency Spacing
2.69 GHz	2.5 GHz	190 MHz (Broad)
2.69 GHz	2.57 GHz	120 MHz (Intermediate)
2.62 GHz	2.57 GHz	50 MHz (Narrow)

achieved by transmitting the DL and UL signals at 2.69 GHz and 2.5 GHz, respectively. Transmitting the DL signal at 2.69 GHz and UL signal at 2.57 GHz will result in 120 MHz frequency spacing, and will be denoted as the intermediate frequency spacing (IFS). Frequency spacing of 50 MHz would be the case for transmitting DL and UL signals at 2.62 GHz and 2.57 GHz, respectively, which is termed as the narrow frequency spacing (NFS). The details of carrier frequencies and the frequency spacing are shown in Table 7.2.

In Figure 7.3(a), transmitting DL signal at 2.69 GHz with the interfering UL signal at 2.5 GHz for BFS, the ACLR is ~-28.59 dBc. In comparison to the half duplex system ACLR of ~-28.60 dBc (Figure 7.2), the BFS transmission resulted in negligible ACLR penalty. As indicated in [155], Rayleigh backscattering increases the noise level around the signal, which should sufficiently increased the ACLR rate. However, the comparison of full duplex system to half duplex system ACLRs show that the proposed architecture effectively mitigates Rayleigh backscattering and other nonlinear effects altogether. Transmitting the DL signal at the aforementioned carrier frequency, with the UL signal at 2.57 GHz for the IFS has resulted in an ACLR of ~-27.91 dBc. Compared to the half duplex system, the full duplex system with the IFS has introduced an ACLR penalty of ~0.69 dB. Further investigation on the IFS with a shift in DL and UL carrier frequencies to 2.62 GHz and 2.5 GHz, respectively, attained an ACLR of ~-27.93 dBc. Both IFS signals resulted in a similar ACLR, thus demonstrating that the degradation of ACLR to be

Table 7.3: Frequency spacing ACLR penalty product

Frequency Spacing	ACLR Penalty- DL	ACLR Penalty- UL
50 MHz	14.16 dB	14.12 dB
120 MHz	0.69 dB	0.6 dB
190 MHz	Negligible	Negligible

frequency spacing dependent and carrier frequency independent. Transmitting at the DL carrier frequency of 2.62 GHz with UL carrier frequency of 2.57 GHz for NFS, resulted in a significantly high ACLR of ~-14.44 dBc. The ACLR penalty for the NFS compared to the half duplex system (Figure 7.2) is ~14.16 dB. It is clear that the implication of IMD with a NFS is critical. Alternative signals that propagate within this spacing would be heavily distorted due to the IMD induced spectral re-growth. The BFS (190 MHz), IFS (120 MHz) and NFS (50 MHz) frequency spacing results in negligible, ~0.69 dB and ~14.16 dB ACLR penalty, respectively, as shown in Table 7.3.

It is necessary to indicate if the ACLR of UL signal would experience similar degradation pattern, with respect to the frequency spacing. Hence, a homogeneous measurement will be carried out for the UL signal, as was performed for the DL signal. In Figure 7.3(b), the UL and DL signals are transmitted at 2 dBm transmit power. The UL signal is transmitted at 2.5 GHz with the interfering DL signal at 2.69 GHz, emerged an ACLR of ~-28.64 dBc for BFS. Comparing the resultant BFS ACLR of ~-28.64 dBc to the half duplex system with ACLR of ~-28.65 dBc (Figure 7.2) shows negligible penalty. Transmitting the UL signal at 2.57 GHz with the intercepting DL signal at 2.69 GHz for IFS, resulted in ACLR of ~-28.05 dBc. Comparatively to the half duplex system, the IFS ACLR penalty is ~0.60 dB.

For the NFS, the UL signal transmission is carried out at 2.57 GHz and DL signal at 2.62 GHz, where the resultant ACLR is ~-14.53 dBc. When compared with the half duplex system, the NFS contemplated an ACLR penalty of ~14.12 dB. The effective ACLR penalty for BFS, IFS and NFS are negligible, ~0.60 dB and ~14.12 dB, respectively, see Table 7.3. As mentioned earlier, the significant ACLR deterioration in the NFS range is due to the high IMD. The ACLRs and ACLR penalties corresponding to DL (Figure 7.3(a)) and UL (Figure 7.3(b)) systems indicate a similar degradation pattern in terms of the frequency spacing. Fundamentally, the similarity shows that the frequency spacing induced distortion is independent of the MCM schemes.

It was shown that the NFS (50 MHz) introduces a high IMD, where ACLR performance metric was adopted to measure the energy of IMD products. Focusing on the NFS, the ACLR metric is utilised to measure the impact of interfering UL and DL signals with varying RF transmit power, on the received DL and UL signals, as shown in Figure 7.4(a) and (b), respectively. The DL and UL signals are transmitted at 2.62 GHz and 2.57 GHz, respectively. For Figure 7.4(a), the DL signal is transmitted at 2 dBm, while the interfering UL signal is varied between 2 dBm and -10 dBm. The response of the interfering UL signal power variation can be observed in Figure 7.5. The RF transmit power of the UL signal in Figure 7.5(a) and (b) are 2 dBm and -10 dBm, respectively, while the DL signal is fixed at 2 dBm.

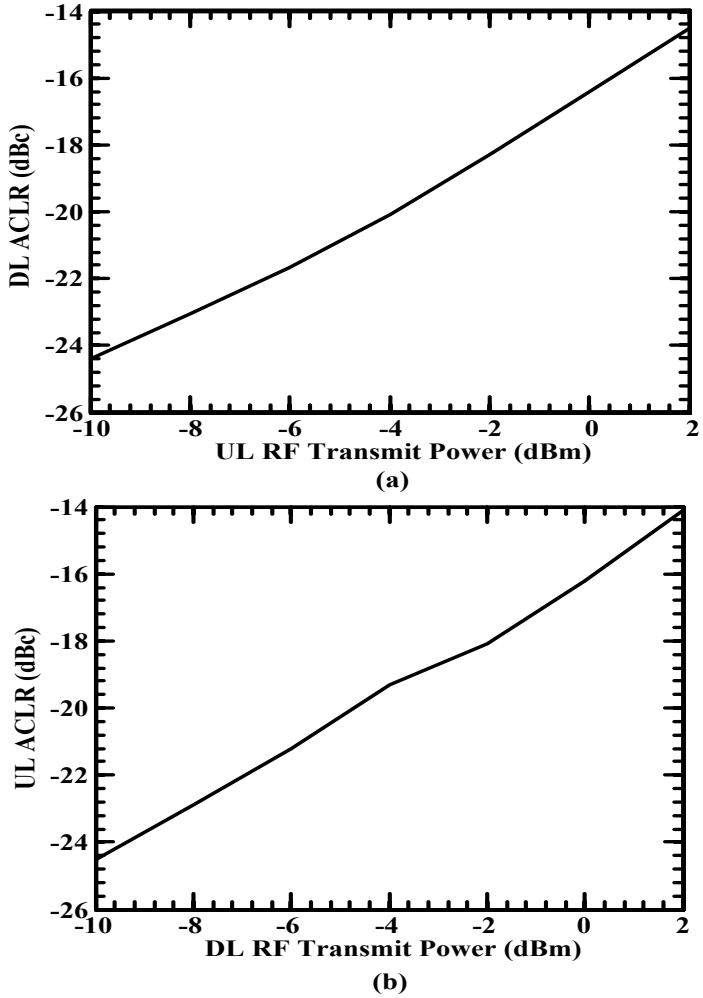

Figure 7.4: The ACLR measurement of (a) DL and (b) UL, with respect to the interfering UL and DL RF transmit power, respectively. The DL signal is transmitted at 2.62 GHz and UL signal at 2.57 GHz

From Figure 7.4(a), transmitting both DL with the interfering UL signals at 2 dBm results in an ACLR of ~-14.44 dBc. The resultant high ACLR is due to the IMD products as shown in Figure 7.5(a). When the RF transmit power of UL signal is reduced to -10 dBm, ACLR of the DL signal enhances to ~-24.41 dBc, thus showing an improvement of ~9.97 dB. The outcome of this improvement can be observed in Figure 7.5(b), which occurs relative to the suppression of IMD products. Similar investigation is carried out for the UL signal with the interfering DL signal as shown in Figure 7.4(b), where the UL and DL signals are maintained at the aforementioned frequencies.

This time around, the DL RF transmit power is varied between 2 dBm and -10 dBm, whilst UL is maintained at 2 dBm. The impact of power variation of the DL signal on the UL signal, in terms of the spectral response can be observed from Figure 7.6. The impact of varying DL transmit power of 2 dBm and -10 dBm on the UL signal is shown in Figure 7.6(a) and (b), respectively. The resultant ACLR observed in Figure 7.4(b) for UL signal is ~-14.53 dBc with the interfering DL signal transmitted at 2 dBm. This high ACLR value is due to the IMD products as shown in Figure 7.6(a). Conversely, transmitting the interfering DL signal at -10 dBm resulted in an ACLR of ~-24.53 dBc. The improvement in ACLR is associated with the IMD suppression as depicted in Figure 7.6(b). From the view point of the OBE, both DL signal (Figure 7.4(a)) and UL signal (Figure 7.4(b)) exhibits similar degradation pattern relative to the interfering signal. Additionally, it is also found that at a NFS, the subcarrier-subcarrier mixing due to photodetection is power dependent and can be mitigated with lowering the interfering signal power. However, the investigation only reveals the response of the OBE, thus the EVM measurement is vital to

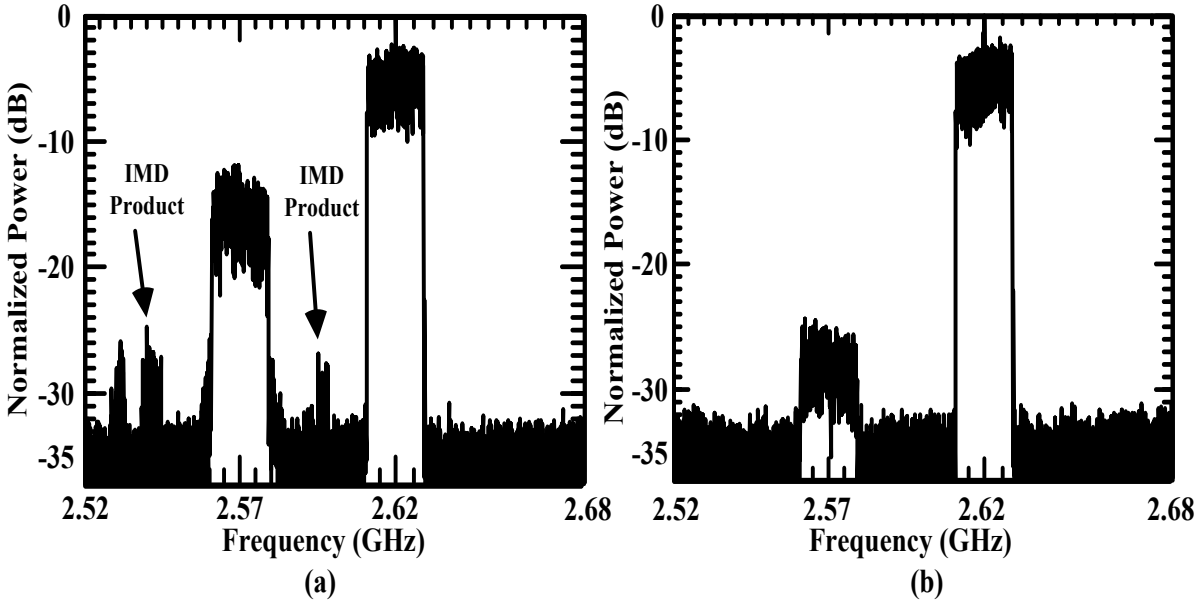

Figure 7.5: Received spectral response of DL signal at 2.62 GHz and UL signal at 2.57 GHz, with varying RF transmit power of the UL signal, (a) 2 dBm and (b) -10 dBm

further investigate the in-band distortion.

Since the EVM metric provides explicit and precise quality of the received signal compared to ACLR metric, the RF transmit power of the received and interfering signals combinations would provide an enhanced guideline on the basis of system design. Therefore, the analysis of multiple EVM combinations at a NFS of DL and UL signals, with respect to the interfering UL and DL signals are given, as shown in Figure 7.7(a) and (b), respectively. The DL signal (Figure 7.7(a)) is transmitted at 2.62 GHz, with a varying power of 2 dBm to -10 dBm, while the interfering UL signal is transmitted at 2.57 GHz with a similar range of varying power. In Figure 7.7(a), transmitting DL signal at 2 dBm, with interfering UL signal at 2 dBm and -10 dBm results in EVM of ~2.67% and ~2.26%, respectively.

At a low RF transmit power of -10 dBm for the DL signal, with an interfering UL signal at 2 dBm and -10 dBm, the observed EVMs are ~11.92% and ~11.55%,

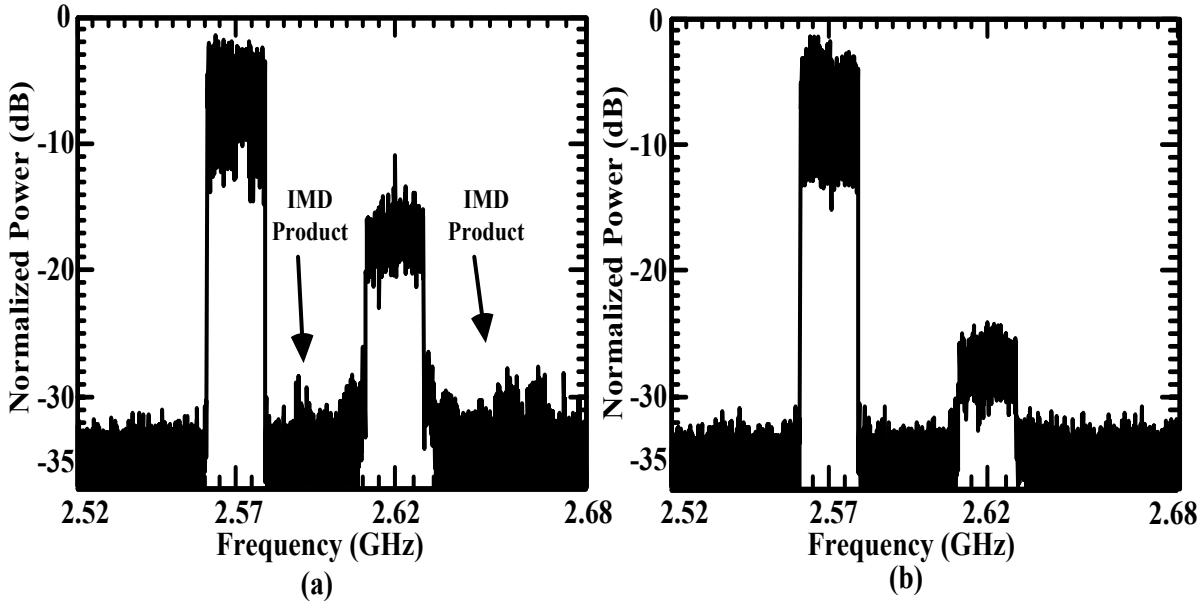

Figure 7.6: Received spectral response of UL signal at 2.57 GHz and DL signal at 2.62 GHz, with varying RF transmit power of the DL signal, (a) 2 dBm and (b) -10 dBm

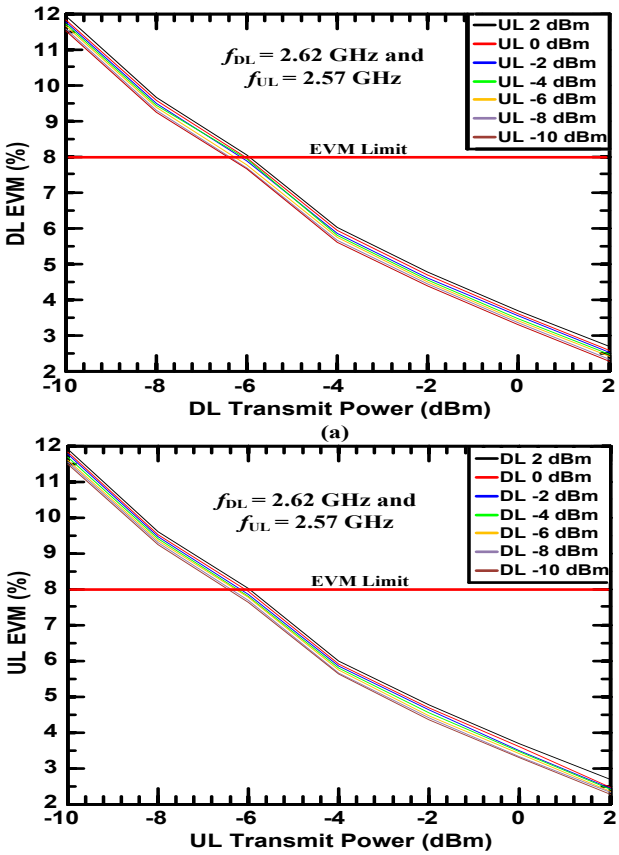

Figure 7.7: Multiple EVM combinations of (a)DL and (b)UL RF transmit power with respect to the interfering UL and DL RF transmit power, respectively

respectively. The interfering signal with a lower power transmission provides an improved EVM for the received signal, which agrees well with the results from the ACLR measurement. In addition, DL signal transmitted at less than -6 dBm would not comply within the 3GPP LTE EVM limit. Thus, it is essential that system designers maintain the RF transmit power within the boundary of higher than -6 dBm. Multiple EVM combinations presented in Figure 7.7(a) reveals that irrespective of the DL RF transmit power, the average EVM deviation is ~0.40% when the interfering UL signal is transmitted between 2 dBm and -10 dBm. The multiple EVM combinations are not presented for QPSK and 16-QAM systems, however the average EVM reductions compared to the 64-QAM system are ~0.15% and ~0.08%, respectively, at all transmission states.

Multiple EVM combinations of the UL system is carried out by measuring the UL signal as the receiving signal, with the interfering DL signal, as shown in Figure 7.7(b). The UL and DL signals are maintained at 2.57 GHz and 2.62 GHz, respectively, while the RF transmit power is varied between 2 dBm and -10 dBm for both signals. The resultant EVMs are ~2.64% and ~2.26% for a fixed UL signal at 2 dBm, while the interfering DL signal at 2 dBm and -10 dBm, respectively. For UL signal with a lower RF transmit power of -10 dBm, the EVMs observed with an interfering DL signal transmitted at 2 dBm and -10 dBm are 11.90% and ~11.47%, respectively. The EVM boundary of UL signal is to maintain the RF transmit power higher than -6 dBm, which is the same for the case of DL signal (Figure 7.7(a)). The EVM deviation is ~0.39% for UL signal at any RF transmit power, with an interfering DL signal transmitted between 2 dBm and -10 dBm, which is approximately equivalent to the EVM deviation in Figure 7.7(a). The EVM reduction for QPSK and 16-QAM of the UL signal for multiple EVM combinations is approximately equivalent to the reduction rate of the DL signal.

The results in Figure 7.7(a) and (b) comprises of a linear pattern with closely related EVMs, thus, such relationship explains that the in-band distortion induces the same impact for OFDM and SC-FDM based MCMs. The summary of EVM from Figure 7.7(a) and (b) are presented in Table 7.4.

As a summary of the overall system performance, the full duplex system of QPSK, 16-

Table 7.4: The EVM impact based on interfering signal power

Interfering signal power	**DL signal**	**UL signal**
2 dBm; -10 dBm	2 dBm: ~2.67%; ~2.26%	2 dBm: ~2.64%;~2.26%
2 dBm; -10 dBm	-10 dBm: ~11.92%; ~11.55%	-10 dBm: ~11.9%; ~11.47%

QAM and 64-QAM SCMs are analysed. The SCMs are evaluated in terms of EVM with respect to the RF transmit power. The DL and UL signals are classified as the best case transmission condition 2.69 GHz and 2.5 GHz (BFS), respectively. The worst case transmission condition is defined for a NFS, where the DL and UL signals are transmitted at 2.62 GHz and 2.57 GHz, respectively. Figure 7.8(a), (b) and (c) depict the QPSK, 16-QAM and 64-QAM, respectively, for DL and UL systems. In the QPSK SCM as shown in Figure 7.8(a), at a transmit power of 2 dBm, the best case and worst case average EVMs are ~2.30% and ~2.54%, respectively. The inset I of Figure 7.8(a) represents the constellation of QPSK at 2 dBm transmit power. The EVM is severely degraded at -10 dBm transmit power for QPSK system, where the best case and worst case transmission conditions resulted in ~11.09% and ~11.43%, respectively. The inset II shows the heavily distorted QPSK constellation at -10 dBm. Since the EVM for -10 dBm is very much higher than the LTE limit, transmission at this power is not advisable. Such profound distortion occurs at -10 dBm is due to the weak OMI. The lowest transmission power that could achieve EVM below 8% is -6 dBm, which is consistent with finding discussed earlier. Therefore, discussion on -10 dBm RF transmit power would not be carried out further for the subsequent modulations.

Similar degradation pattern of QPSK can be observed for 16-QAM and 64-QAM of Figure 7.8(b) and (c), respectively. At 2 dBm transmit power, the EVMs of best case and worst case transmission conditions for 16-QAM (Figure 7.8(b)) are ~2.33% and ~2.61%, respectively. The corresponding constellation diagram for 2 dBm transmit power can be observed in inset I. In 64-QAM SCM (Figure 7.8(c)), the best case and worst case EVMs are ~2.39% and ~2.64%, respectively, while the constellation diagram can be observed in inset I. The overall system achieves EVM below 8% with a transmit power as low as -6 dBm.

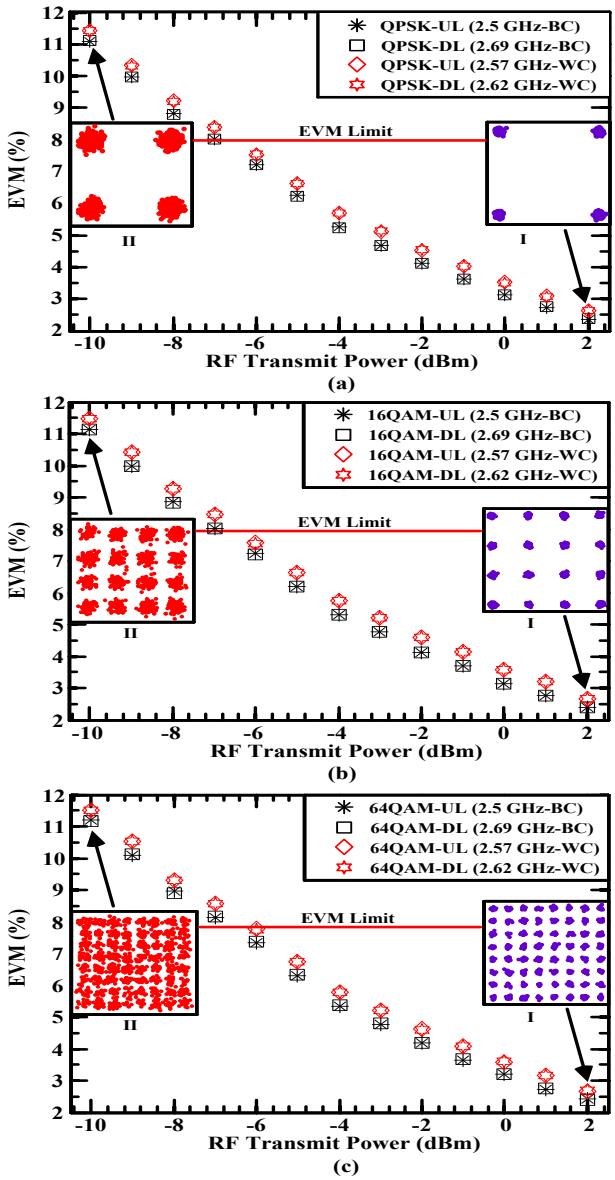

Figure 7.8: EVM against RF transmit power for BC and WC transmission condition of (a) QPSK, (b) 16-QAM and (c) 64-QAM

7.2 Summary

The contribution of this chapter was the seamless integration of the full duplex FDD LTE technology with the 10 km RoF system. The RoF system was designed based on dedicated DMLs for DL and UL systems, with DWDM wavelength spacing and single SMF. The ACLR comparison between half duplex and full duplex system for BFS (190

MHz) transmission revealed that the system to be Rayleigh backscattering and optical interference free.

The DL system with BFS (190 MHz), IFS (120 MHz) and NFS (50 MHz) resulted in negligible, 0.69 dB, and 14.10 dB ACLR penalties, respectively. In the UL system, the aforementioned frequency spacing achieved a close proximity to DL system for the ACLR penalties. The BFS and IFS frequency spacing experienced negligible IMD products. However, the NFS introduced severe IMD products from subcarrier-subcarrier mixing due to the photodetection. Further studies on the interfering signal power was carried out with the aid of ACLR and EVM, where it was found that the subcarrier-subcarrier mixing effect is power dependent. In addition, the multiple EVM combinations are provided for the DL and UL signals with interfering UL and DL signals, respectively, within the range of 2 dBm to -10 dBm RF transmit powers. Investigation showed that, irrespective of RF transmit power for the DL and UL signals, the average EVM deviation is ~0.40% for the interfering UL and DL signals, respectively, within the maximum (2 dBm) and minimum (-10 dBm) RF transmit power.

Finally, the full duplex system reports that the best case transmission condition for QPSK, 16-QAM, and 64-QAM systems achieved the average EVMs of ~2.30%, ~2.33%, and ~2.39%, respectively, at 2 dBm transmit power. In this chapter, the proposed architecture was launched into the intermixing region, due to the deteriorating characteristic of nonlinear propagation region, as shown in the previous chapters. Hence, the next chapter will be dedicated to solve the nonlinear propagation problem, to provide higher power budget for long span transmission.

CHAPTER 8 NONLINEAR COMPENSATION OF LTE ROF LINK

As of the previous chapters, the integration of half duplex LTE and LTE-A with RoF were successfully carried out for eNB cell extension. For the case of LTE technology, the LTE RoF link was further upgraded to accommodate MIMO transmission by utilising FDM over OFDM technique. Additionally, DWDM based full duplex LTE RoF architecture was demonstrated as well. Both the MIMO and full duplex LTE RoF transmissions were launched in the intermixing region, to effectively reduce the linear and nonlinear distortions.

The OLP ranging from ~-2 dBm to ~2 dBm (intermixing region) exhibits minimum system penalty, also known as the optimum OLP range. The proposed LTE-RoF system experiences degradation in the QoS for OLP of less than -2 dBm, and more detrimental for OLP of greater than 2 dBm. At OLP of less than -2 dBm, also known as the linear region, the QoS could be easily improved by including an optical amplifier. However, for OLP of more than 2 dBm (the nonlinear region), the system will initiate a nonlinear propagation state. Considering the LTE signal power required following the photodetection in the RN for UE, it is important for LTE RoF system to operate in the nonlinear region to satisfy the link power budget. Therefore this chapter focuses on the nonlinear compensation of LTE RoF system to provide a higher power budget in the RN for UE transmission.

As explained in Chapter 2, the well known optical fibre nonlinearities are the Kerr effects and the scattering phenomena. SPM, XPM, and FWM are known as the Kerr effects. In terms of the scattering phenomena, the widely known effects are the SBS and the SRS. Since the LTE RoF system throughout this thesis operates based on a single wavelength in the C-band, transmitted through a SMF, XPM, FWM and SRS are clearly negligible [76, 159]. Therefore, the nonlinear region is only SPM and SBS dependent. The SPM phenomenon induces nonlinear phase distortion based on the characteristic of

negative chirping. In other word, SPM exhibits red shifted rising edge and blue shifted trailing edge resulting in signal compression. However, in this chapter, the aim is to provide a higher power budget, which requires higher OLP, hence SBS phenomenon becomes a dominant factor compared to SPM, with a narrow linewidth and incidentally forms a grating that produces a high back-reflecting power [160].

The SBS affect arises due to the light interaction with the acoustic phonons, which effectively forms a grating and known as the most dominant optical fibre nonlinearity [161]. An incident light (optical beam) with intensity above the SBS threshold effectively interferes with the scattered back-reflecting beam, and concurrently give rise to density and pressure variations, which modulates the refractive index. It is also important to note that the back-reflecting beam is Stokes-shifted. The OLP threshold for SBS is well above the Rayleigh scattering OLP level [153]. There are two important factors that could increase the SBS threshold as the compensating agents, namely the effective area of optical fibre A_e and the linewidth $\Delta\nu_L$ of the incident beam measured at full-width half-maximum (FWHM). This hypothesis can be proven with the aid of the following closed form expression for SBS threshold [161]:

$$P_{th}^{SBS} = \frac{21\alpha A_e}{(1-e^{-\alpha L})g_B}\left(\frac{\Delta\nu_B \otimes \Delta\nu_L}{\Delta\nu_B}\right) \tag{8.1}$$

where α is the optical fibre attenuation, L is the transmission span, g_B is the SBS gain, and $\Delta\nu_B$ is the SBS linewidth. It is clear from equation (8.1) that increasing the effective area of optical fibre or the laser linewidth will proportionally increase the SBS threshold.

Additionally, there are also alternative methods of compensating SBS. Downie *et al* [160] introduced a co-propagating signal in a WDM system to induce XPM as the compensating agent for SBS, with the inherent PM. Though this method suffices for SBS

mitigation, it is only applicable for WDM system. Sisto *et al* [162] introduced an optimisation method for a modulator biasing to control OLP, which in turn reduces the SBS effect. However, the biasing optimisation adds on to the system complexity and to the inherent system noise floor due to higher requirement of optical amplification. Sauer *et al* [163] utilised an enhanced SBS threshold optical fibre, which is designed with a bigger effective area to compensate for SBS, which was analytically shown in equation (8.1). Enhanced SBS threshold optical fibre is not applicable for LTE RoF system, because the whole idea of the proposed cross platform integration is based on the existing legacy SMF backhaul to maintain a lower deployment cost.

8.1 Direct Modulation Based Frequency Dithering

Considering the proposed single wavelength based LTE RoF system, with minimum complexity and using the existing SMF infrastructure. For the first time, this chapter proposes the usage of DMFD method for SBS mitigation in a RoF system, and further identifying the SPM and the SBS threshold levels for LTE RoF system. The author have submitted the findings of this chapter to [164] and [165], which were accepted for publications, and [166] currently under review. The DMFD method successfully compensates SBS by broadening the linewidth of a laser, which will be greater than the SBS linewidth and effectively blocking the grating formation induced by acoustic phonons, thus reducing the back-reflected power. Frequency dithering was initially proposed for baseband optical applications [43, 44], where the condition of dithering frequency f_d has to be bigger than twice the highest signal frequency f_m, $\{f_d > 2f_m\}$. The condition of dithering frequency in RoF systems is substantially different compared to the baseband system, where dithering frequency for DMFD method in RoF systems have to be much smaller than the carrier frequency f_{RF}, $\{f_d << f_{RF}\}$. Further discussion on this claim

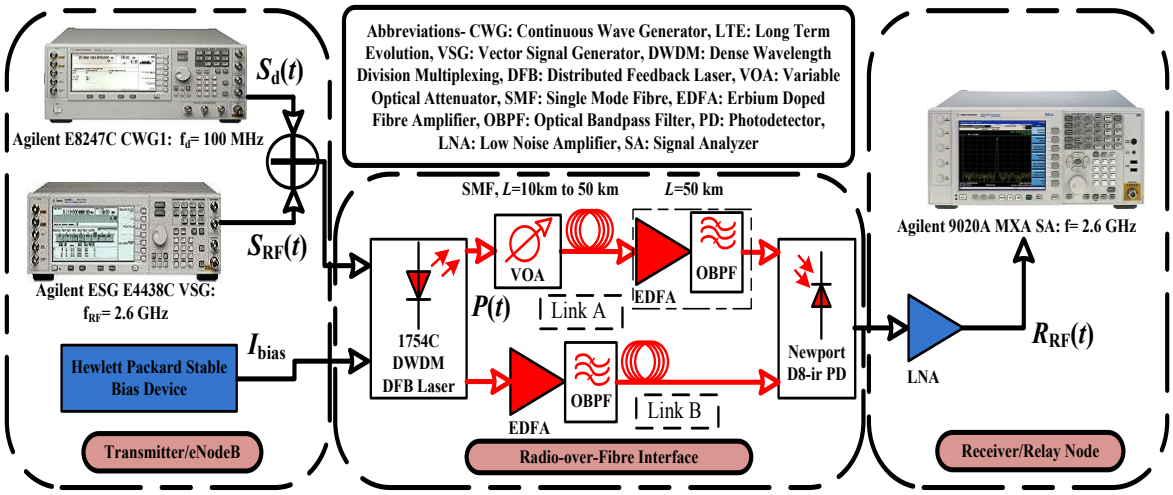

Figure 8.1: Experimental setup of LTE RoF system for SBS mitigation utilising DMFD method

will be carried out in the later section.

The DMFD method is primarily introduced to compensate the severe distortion in the nonlinear region. As it was indicated in the previous chapters, the linear region is PFC and CD dependent. The optimum OLP region depends on the intermixing of linear and nonlinear regions. Since DMFD method intentionally introduces additional frequency chirp, part of the finding in this chapter will be whether DMFD further deteriorates the linear and optimum OLP regions.

8.2 Link Configurations

The experimental setup of LTE-RoF system with DMFD method for SBS mitigation is presented in Figure 8.1 along with the system parameters provided in Table 8.1.

The VSG, Agilent ESG E4438C is utilised for LTE signal generation. The SCMs in the baseband domain are composed of QPSK, 16-QAM and 64-QAM schemes. The SCMs are modulated onto OFDM scheme with occupied subcarriers of 1200 and FFT size of 2048. Subsequently, the OFDM modulated signals are appended with a CP size at the rate of ¼, which resulted in an ARB of 20 MHz. The baseband OFDM modulated signals are up-

Table 8.1: System Parameters

Parameters	Values
Dithering signal frequency and power	100 MHz and 2 dBm
SCM modulations	QPSK, 16-QAM, and 64-QAM
Bit rate	33 Mb/s, 66 Mb/s, and 100 Mb/s
Baseband multiplexing	OFDM
Signal bandwidth	20 MHz
Carrier frequency	2.6 GHz
Signal power	2 dBm
DFB bias current	60 mA
Optical launch power	-8 dBm to 10 dBm
Linewidth	11.4 MHz
SMF length	10 km to 50 km
EDFA- gain, NF	4 dB , 3.5 dB
PD responsivity	0.42
LNA- gain, NF	18 dB to 24 dB, 2.5 dB

converted to the passband signals $\boldsymbol{S}_{RF}(t)$ at the (RF) f_{RF} of 2.6 GHz.

The DFB used in this work is intentionally dithered or frequency chirped with a DMFD signal $S_d(t)$ to broaden the linewidth of the laser. The dithering frequency only effectively dithers the DFB laser at the condition of $\{f_d << f_{RF}\}$ as specified earlier. If the dithering frequency is bigger than the LTE signal frequency $\{f_d > f_{RF}\}$, then it will not generate the dithering phenomenon due to the existing 2nd order harmonics in that frequency region. In other word, DFB laser have already experienced frequency chirping from the modulation of LTE signal and its 2nd order harmonics altogether. Therefore, if dithering frequency is above the LTE signal frequency, it does not induce any additional chirping. This is because the optical PM coupled with the frequency chirping has already occurred in the vicinity of LTE signal and its 2nd order harmonics.

However, the dithering frequency does not display similar characteristic for the baseband system, because the baseband signal itself will be centered or close to DC. Therefore dithering frequency has to be much higher than the baseband signal frequency, which has been defined as twice higher in [43, 44]. Thus, in our work, DMFD signal is generated at the dithering frequency of 100 MHz as a sinusoidal signal from a CWG, Agilent E8247C, which maintains the $\{f_d << f_{RF}\}$ condition.

The LTE and DMFD signals are then combined to directly modulate the DFB laser. Owing to the bipolar nature of the electrical signal, a sufficient amount of bias current I_{bias} is coupled with the combined signals, to form a unipolar signals prior to the modulation of 1754C DWDM DFB laser. The DM of the unipolar signals is carried out by the DFB laser at the operating wavelength of 1551.11 nm.

The linewidth broadening of the DFB laser with DMFD signal can be described from the Van-der-Pol model of laser noise [167]:

$$\begin{aligned} \Delta\phi(t)^2 &= \frac{\zeta(1+LW^2)(t)}{2n_{np}\tau_p} \\ &= \frac{2}{\tau_{coh}(t)} \end{aligned} \tag{8.2}$$

where ζ represents the fraction of spontaneous emission, LW is the linewidth enhancement factor, n_{np} is the number of photons in the laser resonator, τ_p is the photon lifetime, and τ_{coh} is the coherence time of the laser which is inversely related to the FWHM of the DFB laser linewidth by:

$$\Delta\nu_L(t) = \frac{2}{\tau_{coh}(t)} \tag{8.3}$$

The effect DMFD signal is approximately equivalent of producing multiple random spontaneous emission events, which leads to a Wiener process to the phase of the DFB laser [168].

$$\Delta S_{\mathrm{d}}(t)^2 = \frac{2}{\tau_{\mathrm{cohd}}(t)} \tag{8.4}$$

where τ_{cohd} is the coherence time of the DMFD signal. The original coherence time of the DFB laser was τ_{coh}, but by applying the random PM with DMFD signal, the new reduced effective coherence time of the laser at the FWHM is:

$$\frac{1}{T_{\mathrm{coh}}} = \frac{1}{\tau_{\mathrm{coh}}} + \frac{1}{\tau_{\mathrm{cohd}}} \tag{8.5}$$

where the reduced coherence time is equivalent to a broaden linewidth. From equation (8.5), it is clear that the dithered optical signal propagates along the SMF with a broader linewidth and capable of blocking the formation of SBS grating, hence, reducing back-reflected power.

In order to investigate the impact of DMFD method in the linear region, the optimum OLP, and nonlinear regions, the undithered and dithered optical signals are varied between the OLP of -8 to 10 dBm. The lower values of the optical signals are achieved via the Link A of Figure 8.1, which consists of a VOA. The EDFA and the OBPF in the Link A are only utilised for the link span of 50 km and above to compensate for the SMF loss as the PD responsivity is low. The Link B is utilised for higher OLP analysis and performed via EDFA with OBPF.

In this chapter, SMF is utilised as the transmission medium, ranging from 10, 25, 35 and 50 km. After propagating through the varying SMFs, the signal is detected via the Newport D8-ir PD with the DD scheme. Following photodetection, the received RF LTE signal $\boldsymbol{R}_{\mathrm{RF}}$ is passed through a LNA for amplification of the output of which is demodulated via the SA, Agilent 9020A MXA.

8.2.1 Results on the Nonlinear Compensation

In order to analyse the effect of DMFD on the linewidth of the laser, a high resolution OSA was placed after the DFB laser for spectral measurement. Figure 8.2 illustrates the actual LTE RoF signal in the undithered condition (black curve), where the optical carrier is centred at ~193.279 THz and the optically modulated LTE signal is shown as the double sideband modulated at ~193.276 THz and ~193.281 THz. The optical spectrum was captured using the BOSA 200 high resolution OSA by Aragon Photonics. The undithered (DMFD signal off) optical spectral at the output of DFB resulted in a linewidth (FWHM) of ~11.14 MHz. Since SBS linewidth is typically around ~30 MHz [169], most propagating signals are back-reflected due to the formation of grating, arising from the interaction of propagating optical signal with the acoustic phonons.

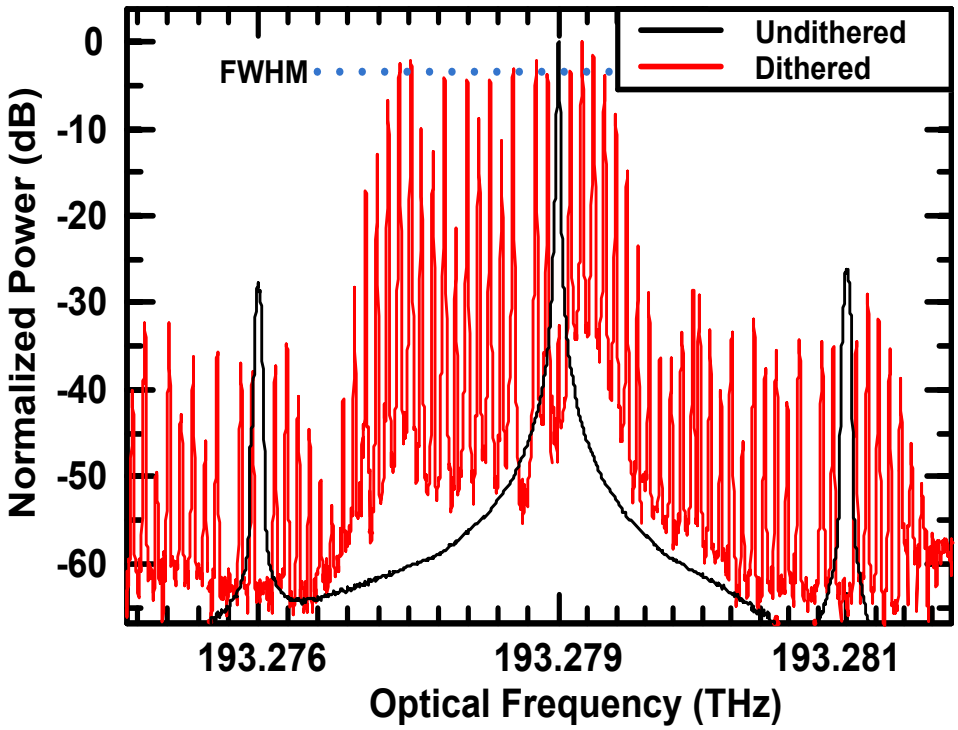

Figure 8.2: Optical spectral of the LTE RoF undithered and dithered signals with narrow and broad linewidth, respectively

The response of the combination of DMFD and LTE signals can be observed in Figure 8.2 (red curve). The dithered (DMFD signal on) output of the DFB shows an optical comb like signal formed by multiple peaks with an FWHM of ~37.47 MHz. Multiple peaks from the combination of DMFD and LTE signals phenomena arises due to nonlinear mixing of the optical carrier, DMFD and LTE signals. The effect of the linewidth broadening and the exploitation of frequency dithering, which achieved a linewidth of ~37.47 MHz can be observed in the electrical spectrum of the SA, see Figure 8.3. Figure 8.3(a) exhibits a

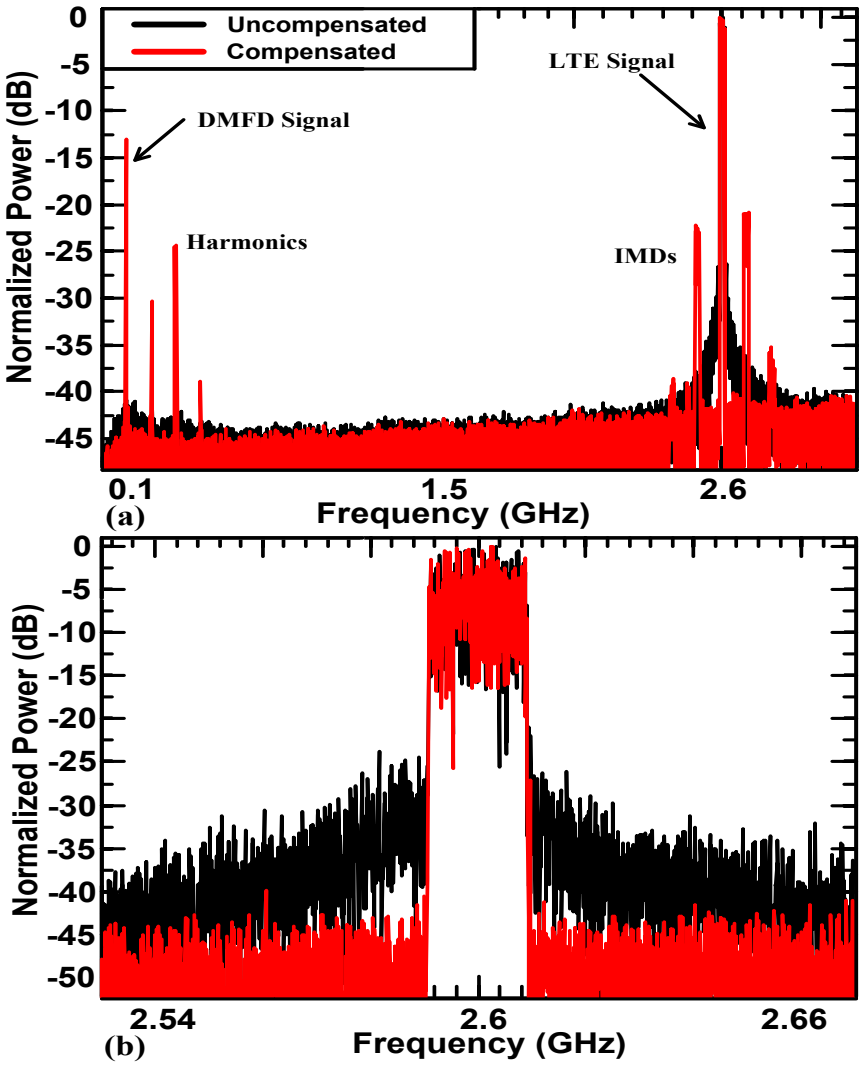

Figure 8.3: Electrical spectrum of the received signal without and with SBS compensation (dithering), (a) spectrum of DMFD and LTE signals, and (b) enhanced view of LTE signal

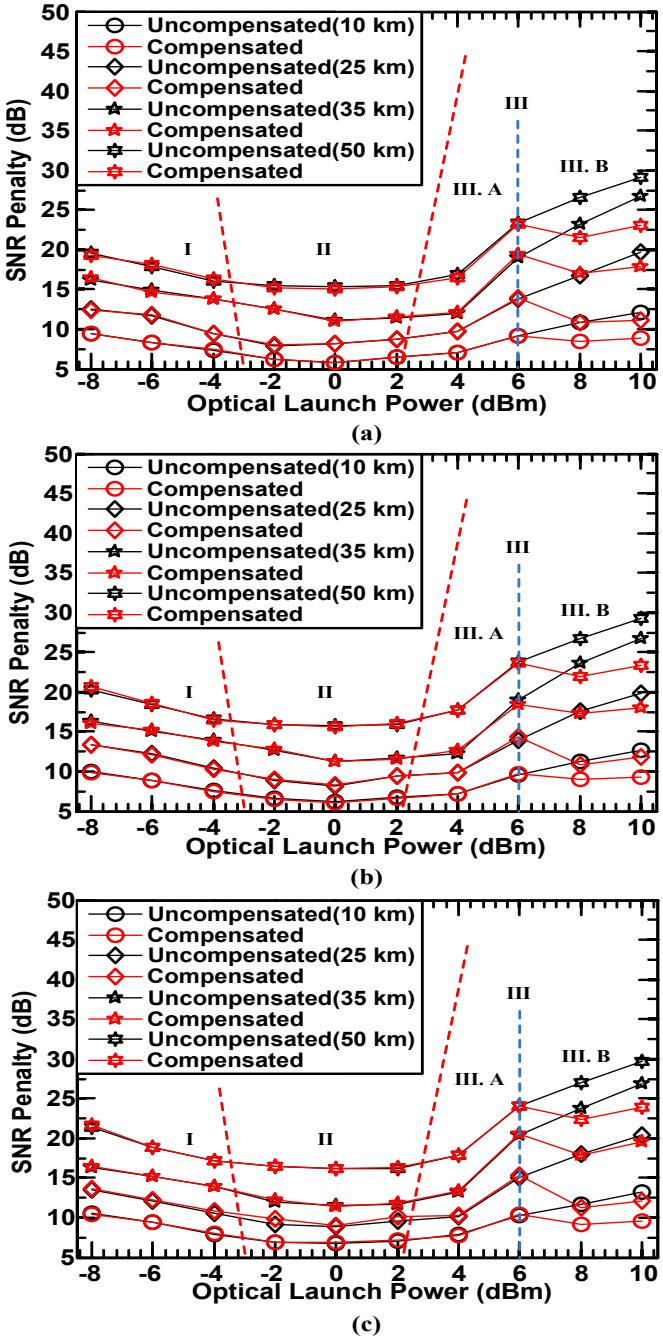

Figure 8.4: OLP against SNR penalty for SBS compensation in (a) QPSK, (b) 16-QAM, and (c) 64-QAM with transmission spans of 10 km to 50 km

decrease in the noise floor surrounding the vicinity of DMFD and LTE signals, with the DMFD method. The harmonics and IMD products associated with DMFD method can be easily filtered at RN prior to UE transmission. Focusing on the LTE signal, Figure 8.3(b) clearly shows the effectiveness of DMFD method on reducing the OBE.

Figure 8.4(a), (b), and (c) depict the OLP against SNR penalty for QPSK, 16-QAM and 64-QAM systems, respectively, for uncompensated transmission spans of 10, 25, 35 and

50 km, as well as the SBS compensated links. There are three major distinctive regions shown in Figure 8.4, namely I) linear region- PFC and CD induced distortion, II) intermixing region- reduced distortion achieved by the interaction between CD and PFC with SPM and SBS, and finally III) nonlinear region- nonlinearity based distortion from SPM and SBS effects.

It is clear from Figure 8.4 that the DMFD method only effectively compensates for SBS in the region III.B, where SBS is dominant above the OLP of ~6 dBm (the SBS threshold). The region III.A does not experience any effect from DMFD method, because it is solely dominated by SPM. In other word, OLP of ~2 dBm to ~6 dBm induces nonlinearity in the form of nonlinear PM, but with no scattering or back-reflecting power. The impairment introduced by SPM can be compensated by adopting digital back-propagation scheme [170, 171]. The operating characteristic of the digital back-propagation is basically emulating the propagation in optical fibre to reverse the

Table 8.2: Uncompensated and compensated SNR penalties at 8 dBm and 10 dBm OLPs

OLP	Modulation schemes	Uncompensated SNR penalties	Compensated SNR penalties	SNR penalties improvement
8 dBm	QPSK	10 km: ~10.83 dB	10 km: ~8.5 dB	10 km: ~2.33 dB
		50 km: ~26.55 dB	50 km: ~21.51 dB	60 km: ~5.04 dB
	16-QAM	10 km: ~11.2 dB	10 km: ~8.95 dB	10 km: ~2.25 dB
		50 km: ~26.29 dB	50 km: ~21.9 dB	60 km: ~4.39 dB
	64-QAM	10 km: ~11.7 dB	10 km: ~9.2 dB	10 km: ~2.5 dB
		50 km: ~26.99 dB	50 km: ~22.4 dB	60 km: ~4.59 dB
10 dBm	QPSK	10 km: ~12.1 dB	10 km: ~8.9 dB	10 km: ~3.2 dB
		50 km: ~29.14 dB	50 km: ~23.1 dB	60 km: ~6.04 dB
	16-QAM	10 km: ~12.7 dB	10 km: ~9.39 dB	10 km: ~3.31 dB
		50 km: ~29.32 dB	50 km: ~23.3 dB	60 km: ~6.02 dB
	64-QAM	10 km: ~13.2 dB	10 km: ~9.65 dB	10 km: ~3.55 dB
		50 km: ~29.67 dB	50 km: ~23.88 dB	60 km: ~5.79 dB

impairment effect. It is a type of nonlinear equalizer that is utilised at the receiver to compensate the nonlinearities. However, since the RN is aimed to operate based on AF scheme, the digital back-propagation scheme is not ideal for the proposed system. Therefore, the LTE signal propagation at OLP of between ~2 dBm and ~6 dBm should be avoided to minimise complexity.

Figure 8.4 depicts that the introduction of DMFD method does not alter the LTE RoF

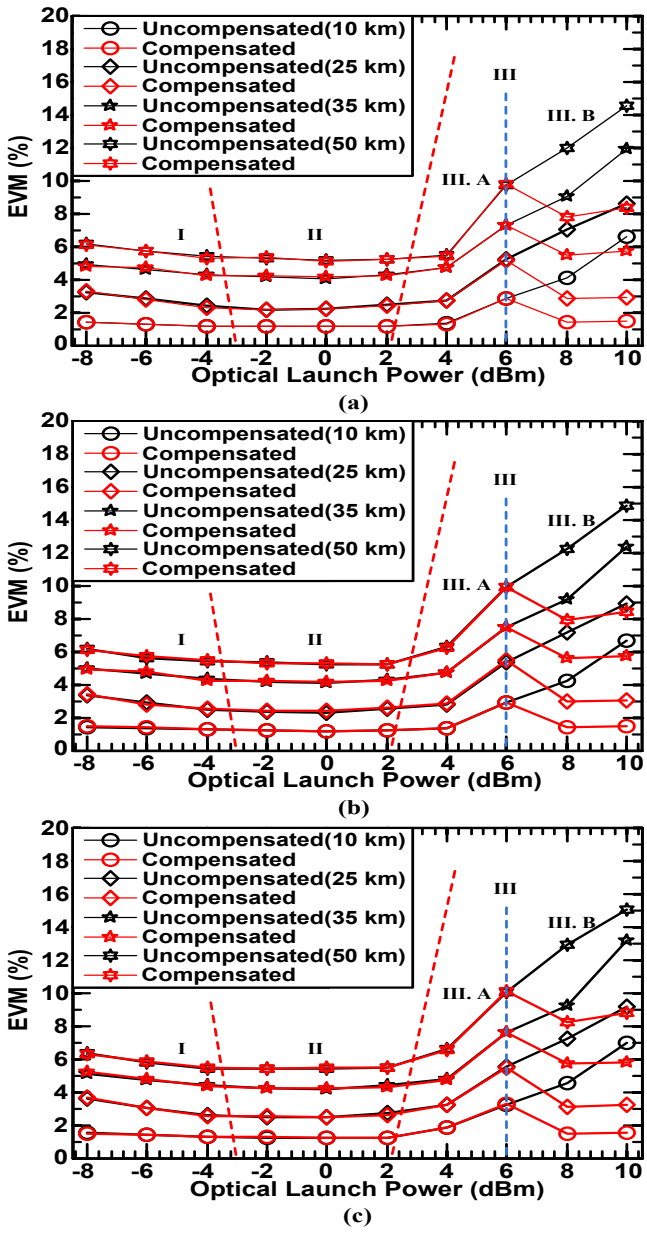

Figure 8.5: OLP against EVM for SBS compensation in (a) QPSK, (b) 16-QAM, and (c) 64-QAM with transmission span of 10 km to 50 km

response for regions I and II. Despite the fact that DMFD method broadens the linewidth of the DFB laser, it does not exhibit a linewidth in the range of a Fabry-Perot laser. A typical Fabry-Perot laser will exhibit linewidth characteristic in the range of ~150 MHz [172], however the DFB laser with DMFD only has a linewidth of ~37.47 MHz, hence regions I and II remains more or less unchanged.

The discussion in Figure 8.4 is focused on the OLP of 8 dBm and 10 dBm within region III.B due to the effectiveness of DMFD method in this range. Furthermore, 10 and 50 km transmission spans are contemplated as the best and worst case scenarios, respectively. At OLP of 8 dBm in Figure 8.4(a), (b), and (c) for QPSK, 16-QAM and 64-QAM, the system improvements observed for the 10 km span are ~2.33 dB, ~2.25 dB and ~2.5 dB, respectively, while the 50 km span experiences improvements of ~5.04 dB, ~4.39 dB and ~4.59 dB, respectively. The detailed measurements are presented in Table 8.2. The improvement of 50 km span is higher than the 10 km span evidently showing the system deterioration is critical due to SBS particularly for higher transmission spans. In terms of 10 dBm of OLP, the improvements for QPSK, 16-QAM and 64-QAM at a 10 km span are ~3.2 dB, ~3.31 dB, and ~3.55 dB, respectively, while at 50 km the improvements are ~6.04 dB, ~6.02 dB, and ~5.79 dB, respectively. The improvement at OLP of 10 dBm is superior to 8 dBm, outlining the linear increase of back-reflecting power with OLP. The system transmission span is limited to 50 km, and anything beyond this limit fails to meet the required EVM and will be discussed in detail with reference to Figure 8.5.

As the SNR penalty only unveils the system impact in terms of the OBE, it is very vital to analyse the in-band distortion by utilising EVM to understand the explicit system QoS. Figure 8.5(a), (b) and (c) illustrate the EVM of QPSK, 16-QAM and 64-QAM systems, respectively. We aim to achieve an EVM of 8% in the system design according to the LTE requirement [134]. The categorization of regions and impact of DMFD in regions I and II in Figure 8.5 is similar to Figure 8.4. Focusing on the region III. B, at 8 dBm of OLP, the EVM improvement associated with QPSK, 16-QAM and 64-QAM for a 10 km span are ~2.67%, ~2.78% and ~3.04%, respectively, while the improvements for a 50 km span are ~4.2%, ~4.35% and ~4.68%, respectively. The improvement observed for 50 km are much higher compared to 10 km, which correlates to the pattern observed in the SNR penalty analysis. At a 10 km span, the EVM improvements of QPSK, 16-QAM and 64-QAM for 10 dBm of OLP are ~5.11%, ~5.16% and ~5.44%, respectively, while the 50 km span exhibits an EVM improvement of ~6.2%, ~6.46% and ~6.21%, respectively. The complete

Table 8.3: Uncompensated and compensated EVM at 8 dBm and 10 dBm OLPs

OLP	Modulation schemes	Uncompensated EVM	Compensated EVM	EVM improvement
8 dBm	QPSK	10 km: ~4.093%	10 km: ~1.42%	10 km: ~2.67%
		50 km: ~11.99%	50 km: ~7.79%	60 km: ~4.2%
	16-QAM	10 km: ~4.22%	10 km: ~1.435%	10 km: ~2.78%
		50 km: ~12.23%	50 km: ~7.88%	60 km: ~4.35%
	64-QAM	10 km: ~4.52%	10 km: ~1.48%	10 km: ~3.04%
		50 km: ~12.88%	50 km: ~8.2%	60 km: ~4.68%
10 dBm	QPSK	10 km: ~6.57%	10 km: ~1.46%	10 km: ~5.11%
		50 km: ~14.53%	50 km: ~8.33%	60 km: ~6.2%
	16-QAM	10 km: ~6.65%	10 km: ~1.49%	10 km: ~5.16%
		50 km: ~14.87%	50 km: ~8.41%	60 km: ~6.46%
	64-QAM	10 km: ~6.97%	10 km: ~1.53%	10 km: ~5.44%
		50 km: ~15.02%	50 km: ~8.81%	60 km: ~6.21%

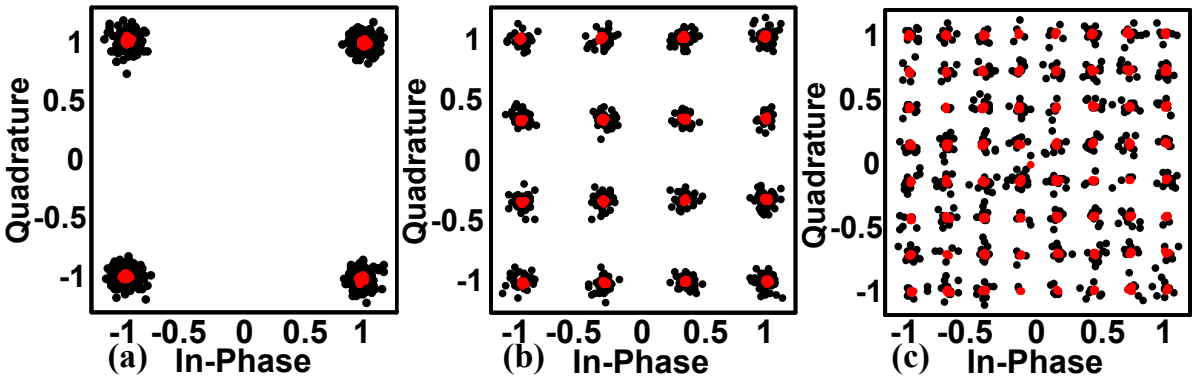

Figure 8.6: Uncompensated (black) and compensated (red) constellation diagrams of (a) QPSK, (b) 16-QAM, and (c) 64-QAM

EVM data can be observed in Table 8.3. The physical improvement of QPSK, 16-QAM and 64-QAM EVM can be observed from Figure 8.6(a), (b) and (c), respectively, which represents the uncompensated and compensated constellation diagrams.

For the 50 km transmission system, the average EVM across all modulation schemes at OLPs of 8 dBm and 10 dBm are ~7.95% and ~8.51%, respectively. The average EVM shows that only OLP of 8 dBm achieved below 8%, hence revealing that the 50 km transmission span is the limit of DMFD method in LTE RoF system.

8.2.2 Optimisation of DMFD Signal

The application of DMFD method in the LTE RoF system for SBS compensation was successfully demonstrated in the previous section. The DFMD signal was fixed at 100 MHz with the condition of $\{f_d << f_{RF}\}$, and with 2 dBm RF power. In order to further investigate on the DMFD signal, this section will carry out the optimisation of DMFD method. The optimisation will be in the perspective of varying frequency and RF power of DMFD signal, and its relative impact on the QPSK-OFDM LTE signal transmitted at 2.6 GHz. The OLP is fixed at 10 dBm throughout this investigation. Figure 8.7 presents the optimisation of DMFD signal, and the corresponding EVM response for LTE signal. In the

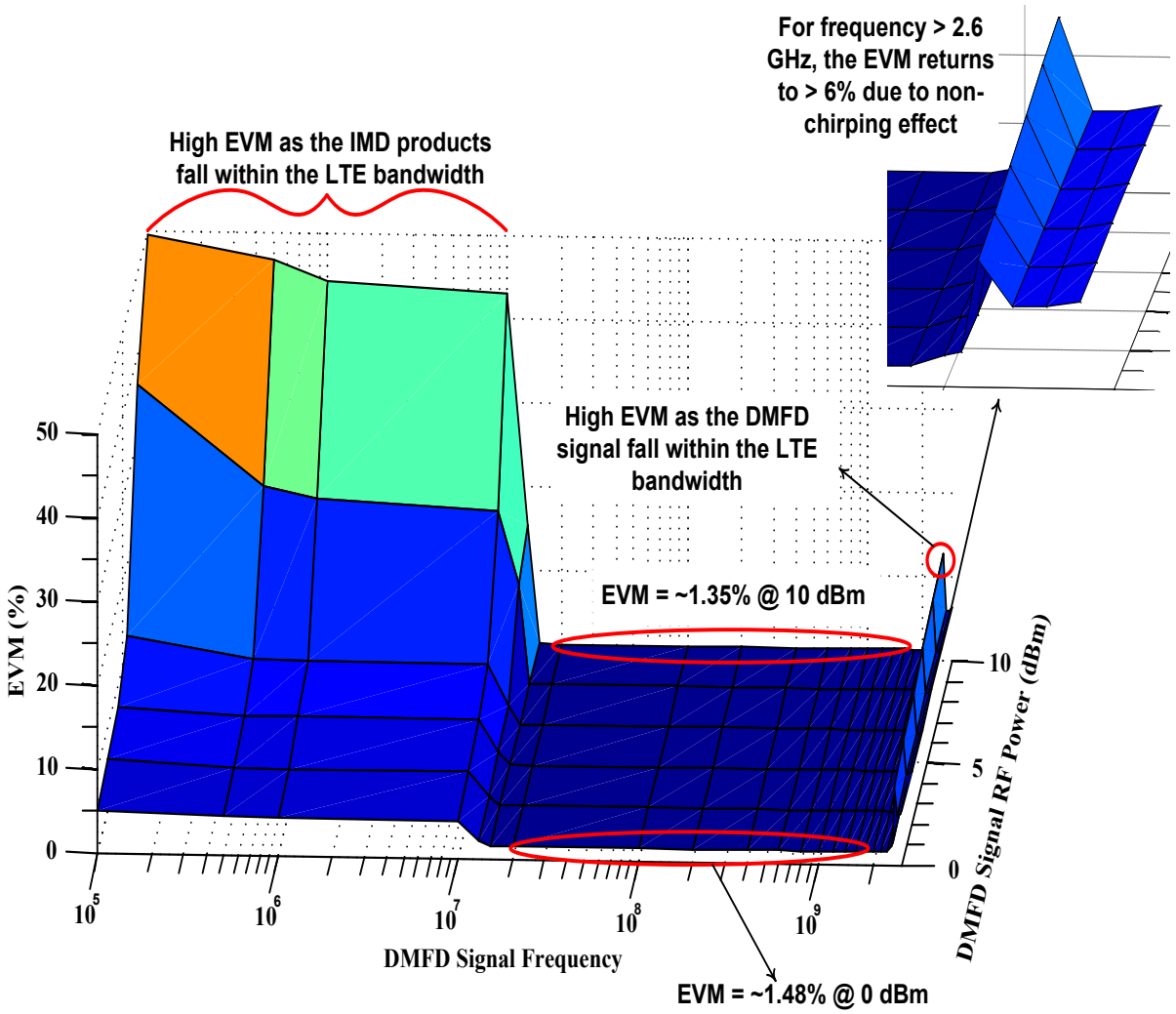

Figure 8.7: Optimization of DMFD signal frequency and RF power, and its relative impact on the QPSK-OFDM LTE signal

x-axis of Figure 8.7 is the varying frequency of DMFD signal with RF power in the y-axis, and the response of the variation is shown in z-axis as the LTE signal EVM.

In Figure 8.7, launching the DMFD signal between 100 kHz and 14 MHz significantly increases the EVM rate. At 0 dBm RF power and 100 kHz DMFD signal frequency increases the EVM rate to ~4.98%, while increasing the power to 10 dBm resulted in EVM of ~49.4%. The result from Table 8.3 indicates that the uncompensated EVM at OLP of 10 dBm was ~6.57%. Transmitting the DMFD signal at 100 kHz does compensate the SBS, but with least effectiveness. This is because, the IMD product arising from the mixing of

DMFD signal at 100 kHz and LTE signal at 2.6 GHz falls within the 20 MHz bandwidth of LTE signal. The higher RF power of 10 dBm further distorts the LTE signal due to the increasing power of the IMD product.

It is clear that as the DMFD signal frequency increases, the EVM relatively decreases until the transition at 15 MHz, where the EVM completely drops to ~1.48% at 0 dBm RF power. The mixing between DMFD and LTE signals at 15 MHz and 2.6 GHz, respectively, resulted in IMD product at 2.585 GHz, which is the explicit out-of-band IMD re-growth point. From DMFD signal frequency of 15 MHz to 2.5 GHz, the observed EVM is as low as ~1.48% at 0 dBm RF power, and can be further improved to ~1.35% by increasing the RF power to 10 dBm. Higher DMFD signal power has the potential of increasing the laser linewidth, as more peaks will cross the FWHM limit, see Figure 8.2. It is shown that further linewidth broadening provides higher potential of SBS compensation, however the improvement is insignificant.

Above 2.5 GHz for DMFD signal, the effect of SBS compensation reduces as the frequency chirping has already occurred in that frequency range by DM of LTE signal. A sharp peak can be observed when the DMFD signal reaches 2.6 GHz, which is due to the modulation within the bandwidth of LTE signal. Launching the DMFD signal above 2.6 GHz resulted in an average EVM of ~6.45%, which achieved a close proximity with the uncompensated EVM of LTE signal. Overall optimisation of DMFD method has shown that the frequency should not be lower than 15 MHz and higher than 2.5 GHz, hence the expression of $\{f_d << f_{RF}\}$ can be rewritten as $\{ f_L < f_d < f_{RF}\}$, where f_L represents the dithering boundary limit of 14 MHz. It is important to state that f_L is bandwidth dependent.

8.2.3 Impact of Optical Modulators for SBS Compensation

It was shown that the condition of DMFD method has changed to $\{ f_L < f_d < f_{RF} \}$. Despite the frequencies below f_L still compensates the SBS affect, but it has to be neglected due to IMD re-growth within the finite bandwidth of the LTE signal. Since DMFD method operates based on frequency chirping, the investigation on the effectiveness of frequency dithering with two different optical modulators is crucial as DM induces PFC and contrariwise for external modulators. Optical modulator optimisation was carried out in Chapter 4 to address the effect of PFC for the proposed LTE-A scheme. The SE-MZM achieved higher SNR of ~3 dB and ~9 dB for 16-QAM and 64-QAM, respectively, compared to DM. Thus, it is shown that PFC induces additional distortion to the system as the data rate increases.

In this section, an investigation on the impact of frequency dithering method relative to the optical modulators will be carried out. It is already shown in Section 8.2.1 that introducing DMFD signal does not additionally distort the frequency chirp dependent regions. However, it is important to rectify the impact of introducing frequency dithering signal into a chirpless optical modulator based system.

Figure 8.8 illustrates the overall experimental setup for LTE RoF system with DMFD and EMFD for SBS compensation. At the transmitter, LTE signal is composed of QPSK, 16-QAM, and 64-QAM with OFDM, transmitted at 2.6 GHz band via the VSG. The LTE signal is then combined with the dithering signal at 100 MHz specifically for DM. The composite signal is then applied to the DFB laser for DM. However, the second case with a DFB source supplied to SE-MZM, the dithering signal is inserted into the DFB source while LTE signal is supplied to SE-MZM for external modulation. The dithering phenomenon for the second case cannot be performed via SE-MZM because it does not

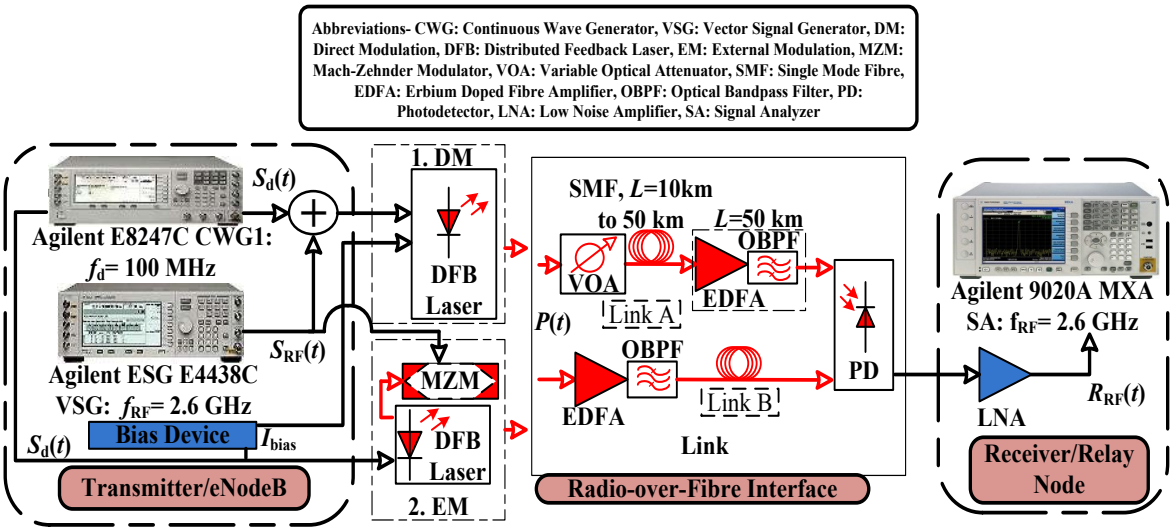

Figure 8.8: LTE-RoF experimental setup for SBS mitigation with DM and EM

induce PFC. In other word, the optical PM required for the linewidth broadening needs to be done via the laser source irrespective of DM or external modulation.

The optical signals are passed through the link A, which consists of a VOA to investigate lower OLP, and SMFs of 10, 25, 35, and 50 km. In link A, EDFA and an OBPF are only utilised for a span of 50 km and above. The optical signals in link B are transmitted through EDFA and OBPF for higher OLP. At the receiver, a PD with a responsivity of 0.42 followed by a LNA and SA are used for the received signal for both links.

Figure 8.9 depict the OLP against the SNR penalty for QPSK, 16-QAM, and 64-QAM systems modulated onto DMFD and EMFD topologies, and transmitted through 10, 25, 35 and 50 km spans. The characteristics of the regions are similar to that presented in Figure 8.4. It is known that DMFD does not enhance the existing PFC effect in regions I and II, and it is shown in Figure 8.9 that EMFD method demonstrates the same characteristic.

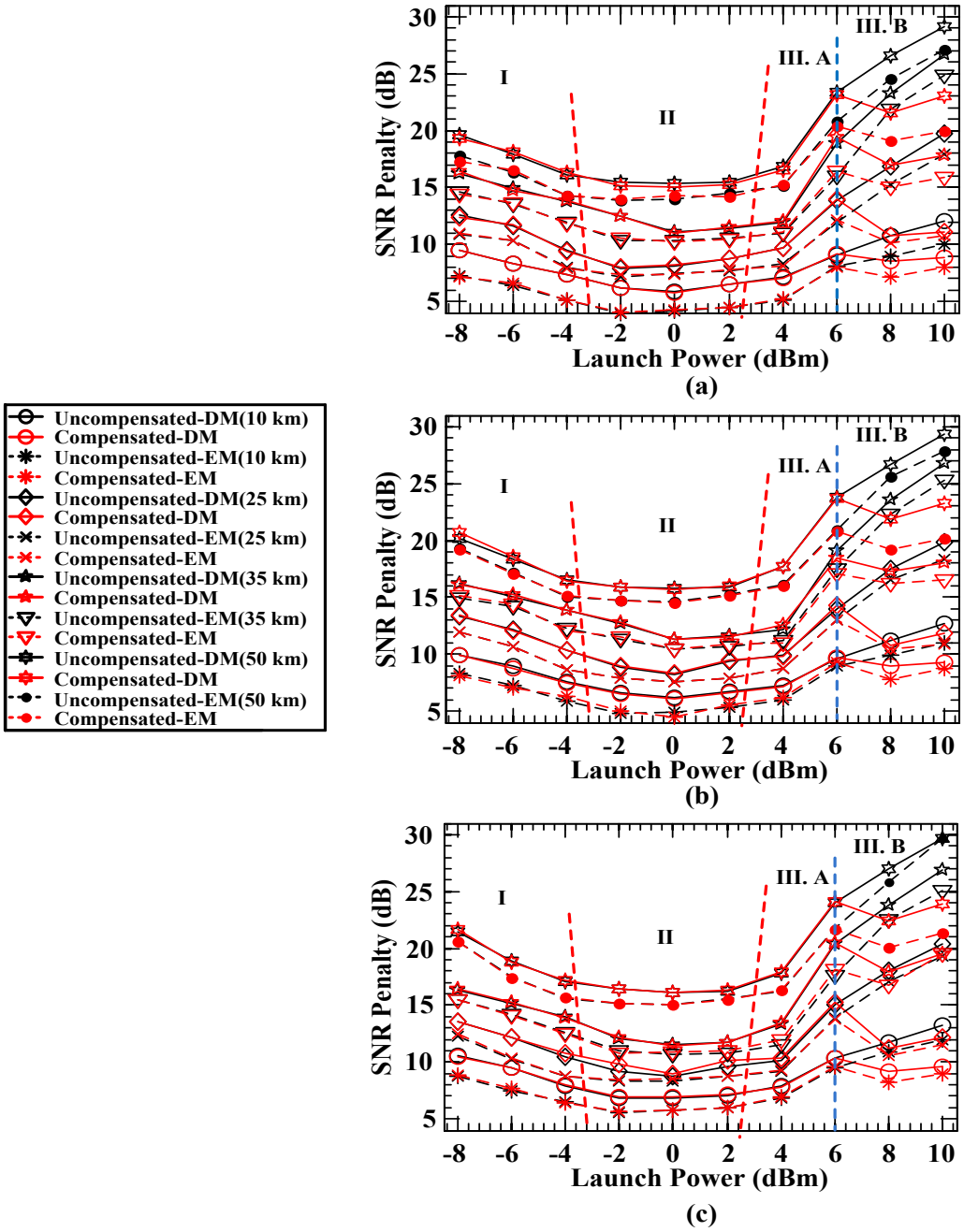

Figure 8.9: OLP against SNR penalty analysis for SBS compensation in (a) QPSK, (b) 16-QAM, and (c) 64-QAM with DMFD and EMFD methods over 10 km to 50 km transmission spans

In Figure 8.9, the concentration is given to the region III.B due to the effectiveness of DMFD and EMFD. Table 8.2 with only DMFD data is updated with the EMFD data as shown in Table 8.4. Overall, the system with DM experiences an average of ~3 dB additional penalty compared to external modulation for LTE RoF system due to the PFC.

Table 8.4: DMFD and EMFD SNR penalties at 8 dBm and 10 dBm OLPs

OLP	Modulation schemes	Uncompensated SNR penalties	Compensated SNR penalties	SNR penalties improvement
8 dBm	DMFD: QPSK	10 km: ~10.83 dB 50 km: ~26.55 dB	10 km: ~8.5 dB 50 km: ~21.51 dB	10 km: ~2.33 dB 60 km: ~5.04 dB
	EMFD: QPSK	10 km: ~8.95 dB 50 km: ~24.55 dB	10 km: ~7.11 dB 50 km: ~19.1 dB	10 km: ~1.84 dB 60 km: ~5.45 dB
	DMFD: 16-QAM	10 km: ~11.2 dB 50 km: ~26.29 dB	10 km: ~8.95 dB 50 km: ~21.9 dB	10 km: ~2.25 dB 60 km: ~4.39 dB
	EMFD: 16-QAM	10 km: ~9.9 dB 50 km: ~25.39 dB	10 km: ~7.8 dB 50 km: ~19.23 dB	10 km: ~2.1 dB 60 km: ~6.16 dB
	DMFD: 64-QAM	10 km: ~11.7 dB 50 km: ~26.99 dB	10 km: ~9.2 dB 50 km: ~22.4 dB	10 km: ~2.5 dB 60 km: ~4.59 dB
	EMFD: 64-QAM	10 km: ~10.88 dB 50 km: ~25.79 dB	10 km: ~8.2 dB 50 km: ~20.1 dB	10 km: ~2.68 dB 60 km: ~5.69 dB
10 dBm	DMFD: QPSK	10 km: ~12.1 dB 50 km: ~29.14 dB	10 km: ~8.9 dB 50 km: ~23.1 dB	10 km: ~3.2 dB 60 km: ~6.04 dB
	EMFD: QPSK	10 km: ~9.9 dB 50 km: ~27.14 dB	10 km: ~7.95 dB 50 km: ~20 dB	10 km: ~1.95 dB 60 km: ~7.14 dB
	DMFD: 16-QAM	10 km: ~12.7 dB 50 km: ~29.32 dB	10 km: ~9.39 dB 50 km: ~23.3 dB	10 km: ~3.31 dB 60 km: ~6.02 dB
	EMFD: 16-QAM	10 km: ~11 dB 50 km: ~27.82 dB	10 km: ~8.7 dB 50 km: ~20.2 dB	10 km: ~2.3 dB 60 km: ~7.62 dB
	DMFD: 64-QAM	10 km: ~13.2 dB 50 km: ~29.67 dB	10 km: ~9.65 dB 50 km: ~23.88 dB	10 km: ~3.55 dB 60 km: ~5.79 dB
	EMFD: 64-QAM	10 km: ~11.99 dB 50 km: ~29.67 dB	10 km: ~8.95 dB 50 km: ~21.3 dB	10 km: ~3 dB 60 km: ~8.37 dB

Due to the lower data rate, the LTE RoF system experiences higher tolerance to PFC, compared to the LTE-A RoF system presented in Chapter 4.

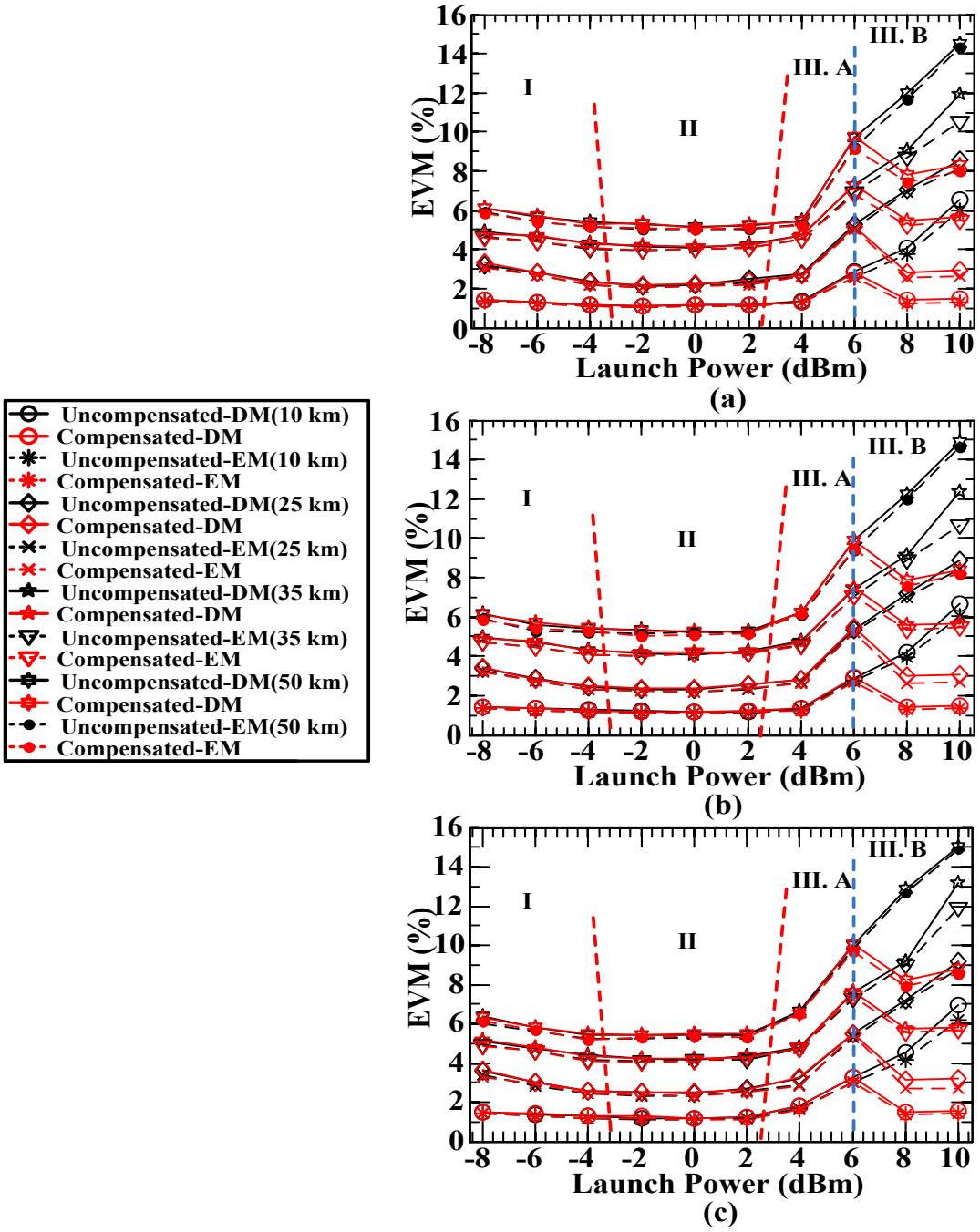

Figure 8.10: OLP against EVM for SBS compensation in (a) QPSK, (b) 16-QAM, and (c) 64-QAM with DMFD and EMFD methods over 10 km to 50 km transmission spans

Figure 8.10(a), (b), and (c) illustrates EVMs of QPSK, 16-QAM, and 64-QAM, respectively, which basically presents the explicit LTE RoF QoS, where the aim is to achieve lower than 8% according to the 3GPP LTE requirement [134]. In terms of EVM, there are no changes observed in regions I and II, thereby agreeing to the response of the SNR penalty shown in Figure 8.9, for both DMFD and EMFD topologies. The complete

measured data for OLP of 8 dBm and 10 dBm, of DFMD and EMFD topologies are given in Table 8.5. Concentrating in the region III.B, at OLP of 8 dBm, EMFD topology enables the LTE RoF system to achieve EVM below 8% for QPSK, 16-QAM, and 64-QAM. However, the 64-QAM LTE RoF system with DMFD topology resulted in an EVM of ~8.2%, which is higher than the 8% limit. At 10 dBm OLP, both DMFD and EMFD topologies exceeded the LTE EVM limit. Although EMFD system is superior to DMFD system by an average of ~ 3 dB SNR gain, EVM differences are comparatively small showing the effectiveness of DMFD system with reduced system complexity for LTE RoF application.

Table 8.5: DMFD and EMFD EVM at 8 dBm and 10 dBm OLPs

OLP	Modulation schemes	Uncompensated EVM	Compensated EVM	EVM improvement
8 dBm	DMFD: QPSK	10 km: ~4.093%	10 km: ~1.42%	10 km: ~2.67%
		50 km: ~11.99%	50 km: ~7.79%	60 km: ~4.2%
	EMFD: QPSK	10 km: ~3.76%	10 km: ~1.25%	10 km: ~2.51%
		50 km: ~11.69%	50 km: ~7.41%	60 km: ~4.28%
	DMFD: 16-QAM	10 km: ~4.22%	10 km: ~1.435%	10 km: ~2.78%
		50 km: ~12.23%	50 km: ~7.88%	60 km: ~4.35%
	EMFD: 16-QAM	10 km: ~3.98%	10 km: ~1.3%	10 km: ~2.68%
		50 km: ~11.96%	50 km: ~7.55%	60 km: ~4.41%
	DMFD: 64-QAM	10 km: ~4.52%	10 km: ~1.48%	10 km: ~3.04%
		50 km: ~12.88%	50 km: ~8.2%	60 km: ~4.68%
	EMFD: 64-QAM	10 km: ~4.15%	10 km: ~1.38%	10 km: ~2.77%
		50 km: ~12.67%	50 km: ~7.89%	60 km: ~4.78%
10 dBm	DMFD: QPSK	10 km: ~6.57%	10 km: ~1.46%	10 km: ~5.11%
		50 km: ~14.53%	50 km: ~8.33%	60 km: ~6.2%
	EMFD: QPSK	10 km: ~5.95%	10 km: ~1.31%	10 km: ~4.64%
		50 km: ~14.33%	50 km: ~8.02%	60 km: ~6%
	16-QAM	10 km: ~6.65%	10 km: ~1.49%	10 km: ~5.16%
		50 km: ~14.87%	50 km: ~8.41%	60 km: ~6.46%
	16-QAM	10 km: ~6.02%	10 km: ~1.36%	10 km: ~4.66%
		50 km: ~14.62%	50 km: ~8.22%	60 km: ~6.4%
	64-QAM	10 km: ~6.97%	10 km: ~1.53%	10 km: ~5.44%
		50 km: ~15.02%	50 km: ~8.81%	60 km: ~6.21%
	64-QAM	10 km: ~6.16%	10 km: ~1.41%	10 km: ~4.75%
		50 km: ~14.89%	50 km: ~8.51%	60 km: ~6.38%

8.3 Summary

In this chapter, the nonlinear compensation of LTE RoF system based on DMFD method was proposed and demonstrated. By utilising this method, the SBS threshold of LTE RoF system was found to be ~6 dBm. Furthermore, it was also shown that despite the

fact that DMFD induces frequency chirp, but it does not deteriorate the signal propagating in the linear and intermixing regions. The LTE RoF system average SNR gain observed at OLP of 8 dBm and 10 dBm for the 50 km transmission span are ~4.81 dB and ~5.97 dB, respectively.

In terms of the DMFD signal, a thorough optimisation was carried out. The investigation revealed that the condition of the dithering signal should meet the requirement of $\{f_L < f_d < f_{RF}\}$. It was also shown that increasing the power of the dithering signal will increase the effectiveness of SBS compensation proportionally, however the EVM improvement was insignificant.

Finally, DMFD and EMFD methods were demonstrated to mitigate SBS for LTE-RoF system. Both topologies do not deteriorate the PFC dependent regions from the intentional linewidth broadening. In addition, external modulation exhibits a ~3 dB of average SNR gain over DM system, however both systems achieved close proximity in the EVM measurement. The obtained result in this chapter has given the ability of utilising high OLP for the LTE RoF system. The following chapter will conclude all the findings and contributions made in this thesis.

CHAPTER 9 CONCLUSIONS AND FUTURE WORK

9.1 Conclusions

The actively growing end user subscriptions with bandwidth hungry, high specification, real-time, and delay-sensitive applications have driven mobile communication and as well as the pure wireless communication technologies to continuously progress. The 3GPP established a standard known as the LTE and build up frameworks as an evolution to the existing 3GPP radio technologies. The LTE frameworks precisely focus on a development path for GSM and UMTS. In radio access network of LTE, eNB functions as a 2-node architecture leading to an operating characteristic of not depending in a central controller. Furthermore, the LTE signal will experience a path loss in excess of 100 dB at 2.6 GHz band and severe multipath propagation in urban area with NLOS connectivity. Therefore the cell size of eNB is much smaller than any of its former technology, where the typical cell radius is 1 km.

Therefore, this thesis aims to seamlessly integrate eNB and AF type RN by adapting RoF as the interface into the LTE networking structure. As a rule of thumb, RoF was designed in a simple and least sophisticated technology for easy adaptability into the LTE networking structure.

The thesis began with an overview of RoF system and its in-build optoelectronics devices in Chapter 2. Due to the importance of optical modulation in RoF system, a detailed explanation was given with fair comparison between DM and external modulation. Along with the RoF system overview, a thorough channel analysis was given to apprehend the importance of RoF system. From the analysis, in comparison with wireless channel (Rayleigh fading) it was found that RoF link could provide a 31 dB of SNR gain, which is a remarkable improvement for commercial application.

Focusing on the RoF link, Chapter 3 explains the core reasons for using DFB as the optical transmitter of this project. Chapter 3 unfolds that DFB outperforms Fabry-Perot laser and VCSEL in various technical aspects, including the most important requirement of DSM operation. In a DFB, PFC is an important impairment for long haul transmission because of its ability to correlate with CD and jointly distort the optical signal. The existing mathematical expression does not precisely explain on how rate equations contribute to PFC that effectively distorts the modulated optical signal. Therefore, Chapter 3 analytically presented a new closed form expression for PFC via the derivation of rate equations.

In Chapter 4, LTE-A was optimised relative to the electrical and optical transmitters, with introducing varying FFT sizes instead of carrier aggregation. In the first phase, a range of FFT sizes were introduced, and the optimisation was carried out with varying OLP. The optimum OLP or the intermixing region, which mostly falls in the range of ~-6 dBm to ~0 dBm for QPSK, 16-QAM, and 64-QAM were discovered. This particular region was achieved by the interchangeable compensation between PFC and CD, with SPM. For the FFT size-64, the analysis unfold that the walk-off rate gradually decreases with the increase of data rate, especially for 16-QAM and 64-QAM schemes. For FFT size of more than 256, the SNR penalty increases significantly for QPSK, 16-QAM, and 64-QAM due to the vulnerability towards ICI. The finding for FFT size optimisation reveals that FFT size-128 provides the minimum SNR penalty across all investigated modulation schemes. The symbol length and subcarrier frequency spacing of FFT size-128 could provide enough tolerance and higher walk off to ISI and ICI, respectively.

After determining the optimum FFT size for electrical transmitter in Chapter 4, the second phase of the investigation was further carried out on the performance evaluation

and optimisation of optical modulators, using DML and external modulators. The optimum OLP was consistent and conforms to the range that was discovered in the previous investigation. The investigation shows that the performance of external modulation schemes in terms of transmission distance is superior to DML scheme. Between SE-MZM and DE-MZM, the latter proved to be a preferred option for externally modulating the signal since it offers improved immunity to the fibre CD, hence achieved longer transmission span. However, DE-MZM is vulnerable towards nonlinearity due to the modulation taking place in the phase of the optical source. It is clearly shown that the cell extension with a simple DFB modulated RoF configuration could extend the coverage of eNB beyond its area, and even further with external modulation. Overall, Chapter 4 provided an in-depth design of the proposed varying FFT-sizes based LTE-A and its integration with RoF.

All the previous chapters concentrated on the theoretical development of the proposed RoF systems. It is vital that the seamless integration of LTE and RoF should be practically realizable, hence Chapter 5 presented the experimental system design of LTE RoF. An end-to-end experimental optimisation was carried out in Chapter 5 to ascertain a flawless performance. The optimisation was initiated with OMI for the DML. A new region termed as OMR was introduced, where QPSK, 16-QAM, and 64-QAM achieved average EVM across all ARBs of ~0.97%, ~1.01%, and ~1.06%, respectively. In this operating scenario, the system achieved significantly lower than the 3GPP EVM margin of 8%.

As a further improvement to the system, the intermixing region was deliberately introduced in Chapter 5 as a function of OLP. In this region, the QPSK, 16-QAM and 64-QAM average EVM further trimmed to ~0.93%, ~0.96% and ~0.99%, respectively. The results also revealed that, for low OMI, nonlinear propagation significantly adds to the

existing gain compression affect, thus strictly needs to be avoided. In terms of higher transmission distance, investigation on transmission up to 60 km shown that intermixing region does not deviate from its nominal range. Chapter 5 finally presents the DM nonlinear threshold for LTE RoF system. The investigation shows that both linear and nonlinear distortion increases linearly, and that the system experiences severe nonlinear distortion for OLP of more than 6 dBm.

Progressing from the basic LTE RoF experimental link, Chapter 6 proposes an alternative method for 2×2 MIMO systems in LTE over 60 km RoF. The implementation of the alternative method was realized by introducing DD-FDM. Taking into account the advantage of LTE spectrum allocation and the proposed solution, a two-fold gain in the peak data rate has been achieved in the 2x2 MIMO configurations. The studies revealed that the resulting output quality of the signal is almost identical for both the 2 GHz and 2.6 GHz bands. At 200 Mb/s (64-QAM), the experimental system could achieve EVMs of ~5.935% and ~5.99%, for 2GHz and 2.6 GHz system, respectively.

A complete solution of the proposed LTE RoF system was introduced in Chapter 7, where the seamless integration of the full duplex FDD LTE technology with the 10 km RoF system was carried out. The RoF system was designed based on dedicated DMLs for DL and UL systems, with DWDM wavelength spacing and a SMF. The ACLR comparison between half duplex and full duplex system for BFS of 190 MHz revealed that the system to be Rayleigh backscattering and optical interference free. The DL system with BFS of 190 MHz, IFS of 120 MHz and NFS of 50 MHz resulted in negligible, 0.69 dB, and 14.10 dB ACLR penalties, respectively. In the UL system, the aforementioned frequencies spacing achieved a close proximity to DL system for the ACLR penalties. The BFS and IFS frequency spacing experienced negligible IMD products. However, the NFS

introduced severe IMD products from subcarrier-subcarrier mixing due to the photodetection. In addition, the full duplex system reported that the best case transmission condition for QPSK, 16-QAM, and 64-QAM systems achieved the average EVMs of ~2.30%, ~2.33%, and ~2.39%, respectively, at 2 dBm transmit power.

The research work carried out in Chapters 3, 4, and 5 have shown the criticalness of nonlinear propagation, therefore Chapters 6 and 7 completely focused on the intermixing region. In order to compensate the distortion induced by nonlinear propagation, Chapter 8 introduces a novel nonlinear compensation technique for LTE RoF system utilising the DMFD method. By utilising the DMFD method, the SBS threshold of LTE RoF system was found to be ~6 dBm. Furthermore, it was also shown that despite the fact that DMFD induces frequency chirp, but it does not deteriorate the signal propagating in the linear and intermixing regions. The LTE RoF system average SNR gain observed at OLP of 8 dBm and 10 dBm for the 50 km transmission span are ~4.81 dB and ~5.97 dB, respectively.

In terms of the DMFD signal, a thorough optimisation was carried out. The investigation revealed that the condition of the dithering signal should meet the requirement of $\{f_L < f_d < f_{RF}\}$. It was also shown that increasing the power of the dithering signal proportionally increases the effectiveness of SBS compensation, however the EVM improvement was insignificant.

Finally, DMFD and EMFD methods were demonstrated to mitigate SBS for LTE RoF system. Both topologies do not deteriorate the PFC dependent regions from the intentional linewidth broadening. In addition, external modulation exhibits a ~3 dB of average SNR gain over DML, however both systems achieved close proximity in the EVM measurement. The obtained results in this chapter have given the ability of utilising high OLP for the LTE RoF system.

9.2 Future Work

Within the given time frame, this thesis has contributed to the design and development of LTE RoF integration. But, in the perspective of research, the improvements and contribution to a particular field could be endless. Therefore, this section suggests and discusses the next level of design and development for LTE RoF system.

This thesis has given significant attention to the optical modulation methods and its relevant impact on the LTE RoF performance. In order to further emphasize on DML, Fabry-Perot laser and VCSELs can be introduced into the system and further optimisation can be carried out, to commercially provide a wide range of selection in terms of optical transmitters. Recently, reflective semiconductor optical amplifier (RSOA) has captured a wide attention as an optical modulator in the optical communication research community. The major application area of RSOA is for the full duplex link based on the wavelength reuse scheme. An end-to-end design of a full duplex LTE system with RSOA can be carried out, and propose a new Rayleigh backscattering mitigation technique, to provide an alternative to the proposed DWDM architecture within this thesis.

The LTE RoF system proposed in this thesis is completely designed based on SMF. There are various types of optical fibres, namely dispersion-shifted fibre and non-zero dispersion-shifted fibre that provide a higher tolerance for dispersion and nonlinearity, respectively. The intermixing region introduced for SMF could be investigated with dispersion-shifted fibre and non-zero dispersion-shifted fibre, and analyses the nominal region for optimum OLP. By performing the various fibre channel investigation, the LTE network operator will have the ability of adopting the appropriate channel relative to the application. All the aforementioned optical fibres are widely utilised for outdoor applications, the proposed LTE RoF integration in this thesis can also be extended for in-

building coverage with distributed antenna system for femtocell deployment. It is possible to achieve the indoor extension by coupling the SMF dependent network to a MMF or plastic optical fibre for in-building coverage, hence a complete LTE RoF solution will be achieved starting from the end-users located close to the eNB until up to the end-users situated inside a building.

Finally, the optical receiver utilised in this thesis was solely based on DD. Coherent detection has been widely used as an alternative to DD. The LTE RoF system could be redesigned with coherent detection, based on CO-OFDM over DD-OOFDM to investigate the effectiveness in a long span transmission.

REFERENCE

[1] "The Little Data Book on Information and Communication Technology " *International Telecommunication Union and World Bank,* 2012.

[2] "Measuring the Information Society," *International Telecommunication Union* 2012.

[3] M. S. David, F. M. Jose, C. P. Jorge, C. Daniel, G. Salvador, and C. Narcis, "On the way towards Fourth-Generation Mobile: 3GPP LTE and LTE-Advanced," *EURASIP Journal on Wireless Communications and Networking,* vol. 2009, p. 10, 2009.

[4] D. Gilstrap, "Traffic and Market Report: On The Pulse of the Networked Society," *Ericsson Traffic and Market Report,* 2012.

[5] OECD, *OECD Communications Outlook*: OECD Publishing, 2011.

[6] M. P. Clark, *Wireless access networks: fixed wireless access and WLL networks--design and operation*: John Wiley, 2000.

[7] T. Halonen, J. Romero, and J. Melero, *GSM, GPRS and EDGE Performance: Evolution Towards 3G/UMTS*: Wiley, 2004.

[8] N. Salman, I. Rasool, and A. H. Kemp, "Overview of the IEEE 802.15.4 standards family for Low Rate Wireless Personal Area Networks," in *Wireless Communication Systems (ISWCS), 2010 7th International Symposium on*, 2010, pp. 701-705.

[9] *Wi-Fi Alliance. Wi-Fi CERTIFIED™ n: Longer-Range, Faster-Throughput, Multimedia-Grade Wi-Fi® Networks [Online]*. Available: Available: http://www.wi-fi. org/register.php?file=wp_Wi-Fi_CERTIFIED_n_Industry.pdf. [accessed: 12/7/2012]

[10] *IEEE 802.15 WPAN Task Group 1 (TG1). IEEE 802.15 Bluetooth standard for wireless personal area network [Online]*. Available: http://ieee802.org/15/pub/ TG1 .html. [accessed: 17/12/2012]

[11] P. Cheolhee and T. S. Rappaport, "Short-Range Wireless Communications for Next-Generation Networks: UWB, 60 GHz Millimeter-Wave WPAN, And ZigBee," *Wireless Communications, IEEE,* vol. 14, pp. 70-78, 2007.

[12] B. H. Walke, P. Seidenberg, and P. Althoff, *UMTS: The Fundamentals*: Wiley, 2003.

[13] E. Dahlman, S. Parkvall, and J. Sköld, *LTE: The 4G Solution for Mobile Broadband*: Academic Press, 2011.

[14] Ericsson, "LTE - A 4G Solution," *Ericsson White Paper,* 2011.

[15] Z. Junman and Z. Jing, "ZTE's UMTS Home Access Solution," *ZTE Technologies: PTN Brings a Shift to Packet-Centric Optical Transport,* vol. 10, pp. 14-17, 2008.

[16] Alcatel-Lucent, "Long Term Evolution (LTE) Overview," *White Paper,* 2008.

[17] IXIA, "eNodeB Wraparound Testing: A Comprehensive Guide," 2009.

[18] K. Dimou, W. Min, Y. Yu, M. Kazmi, A. Larmo, J. Pettersson, W. Muller, and Y. Timner, "Handover within 3GPP LTE: Design Principles and Performance," in *Vehicular Technology Conference Fall (VTC 2009-Fall), 2009 IEEE 70th*, 2009, pp. 1-5.

[19] K. Hoon, C. Jae Hun, K. Sangho, S. Ki-Uk, L. Hanlim, L. Jaehoon, K. Byungjik, O. Yunje, L. Jaekon, and H. Seongtaek, "Radio-Over-Fiber System for TDD-Based

OFDMA Wireless Communication Systems," *Lightwave Technology, Journal of,* vol. 25, pp. 3419-3427, 2007.

[20] S.W.Peters, A.Y.Panah, K.T.Truong, and J. R.W.Heath, "Relay Architectures for 3GPP LTE-Advanced," *EURASIP Journal on Wireless Communications and Networking,* vol. 2009, p. 14, 2009.

[21] Y. Guangxiang, Z. Xiang, W. Wenbo, and Y. Yang, "Carrier aggregation for LTE-advanced mobile communication systems," *Communications Magazine, IEEE,* vol. 48, pp. 88-93, 2010.

[22] G. Boudreau, J. Panicker, G. Ning, C. Rui, W. Neng, and S. Vrzic, "Interference coordination and cancellation for 4G networks," *Communications Magazine, IEEE,* vol. 47, pp. 74-81, 2009.

[23] P. Mugen, Y. Na, W. Wenbo, and C. Hsiao-Hwa, "On Interference Coordination for Directional Decode-And-Forward Relay in TD-LTE Systems," in *Communications (ICC), 2010 IEEE International Conference on*, 2010, pp. 1-6.

[24] E. Lang, S. Redana, and B. Raaf, "Business Impact of Relay Deployment for Coverage Extension in 3GPP LTE-Advanced," in *Communications Workshops, 2009. ICC Workshops 2009. IEEE International Conference on*, 2009, pp. 1-5.

[25] T. Wirth, V. Venkatkumar, T. Haustein, E. Schulz, and R. Halfmann, "LTE-Advanced Relaying for Outdoor Range Extension," in *Vehicular Technology Conference Fall (VTC 2009-Fall), IEEE 70th*, 2009, pp. 1-4.

[26] Y. Yang, H. Honglin, X. Jing, and M. Guoqiang, "Relay technologies for WiMax and LTE-advanced mobile systems," *Communications Magazine, IEEE,* vol. 47, pp. 100-105, 2009.

[27] S. Nagata, Y. Yan, X. Gao, A. Li, H. Kayama, T. Abe, and T. Nakamura, "Investigation on System Performance of L1/L3 Relays in LTE-Advanced Downlink," in *Vehicular Technology Conference (VTC Spring), 2011 IEEE 73rd*, 2011, pp. 1-5.

[28] T. Beniero, S. Redana, J. Hamalainen, and B. Raaf, "Effect of Relaying on Coverage in 3GPP LTE-Advanced," in *Vehicular Technology Conference, 2009. VTC Spring 2009. IEEE 69th*, 2009, pp. 1-5.

[29] S. M. Alamouti, "A Simple Transmit Diversity Technique for Wireless Communications," *Selected Areas in Communications, IEEE Journal on,* vol. 16, pp. 1451-1458, 1998.

[30] A. Nagate, K. Hoshino, M. Mikami, and T. Fujii, "A Field Trial of Multi-Cell Cooperative Transmission over LTE System," in *Communications (ICC), 2011 IEEE International Conference on*, 2011, pp. 1-5.

[31] D. Turner. (2011, Evolution to LTE and the surrounding challenges for in-building coverage. *Zinwave*.

[32] O. Tipmongkolsilp, S. Zaghloul, and A. Jukan, "The Evolution of Cellular Backhaul Technologies: Current Issues and Future Trends," *Communications Surveys & Tutorials, IEEE,* vol. 13, pp. 97-113, 2011.

[33] X. Zheng, X. Q. Jin, R. P. Giddings, J. L. Wei, E. Hugues-Salas, Y. H. Hong, and J. M. Tang, "Negative Power Penalties of Optical OFDM Signal Transmissions in Directly Modulated DFB Laser-Based IMDD Systems Incorporating Negative Dispersion Fibers," *Photonics Journal, IEEE,* vol. 2, pp. 532-542, 2010.

[34] S. L. Jansen, A. Al Amin, H. Takahashi, I. Morita, and H. Tanaka, "132.2-Gb/s PDM-8QAM-OFDM Transmission at 4-b/s/Hz Spectral Efficiency," *Photonics Technology Letters, IEEE,* vol. 21, pp. 802-804, 2009.

[35] S. Adhikari, B. Inan, O. Karakaya, W. Rosenkranz, and S. L. Jansen, "FFT optimization for practical OFDM implementations," in *Optical Communication (ECOC), 2011 37th European Conference and Exhibition on*, 2011, pp. 1-3.

[36] D. T. Pham, M.-K. Hong, J.-M. Joo, E.-S. Nam, and S.-K. Han, "Laser phase noise and OFDM symbol duration effects on the performance of direct-detection based optical OFDM access network," *Optical Fiber Technology,* vol. 17, pp. 252-257, 2011.

[37] A. Lowery and J. Armstrong, "Orthogonal-frequency-division multiplexing for dispersion compensation of long-haul optical systems," *Opt. Express,* vol. 14, pp. 2079-2084, 2006.

[38] Bruno Clerckx, Angel Lozano, Stefania Sesia, Cornelius van Rensburg, and C. B. Papadias, "3GPP LTE and LTE-Advanced," *EURASIP Journal on Wireless Communications and Networking,* vol. 2009, pp. 1-3, 2009.

[39] S. L. Jansen, I. Morita, and H. Tanaka, "16x52.5-Gb/s, 50-GHz spaced, POLMUX-CO-OFDM transmission over 4,160 km of SSMF enabled by MIMO processing," *Optical Communication - Post-Deadline Papers (published 2008), 2007 33rd European Conference and Exhibition of,* pp. 1-2, 2007.

[40] T. Kobayashi, A. Sano, E. Yamada, Y. Miyamoto, H. Takara, and A. Takada, "Electro-optically multiplexed 110 Gbit/s optical OFDM signal transmission over 80 km SMF without dispersion compensation," *Electronics Letters,* vol. 44, pp. 225-226, 2008.

[41] L. Chin-Pang and A. J. Seeds, "Transmission of Wireless MIMO-Type Signals Over a Single Optical Fiber Without WDM," *Microwave Theory and Techniques, IEEE Transactions on,* vol. 58, pp. 3094-3102, 2010.

[42] R. Letian, S. E. Elayoubi, and O. B. Haddada, "Impact of Relays on LTE-Advanced Performance," in *Communications (ICC), 2010 IEEE International Conference on*, 2010, pp. 1-6.

[43] A. Yariv, H. Blauvelt, D. Huff, and H. Zarem, "An experimental and theoretical study of the suppression of interferometric noise and distortion in AM optical links by phase dither," *Lightwave Technology, Journal of,* vol. 15, pp. 437-443, 1997.

[44] F. W. Willems, W. Muys, and J. S. Leong, "Simultaneous suppression of stimulated Brillouin scattering and interferometric noise in externally modulated lightwave AM-SCM systems," *Photonics Technology Letters, IEEE,* vol. 6, pp. 1476-1478, 1994.

[45] G. L. Li and P. K. L. Yu, "Optical intensity modulators for digital and analog applications," *Lightwave Technology, Journal of,* vol. 21, pp. 2010-2030, 2003.

[46] A. J. Cooper, "'Fibre/radio' for the provision of cordless/mobile telephony services in the access network," *Electronics Letters,* vol. 26, pp. 2054-2056, 1990.

[47] J. E. Mitchell, A. Shami, M. Maier, and C. Assi, "Radio-over-Fiber (RoF) Networks

Broadband Access Networks," ed: Springer US, 2009, pp. 283-300.

[48] H. Al-Raweshidy and S. Komaki, *Radio over Fiber Technologies for Mobile Communications Networks*: Artech House, Incorporated, 2002.

[49] T. Jia, S. Zheng, X. Zhang, X. Jin, X. Ai, and J. Xu, "Characteristics of radio transmission over polymer optical fiber for indoor wireless coverage," *Optics Communications,* vol. 264, pp. 142-147, 2006.

[50] A. Nirmalathas, C. Lim, D. Novak, and R. Waterhouse, "Progress in millimeter-wave fiber-radio access networks," *Annals of Telecommunications,* vol. 56, pp. 27-38, 2001.

[51] http://www.andrew.com. (08/10, 2012.
[52] http://www.zinwave.com. (08/10, 2012.
[53] http://www.lgcwireless.com, 08/10, 2012.
[54] http://www.adc.com. (08/10, 2012.
[55] R. E. Schuh, "Hybrid fiber radio for second and third generation wireless systems," in *Microwave Photonics, 1999. MWP '99. International Topical Meeting on*, 1999, pp. 213-216 vol.1.
[56] R. Yuen and X. N. Fernando, "Enhanced Wireless Hotspot Downlink Supporting IEEE802.11 and WCDMA," in *Personal, Indoor and Mobile Radio Communications, 2006 IEEE 17th International Symposium on*, 2006, pp. 1-6.
[57] P. Hartmann, Q. Xin, A. Wonfor, R. V. Penty, and I. H. White, "1-20 GHz Directly Modulated Radio over MMF Link," in *Microwave Photonics, 2005. MWP 2005. International Topical Meeting on*, 2005, pp. 95-98.
[58] A. J. Antos and D. K. Smith, "Design and characterization of dispersion compensating fiber based on the LP₀₁ mode," *Lightwave Technology, Journal of,* vol. 12, pp. 1739-1745, 1994.
[59] I. Dayoub, Y. Zouin, A. Okasa M'Foubat, J. M. Rouvaen, J. P. Vilcot, and D. Decoster, "Radio over Fibre networks: Low cost solution for different applications and emerging technologies," in *Information and Communication Technologies, 2006. ICTTA '06. 2nd*, 2006, pp. 2537-2542.
[60] G. P. Agrawal and N. K. Dutta, *Long-wavelength semiconductor lasers*: Van Nostrand Reinhold, 1986.
[61] E. Goutain, J. C. Renaud, M. Krakowski, D. Rondi, R. Blondeau, and D. Decoster, "30 GHz bandwidth, 1.55 μm MQW-DFB laser diode based on a new modulation scheme," *Electronics Letters,* vol. 32, pp. 896-897, 1996.
[62] L. Bach, W. Kaiser, J. P. Reithmaier, A. Forchel, T. W. Berg, and B. Tromborg, "Enhanced direct-modulated bandwidth of 37 GHz by a multi-section laser with a coupled-cavity-injection-grating design," *Electronics Letters,* vol. 39, pp. 1592-1593, 2003.
[63] L. Chrostowski, X. Zhao, C. J. Chang-Hasnain, R. Shau, M. Ortsiefer, and M. C. Amann, "50 GHz directly-modulated injection-locked 1.55 μm VCSELs," in *Optical Fiber Communication Conference, 2005. Technical Digest. OFC/NFOEC*, 2005, p. 3 pp. Vol. 4.
[64] E. K. Lau, S. Hyuk-Kee, and M. C. Wu, "Ultra-high, 72 GHz resonance frequency and 44 GHz bandwidth of injection-locked 1.55-/spl mu/m DFB lasers," in *Optical Fiber Communication Conference, 2006 and the 2006 National Fiber Optic Engineers Conference. OFC 2006*, 2006, p. 3 pp.
[65] L. A. Coldren and S. W. Corzine, *Diode Lasers and Photonic Integrated Circuits*. New York: John Wiley and Sons Inc, 1995.
[66] K. Petermann, *Laser Diode Modulation and Noise*: Springer, 1988.
[67] M. Osinski and J. Buus, "Linewidth broadening factor in semiconductor lasers--An overview," *Quantum Electronics, IEEE Journal of,* vol. 23, pp. 9-29, 1987.
[68] G. Morthier and P. Vankwikelberge, *Handbook of Distributed Feedback Lasers*. Boston, MA: Artech House Inc, 1997.
[69] T. Shao, F. Paresys, Y. Le Guennec, G. Maury, N. Corrao, and B. Cabon, "Convergence of 60 GHz Radio Over Fiber and WDM-PON Using Parallel Phase Modulation With a Single Mach–Zehnder Modulator," *Lightwave Technology, Journal of,* vol. 30, pp. 2824-2831, 2012.

[70] D. M. Gill, L. Xiang, W. Xing, S. Banerjee, and S. Yikai, "/spl pi//2 alternate-phase ON-OFF keyed 40-Gb/s transmission on standard single-mode fiber," *Photonics Technology Letters, IEEE,* vol. 15, pp. 1776-1778, 2003.

[71] J. T. Gallo and R. Whiteman, "Optical modulators for fiber systems," in *Gallium Arsenide Integrated Circuit (GaAs IC) Symposium, 2003. 25th Annual Technical Digest 2003. IEEE*, 2003, pp. 145-148.

[72] W. Shieh and I. Djordjevic, *OFDM for Optical Communications*: Academic Press/Elsevier, 2010.

[73] C. H. Cox, *Analog Optical Links: Theory and Practice*: Cambridge University Press, 2004.

[74] J. Toulouse, "Optical nonlinearities in fibers: review, recent examples, and systems applications," *Lightwave Technology, Journal of,* vol. 23, pp. 3625-3641, 2005.

[75] B. Inan, S. Randel, S. L. Jansen, A. Lobato, S. Adhikari, and N. Hanik, "Pilot-tone-based nonlinearity compensation for optical OFDM systems," in *Optical Communication (ECOC), 2010 36th European Conference and Exhibition on*, 2010, pp. 1-3.

[76] F. S. Yang, M. E. Marhic, and L. G. Kazovsky, "Nonlinear crosstalk and two countermeasures in SCM-WDM optical communication systems," *Lightwave Technology, Journal of,* vol. 18, pp. 512-520, 2000.

[77] S. L. Jansen, I. Morita, K. Forozesh, S. Randel, D. van den Borne, and H. Tanaka, "Optical OFDM, a hype or is it for real?," in *Optical Communication, 2008. ECOC 2008. 34th European Conference on*, 2008, pp. 1-4.

[78] G. R. Walker, D. M. Spirit, P. J. Chidgey, E. G. Bryant, and C. R. Batchellor, "Effect of fibre dispersion on four-wave mixing in multichannel coherent optical transmission system," *Electronics Letters,* vol. 28, pp. 989-991, 1992.

[79] W. S. C. Chang, *RF Photonic Technology in Optical Fiber Links*: Cambridge University Press, 2002.

[80] K. N. S. Kumar, M. Kata, P. Chaitanya, and D. Mukkollu. (2009) LTE-Advanced: Future of Mobile Broadband. *Tata Consultancy Services (TCS) White Paper*.

[81] Real.Wireless, "LTE and HSPA Device Availability in UK-Relevant Frequency Bands," *OFCOM,* 2012.

[82] J. B. Andersen, T. S. Rappaport, and S. Yoshida, "Propagation measurements and models for wireless communications channels," *Communications Magazine, IEEE,* vol. 33, pp. 42-49, 1995.

[83] M. O. Hasna and M. S. Alouini, "End-to-end performance of transmission systems with relays over Rayleigh-fading channels," *Wireless Communications, IEEE Transactions on,* vol. 2, pp. 1126-1131, 2003.

[84] A. F. Molisch, J. R. Foerster, and M. Pendergrass, "Channel models for ultrawideband personal area networks," *Wireless Communications, IEEE,* vol. 10, pp. 14-21, 2003.

[85] W. P. Ng, W. Loedhammacakra, Z. Ghassemlooy, and R. A. Cryan, "Characterisation of a parallel optical all pass filter for chromatic dispersion equalisation in 10 Gb/s system," *Circuits, Devices & Systems, IET,* vol. 2, pp. 112-118, 2008.

[86] T. Kanesan, W. P. Ng, Z. Ghassemlooy, and J. Perez, "Radio Relaying for Long Term Evolution Employing Radio-over-Fibre " in *16th European Conference on Networks and Optical Communications/6th Conference on Optical Cabling and Infrastructure (NOC/OC&I 2011), IEEE,* Newcastle Upon Tyne, pp. 212-215, 20-22 July 2011.

[87] R. Schmogrow, B. Nebendahl, M. Winter, A. Josten, D. Hillerkuss, S. Koenig, J. Meyer, M. Dreschmann, M. Huebner, C. Koos, J. Becker, W. Freude, and J. Leuthold, "Error Vector Magnitude as a Performance Measure for Advanced Modulation Formats," *Photonics Technology Letters, IEEE,* vol. 24, pp. 61-63, 2012.
[88] G. R. Aiello and G. D. Rogerson, "Ultra-wideband wireless systems," *Microwave Magazine, IEEE,* vol. 4, pp. 36-47, 2003.
[89] R. V. Dalal, "Investigation of High Linearity DFB Lasers for Analog Communications," Master of Engineering in Electrical Engineering and the Bachelors of Physics, Department of Electrical Engineering and Computer Science and Department of Physics, Massachusetts Institute of Technology, Boston, 1998.
[90] S. Mohrdiek, H. Burkhard, F. Steinhagen, H. Hillmer, R. Losch, W. Schlapp, and R. Gobel, "10-Gb/s standard fiber transmission using directly modulated 1.55-μm quantum-well DFB lasers," *Photonics Technology Letters, IEEE,* vol. 7, pp. 1357-1359, 1995.
[91] M. Cvijetic, *Optical Transmission Systems Engineering*: Artech House, 2004.
[92] H. Jiang and J. Lin, "Semiconductor lasers: Expanding into blue and green," *Nat Photon,* vol. 5, pp. 521-522, 2011.
[93] H. Kogelnik and C. V. Shank, "Coupled-Wave Theory of Distributed Feedback Lasers," *Journal of Applied Physics,* vol. 43, pp. pp. 2327-2335, 1972.
[94] J. M. Liu, *Photonic Devices*. New York: Cambridge University Press, 2005.
[95] J. M. Tang, P. M. Lane, and K. A. Shore, "High-speed transmission of adaptively modulated optical OFDM signals over multimode fibers using directly Modulated DFBs," *Lightwave Technology, Journal of,* vol. 24, pp. 429-441, 2006.
[96] P. Krehlik, "Characterization of semiconductor laser frequency chirp based on signal distortion in dispersive optical fiber," *Opto-Electronics Review,* vol. 14, pp. 119-124, 2006.
[97] W. W. Feng and N. H. Zhu, "Analysis of chirp characteristics of DFB lasers and integrated laser-modulators," *Optical and Quantum Electronics,* vol. 36, pp. 1237-1245, 2004.
[98] P. Krehlik, "Characterization of semiconductor laser frequency chirp based on signal distortion in dispersive optical fiber," *OPTO-ELECTRONICS REVIEW,* vol. 14, pp. 123-128, 2006.
[99] A. Brizido, M. Lima, R. Nogueira, P. Andre, and A. Teixeira, "3G radio distribution based on directly modulated lasers over passive transparent optical networks," in *Microwave and Optoelectronics Conference, 2007. IMOC 2007. SBMO/IEEE MTT-S International*, 2007, pp. 658-661.
[100] L. Bjerkan, A. Royset, L. Hafskjaer, and D. Myhre, "Measurement of laser parameters for simulation of high-speed fiberoptic systems," *Lightwave Technology, Journal of,* vol. 14, pp. 839-850, 1996.
[101] T. Kanesan, W. P. Ng, Z. Ghassemlooy, and J. Perez, "Optimization of Optical Modulator for LTE RoF in Nonlinear Fiber Propagation," *Photonics Technology Letters, IEEE* vol. 24, pp. 617-619, 2012.
[102] E. Seidel. (2012) LTE-A Carrier Aggregation Enhancements in Release 11. *nomor research*.
[103] R. Bendlin, T. Ekpenyong, and D. Greenstreet, "Paving the path for wireless capacity expansion," *Texas Instruments White Paper,* 2012.

[104] S. Weinstein and P. Ebert, "Data Transmission by Frequency-Division Multiplexing Using the Discrete Fourier Transform," *Communication Technology, IEEE Transactions on,* vol. 19, pp. 628-634, 1971.
[105] R. G. Lyons, *Understanding Digital Signal Processing*: Prentice Hall, 2010.
[106] U. Barth, "3GPP Long-Term Evolution/System Architecture Evolution Overview," *Alcatel,* 2006.
[107] M. Sung, S. Kang, J. Shim, J. Lee, and J. Jeong, "DFT-Precoded Coherent Optical OFDM With Hermitian Symmetry for Fiber Nonlinearity Mitigation," *Lightwave Technology, Journal of,* vol. 30, pp. 2757-2763, 2012.
[108] T. Kanesan, W. P. Ng, Z. Ghassemlooy, and C. Lu, "FFT size optimization for LTE RoF in nonlinear fibre propagation," in *Communication Systems, Networks & Digital Signal Processing (CSNDSP), IEEE 8th International Symposium on*, 2012, pp. 1-5, 18-20 July 2012.
[109] F. Ramos, J. Marti, V. Polo, and J. M. Fuster, "On the use of fiber-induced self-phase modulation to reduce chromatic dispersion effects in microwave/millimeter-wave optical systems," *Photonics Technology Letters, IEEE,* vol. 10, pp. 1473-1475, 1998.
[110] L. N. Binh, *Optical Fiber Communications Systems: Theory, Practice, and Matlab Simulink Models*: Taylor & Francis, 2008.
[111] R. A. Saunders, J. P. King, and I. Hardcastle, "Wideband chirp measurement technique for high bit rate sources," *Electronics Letters,* vol. 30, pp. 1336-1338, 1994.
[112] Y. K. Park, T. V. Nguyen, P. A. Morton, J. E. Johnson, O. Mizuhara, J. Jeong, L. D. tzeng, P. D. Yeates, T. Fullowan, P. F. Sciortino, A. M. Sergent, W. T. Tsang, and R. D. Yadvish, "Dispersion-penalty-free transmission over 130-km standard fiber using a 1.55-μm, 10-Gb/s integrated EA/DFB laser with low-extinction ratio and negative chirp," *Photonics Technology Letters, IEEE,* vol. 8, pp. 1255-1257, 1996.
[113] P. Sang-Gyu, A. H. Gnauck, J. M. Wiesenfeld, and L. D. Garrett, "40-Gb/s transmission over multiple 120-km spans of conventional single-mode fiber using highly dispersed pulses," *Photonics Technology Letters, IEEE,* vol. 12, pp. 1085-1087, 2000.
[114] V. Ali, J. Leibrich, and W. Rosenkranz, "Impact of Nonlinearities on Optical OFDM with Direct Detection," *Optical Communication (ECOC), 2007 33rd European Conference and Ehxibition of,* pp. 1-2, 2007.
[115] Y. Benlachtar, G. Gavioli, V. Mikhailov, and R. I. Killey, "Experimental investigation of SPM in long-haul direct-detection OFDM systems," *Opt. Express,* vol. 16, pp. 15477-15482, 2008.
[116] A. J. Lowery, D. Liang Bangyuan, and J. Armstrong, "Performance of Optical OFDM in Ultralong-Haul WDM Lightwave Systems," *Lightwave Technology, Journal of,* vol. 25, pp. 131-138, 2007.
[117] H. Bao and W. Shieh, "Transmission simulation of coherent optical OFDM signals in WDM systems," *Opt. Express,* vol. 15, pp. 4410-4418, 2007.
[118] E. Zehavi, "8-PSK trellis codes on Rayleigh channel," in *Military Communications Conference, 1989. MILCOM '89. Conference Record. Bridging the Gap. Interoperability, Survivability, Security., 1989 IEEE*, 1989, pp. 536-540 vol.2.
[119] M. Ohm and T. Freckmann, "Comparison of different DQPSK transmitters with NRZ and RZ impulse shaping," in *Advanced Modulation Formats, 2004 IEEE/LEOS Workshop on*, 2004, pp. 7-8.

[120] D. J. F. Barros and J. M. Kahn, "Optical Modulator Optimization for Orthogonal Frequency-Division Multiplexing," *Lightwave Technology, Journal of,* vol. 27, pp. 2370-2378, 2009.
[121] Motorola. (2007, Long Term Evolution (LTE): A Technical Overview.
[122] P. Wei-Ren, W. Xiaoxia, V. R. Arbab, F. Kai-Ming, B. Shamee, L. C. Christen, Y. Jeng-Yuan, A. E. Willner, and C. Sien, "Theoretical and Experimental Investigations of Direct-Detected RF-Tone-Assisted Optical OFDM Systems," *Lightwave Technology, Journal of,* vol. 27, pp. 1332-1339, 2009.
[123] K. Forozesh, S. L. Jansen, S. Randel, I. Morita, and H. Tanaka, "The influence of the dispersion map in coherent optical OFDM transmission systems," in *IEEE/LEOS Summer Topical Meetings, 2008 Digest of the*, 2008, pp. 135-136.
[124] L. Christina, L. Ka-Lun, A. Nirmalathas, D. Novak, and R. Waterhouse, "Impact of chromatic dispersion on 60 GHz radio-over-fiber transmission," in *IEEE Lasers and Electro-Optics Society, 2008. LEOS 2008. 21st Annual Meeting of the*, 2008, pp. 89-90.
[125] DiGiWORLD. Markets & Trends, Facts & Figures. *IDATE, 2012*.
[126] J. Gozalvez, "Long-Term Evolution advanced Demonstrations [Mobile Radio]," *Vehicular Technology Magazine, IEEE,* vol. 6, pp. 4-9, 2011.
[127] Agilent Technologies, "Digital Communication Analyzer (DCA), Measure Relative Intensity Noise (RIN)," 2008.
[128] H. Jia-Sheng, L. Hanh, and S. Hui, "Ultra-high power, low RIN and narrow linewidth lasers for 1550nm DWDM 100km long-haul fiber optic link," in *IEEE Lasers and Electro-Optics Society, 2008. LEOS 2008. 21st Annual Meeting of the*, 2008, pp. 894-895.
[129] G. S. D. Gordon, M. J. Crisp, R. V. Penty, and I. H. White, "High-Order Distortion in Directly Modulated Semiconductor Lasers in High-Loss Analog Optical Links With Large RF Dynamic Range," *Lightwave Technology, Journal of,* vol. 29, pp. 3577-3586, 2011.
[130] M. N. Draa, J. Ren, D. C. Scott, W. S. C. Chang, and P. K. L. Yu, "Three laser two-tone setup for measurement of photodiode intercept points," *Opt. Express,* vol. 16, pp. 12108-12113, 2008.
[131] S. Sesia, M. Baker, and I. Toufik, *LTE, The UMTS Long Term Evolution: From Theory to Practice*: Wiley, 2009.
[132] L. Chen, B. Krongold, and J. Evans, "Theoretical Characterization of Nonlinear Clipping Effects in IM/DD Optical OFDM Systems," *Communications, IEEE Transactions on,* vol. 60, pp. 2304-2312, 2012.
[133] T. Yan, W. Shieh, Y. Xingwen, and R. Evans, "Optimum Design for RF-to-Optical Up-Converter in Coherent Optical OFDM Systems," *Photonics Technology Letters, IEEE,* vol. 19, pp. 483-485, 2007.
[134] 3GPP, "EVM for LTE Repeater (3GPP TSG-RAN4 Meeting #52, TS 36.143, Rel-8)," 2009.
[135] T. Kanesan, W. P. Ng, Z. Ghassemlooy, and C. Lu, "Experimental Verification of Optimized LTE-RoF System for eNB Cell Radius Improvement," *Photonics Technology Letters, IEEE,* vol. 24, pp. 2210-2213, 2012.
[136] L. Romano, L. Panseri, C. Samori, and A. L. Lacaita, "Matching requirements in LINC transmitters for OFDM signals," *Circuits and Systems I: Regular Papers, IEEE Transactions on,* vol. 53, pp. 1572-1578, 2006.
[137] W. P. Ng, T. Kanesan, Z. Ghassemlooy, and C. Lu, "Theoretical and Experimental Optimum System Design for LTE-RoF Over Varying Transmission Span and

Identification of System Nonlinear Limit," *Photonics Journal, IEEE,* vol. 4, pp. 1560-1571, 2012.
[138] Y. Aoki, K. Tajima, and I. Mito, "Input power limits of single-mode optical fibers due to stimulated Brillouin scattering in optical communication systems," *Lightwave Technology, Journal of,* vol. 6, pp. 710-719, 1988.
[139] D. Gesbert, M. Shafi, S. Da-shan, P. J. Smith, and A. Naguib, "From theory to practice: an overview of MIMO space-time coded wireless systems," *Selected Areas in Communications, IEEE Journal on,* vol. 21, pp. 281-302, 2003.
[140] A. Al Amin, A. Li, S. Chen, X. Chen, G. Gao, and W. Shieh, "Dual-LP11 mode 4x4 MIMO-OFDM transmission over a two-mode fiber," *Opt. Express,* vol. 19, pp. 16672-16679, 2011.
[141] R. Ryf, S. Randel, A. H. Gnauck, C. Bolle, A. Sierra, S. Mumtaz, M. Esmaeelpour, E. C. Burrows, R. Essiambre, P. J. Winzer, D. W. Peckham, A. H. McCurdy, and R. Lingle, "Mode-Division Multiplexing Over 96 km of Few-Mode Fiber Using Coherent 6<formula formulatype="inline"> <tex Notation="TeX">$,times,$</tex></formula>6 MIMO Processing," *Lightwave Technology, Journal of,* vol. 30, pp. 521-531, 2012.
[142] T. Banham. (2010) Mobile Communications Supplement: The LTE Supplement. *informa telecoms & media*.
[143] W. C. Liu and W. R. Chen, "CPW-fed compact meandered patch antenna for dual-band operation," *Electronics Letters,* vol. 40, pp. 1094-1095, 2004.
[144] T. Kanesan, W. P. Ng, Z. Ghassemlooy, and C. Lu, "Theoretical and Experimental Design of an Alternative System to 2x2 MIMO for LTE over 60 km Directly Modulated RoF Link," in *Global Telecommunications Conference (GLOBECOM 2012), IEEE*, Anaheim, California, pp. 1-4, 03-07 Dec 2012.
[145] W. P. Ng, T. Kanesan, Z. Ghassemlooy, and C. Lu, "Experimental Full Duplex Simultaneous Transmission of LTE over DWDM Directly Modulated RoF System," *Lightwave Technology, IEEE/OSA Journal of* vol. -, pp. -, 2013 (Under Review).
[146] R. Letian, S. E. Elayoubi, and O. B. Haddada, "Impact of Relays on LTE-Advanced Performance," in *Communications (ICC), 2010 IEEE International Conference on*, pp. 1-6.
[147] S. Po-Tsung, A. Ng'oma, L. Chun-Ting, F. Annunziata, C. Jyehong, J. George, M. Sauer, and C. Sien, "2x21 Gbps symmetrical full-duplex transmission of OFDM wireless signals over a bidirectional IMDD Radio-over-Fiber system at 60 GHz," in *Optical Communication (ECOC), 2010 36th European Conference and Exhibition on*, pp. 1-3.
[148] M. Milosavljevic, M. P. Thakur, P. Kourtessis, J. E. Mitchell, and J. M. Senior, "Demonstration of Wireless Backhauling Over Long-Reach PONs," *Lightwave Technology, Journal of,* vol. 30, pp. 811-817, 2012.
[149] J. Ho-Chul, K. Hoon, and C. Yun Chur, "Full-Duplex Radio-Over-Fiber System Using Phase-Modulated Downlink and Intensity-Modulated Uplink," *Photonics Technology Letters, IEEE,* vol. 21, pp. 9-11, 2009.
[150] K. Hyoung-Jun and S. Jong-In, "Full-Duplex WDM-Based RoF System Using All-Optical SSB Frequency Upconversion and Wavelength Re-Use Techniques," *Microwave Theory and Techniques, IEEE Transactions on,* vol. 58, pp. 3175-3180, 2010.
[151] Y. Jianjun, J. Zhensheng, W. Ting, and C. Gee Kung, "Centralized Lightwave Radio-Over-Fiber System With Photonic Frequency Quadrupling for High-

Frequency Millimeter-Wave Generation," *Photonics Technology Letters, IEEE,* vol. 19, pp. 1499-1501, 2007.

[152] M. Bakaul, A. Nirmalathas, and C. Lim, "Multifunctional WDM optical interface for Millimeter-wave fiber-radio antenna base station," *Lightwave Technology, Journal of,* vol. 23, pp. 1210-1218, 2005.

[153] E. Hugues-Salas, R. P. Giddings, X. Q. Jin, Y. Hong, T. Quinlan, S. Walker, and J. M. Tang, "REAM intensity modulator-enabled 10Gb/s colorless upstream transmission of real-time optical OFDM signals in a single-fiber-based bidirectional PON architecture," *Opt. Express,* vol. 20, pp. 21089-21100, 2012.

[154] P. J. Urban, A. M. J. Koonen, G. D. Khoe, and H. d. Waardt, "Coherent Crosstalk-suppression in WDM Access Networks employing Reflective Semiconductor Optical Amplifiers," *Optical Communication (ECOC), 2007 33rd European Conference and Ehxibition of,* pp. 1-2, 2007.

[155] J. L. Wei, E. Hugues-Salas, R. P. Giddings, X. Q. Jin, X. Zheng, S. Mansoor, and J. M. Tang, "Wavelength reused bidirectional transmission of adaptively modulated optical OFDM signals in WDM-PONs incorporating SOA and RSOA intensity modulators," *Opt. Express,* vol. 18, pp. 9791-9808, 2010.

[156] I. Papagiannakis, M. Omella, D. Klonidis, J. A. L. Villa, A. N. Birbas, J. Kikidis, I. Tomkos, and J. Prat, "Design Characteristics for a Full-Duplex IM/IM Bidirectional Transmission at 10 Gb/s Using Low Bandwidth RSOA," *Lightwave Technology, Journal of,* vol. 28, pp. 1094-1101, 2010.

[157] 3GPP, "Evolved Universal Terrestrial Radio Access (E-UTRA); Physical channels and modulation (3GPP TS 36.211 V10.4.0 Rel-10)," 2011.

[158] 3GPP, "Evolved Universal Terrestrial Radio Access (EUTRA); User Equipment (UE) radio transmission and reception (3GPP TS 36.101 V10.4.0, Rel-10)," 2011.

[159] M. Jaworski and M. Marciniak, "Counteracting of stimulated Brillouin scattering in externally modulated lightwave AM-CATV systems," in *Laser and Fiber-Optical Networks Modeling, 2000. Proceedings of LFNM 2000. 2nd International Workshop on*, 2000, pp. 71-73.

[160] J. D. Downie and J. Hurley, "Experimental study of SBS mitigation and transmission improvement from cross-phase modulation in 10.7 Gb/s unrepeatered systems," *Opt. Express,* vol. 15, pp. 9527-9534, 2007.

[161] A. Kobyakov, M. Mehendale, M. Vasilyev, S. Tsuda, and A. F. Evans, "Stimulated Brillouin scattering in Raman-pumped fibers: a theoretical approach," *Lightwave Technology, Journal of,* vol. 20, pp. 1635-1643, 2002.

[162] M. M. Sisto, S. LaRochelle, and L. A. Rusch, "Carrier-to-noise ratio optimization by modulator bias control in radio-over-fiber links," *Photonics Technology Letters, IEEE,* vol. 18, pp. 1840-1842, 2006.

[163] M. Sauer, A. Kobyakov, and A. B. Ruffin, "Radio-Over-Fiber Transmission With Mitigated Stimulated Brillouin Scattering," *Photonics Technology Letters, IEEE,* vol. 19, pp. 1487-1489, 2007.

[164] T. Kanesan, W. P. Ng, Z. Ghassemlooy, and C. Lu, "Experimental Demonstration of the Compensation of Nonlinear Propagation in LTE RoF system with Directly Modulated Laser," in *Communications (ICC), IEEE International Conference on*, Budaphest, Hungary, pp. 1-4, 09-13 June, 2013. (Accepted for Publication).

[165] T. Kanesan, W. P. Ng, Z. Ghassemlooy, and C. Lu, "Impact of Optical Modulators in LTE RoF System with Nonlinear Compensator for Enhanced Power Budget," in *Optical Fiber Communication (OFC), collocated National Fiber Optic Engineers*

Conference, Conference on (OFC/NFOEC) Anaheim, USA, pp. 1-3, 19-21 March 2013. (Accepted for Publication).

[166] W. P. Ng, T. Kanesan, Z. Ghassemlooy, and C. Lu, "Optical Modulators Diversity for Optimized Nonlinear Compensator in a LTE RoF System " *Lightwave Technology, IEEE/OSA Journal of,* vol. -, pp. -, 2013 (Under Review).

[167] K. Vahala and A. Yariv, "Semiclassical theory of noise in semiconductor lasers - Part I, II," *Quantum Electronics, IEEE Journal of,* vol. 19, pp. 1096-1101, 1983.

[168] S. Karlin and H. M. Taylor, *A First Course in Stochastic Processes*, 2nd ed. New York: Academic Press, 1975.

[169] A. Villafranca, J. Lázaro, ñ. Salinas, and I. Garcés, "Stimulated Brillouin scattering gain profile characterization by interaction between two narrow-linewidth optical sources," *Opt. Express,* vol. 13, pp. 7336-7341, 2005.

[170] G. Goeger, "Modulation Format with Enhanced SPM-Robustness for Electronically Pre-Distorted Transmission," in *Optical Communications, 2006. ECOC 2006. European Conference on*, 2006, pp. 1-2.

[171] Y. Cai, D. G. Foursa, C. R. Davidson, J. X. Cai, O. Sinkin, M. Nissov, and A. Pilipetskii, "Experimental demonstration of coherent MAP detection for nonlinearity mitigation in long-haul transmissions," in *Optical Fiber Communication (OFC), collocated National Fiber Optic Engineers Conference, 2010 Conference on (OFC/NFOEC)*, 2010, pp. 1-3.

[172] P. J. Probert and J. E. Carroll, "Lumped circuit model for prediction of linewidth in Fabry Perot and DFB lasers, including external cavity devices," *Optoelectronics, IEE Proceedings J,* vol. 136, pp. 22-32, 1989.